AFRL-AFOSR-VA-TR-2017-0100

Single photons to multiple octaves:Engineering nonlinear optics in micro-
and nano-structured media

Martin Fejer
LELAND STANFORD JUNIOR UNIV CA
450 SERRA MALL
STANFORD, CA 94305-2004

05/18/2017
Final Report

Air Force Research Laboratory
AF Office Of Scientific Research (AFOSR)/RTB1

FORM SF 298

REPORT DOCUMENTATION PAGE

Form Approved
OMB No. 0704-0188

The public reporting burden for this collection of information is estimated to average 1 hour per response, including the time for reviewing instructions, searching existing data sources, gathering and maintaining the data needed, and completing and reviewing the collection of information. Send comments regarding this burden estimate or any other aspect of this collection of information, including suggestions for reducing the burden, to Department of Defense, Executive Services, Directorate (0704-0188). Respondents should be aware that notwithstanding any other provision of law, no person shall be subject to any penalty for failing to comply with a collection of information if it does not display a currently valid OMB control number.
PLEASE DO NOT RETURN YOUR FORM TO THE ABOVE ORGANIZATION.

1. REPORT DATE *(DD-MM-YYYY)*	2. REPORT TYPE	3. DATES COVERED *(From - To)*
18-05-2017	Final Performance	01 Apr 2012 to 31 Mar 2015

4. TITLE AND SUBTITLE
Single photons to multiple octaves:Engineering nonlinear optics in micro- and nano-structured media

5a. CONTRACT NUMBER

5b. GRANT NUMBER
FA9550-12-1-0110

5c. PROGRAM ELEMENT NUMBER
61102F

6. AUTHOR(S)
Martin Fejer

5d. PROJECT NUMBER

5e. TASK NUMBER

5f. WORK UNIT NUMBER

7. PERFORMING ORGANIZATION NAME(S) AND ADDRESS(ES)
LELAND STANFORD JUNIOR UNIV CA
450 SERRA MALL
STANFORD, CA 94305-2004 US

8. PERFORMING ORGANIZATION REPORT NUMBER

9. SPONSORING/MONITORING AGENCY NAME(S) AND ADDRESS(ES)
AF Office of Scientific Research
875 N. Randolph St. Room 3112
Arlington, VA 22203

10. SPONSOR/MONITOR'S ACRONYM(S)
AFRL/AFOSR RTB1

11. SPONSOR/MONITOR'S REPORT NUMBER(S)
AFRL-AFOSR-VA-TR-2017-0100

12. DISTRIBUTION/AVAILABILITY STATEMENT
A DISTRIBUTION UNLIMITED: PB Public Release

13. SUPPLEMENTARY NOTES

14. ABSTRACT
The two main topics in the proposed work were few-photon nonlinear optics, and generation and amplification of ultrafast IR pulses. Both efforts took advantage of microstructured nonlinear media, e.g. quasi-phasematched (QPM) interactions in periodically-poled ferroelectrics and orientation- patterned semiconductors. Guided-wave interactions were used in some cases to further enhance the wave-mixing efficiency, especially for low-power devices. Because errors in fabrication of waveguides and quasi-phasematching gratings are unavoidable, understanding the effects of
such errors became another important component of the work. Key mid-IR results include design rules for and experimental demonstration of optical parametric chirped pulse amplifiers (OPCPA) in apodized aperiodic QPMgratings for high repetition rate, high average power generation of carrier envelope phase stable mid-IR pulses, and waveguide-OPA-based sources of offset-free seed pulses. Results for quantum frequency conversion
include picosecond time gated conversion of single photons as a key component in a quantum dot spin-photon entanglement experiment. Another important direction was elimination of inelastic scattering noise in visible-to-telecom band conversion via a two-step cascaded process.

15. SUBJECT TERMS
microstructure, nonlinear optics, single photon, frequency conversion

16. SECURITY CLASSIFICATION OF:			17. LIMITATION OF ABSTRACT	18. NUMBER OF	19a. NAME OF RESPONSIBLE PERSON
a. REPORT	b. ABSTRACT	c. THIS PAGE			LUGINSLAND, JOHN

Standard Form 298 (Rev. 8/98)
Prescribed by ANSI Std. Z39.18

FORM SF 298

Unclassified	Unclassified	Unclassified	UU	**PAGES**	**19b. TELEPHONE NUMBER** *(Include area code)* 703-588-1775

Final Technical Report

1. AFOSR GRANT NUMBER: Grant # FA9550-12-1-0110

2. PERIOD COVERED BY REPORT: 04/01/2012 – 03/31/2015

3. TITLE OF PROPOSAL: Single photons to multiple octaves:Engineering nonlinear optics in micro- and nano-structured media

4. LIST OF 17 MANUSCRIPTS SUBMITTED OR PUBLISHED UNDER AFOSR SPONSORSHIP DURING THIS REPORTING PERIOD (chronological by publication date)

a) C. Heese, C.R. Phillips, L. Gallman, M.M. Fejer, and U. Keller, "Role of apodization in optical parametric amplifiers based on aperiodic quasi-phasematching gratings," *Opt. Express* **20**, pp. 18066-71 (July 2012)

b) J.S. Pelc, P.S. Kuo, O. Slattery, L.J. Ma, X. Tang, M.M. Fejer, "Dual-channel, single-photon upconversion detector at 1.3 μm," *Opt. Express* **20**, pp. 19075-87 (August 2012).

c) K. De Greve, L. Yu, P.L. McMahon, J.S. Pelc, C.M. Natarajan, N.Y. Kim, E. Abe, S. Maier, C. Schneider, M. Kamp, S. Hofling, R.H. Hadfield, A. Forchel, A M.M. Fejer, Y. Yamamoto, "Quantum-dot spin-photon entanglement via frequency downconversion to telecom wavelength," *Nature* **491**, p. 421 (November 2012)

d) C. Heese, C.R. Phillips, B.W. Mayer, L. Gallmann, M.M. Fejer, U. Keller, "75 MW few-cycle mid-infrared pulses from a collinear apodized APPLN-based OPCPA," *Opt. Express* **20**, pp. 26888-94 (November 2012).

e) C.R. Phillips, J.S. Pelc, M.M. Fejer, "Parametric processes in quasi-phasematching gratings with random duty cycle errors," *JOSA-B* **30**, pp. 982-93 (April 2013).

f) C.R. Phillips, C. Langrock, D. Chang, Y.W. Lin, L. Gallmann, "Apodization of chirped quasi-phasematching devices," *JOSA-B* **30**, pp. 1551-68 (June 2013).

g) G.L. Shentu, J.S. Pelc, X.D. Wang, Q.C. Sun, M.Y. Zheng, M.M. Fejer, Q. Zhang, J.W. Pan, "Ultralow noise up-conversion detector and spectrometer for the telecom band," *Opt. Express* **21**, pp. 13986-13991 (June 2013).

h) K. De Greve, P.L. McMahon, L. Yu, J.S. Pelc, C. Jones, C.M. Natarajan, N.Y. Kim, E. Abe, S. Maier, C. Schneider, M. Kamp, S. Hofling, R.H. Hadfield, A. Forchel, M.M. Fejer, Y. Yamamoto, "Complete tomography of a high-fidelity solid-state entangled spin-photon qubit pair," *Nature Communications* **4**, art. 2228 (July 2013)

i) G.L. Shentu, Q.C. Sun, X. Jiang, X.D. Wang, J.S. Pelc, M.M. Fejer, Q. Zhang, J.W. Pan, "217 km long distance photon-counting optical time-domain reflectometry based on ultra-low noise up-conversion single photon detector," *Opt. Express* **21**, pp. 24674-79 (Oct. 2013).

j) B.W. Mayer, C.R. Phillips, L. Gallmann, M.M. Fejer, U. Keller, "Sub-four-cycle laser pulses directly from a high-repetition-rate optical parametric chirped-pulse amplifier at 3.4 μm," *Opt. Lett.* **38**, pp. 4265-68 (Nov. 2013).

k) G.L. Shentu, X.X. Xia, Q.C. Sun, J.S. Pelc, M.M. Fejer, Q. Zhang, J.W. Pan, "Upconversion detection near 2 μm at the single photon level," *Opt. Lett.* **38**, pp. 4985-87 (Dec. 2013).

l) C.R. Phillips, B.W. Mayer, L. Gallmann, M.M. Fejer, U. Keller, "Design constraints of optical parametric chirped pulse amplification based on chirped quasi-phase-matching gratings," *Opt. Express* **22**, pp. 9627-58, (April 2014).

m) T. Guerreiro, E. Pomarico, B. Sanguinetti, N. Sangouard, J.S. Pelc, C. Langrock, M.M. Fejer, H. Zbinden, R.T. Thew, N. Gisin, "Nonlinear interaction of independent single photons based on integrated nonlinear optics," *Nature Communications* **4**, art. 2324 (August 2014).

n) D. Chang, C. Langrock, Y.W. Lin, C.R. Phillips, C.V. Bennett, M.M. Fejer, "Complex-transfer-function analysis of optical-frequency converters," *Opt. Lett.* **39**, pp. 5106-09 (September 2014).

o) T. Guerreiro, A. Martin, B. Sanguinetti, J.S. Pelc, C. Langrock, M.M. Fejer, N. Gisin, H. Zbinden, N. Sangouard, R.T. Thew, "Nonlinear Interaction between Single Photons," *Phys. Rev. Lett.* **113**, art. no. 173601 (Oct. 2014).

p) Derek Chang, Yu-Wei Lin, C. Langrock, C.R. Phillips, C.V. Bennett, M.M. Fejer, "Phase-mismatched localized fields in A-PPLN waveguide devices," *Opt. Lett.* **41**, pp 400-3 (January 2016).*

q) A.S. Mayer, C.R. Phillips, C. Langrock, A. Klenner, A.R. Johnson, K. Luke, Y. Okawachi, M. Lipson, A.L. Gaeta, M.M. Fejer, U. Keller, "Offset-Free Gigahertz Mid-infrared Frequency Comb Based on Optical Parametric Amplification in a Periodically Poled Lithium Niobate Waveguide," *Phys. Rev. Applied* **6**, art. no. 054009 (November 2016).*

* submitted after the performance period, but acknowledges AFOSR support that occurred during the performance period

5. SCIENTIFIC PERSONNEL SUPPORTED BY THIS PROJECT AND DEGREES AWARDED DURING THIS REPORTING PERIOD:

> Faculty - M.M. Fejer
> Senior Staff – C. Langrock
> Students – D. Chang (Ph.D. awarded 2014), Jason Pelc (Ph.D. awarded 2012), C.R. Phillips (Ph.D. awarded 2012), Yu-Wei Lin

6. REPORT OF INVENTIONS BY TITLE ONLY

7. SCIENTIFIC PROGRESS AND ACCOMPLISHMENTS: See Final Technical Report

8. TECHNOLOGY TRANSFER:
This program explores micro-structured nonlinear optical materials and quasi-phasematched (QPM) nonlinear devices based on them for ultrafast and few-photon nonlinear optics. Technology developed under this and predecessor programs has let to numerous collaborations with industry and academic institutions. Most recently we have collaborated with LLNL, UC Davis, U. Geneva, NIST-Gaithersburg, ETH Zurich, Harvard U.. Working under DARPA support, we are transferring the fabrication technology for quantum frequency conversion waveguides, developed in large part under AFOSR support, to AdVR, Inc. for commercialization.

9. CORRESPONDENCE ADDRESS:
> Martin M. Fejer, P.I.
> Ginzton Laboratory   (tel) 650-799-3076
> Stanford University   (fax) 650-723-2666
> Stanford, CA 94305   fejer@stanford.edu

Summary of Results

I. Introduction

This final technical report summarizes progress in a three-year program with AFOSR support under #FA9550-12-1-0110. This program is a continuation of research carried out under AFOSR awards, FA9550-05-1-0180, F49620-99-1-0270 and F49620-02-1-0240.

There were two main topics in the proposed work: few-photon nonlinear optics, and generation and amplification of ultrafast pulses. Both efforts took advantage of microstructured nonlinear media, in particular quasi-phasematched interactions in periodically-poled ferroelectrics and orientation-patterned semiconductors. Guided-wave interactions were used in some cases to further enhance the wave-mixing efficiency, especially for low-power devices. Because errors in fabrication of waveguides and QPM gratings are unavoidable, understanding the effects of such errors on device performance was important for both few-photon and ultrafast devices, and so became another important component of the work.

This report will be structured as a brief summary of the results of the key results described in the 16 supported publications (also appended at the end of the report), along with outlooks for future work in those areas. It is divided into three sections: ultrafast interactions, few-photon interactions, and imperfect nonlinear structures.

II. Technical Report

II.1 Ultrafast pulse amplification

The generation of energetic few-cycle pulses in the mid-IR is of interest for applications such as high-harmonic generation and molecular dynamics. While amplification of few-cycle pulses in the near-IR to millijoule levels and above is now well developed in laser amplifiers based on Ti:sapphire and various Yb hosts, the lack of suitable mid-IR hosts has led to investigation of optical parametric chirped-pulse amplification (OPCPA) as method to generate energetic few-cycle pulses in this spectral region. In our previous three-year program, we showed that the bandwidth and phase response of quasi-phasematched optical parametric amplifiers (OPA) can be engineered fairly arbitrarily through the use of aperiodic quasi-phasematching, i.e. using chirped QPM gratings to broaden the phasematching and hence the gain spectrum, as well as to manipulate the spectral phase of the generated pulses. The student who worked on this project here at Stanford subsequently became a post-doc in Ursula Keller's group at the ETH Zurich, with whose group we continued this work bringing it to fruition as the highest average power (at the time) source of few-cycle mid-IR pusles. This work is described in

C. Heese, C.R. Phillips, L. Gallman, M.M. Fejer, and U. Keller, "Role of apodization in optical parametric amplifiers based on aperiodic quasi-phasematching gratings," *Opt. Express* **20**, pp. 18066-71 (July 2012)

C. Heese, C.R. Phillips, B.W. Mayer, L. Gallmann, M.M. Fejer, U. Keller, "75 MW few-cycle mid-infrared pulses from a collinear apodized APPLN-based OPCPA," *Opt. Express* **20**, pp. 26888-94 (November 2012).

C.R. Phillips, J.S. Pelc, M.M. Fejer, "Parametric processes in quasi-phasematching gratings with random duty cycle errors," *JOSA-B* **30**, pp. 982-93 (April 2013).

B.W. Mayer, C.R. Phillips, L. Gallmann, M.M. Fejer, U. Keller, "Sub-four-cycle laser pulses directly from a high-repetition-rate optical parametric chirped-pulse amplifier at 3.4 μm," *Opt. Lett.* **38**, pp. 4265-68 (Nov. 2013)

C.R. Phillips, B.W. Mayer, L. Gallmann, M.M. Fejer, U. Keller, "Design constraints of optical parametric chirped pulse amplification based on chirped quasi-phase-matching gratings," *Opt. Express* **22**, pp. 9627-58, (April 2014).

Recently a system using a PPLN waveguide OPA to generate a carrier-envelope-offset-free gigahertz frequency comb tunable from 2.5-4.2 μm requiring two orders of magnitude less pump power than conventional methods was demonstrated for use as a seed for subsequent high-pulse-energy devices. This work is described in

A.S. Mayer, C.R. Phillips, C. Langrock, A. Klenner, A.R. Johnson, K. Luke, Y. Okawachi, M. Lipson, A.L. Gaeta, M.M. Fejer, U. Keller, "Offset-Free Gigahertz Mid-infrared Frequency Comb Based on Optical Parametric Amplification in a Periodically Poled Lithium Niobate Waveguide," *Phys. Rev. Applied* **6**, art. no. 054009 (November 2016).

The work on power scaling of mid-IR OPAs has continued at ETH Zurich subsequent to the completion of this AFOSR program. The current goal of the work is demonstration of a 50-W average power (50 kHz, 1 mJ) of 3.5 μm pulses of ~30-fs duration, a carrier-envelope-phase stabilized source whose combination of high repetition rate, high pulse energy, and few-cycle duration that would be of exceptional value for high-field and high-harmonic generation experiments in the mid-IR.

In the area of microstructured semiconductors, we have, in collaboration with the Sorokina group at the Norwegian University of Science and Technology (NTNU) demonstrated generation of mid-IR frequency combs with femtosecond degenerate synchronously pumped optical parametric oscillators in both orientation patterned GaAs (OP-GaAs) and orientation patterned GaP (OP-GaP), and compared performance between these novel microstructured materials. In OP-GaP three cycle pulses at 4.2 μm were generated with ~60% slope efficiency, the best performance to date for a source in this spectral range. A paper on this work acknowledging AFOSR support is in draft.

We are also currently exploring the use of tightly confining PPLN waveguides in collaboration with the Loncar group at Harvard under NSF support to accomplish dispersion engineering in travelling-wave quasi-phasematched frequency-comb generation of the type discussed in the proposal for # FA9550-12-1-0110.

II.2 Few-photon nonlinear devices

In our previous AFOSR program we demonstrated various devices based on efficient mixing of single photons at frequency ω_s with a classical pump at frequency ω_p in order to up- or down-shift the carrier frequency of the photon ($\omega_{out} = \omega_s \pm \omega_p$) while maintaining its coherence properties. Common applications are upconversion of IR photons to enable detection with convenient single-photon detectors in the near-IR/visible (e.g. silicon avalanche photodiodes) or downconversion of visible or near-IR photons from ions, NV centers, or quantum dots to 1.5 µm for transmission down optical fibers for quantum communication schemes.

Another useful feature of these devices is that they can manipulate the spectral or temporal structure of the converted photons. For example, a pulsed pump serves as a time-gated mixer. We took advantage of this feature to both down-convert 911-nm single photons from a quantum dot to 1.5 µm and to gate the mixing process with a ~10 ps window. The latter served to erase which-path information and enable the entanglement of a photon with the spin of a quantum-dot. Aspects of this work, done in collaboration with Yoshihisa Yamamoto's group at Stanford, were described in

> K. De Greve, L. Yu, P.L. McMahon, J.S. Pelc, C.M. Natarajan, N.Y. Kim, E. Abe, S. Maier, C. Schneider, M. Kamp, S. Hofling, R.H. Hadfield, A. Forchel, A M.M. Fejer, Y. Yamamoto, "Quantum-dot spin-photon entanglement via frequency downconversion to telecom wavelength," *Nature* **491**, p. 421 (November 2012)

> K. De Greve, P.L. McMahon, L. Yu, J.S. Pelc, C. Jones, C.M. Natarajan, N.Y. Kim, E. Abe, S. Maier, C. Schneider, M. Kamp, S. Hofling, R.H. Hadfield, A. Forchel, M.M. Fejer, Y. Yamamoto, "Complete tomography of a high-fidelity solid-state entangled spin-photon qubit pair," *Nature Communications* **4**, art. 2228 (July 2013)

> K. De Greve, P.L. McMahon, L. Yu, J.S. Pelc, C. Jones, C.M. Natarajan, N.Y. Kim, E. Abe, S. Maier, C. Schneider, M. Kamp, S. Hofling, R.H. Hadfield, A. Forchel, M.M. Fejer, Y. Yamamoto, "Complete tomography of a high-fidelity solid-state entangled spin-photon qubit pair," *Nature Communications* **4**, art. 2228 (July 2013)

Another use of time-gated mixing is to increase the timing resolution or the counting rate beyond that obtainable from the detector properties alone. An example of this use, two-channel up-conversion mixing to double the possible counting rate for single photons in a silicon APD, an experiment carried out in collaboration with Tang *et al* at NIST-Gaithersburg is discussed in

> J.S. Pelc, P.S. Kuo, O. Slattery, L.J. Ma, X. Tang, M.M. Fejer, "Dual-channel, single-photon upconversion detector at 1.3 µm," *Opt. Express* **20**, pp. 19075-87 (August 2012).

An issue with these devices is that inelastic scattering of the classical pump can produce spontaneous photons at longer wavelengths that are indistinguishable from the single signal photons, and hence are a noise source in the mixing process. Both Raman processes and spontaneous parametric fluorescence (phasematched due to errors in the domain patterning, discussed in the following section) can both contribute to this undesired inelastic scattering. The most convenient way to evade these scattering processes is through the use of a pump whose wavelength is longer than the signal input or output photons, so that the noise photons do not exist in spectral ranges of interest. Two experiments using a 1950-nm Tm:fiber laser as a pump for low-noise up-conversion of 1.5-µm band photons in the range of silicon APDs, one as an ultrasensitive time-domain reflectometer (detecting defects over a 217-km range) and the other as an ultrasensitive single-pixel spectrometer are reported in

G.L. Shentu, Q.C. Sun, X. Jiang, X.D. Wang, J.S. Pelc, M.M. Fejer, Q. Zhang, J.W. Pan, "217 km long distance photon-counting optical time-domain reflectometry based on ultra-low noise up-conversion single photon detector," *Opt. Express* **21**, pp. 24674-79 (Oct. 2013).

G.L. Shentu, J.S. Pelc, X.D. Wang, Q.C. Sun, M.Y. Zheng, M.M. Fejer, Q. Zhang, J.W. Pan, "Ultralow noise up-conversion detector and spectrometer for the telecom band," *Opt. Express* **21**, pp. 13986-13991 (June 2013).

Such a long-wave pump imposes limitations on the possible mixing process, since frequencies of the signal and output photons cannot differ by more than a factor of two if the pump photon is kept as the longest wavelength of the three photons involved. A solution to this issue described in the proposal is to use a cascaded process, where the pump photon first mixes with the signal photon to produce an intermediate frequency photon ($\omega_{int} = \omega_s \pm \omega_p$), and then a second pump photon mixes with the intermediate frequency photon to generate the output, so that ($\omega_{out} = \omega_s \pm 2\omega_p$). With this cascaded scheme, visible photons can be interconverted with 1.5 µm photons with minimal spontaneous scattering noise. A waveguide device using a 2.1-µm pump to down-convert red (650 nm) to 1.5 µm photons to by such a cascaded mixing process in a novel "U-bend" configuration was reported at CLEO this year (paper FTh4A.4), and is in draft as a publication which will acknowledge AFOSR support.

A more extreme example of nonlinear optics with few photons was the demonstration of summing of photons from two independent heralded sources in a PPLN waveguide. In addition to being an extreme example of nonlinear optics at the quantum level, these experiments show prospects for heralding of maximally entangled photon pairs created at a distance, and photon triplets for study of exotic quantum optical phenomena, especially if the more highly nonlinear waveguides under development with the Loncar group at Harvard mentioned earlier become available.

T. Guerreiro, E. Pomarico, B. Sanguinetti, N. Sangouard, J.S. Pelc, C. Langrock, M.M. Fejer, H. Zbinden, R.T. Thew, N. Gisin, "Nonlinear interaction of independent single photons based on integrated nonlinear optics," *Nature Communications* **4**, art. 2324 (August 2014).

T. Guerreiro, A. Martin, B. Sanguinetti, J.S. Pelc, C. Langrock, M.M. Fejer, N. Gisin, H. Zbinden, N. Sangouard, R.T. Thew, "Nonlinear Interaction between Single Photons," *Phys. Rev. Lett.* **113**, art. no. 173601 (Oct. 2014).

These sorts of quantum frequency conversion devices developed under AFOSR support are now widely viewed as essential for practical quantum information networks. We now have a program under DARPA support to improve and transfer the basic PPLN waveguide technology to a commercial vendor, AdvR, Inc.. More advanced devices are being developed in collaboration with the Institute for Quantum Optics in Innsbruck under ARL support. Under NSF support we are investigating tightly confining waveguide architectures based on ion-sliced PPLN waveguides that would offer order-of-magnitude increases in conversion efficiency compared to the proton-exchange waveguides we have been using to date, as well as the possibility of dispersion engineering to manipulate spectral and temporal behavior of the devices.

II.3 Design and tolerances for QPM devices

Aperiodic QPM gratings arise both as a design tool, for engineering the spectral response of nonlinear mixing devices, and as a result of unavoidable errors that occur in the fabrication of quasi-phasematching gratings. The resulting deviations of the spectral behavior of nonlinear mixing processes in these non-ideal devices can have serious effects on the performance of devices based on them. We therefore undertook theoretical and experimental studies to quantify the effects of such errors, to understand whether they could explain observed degradation of device performance, and to enable setting of fabrication tolerances for future device designs.

The design of aperiodic gratings, in particular ones that adiabatically turn on and turn off the nonlinear mixing process, are essential to avoid spectral ripples that would otherwise result from the abrupt transitions in the mixing efficiency. Various approaches and resulting design rules for such adiabatic gratings are discussed in

> C.R. Phillips, C. Langrock, D. Chang, Y.W. Lin, L. Gallmann, "Apodization of chirped quasi-phasematching devices," *JOSA-B* **30**, pp. 1551-68 (June 2013).

Small random errors in the duty-cycle of QPM gratings do not significantly affect the conversion near the spectral peak of the phasematching, but do add a very broad spectral pedestal that causes a small, but in some contexts significant, nonlinear mixing efficiency to occur for processes that would be forbidden in a perfect QPM grating. The most important manifestation of these weak "disorder phasematched" processes is the parametric fluorescence noise that arises in quantum frequency conversion devices. Detailed theoretical predictions for such noise pedestals as well as other manifestations such as distortion of transfer functions for ultrafast devices were investigated in

> C.R. Phillips, J.S. Pelc, M.M. Fejer, "Parametric processes in quasi-phasematching gratings with random duty cycle errors," *JOSA-B* **30**, pp. 982-93 (April 2013).

Another type of fabrication error that can arise in waveguide devices is geometric inhomogeneity along the length of the waveguide. These errors can distort the shape of the spectral response of the mixing process, especially in the vicinity of the phasematching peak, and so are in some sense complementary to the effects arising from duty cycle errors in the QPM grating. An experimental technique for characterizing these spectral distortions, and inferring the geometrical errors in the waveguides that must exist to cause these distortions, was developed based on measuring the complex amplitude of the generated pulse to allow computation of the complex transfer function of the device, given the complex spectrum of the input pulse. From this transfer function, the errors in the waveguide geometry can be computed via an inverse Fourier transform. The method is described in

> D. Chang, C. Langrock, Y.W. Lin, C.R. Phillips, C.V. Bennett, M.M. Fejer, "Complex-transfer-function analysis of optical-frequency converters," *Opt. Lett.* **39**, pp. 5106-09 (September 2014).

Even in hypothetical perfectly fabricated devices, undesired mixing products in ultrafast nonlinear interactions can occur, even highly phase-mismatched processes, due to so-called "localized fields" that depend on the interplay of group-velocity mismatch, phase mismatch, and pump depletion. A model for these effects, its experimental verification, and methods to reduce the strength of the "localized fields" are presented in

> Derek Chang, Yu-Wei Lin, C. Langrock, C.R. Phillips, C.V. Bennett, M.M. Fejer, "Phase-mismatched localized fields in A-PPLN waveguide devices," *Opt. Lett.* **41**, pp 400-3 (January 2016).

III. Summary

We report results in three areas involving nonlinear devices in microstructured media: ultrafast pulse generation, especially carrier-envelope-phase-stable pulses and frequency combs in the mid-IR, quantum frequency conversion devices, and general design and tolerance models for quasi-phasematched devices. A total of 17 papers were published, including one Nature, two Nature Communications, one Physical Review Letter, and four Optics Letters. Four graduate students were supported, three of which obtained Ph.D.'s during the reporting period.

Prospects for continued progress in these fields by extending the design concepts and fabrication methods developed here are excellent. Our work resulted in the then-highest efficiency and highest average power generation of femtosecond mid-IR pulses, and is on the way to scaling to 50 W average powers at millijoule pulse energies at ETH Zurich. The waveguide quantum frequency conversion devices are in increasingly wide use by many groups involved in quantum information research. This project has had follow-up support from the Army Research Laboratory (CDQI) and NSF; we are in the process of DARPA-funded technology transfer to a commercial vendor, AdvR, Inc.

IV. Copies of manuscripts submitted or published under AFOSR sponsorship during this reporting period

LIST OF 17 MANUSCRIPTS SUBMITTED OR PUBLISHED UNDER AFOSR
SPONSORSHIP DURING THIS REPORTING PERIOD (chronological by publication date)

a) C. Heese, C.R. Phillips, L. Gallman, M.M. Fejer, and U. Keller, "Role of apodization in optical parametric amplifiers based on aperiodic quasi-phasematching gratings," *Opt. Express* **20**, pp. 18066-71 (July 2012)

b) J.S. Pelc, P.S. Kuo, O. Slattery, L.J. Ma, X. Tang, M.M. Fejer, "Dual-channel, single-photon upconversion detector at 1.3 μm," *Opt. Express* **20**, pp. 19075-87 (August 2012).

c) K. De Greve, L. Yu, P.L. McMahon, J.S. Pelc, C.M. Natarajan, N.Y. Kim, E. Abe, S. Maier, C. Schneider, M. Kamp, S. Hofling, R.H. Hadfield, A. Forchel, A M.M. Fejer, Y. Yamamoto, "Quantum-dot spin-photon entanglement via frequency downconversion to telecom wavelength," *Nature* **491**, p. 421 (November 2012)

d) C. Heese, C.R. Phillips, B.W. Mayer, L. Gallmann, M.M. Fejer, U. Keller, "75 MW few-cycle mid-infrared pulses from a collinear apodized APPLN-based OPCPA," *Opt. Express* **20**, pp. 26888-94 (November 2012).

e) C.R. Phillips, J.S. Pelc, M.M. Fejer, "Parametric processes in quasi-phasematching gratings with random duty cycle errors," *JOSA-B* **30**, pp. 982-93 (April 2013).

f) C.R. Phillips, C. Langrock, D. Chang, Y.W. Lin, L. Gallmann, "Apodization of chirped quasi-phasematching devices," *JOSA-B* **30**, pp. 1551-68 (June 2013).

g) G.L. Shentu, J.S. Pelc, X.D. Wang, Q.C. Sun, M.Y. Zheng, M.M. Fejer, Q. Zhang, J.W. Pan, "Ultralow noise up-conversion detector and spectrometer for the telecom band," *Opt. Express* **21**, pp. 13986-13991 (June 2013).

h) K. De Greve, P.L. McMahon, L. Yu, J.S. Pelc, C. Jones, C.M. Natarajan, N.Y. Kim, E. Abe, S. Maier, C. Schneider, M. Kamp, S. Hofling, R.H. Hadfield, A. Forchel, M.M. Fejer, Y. Yamamoto, "Complete tomography of a high-fidelity solid-state entangled spin-photon qubit pair," *Nature Communications* **4**, art. 2228 (July 2013)

i) G.L. Shentu, Q.C. Sun, X. Jiang, X.D. Wang, J.S. Pelc, M.M. Fejer, Q. Zhang, J.W. Pan, "217 km long distance photon-counting optical time-domain reflectometry based on ultra-low noise up-conversion single photon detector," *Opt. Express* **21**, pp. 24674-79 (Oct. 2013).

j) B.W. Mayer, C.R. Phillips, L. Gallmann, M.M. Fejer, U. Keller, "Sub-four-cycle laser pulses directly from a high-repetition-rate optical parametric chirped-pulse amplifier at 3.4 μm," *Opt. Lett.* **38**, pp. 4265-68 (Nov. 2013).

k) G.L. Shentu, X.X. Xia, Q.C. Sun, J.S. Pelc, M.M. Fejer, Q. Zhang, J.W. Pan, "Upconversion detection near 2 μm at the single photon level," *Opt. Lett.* **38**, pp. 4985-87 (Dec. 2013).

l) C.R. Phillips, B.W. Mayer, L. Gallmann, M.M. Fejer, U. Keller, "Design constraints of optical parametric chirped pulse amplification based on chirped quasi-phase-matching gratings," *Opt. Express* **22**, pp. 9627-58, (April 2014).

m) T. Guerreiro, E. Pomarico, B. Sanguinetti, N. Sangouard, J.S. Pelc, C. Langrock, M.M. Fejer, H. Zbinden, R.T. Thew, N. Gisin, "Nonlinear interaction of independent single photons based on integrated nonlinear optics," *Nature Communications* **4**, art. 2324 (August 2014).

n) D. Chang, C. Langrock, Y.W. Lin, C.R. Phillips, C.V. Bennett, M.M. Fejer, "Complex-transfer-function analysis of optical-frequency converters," *Opt. Lett.* **39**, pp. 5106-09 (September 2014).

o) T. Guerreiro, A. Martin, B. Sanguinetti, J.S. Pelc, C. Langrock, M.M. Fejer, N. Gisin, H. Zbinden, N. Sangouard, R.T. Thew, "Nonlinear Interaction between Single Photons," *Phys. Rev. Lett.* **113**, art. no. 173601 (Oct. 2014).

p) Derek Chang, Yu-Wei Lin, C. Langrock, C.R. Phillips, C.V. Bennett, M.M. Fejer, "Phase-mismatched localized fields in A-PPLN waveguide devices," *Opt. Lett.* **41**, pp 400-3 (January 2016).*

q) A.S. Mayer, C.R. Phillips, C. Langrock, A. Klenner, A.R. Johnson, K. Luke, Y. Okawachi, M. Lipson, A.L. Gaeta, M.M. Fejer, U. Keller, "Offset-Free Gigahertz Mid-infrared Frequency Comb Based on Optical

Parametric Amplification in a Periodically Poled Lithium Niobate Waveguide," *Phys. Rev. Applied* **6**, art. no. 054009 (November 2016).*

* submitted after the performance period, but acknowledges AFOSR support that occurred during the performance period

a) C. Heese, C.R. Phillips, L. Gallman, M.M. Fejer, and U. Keller, "Role of apodization in optical parametric amplifiers based on aperiodic quasi-phasematching gratings," *Opt. Express* **20**, pp. 18066-71 (July 2012)

Role of apodization in optical parametric amplifiers based on aperiodic quasi-phasematching gratings

C. Heese,[1,*] C. R. Phillips,[2] L. Gallmann,[1] M. M. Fejer,[2] and U. Keller[1]

[1]*Department of Physics, Institute of Quantum Electronics, ETH Zurich, 8093 Zurich, Switzerland*
[2]*Edward L. Ginzton Laboratory, Stanford University, Stanford, California 94305, USA*
[*]*heese@phys.ethz.ch*

Abstract: We experimentally demonstrate and analyze two different techniques for apodizing the nonlinear coupling in aperiodically poled MgO:LiNbO$_3$ (APPLN) used in an ultrabroadband optical parametric chirped pulse amplifier (OPCPA). With an adiabatic increase of the nonlinear coupling, a smooth gain spectrum and spectral phase is preserved during amplification in such media. The two approaches we explore are poling period apodization (PPA) and duty cycle apodization (DCA). For the first implementation of the apodized APPLN amplifier we use a constant chirp-rate in the grating k-vector. The nonlinear coupling is apodized over 10% of the total length at each side of the APPLN chip. This allows us to achieve high-intensity output pulses with clean temporal structure.

©2012 Optical Society of America

OCIS codes: (140.7090) Ultrafast lasers; (190.4970) Parametric oscillators and amplifiers; (140.3580) Lasers, solid-state.

References and links

1. P. Colosimo, G. Doumy, C. I. Blaga, J. Wheeler, C. Hauri, F. Catoire, J. Tate, R. Chirla, A. M. March, G. G. Paulus, H. G. Muller, P. Agostini, and L. F. DiMauro, "Scaling strong-field interactions towards the classical limit," Nat. Phys. **4**(5), 386–389 (2008).
2. D. Brida, C. Manzoni, G. Cirmi, M. Marangoni, S. Bonora, P. Villoresi, S. De Silvestri, and G. Cerullo, "Few-optical-cycle pulses tunable from the visible to the mid-infrared by optical parametric amplifiers," J. Opt. **12**(1), 013001 (2010).
3. M. Charbonneau-Lefort, B. Afeyan, and M. M. Fejer, "Optical parametric amplifiers using chirped quasi-phase-matching gratings I: practical design formulas," J. Opt. Soc. Am. B **25**(4), 463–480 (2008).
4. M. Charbonneau-Lefort, M. M. Fejer, and B. Afeyan, "Tandem chirped quasi-phase-matching grating optical parametric amplifier design for simultaneous group delay and gain control," Opt. Lett. **30**(6), 634–636 (2005).
5. C. R. Phillips and M. M. Fejer, "Efficiency and phase of optical parametric amplification in chirped quasi-phase-matched gratings," Opt. Lett. **35**(18), 3093–3095 (2010).
6. C. Heese, L. Gallmann, U. Keller, C. R. Phillips, and M. M. Fejer, "Ultrabroadband, highly flexible amplifier for ultrashort midinfrared laser pulses based on aperiodically poled Mg:LiNbO$_3$," Opt. Lett. **35**(14), 2340–2342 (2010).
7. R. Trebino and D. J. Kane, "Using phase retrieval to measure the intensity and phase of ultrashort pulses: frequency-resolved optical gating," J. Opt. Soc. Am. A **10**(5), 1101–1111 (1993).
8. T. Umeki, M. Asobe, T. Yanagawa, O. Tadanaga, Y. Nishida, K. Magari, and H. Suzuki, "Broadband wavelength conversion based on apodized χ$^{(2)}$ grating," J. Opt. Soc. Am. B **26**(12), 2315–2322 (2009).
9. J. Huang, X. P. Xie, C. Langrock, R. V. Roussev, D. S. Hum, and M. M. Fejer, "Amplitude modulation and apodization of quasiphase-matched interactions," Opt. Lett. **31**(5), 604–606 (2006).
10. G. Steinmeyer, D. H. Sutter, L. Gallmann, N. Matuschek, and U. Keller, "Frontiers in ultrashort pulse generation: pushing the limits in linear and nonlinear optics," Science **286**(5444), 1507–1512 (1999).
11. I. A. Walmsley, L. Waxer, and C. Dorrer, "The role of dispersion in ultrafast optics," Rev. Sci. Instrum. **72**(1), 1–29 (2001).
12. M. M. Fejer, G. A. Magel, D. H. Jundt, and R. L. Byer, "Quasi-phase-matched second harmonic generation: tuning and tolerances," IEEE J. Quantum Electron. **28**(11), 2631–2654 (1992).
13. C. Erny, C. Heese, M. Haag, L. Gallmann, and U. Keller, "High-repetition-rate optical parametric chirped-pulse amplifier producing 1-μJ, sub-100-fs pulses in the mid-infrared," Opt. Express **17**(3), 1340–1345 (2009).

14. C. Heese, A. E. Oehler, L. Gallmann, and U. Keller, "High-energy picosecond Nd:YVO$_4$ slab amplifier for OPCPA pumping," Appl. Phys. B **103**(1), 5–8 (2011).
15. P. Russbueldt, T. Mans, G. Rotarius, J. Weitenberg, H. D. Hoffmann, and R. Poprawe, "400 W Yb:YAG Innoslab fs-Amplifier," Opt. Express **17**(15), 12230–12245 (2009).
16. C. Erny, L. Gallmann, and U. Keller, "High-repetition-rate femtosecond optical parametric chirped-pulse amplifier in the mid-infrared," Appl. Phys. B **96**(2-3), 257–269 (2009).
17. O. Chalus, P. K. Bates, M. Smolarski, and J. Biegert, "Mid-IR short-pulse OPCPA with micro-Joule energy at 100kHz," Opt. Express **17**(5), 3587–3594 (2009).

1. Introduction

There is a growing interest in high-intensity ultrashort laser pulses at wavelengths which cannot directly be accessed with laser oscillators. Long wavelengths in the mid-infrared are of special interest for the investigation of the wavelength scaling of non-perturbative laser-matter interactions [1]. A common technique to reach these spectral regions is to convert available laser radiation to the desired spectral region by nonlinear frequency mixing [2]. A very popular class of such sources exploits the second-order nonlinear susceptibility, χ_2, for implementing parametric amplification schemes. Parametric processes are particularly interesting for high-power applications, because in principle no energy needs to be deposited in the amplification medium and thus thermal load is kept at a minimum.

One promising χ_2 medium is aperiodically poled lithium niobate (APPLN) to custom design the quasi-phase matching (QPM) for broadband operation [3]. For parametric amplification with such non-uniform QPM structures we can engineer the gain spectrum and spectral phase over an almost arbitrary bandwidth [4], and we can effectively suppress back-conversion upon saturation of the pump [5]. With a linearly chirped grating we have achieved more than 800-nm amplification bandwidth at µJ-level output pulse energy [6]. However, such a simple linearly chirped QPM design cannot maintain a smooth spectral phase of the amplified pulse, because of the abrupt onset of the nonlinear coupling at the edges of the grating [3].
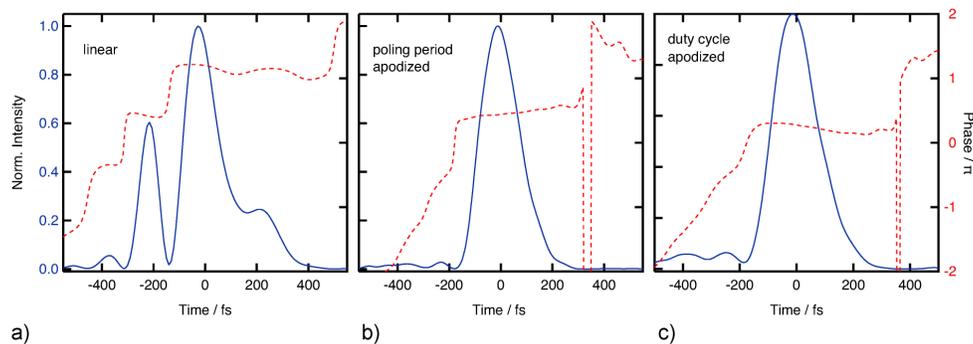

Fig. 1. Measured temporal pulse intensities (solid blue line) and phase (dashed red line) after amplification in an unapodized linear (a), a poling period apodized (b), and a duty cycle apodized (c) APPLN amplifier using a SHG-FROG [7].

2. Apodization of nonlinear interaction

In this paper we experimentally demonstrate two methods to improve a linearly chirped QPM grating to obtain a smooth spectrum and spectral phase after amplification. These methods thus yield pulses with clean temporal profiles holding almost all the energy in the main pulse (see Fig. 1). Both methods are based on the idea to gradually turning on and off the nonlinear coupling between the pump, signal and idler fields at the edges of the grating. This adiabatic approach is also referred to as apodization [3]. One method smoothly detunes the poling period away from the phase-matching condition (poling period apodization, PPA). Another method varies the duty cycle away from the 50% condition necessary for first order QPM (duty cycle apodization, DCA) [8, 9]. To our knowledge, this is the first practical

implementation of an optical parametric amplifier (OPA) that uses apodization techniques to preserve a smooth spectral phase as required for few-cycle pulse generation [10, 11].
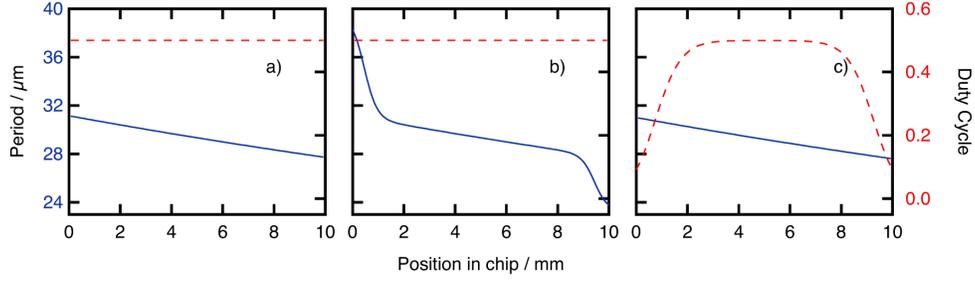

Fig. 2. QPM structures used in the amplifier: (a) linear grating (no apodization), (b) apodization by poling-period change (PPA) and (c) duty cycle apodization (DCA). The blue solid line represents the poling period whereas the duty cycle is plotted as a red dashed line.

With QPM the wave-vector mismatch Δk can be minimized for efficient energy transfer between the interacting waves. This is achieved by an additional k-vector K_g provided by the quasi-phasematching grating: $\Delta k = k_p - k_s - k_i - K_g$. In uniform QPM gratings with a fixed poling period $\Lambda_g = 2\pi/K_g$, $\Delta k = 0$ is achieved for only a single frequency. In APPLN $K_g(z)$ is varied along the grating to produce perfect phase-matching points (PPMP) for many frequencies at differing spatial positions [3]. In our case the linear chirp has the form $K_{g0}(z) = K_{gc} - \kappa'(z - L/2)$, with K_{gc} phase-matching the center frequency. In a QPM grating of finite length and with just a linear chirp profile, there is an abrupt turn-on of the nonlinear coupling between the interacting waves at the edges of the crystal. This abrupt change results in oscillatory structures in the spatial frequency spectrum of the grating. As discussed in Ref [3], such modulations lead to a ripple in the optical frequency spectrum of the output signal and idler waves in a high-gain OPA device. This is the direct origin of the ripples in the gain spectrum and the oscillatory spectral phase contributions.

To avoid such distortions of the amplified pulses, the nonlinear coupling is turned on and off adiabatically at the start and end of the QPM grating. We have chosen smooth tanh-shaped apodization profiles. A possible implementation of the nonlinear coupling apodization is to rapidly detune the poling period from the phase-matched conditions otherwise found toward the ends of the grating. This method is referred to as poling-period apodization (PPA). A possible PPA implementation uses a grating vector of the form:

$$K_g(z) = \left\{1 - K_{apod}(z)\right\} K_{g0}(z) +$$

$$K_{apod}\left\{K_{gc} - a(z)K_a\right\}$$

$$K_{apod}(z) = \frac{1 - \tan h\left(\dfrac{z - l_r}{w_r}\right)\tan h\left(\dfrac{L - z - l_r}{w_r}\right)}{1 - \tan h\left(-\dfrac{l_r}{w_r}\right)}$$

$$a(z) = \begin{cases} 1 & \text{for } z < L/2 \\ -1 & \text{for } z \geq L/2 \end{cases}$$

Apodization begins at a distance of $l_r = 1$ mm from the edges of the grating with a width of $w_r = 0.5$ mm and extends all the way to the edges on either side of the grating as shown in Fig. 2(b). The total length of the grating is $L = 10$mm and $K_a = 5$ cm^{-1} determines the degree of phase-mismatch at the edges of the grating. $K_{apod}(z)$ increases monotonically towards

$K_{apod}(0) = 1$ and $K_{apod}(L) = 1$ at the edges and is zero in the middle, leaving the linearly chirped center unmodified.

Another apodization method, which we refer to as duty-cycle apodization (DCA), is to adiabatically change the duty cycle away from the usual 50% used in first-order QPM [9, 12]. In this context, duty cycle refers to the ratio of the lengths of two neighboring ferro-electric domains with opposite poling. In conventional, periodically poled devices, a duty cycle of 50% (equal length of neighboring domains) is chosen since this maximizes the amplitude of the first Fourier order of the grating, and hence the conversion efficiency. The variation of the duty cycle $D(z)$ along the propagation direction takes the following form:

$$D(z) = 0.5\,D_{apod}(z)$$

$$D_{apod}(z) = \frac{1}{4}\left\{1 + \tan h\left(\frac{z - l_d}{w_d}\right)\left[1 + \tan h\left(\frac{L - z - l_d}{w_d}\right)\right]\right\}$$

The distance to the end of the grating is indicated by $l_d = 0.75$ mm and the width of the apodizing hyperbolic tangent function is $w_d = 1$ mm (Fig. 2(c)). With DCA the nonlinear coupling of the interacting waves cannot be turned off completely. Even for very small duty cycles approaching zero, zero order QPM result in a finite coupling. We just reduce the duty cycle so far, that in numerical simulations a smooth spectral gain is achieved.

One difficulty of the DCA lies in the manufacturing of the very short ferroelectric domains ($\Lambda_{min} = D(L)K_g(L) = 2.6$ μm) that need to be realized toward the edges of the grating. In comparison, the smallest grating period that occurs with poling period apodization is $\Lambda_{min} = 14.8$ μm, which is much easier to realize. However, the smallest periods occur at the edges of the grating structure, where apodization is only completing the switch-off of the coupling that started with longer periods towards the center of the grating. Manufacturing errors at these most extreme values do therefore not significantly affect the quality of the overall apodization effect.

3. Experimental demonstration

We investigated the influence of the amplification process in APPLN on the spectral phase in the context of a few-cycle mid-infrared (MIR) two-stage OPCPA [6, 13]. A mode-locked femtosecond 1.56-μm fiber laser seeds the first OPA with 160 pJ pulse energy. The pulses are temporally stretched with a sequence of a 2-prism and a grating stretcher to a duration of ~3 ps and overlapped with our 1-μm pump beam. The pump system consists of an industry-grade 12-ps passively mode-locked master-oscillator
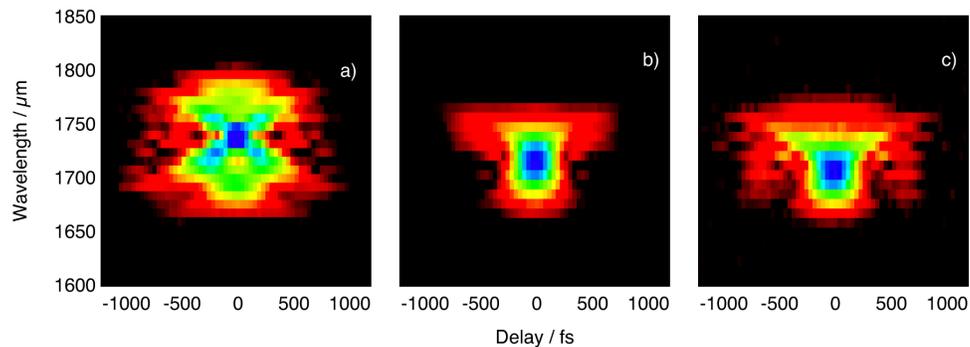

Fig. 3. SHG-FROG traces of pulses after amplification in linearly chirped APPLN. (a) without apodization (b) with rapid-poling-period-change apodization and (c) with duty-cycle apodization. Breakup into multiple sub-pulses occurs without proper apodization of the nonlinear coupling.

power amplifier system operating at 100 kHz repetition rate with 120 µJ pulse energy (Time-Bandwidth Products Inc., Duetto). Part of the Duetto output is further amplified to 460 µJ by a Nd:YVO$_4$ slab amplifier [14, 15]. The pulse train of this laser is stabilized to the pulse train of the seed laser with a phase locked loop (PLL) yielding a timing jitter of less than 150 fs rms.

The 1.56 µm signal beam is amplified in two subsequent OPA stages. The 3.4 µm idler wave is kept only after the last stage. With the help of the prism and grating stretchers we are able to precisely pre-compensate the total dispersion mismatch between the stretcher section and the 150-mm-long Al$_2$O$_3$ bulk compressor. Pump and seed beams are overlapped in the first and second OPA stage at pump intensities of 3.2 GW/cm^2 $(r_{1/e^2} = 250 \, \mu\text{m})$ and 4.7 GW/cm^2 $(r_{1/e^2} = 400 \, \mu\text{m})$, respectively. In both stages we use a $L = 10$ mm long, 1-mm-thick APPLN chip made from MgO-doped lithium niobate (Crystal Technology, LLC). A chirp-rate of $\kappa' = -250$ cm^{-2} is used to achieve a broad phase-matching spectral window ranging from 2.71 to 4.24 µm.

We examined three different quasi-phase matching gratings implemented in APPLN with linear chirp and no apodization (a), rapid-poling-period-change apodization (b) and duty cycle apodization (c) (see Fig. 2). The poling quality in the OPA section of the QPM grating common to all three designs is excellent, which can be attributed to the moderate change in poling period in this region. The output pulse energy after the first OPA is 3.0 nJ, 2.5 nJ, and 1.8 nJ, respectively. The pulses are pre-amplified in OPA1 just enough to enable characterization by second harmonic generation frequency-resolved optical gating (SHG FROG) after amplification in OPA2 to ~1 µJ (gain < 30 dB). This operation point of OPA1 is well in the unsaturated pump regime. In our QPM grating designs, we used a moderate range of periods in order to facilitate more reliable fabrication, and the QPM duty cycle is limited by the poling process. The imperfections in nonlinear coupling apodization resulting from these factors become exaggerated by pump depletion effects. We therefore avoided excessive pump saturation in both amplifiers to minimize these distortions. This enables us to properly study the impact of our apodization schemes on pulse quality. For all measurements identical gratings are used in OPA1 and OPA2. The influence of the apodization can be directly seen in the FROG trace (see Fig. 3). In the case of no apodization, breakup into multiple sub-pulses in the time-frequency domain occurs. By the use of either type of apodization the pulse energy is contained in one contiguous area. In the case of duty-cycle apodization some remaining side-lobes are present. This can be attributed to the more difficult poling of the small ferroelectric domains in the apodization section at both ends of the grating and the resulting manufacturing errors.

After reconstruction of the temporal pulse profile, the difference becomes even more pronounced (see Fig. 1). Without apodization non-polynomial spectral phase contributions of the amplification process cause the energy to be spread over many overlapping sub-pulses.

5. Conclusion and outlook

We have experimentally demonstrated the importance of nonlinear coupling apodization in aperiodic QPM for OPA applications. An adiabatic turning-on and turning-off of the coupling can be achieved by either tapering off the duty cycle of the QPM periods on either side of the QPM structure or by dephasing the waves through a smooth variation of the QPM periods. Our data shows a significant improvement in pulse quality through both apodization techniques. Due to the easier manufacturing and thus better device quality, poling-period apodization is found to yield slightly better results.

With APPLN one can overcome the bandwidth limitations of conventional PPLN in a collinear OPCPA [16, 17] and the common energy-bandwidth trade-off for few-cycle pulse amplification [5]. Amplification in a linear chirped QPM grating can distort the pulse structure of few-cycle pulses. With a proper apodization non-polynomial spectral phase

contributions can be easily avoided. The presented concept of apodized quasi-phasematched amplification is not limited to APPLN, but can be implemented in any QPM material. By choosing a proper range of grating k-vectors, pulses can be amplified within the whole transparency range of the selected crystal.

With apodized QPM in APPLN we expect to significantly raise the output energy and peak intensity of our high-power MIR OPCPA system while maintaining clean pulses. This will allow us to explore the non-perturbative regime of laser-matter interaction at long wavelength.

Acknowledgments

b) J.S. Pelc, P.S. Kuo, O. Slattery, L.J. Ma, X. Tang, M.M. Fejer, "Dual-channel, single-photon upconversion detector at 1.3 μm," *Opt. Express* **20**, pp. 19075-87 (August 2012).

Dual-channel, single-photon upconversion detector at 1.3 μm

J. S. Pelc,[1,4,*] Paulina S. Kuo,[2,3,4,5] Oliver Slattery,[2] Lijun Ma,[2] Xiao Tang,[2] and M. M. Fejer[1]

[1]*E. L. Ginzton Laboratory, Stanford University, Stanford, California 94305, USA*
[2]*Information Technology Laboratory, National Institute of Standards and Technology, Gaithersburg, Maryland 20899, USA*
[3]*Joint Quantum Institute, National Institute of Standards & Technology and University of Maryland, Gaithersburg, Maryland 20899, USA*
[4] *These authors contributed equally to this work*
[5]*paulina.kuo@nist.gov*
[*]*jpelc@stanford.edu*

Abstract: We demonstrate a two-channel, upconversion detector for counting 1300-nm-wavelength photons. By using two pumps near 1550 nm, photons near 1300 nm are converted to two spectrally distinct channels near 710 nm using sum-frequency generation (SFG) in a periodically poled LiNbO$_3$ (PPLN) waveguide. We used spectral-conversion engineering to design the phase-modulated PPLN waveguide for simultaneous quasi-phasematching of two SFG processes. The two channels exhibit 31% and 25% full-system photon detection efficiency, and very low dark count rates (650 and 550 counts per second at a peak external conversion efficiency of 70%) through filtering using a volume Bragg grating. We investigate applications of the dual-channel upconversion detector as a frequency-shifting beamsplitter, and as a time-to-frequency converter to enable higher-data-rate quantum communications.

©2012 Optical Society of America

OCIS codes: (040.5570) Quantum detectors; (190.4410) Nonlinear optics, parametric processes; (270.5565) Quantum communications.

References and links

1. A. P. Vandevender and P. G. Kwiat, "High efficiency single photon detection via frequency up-conversion," J. Mod. Opt. **51**(9–10), 1433–1445 (2004).
2. M. A. Albota and F. N. C. Wong, "Efficient single-photon counting at 1.55 microm by means of frequency upconversion," Opt. Lett. **29**(13), 1449–1451 (2004).
3. C. Langrock, E. Diamanti, R. V. Roussev, Y. Yamamoto, M. M. Fejer, and H. Takesue, "Highly efficient single-photon detection at communication wavelengths by use of upconversion in reverse-proton-exchanged periodically poled LiNbO$_3$ waveguides," Opt. Lett. **30**(13), 1725–1727 (2005).
4. L. Ma, O. Slattery, and X. Tang, "Experimental study of high sensitivity infrared spectrometer with waveguide-based up-conversion detector(1)," Opt. Express **17**(16), 14395–14404 (2009).
5. J. S. Pelc, L. Ma, C. R. Phillips, Q. Zhang, C. Langrock, O. Slattery, X. Tang, and M. M. Fejer, "Long-wavelength-pumped upconversion single-photon detector at 1550 nm: performance and noise analysis," Opt. Express **19**(22), 21445–21456 (2011).
6. R. H. Hadfield, "Single-photon detectors for optical quantum information applications," Nat. Photonics **3**(12), 696–705 (2009).
7. M. D. Eisaman, J. Fan, A. Migdall, and S. V. Polyakov, "Invited Review Article: Single-photon sources and detectors," Rev. Sci. Instrum. **82**(7), 071101 (2011).
8. A. E. Lita, A. J. Miller, and S. W. Nam, "Counting near-infrared single-photons with 95% efficiency," Opt. Express **16**(5), 3032–3040 (2008).
9. H. Takesue, S. W. Nam, Q. Zhang, R. H. Hadfield, T. Honjo, K. Tamaki, and Y. Yamamoto, "Quantum key distribution over a 40-dB channel loss using superconducting single-photon detectors," Nat. Photonics **1**(6), 343–348 (2007).
10. H. Xu, L. Ma, A. Mink, B. Hershman, and X. Tang, "1310-nm quantum key distribution system with up-conversion pump wavelength at 1550 nm," Opt. Express **15**(12), 7247–7260 (2007).
11. L. Ma, J. C. Bienfang, O. Slattery, and X. Tang, "Up-conversion single-photon detector using multi-wavelength sampling techniques," Opt. Express **19**(6), 5470–5479 (2011).

12. A. P. VanDevender and P. G. Kwiat, "Quantum transduction via frequency upconversion," J. Opt. Soc. Am. B **24**(2), 295–299 (2007).
13. L. Ma, M. T. Rakher, M. J. Stevens, O. Slattery, K. Srinivasan, and X. Tang, "Temporal correlation of photons following frequency up-conversion," Opt. Express **19**(11), 10501–10510 (2011).
14. S. Tanzilli, W. Tittel, M. Halder, O. Alibart, P. Baldi, N. Gisin, and H. Zbinden, "A photonic quantum information interface," Nature **437**(7055), 116–120 (2005).
15. H. Takesue, "Erasing distinguishability using quantum frequency up-conversion," Phys. Rev. Lett. **101**(17), 173901 (2008).
16. M. T. Rakher, L. Ma, O. Slattery, X. Tang, and K. Srinivasan, "Quantum transduction of telecommunications-band single photons from a quantum dot by frequency upconversion," Nat. Photonics **4**(11), 786–791 (2010).
17. M. T. Rakher, L. Ma, M. Davanço, O. Slattery, X. Tang, and K. Srinivasan, "Simultaneous Wavelength Translation and Amplitude Modulation of Single Photons from a Quantum Dot," Phys. Rev. Lett. **107**(8), 083602 (2011).
18. M. Asobe, O. Tadanaga, H. Miyazawa, Y. Nishida, and H. Suzuki, "Multiple quasi-phase-matched LiNbO$_3$ wavelength converter with a continuously phase-modulated domain structure," Opt. Lett. **28**(7), 558–560 (2003).
19. P. Kumar, "Quantum frequency conversion," Opt. Lett. **15**(24), 1476–1478 (1990).
20. M. H. Chou, K. R. Parameswaran, M. M. Fejer, and I. Brener, "Multiple-channel wavelength conversion by use of engineered quasi-phase-matching structures in LiNbO$_3$ waveguides," Opt. Lett. **24**(16), 1157–1159 (1999).
21. Y. W. Lee, F. C. Fan, Y. C. Huang, B. Y. Gu, B. Z. Dong, and M. H. Chou, "Nonlinear multiwavelength conversion based on an aperiodic optical superlattice in lithium niobate," Opt. Lett. **27**(24), 2191–2193 (2002).
22. K. R. Parameswaran, R. K. Route, J. R. Kurz, R. V. Roussev, M. M. Fejer, and M. Fujimura, "Highly efficient second-harmonic generation in buried waveguides formed by annealed and reverse proton exchange in periodically poled lithium niobate," Opt. Lett. **27**(3), 179–181 (2002).
23. Excelitas Technologies, "SPCM-AQRH: Single Photon Counting Module," http://www.excelitas.com/downloads/DTS_SPCM_AQRH.pdf
24. K. J. Gordon, V. Fernandez, G. S. Buller, I. Rech, S. D. Cova, and P. D. Townsend, "Quantum key distribution system clocked at 2 GHz," Opt. Express **13**(8), 3015–3020 (2005).
25. J. C. Bienfang, A. Restelli, and A. Migdall, "SPAD electronics for high-speed quantum communications," Proc. SPIE **7945**, 79452N, 79452N-5 (2011).
26. P. A. Andrekson and M. Westlund, "Nonlinear optical fiber based high resolution all-optical waveform sampling," Laser Photon. Rev. **1**(3), 231–248 (2007).
27. O. Kuzucu, F. N. C. Wong, S. Kurimura, and S. Tovstonog, "Time-resolved single-photon detection by femtosecond upconversion," Opt. Lett. **33**(19), 2257–2259 (2008).
28. J. Huang, C. Langrock, X. P. Xie, and M. M. Fejer, "Monolithic 160 Gbit/s optical time-division multiplexer," Opt. Lett. **32**(16), 2420–2422 (2007).
29. W. Robert, Boyd, *Nonlinear Optics,* 2nd ed. (Academic Press, 2003).
30. J. R. Kurz, J. Huang, X. Xie, T. Saida, and M. M. Fejer, "Mode multiplexing in optical frequency mixers," Opt. Lett. **29**(6), 551–553 (2004).
31. B. H. Kolner and M. Nazarathy, "Temporal imaging with a time lens," Opt. Lett. **14**(12), 630–632 (1989).
32. B. H. Kolner, "Space-time duality and the theory of temporal imaging," IEEE J. Quantum Electron. **30**(8), 1951–1963 (1994).
33. C. V. Bennett and B. H. Kolner, "Principles of Parametric Temporal Imaging —Part I: System Configurations," IEEE J. Quantum Electron. **36**(4), 430–437 (2000).
34. C. Niclass, C. Favi, T. Kluter, M. Gersbach, and E. Charbon, "A 128 × 128 Single-Photon Image Sensor with Column-Level 10-Bit Time-to-Digital Converter Array," IEEE J. Solid-state Circuits **43**(12), 2977–2989 (2008).

1. Introduction

Single-photon upconversion detectors for counting 1.3- and 1.5-μm-wavelength photons are attractive alternatives to direct detection by either InGaAs avalanche photodiodes (APDs) or superconducting single-photon detectors (SSPDs). The 1.3- and 1.5-μm wavelengths are of interest for optical-fiber-based quantum communication systems as silica fibers have minimum attenuation in these wavelength windows. Upconversion detection is based on highly efficient sum-frequency generation (SFG) that converts near-infrared photons to shorter-wavelength photons that can be detected by Si APDs, which offer higher detection efficiencies and lower dark count rates than their InGaAs-based counterparts [1–5]. InGaAs APDs are generally gated to reduce dark counts and avoid after-pulsing, which may also limit the speed at which events can be detected. SSPDs can also be used to detect near-infrared photons with very good sensitivity and dark count rates [6–9], but they require cryogenic operating temperatures, and are therefore of limited utility in practical quantum communications systems.

Upconversion detectors have been used for a number of applications. Improved system performance of a quantum key distribution system has been shown using 1306-nm

upconversion detectors [10]. Multiwavelength sampling using an upconversion detector has been used to increase temporal resolution of the detector system [11]. The upconversion process has been shown to preserve phase coherence [12] and temporal correlations up to fourth order [13]. Frequency upconversion has enabled a quantum information interface between widely separated wavelengths [14] and erasing of frequency distinguishability between two single photons [15]. Upconversion is a useful tool for hybrid quantum systems such as those combining quantum dots with photonic qubits [16, 17].

Here, we demonstrate a single-photon upconversion detector that has two spectrally distinct channels. Through quasi-phasematching (QPM) and spectral-conversion engineering [18], we can achieve efficient upconversion to multiple wavelengths in a single periodically poled lithium niobate (PPLN) waveguide. Specifically, we engineer the PPLN waveguide for two simultaneous SFG processes: 1302 nm + 1556 nm $\rightarrow$ 709 nm and 1302 nm + 1571 nm $\rightarrow$ 712 nm. We observed 70% conversion efficiency for both channels in the PPLN waveguide (including waveguide coupling losses), which led to system photon-detection efficiencies greater than 25%. In addition to sensitive detection of 1.3-μm signal photons, such a device acts like a beamsplitter or demultiplexer for the signal photons. We explore applications of this additional functionality for improving system performance. We show higher count rates before the onset of saturation, and better timing resolution by using time- to wavelength-division multiplexing. Simultaneously, we show ultra-low dark count rates (<700 s^{-1} at peak conversion efficiency) for both channels by narrowband filtering using a volume Bragg grating.

2. Theory

Consider a waveguide in which the following SFG processes can be simultaneously quasi-phasematched:

$$
\begin{aligned}
\omega_0 + \omega_{p1} &= \omega_1 \\
\omega_0 + \omega_{p2} &= \omega_2 \quad . \\
&\vdots \\
\omega_0 + \omega_{pN} &= \omega_N
\end{aligned}
\tag{1}
$$

A single-photon signal at ω_0 can undergo simultaneous sum-frequency generation with N strong pumps at frequencies ω_{p1} to ω_{pN}. Considering the simplest, non-trivial case of $N = 2$, the coupled wave equations for the electric fields, a_j (normalized such that $|a_j|^2$ has units of photons per second), are

$$
\begin{aligned}
\frac{da_0}{dz} &= -\gamma_1 a_1 - \gamma_2 a_2 \\
\frac{da_1}{dz} &= \gamma_1 a_0 \\
\frac{da_2}{dz} &= \gamma_2 a_0
\end{aligned}
\quad ,
\tag{2}
$$

where $\gamma_j = \sqrt{\eta_{\text{nor}} P_{pj}}$ and η_{nor} is the normalized efficiency defined in Ref [5]. The pumps at ω_{p1} and ω_{p2} are assumed to be undepleted (valid for the weak input signals considered here), both processes are phasematched (which can be achieved using a phase-modulated QPM grating described below), and the propagation losses are negligible. By taking the second derivative with respect to z of the first equation and substituting the second two expressions, we obtain

$$\frac{d^2 a_0}{dz^2} = -(\gamma_1{}^2 + \gamma_2{}^2) a_0 . \tag{3}$$

Substituting $\Gamma = \sqrt{\gamma_1{}^2 + \gamma_2{}^2}$, this equation is solved by

$$a_0(z) = A \cos \Gamma z + B \sin \Gamma z . \tag{4}$$

We solve the remaining two equations and insert the initial conditions $a_0(0)$, $a_1(0)$, and $a_2(0)$ to yield:

$$a_0(L) = a_0(0) \cos \Gamma L - [\bar{\gamma}_1 a_1(0) + \bar{\gamma}_2 a_2(0)] \sin \Gamma L ,$$
$$a_1(L) = \bar{\gamma}_1 a_0(0) \sin \Gamma L + [\bar{\gamma}_1{}^2 a_1(0) + \bar{\gamma}_1 \bar{\gamma}_2 a_2(0)] \cos \Gamma L + \bar{\gamma}_2{}^2 a_1(0) - \bar{\gamma}_1 \bar{\gamma}_2 a_2(0) , \tag{5}$$
$$a_2(L) = \bar{\gamma}_2 a_0(0) \sin \Gamma L + [\bar{\gamma}_1 \bar{\gamma}_2 a_1(0) + \bar{\gamma}_2{}^2 a_2(0)] \cos \Gamma L - \bar{\gamma}_1 \bar{\gamma}_2 a_1(0) + \bar{\gamma}_1{}^2 a_2(0)$$

where $\bar{\gamma}_j = \gamma_j / \Gamma$ are the normalized coupling constants. Equation (5) can be easily generalized for N pumps where $\Gamma = \left(\sum_j \gamma_j{}^2 \right)^{1/2}$ and $\sum_j \bar{\gamma}_j{}^2 = 1$.

In an ideal device with no loss and $a_1(0) = a_2(0) = 0$, complete signal-photon conversion is obtained when $\Gamma L = \pi/2$. For the trivial case of one strong pump, 100% conversion is achieved when the pump power is $P_p = \pi^2 / 4\eta_{nor} L^2$ and corresponds to the case when one photon at ω_0 is annihilated to produce one photon at the sum frequency ω_1. For multiple pumps at 100% conversion, a single photon at ω_0 is annihilated while a sum-frequency photon at ω_j is produced with probability $\bar{\gamma}_j{}^2$. The multi-channel upconverter acts like a beamsplitter that routes the signal photon to N possible outputs corresponding to different frequencies ω_j. The splitting ratio is variable and depends on the choice of pump power for each channel. At $\Gamma L = \pi/2$, the device behaves as a quantum frequency converter [19] that translates the quantum properties of the photons at ω_0 to photons at ω_j.

In real-world devices, there are losses and incomplete conversion. For quantum information applications, the effects of loss and incomplete conversion are similar. The key exchange rate in a quantum key distribution system is reduced by system losses, whether they result from link losses, detector inefficiencies or incomplete upconversion. The effect of loss on two-photon interference measurements (which are the basis for many quantum entanglement experiments) is to reduce visibility and increase background noise counts, but the correlation signature is preserved. The multi-channel upconverter acts like a lossy beamsplitter where incomplete conversion contributes to the system loss.

3. QPM design and fabrication

To fabricate a multichannel upconversion device, we employed the QPM phase-modulation technique developed by Asobe and associates [18]. The phase-modulation technique is one of several techniques [20, 21] that have been developed in order to engineer the phasematching profile of a device. In the phase-modulation technique, one starts with a QPM grating with period Λ_G. The QPM pattern is modulated by a phase-modulation function $\phi(z)$ that is periodic in z with period Λ_{ph}. The phase modulation consist of shifting position of a domain boundary z_n with respect to its nominal location $z_{n,0}$ of a periodic grating so that the modulation phase is $\phi(z) = 2\pi(z_n - z_{n,0})/\Lambda_G$. Using Fourier analysis, it can be shown that QPM peaks are obtained when the relation

$$\Delta k = k_j - k_0 - k_{pj} = 2\pi\left(\frac{1}{\Lambda_G} + \frac{m}{\Lambda_{ph}}\right) \qquad (6)$$

is satisfied for integer m. k_j, k_0, and k_{pj} are the wavevectors for sum-frequency ω_j, signal ω_0, and pump ω_{pj}, respectively. We used a simplex convex optimization algorithm to successfully optimize $\phi(z)$ to phasematch two simultaneous SFG processes corresponding to $m = +1$ and -1; for the two-peaked QPM tuning curve, the desired form of $\phi(z)$ is found to be a rectangle function. A calculated QPM tuning curve is shown in Fig. 1a. We found that Λ_{ph} varied inversely with the wavelength difference between the two QPM peaks. We computed the Δk values from simulated dispersion data for reverse-proton exchange (RPE) [22] PPLN waveguides. Setting $m = +1$ and -1 in Eq. (6), we can solve for the required poling period Λ_G and phase-modulation period Λ_{ph} for a given pair of wavelengths. For channel separations (defined as $\Delta\lambda = \lambda_{p2} - \lambda_{p1}$) of 5, 10, and 15 nm, we found that the required phase-modulation periods Λ_{ph} were 7.1, 3.94, and 2.56 μm, respectively.

We fabricated two-channel upconversion RPE PPLN waveguides for SFG between a 1.3-μm signal and two 1.55-μm-band pumps, with $\Lambda_G = 13.5$ μm. The 52-mm-long devices were antireflection coated for wavelengths of 1310 and 1550 nm at the input between LiNbO$_3$ and optical fiber, and for 1310, 1550, and 710 nm at the output between LiNbO$_3$ and air. The devices were fiber pigtailed at the inputs and were measured to have total optical throughputs of −1.3 dB at 1550 nm and −2.4 dB at 1319 nm. The tuning curve vs. pump wavelength of a device measured with the signal wavelength fixed to $\lambda_0 = 1319$ nm is shown in Fig. 1b. The conversion efficiencies of the two channels (at 1533 nm and 1548 nm pump wavelengths) are nearly equal. Lower-efficiency side peaks for odd m were also observed, which are a consequence of the phase-modulation design.
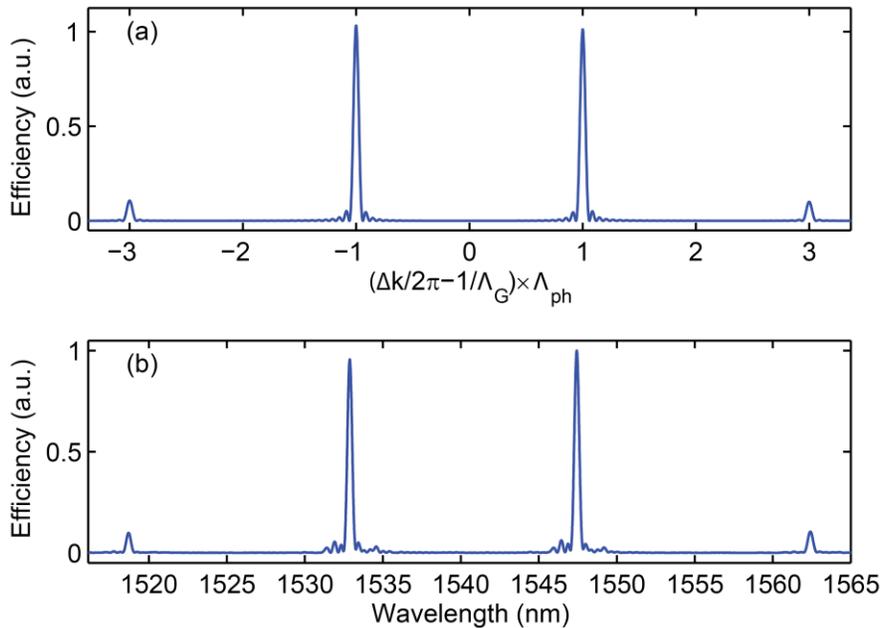

Fig. 1. (a) Theoretical and (b) measured SFG conversion efficiency for the two-channel, phase-modulated PPLN waveguide with signal wavelength fixed at $\lambda_0 = 1319$ nm.

4. Experiments

We first characterized the performance of each channel of the upconversion detector by measuring the photon detection efficiency (PDE) and dark count rate (DCR) using continuous wave (CW) pumping. We then explored the multiplexing capabilities of the device for several applications. These applications can be separated into two categories: use of the multi-channel device as a beamsplitter and as a switch. We used the dual channel device as a beamsplitter to exceed the saturation-limited maximum count rate of a single detector. Using the device as a switch, we demonstrated increased clock rate above the jitter-limited clock rate of a single-channel upconversion detection system.

4.1 Photon detection efficiency and dark counts

A diagram of the experimental setup is shown in Fig. 2. In order to pump both upconversion channels simultaneously, two pump lasers were used: one in the C-band ($\lambda < 1568$ nm) and one in the L-band ($\lambda > 1568$ nm). The two pumps were combined with a C/L-band wavelength division multiplexer (WDM) and amplified in a 0.5W erbium-doped fiber amplifier (EDFA). The EDFA was followed by a 1300/1550 WDM acting as a filter to reject 1310-nm noise produced in the EDFA, as has been described in Ref [4]. The amplified pumps were combined with a 1310-nm signal laser attenuated down to single-photon-level and sent into the fiber-pigtailed, phase-modulated PPLN waveguide. Polarization controllers were used for both pumps and the signal to align the input light to the z-axis of the PPLN waveguide, which supports only e-polarized light.
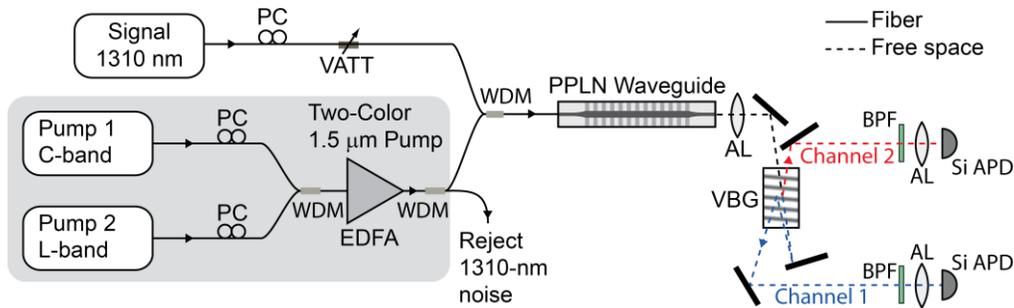

Fig. 2. General experimental setup. The strong, two-color pump near 1.5 μm is combined with the signal near 1310 nm in the PPLN waveguide with phase-modulated QPM grating. The output is separated by a volume Bragg grating (VBG) and sent to two silicon avalanche photodiodes (Si APD). PC, polarization controller; WDM, wavelength-division multiplexer; EDFA, erbium-doped fiber amplifier; VATT, variable attenuator; AL, aspheric lens; BPF, 20-nm band-pass filter.

Following the waveguide, an anti-reflection-coated aspheric lens (AL) was used to collimate the output radiation from the waveguide. To separate the outgoing pump light and filter the two up-converted channels at λ_1 and λ_2, we used a volume Bragg grating (VBG). In reflection, the VBG acts as a narrowband filter, where the reflected wavelength depends sensitively on the angle of incidence. We measured the full-width-half-maximum (FWHM) reflection bandwidth of the VBG to be 0.04 nm. The VBG was aligned such that the long-wavelength channel at λ_2 was reflected back through the input facet of the VBG (see Fig. 2). The upconverted light at λ_1 passed through the VBG and was redirected back into the VBG using a mirror at a slight angle so that high reflection of λ_1 was achieved through the second surface of the VBG. One key advantage of using the VBG filter compared to an earlier approach using a holographic diffraction grating [11] is that narrowband wavelength selectivity, and therefore very low noise counts, can be achieved using a very small footprint. The two upconverted channels were then sent to two Si APDs (PerkinElmer SPCM-AQR-14). We used a 20-nm bandpass filter at the entrance to each Si APD to block any stray light or parasitic pump-second-harmonic radiation. An unintended consequence of the phase-

modulated QPM design was the appearance of several accidental second-harmonic generation QPM peaks. We chose the pump wavelengths, λ_{p1} and λ_{p2}, such that these undesired peaks were avoided.

The measured CW system photon detection efficiencies and dark count rates for both channels are shown in Fig. 3. The PDEs and DCRs were measured with only one pump present at a time. The signal wavelength was fixed to 1302 nm so that channel 1 corresponded to the SFG process 1302 nm + 1556 nm $\rightarrow$ 709 nm, while channel 2 corresponded to 1302 nm + 1571 nm $\rightarrow$ 712 nm. For the PPLN waveguide itself, we observed 70% peak external conversion efficiency in both channels, a value which included input and output coupling losses. The optical path following the PPLN waveguide had higher loss for channel 1 than channel 2, primarily due to traversing the VBG twice; we estimated 45% and 32% loss for the optical path after the waveguide for channel 1 and 2, respectively, which includes loss from the 20-nm band-pass filter. Combined with the 65% PDE of the Si APD [23], the system peak photon detection efficiencies were 25% for channel 1 and 31% for channel 2 (see Fig. 3a). The solid lines in Fig. 3a represent fits to $\eta_{tot}(P_p) = \eta_0 \sin^2(\pi/2\sqrt{P_p/P_{max}})$, where η_{tot} is the PDE, P_p is the pump power, and P_{max} is the pump power at maximum conversion. $P_{max} \approx 135$ mW is nearly the same for channels 1 and 2, as we expected from the nearly equal peak heights in Fig. 1b.

At maximum conversion, the dark count rates are 550 s^{-1} and 650 s^{-1} for channels 1 and 2, respectively. The DCRs at low pump power are dominated by the intrinsic DCRs of the Si APDs. The dark count rates observed here represent substantial improvements compared to other CW 1.3-μm-band upconversion detectors that showed 1.5×10^4 s^{-1} [3] and 2.5×10^3 s^{-1} [4] DCRs. Our low DCRs are due to the very narrowband reflectance of the VBG. In this system, the noise is primarily due to upconverted anti-Stokes Raman photons generated by the strong pump, which fill the PPLN upconversion acceptance bandwidth [3–5]. The VBG acts as a filter narrower than the QPM acceptance bandwidth, so that most of the noise photons are eliminated. There is a tradeoff between system speed and noise performance. The narrow VBG (24 GHz) and QPM acceptance (46 GHz) bandwidths set a limit to the response rate of the system; broadening both of these bandwidths would allow faster rates at the expense of greater total noise counts.
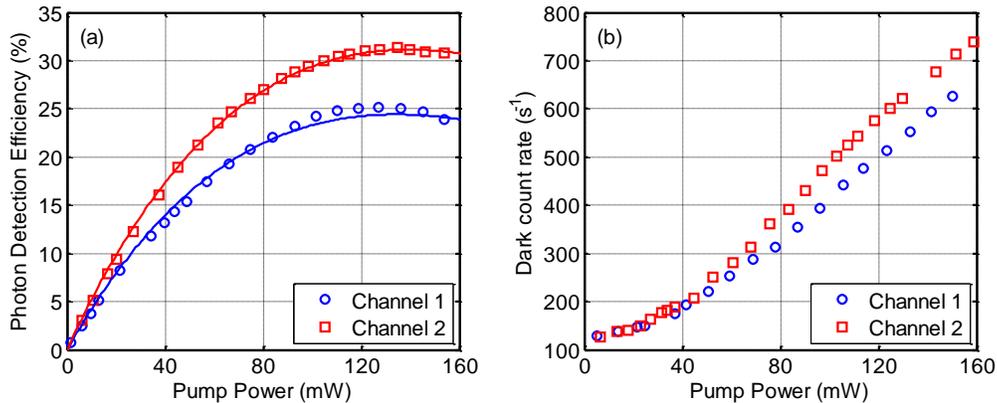

Fig. 3. Measured (a) photon detection efficiencies and (b) dark count rates for channel 1 (1302 nm + 1556 nm $\rightarrow$ 709 nm) and channel 2 (1302 nm + 1571 nm $\rightarrow$ 712 nm). The intrinsic dark count rates of the Si APDs are about 100 s^{-1}.

4.2 Classical beamsplitter applications

When both pump frequencies are present at the same time, the dual-channel upconverter with VBG output filter acts like a classical beamsplitter that probabilistically divides the input to two outputs. Photons at 1302 nm are frequency-converted by the device and sent to the 709- or 712-nm output paths. Beamsplitters have many uses in quantum optics. We demonstrated application of our device for splitting high-count-rate signals onto two Si APDs to enable single-photon count rates above the dead-time-limited value of a single detector.

The maximum count rate of an APD is related to the dead time of the detector, τ_D. As the incident photon rate R_{inc} begins to approach $1/\tau_D$, the detector begins to saturate [23]. Consider a single photon at ω_0 incident at the input of the dual-channel upconverter device. The pump powers P_{p1} and P_{p2} can be chosen such that with 50% probability, the photon is converted to ω_1 or ω_2. Therefore, much like a classical beamsplitter, the dual-channel upconverter will probabilistically divide the incident 1.3-μm signal to the two upconverted channels that can be detected by two APDs.

We measured the saturation of a Perkin-Elmer SPCM by varying R_{inc} and measuring the count rate R of a single detector (Fig. 4). The input signal rate R_{inc} at $\lambda_0 = 1302$ nm was controlled by a programmable optical attenuator in 2 dB increments from a level of 41 photons/s to 2×10^9 photons/s. With only pump 1 turned on, we measured the count rates for both channels (R_1 and R_2). R_2 was very low and reflected detector dark counts and cross-talk counts. The count rate R_1 is shown as blue circles in Fig. 4. The solid blue curve is a simulation of the expected counting statistics of coherent light (with Poissonian photon arrival statistics) assuming a detector dark count rate $D = 250$ s^{-1} and a dead time of 67 ns. By comparing the rates R_1 and R_2 with only pump 1 turned on, we observed a very low channel crosstalk of −44 dB, which is likely due to a combination of amplified spontaneous emission (ASE) from the EDFA and imperfect isolation of the VBG channels.

With both pumps turned on, we then set the pump powers P_{p1} and P_{p2} such that, including free-space losses, equal count rates were obtained at the two detectors. We measured the summed count rate $R_s = R_1 + R_2$ at the same overall conversion efficiency as in the pump-1-only case. The observed R_s versus R_{inc} is plotted as green squares in Fig. 5, along with a simulation of the counting statistics. We see that at low R_{inc}, the dual-channel case has a DCR
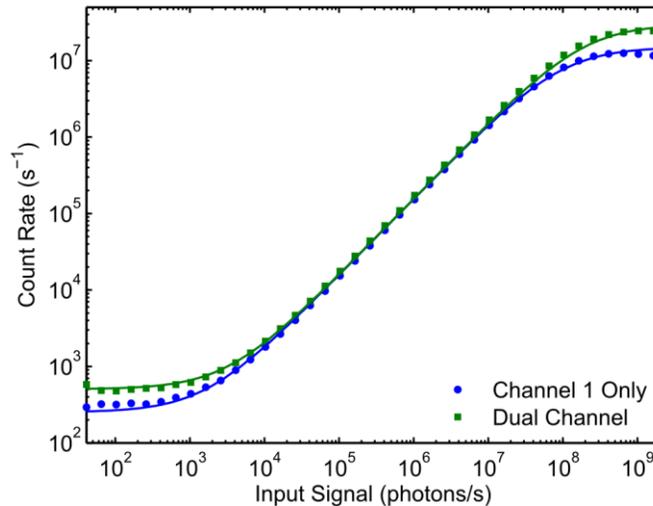

Fig. 4. Measured count rates for a single detector (blue dots) and a combined, dual-channel detector (green squares) as a function of input signal rate R_{inc}. The maximum, saturated count rate for the dual-channel system is twice that of the single detector, but the dark count rate is also doubled. The solid curves are simulated counting statistics for coherent light.

of approximately $2D$ and saturates at $2R_{max}$, where D is the DCR for a single channel and R_{max} is the maximum, dead-time-limited count rate obtained with one detector. From this result, we extrapolate that for an N-pump upconverter, the system count rate would saturate at NR_{max} at the expense of increased DCR of ND.

4.3 Demultiplexing applications

In the previous section, we discussed application of a multichannel upconverter as a classical beamsplitter when the pump sources are simultaneously on. In that demonstration, the splitting of an input signal to multiple output ports happened probabilistically. If, however, the two pumps were controlled in time using external modulators, one may achieve deterministic control of the output channel for a particular time bin by, for example, switching the pumps on and off sequentially. Such a multichannel detector can be used to switch the output from one channel to another like a router or demultiplexer. One application of such functionality is to achieve higher speeds by using multiple Si APDs.

High speed detectors are of interest for quantum key distribution (QKD) systems. The exchange rate of the secret key is much slower than the system clock rate due to post-selection protocols [24, 25]. The quantum-key transmission rate is further reduced by losses and other errors, especially in long-distance transmission systems. Hence, increasing the system clock rate can enable faster QKD systems over longer distances. The speed limitation for such systems is typically caused by the detectors. For a system based on upconversion detection using a continuous-wave pump, timing jitter in the Si APD limits the temporal resolution. Pulsed pumps can be used to increase the temporal resolution. Picosecond [26] and femtosecond [27] pump pulses generated by mode-locked lasers have been used to demonstrate fast optical sampling. However, these schemes are based on varying the delay of the sampling pulse and collecting data over a number of repeated waveforms, which is not possible in a communications system. Alternatively, the pump pulses can be used to demultiplex a fast data train into multiple slower trains that can be resolved with slower detectors. Such a scheme is analogous to a frequency-converting, optical time-division multiplexer [28], which was used to quadruple the data rate by combining four wavelength channels.

High-speed upconversion detection using time- to wavelength-division multiplexing has previously been demonstrated using a short, PPLN waveguide [11]. The 1-cm waveguide used in Ref [11]. was chosen to permit two spectrally distinct pumps to fit under the same phasematching peak. The FWHM pump-acceptance bandwidth was 2.5 nm centered at 1549.6 nm, which allowed the use of pumps at 1549.2 nm and 1550.0 nm, but produced low conversion efficiency due to the 1-cm length of the QPM grating. One major advantage of the phase-modulated PPLN waveguide used here is the higher photon detection efficiency for both channels. Our 52-mm-long device showed up to 31% system PDE (see Fig. 4a) while the 10-mm-long waveguide in Ref [11]. had only 7% maximum PDE, limited by the available pump power. We were able to reach the point of maximum signal conversion at 135 mW pump power, while Ref [11]. had insufficient pump power to reach the maximum conversion point. The phase-modulated QPM technique used here can provide a scalable approach to increase the number of channels. High conversion efficiency for each channel is obtained without decreasing channel spacing, which would make the spectral filtering of the output channels more difficult.

The dual-channel device allows access to higher data rates. Let τ_{det} be the shortest time bin allowed by a Si APD while still maintaining acceptably low inter-symbol interference (ISI); using the dual-channel upconversion device, a faster train of signal pulses with time bin $\tau_{det}/2$ can enter the device and interact with a two-color pump consisting of interleaved pumps pulses at λ_{p1} and λ_{p2}. The period of the pump pulses at each wavelength is τ_{det}. A train of upconverted pulses is generated in the PPLN waveguide, where pulses in adjacent time slots have different wavelengths, which can be spectrally separated using a dispersive optic (here, a VBG) and sent to two Si APDs. The phase-modulated PPLN waveguide and VBG together act like a time-division demultiplexer that produces two trains of pulses, each at half the

signal clock rate. The dual-channel upconverter therefore allows detection of a train of signal pulses whose rate is twice larger than the detector-limited rate $(1/\tau_{det})$.

A detailed diagram of the experimental setup is shown in Fig. 5. The two pumps and signal are modulated by electro-optic intensity modulators (IMs) using the timing diagram shown in Fig. 6 (with 1.6 GHz clock rate). The electrical pulses driving the IMs are produced with a data generator, which is also used to trigger the time-correlated single-photon counting (TCSPC) system. The optical pulses are combined and sent to the phase-modulated PPLN waveguide. The two-color SFG output is filtered and separated with the VBG and detected with two Si APDs.
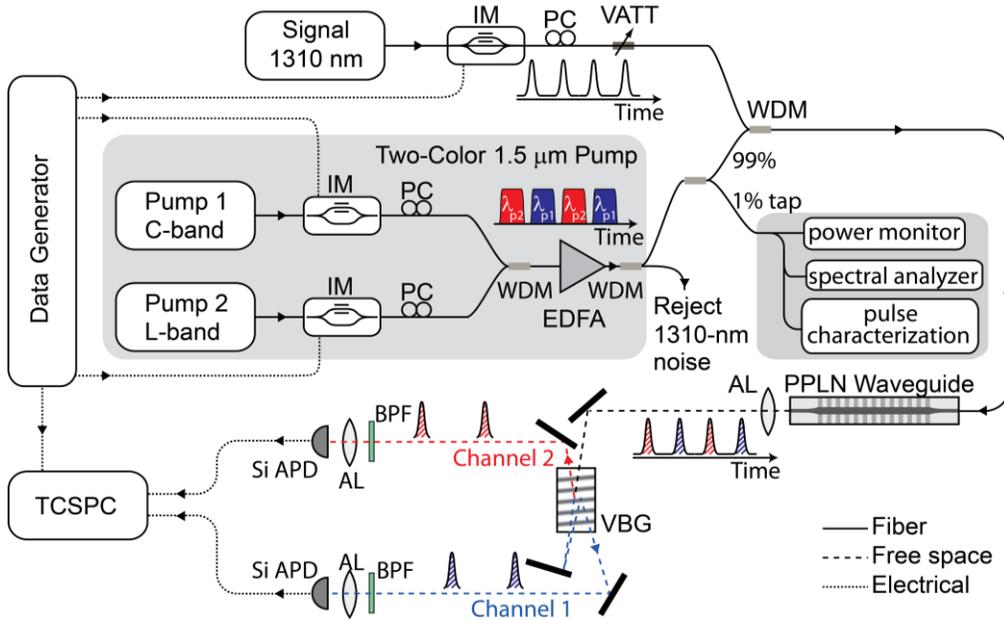

Fig. 5. Experimental setup for the dual-wavelength demultiplexing experiment. A fast train of signal pulses interacts in the PPLN waveguide with a two-color pump pulse train consisting of alternating pulses at λ_{p1} and λ_{p2} to produce SFG pulses that can be spectrally separated with the VBG. The pulses arrive at each Si APD at half the rate of the original signal pulse train. A data generator drives the electro-optic intensity modulators (IM) and also triggers the time-correlated single-photon counting (TCSPC) system. A 1% tap coupler is placed after the EDFA and used to monitor the power, optical spectrum and temporal characteristics of the pump pulses. The resulting dual-channel SFG pulses are separated and filtered by the VBG and routed to two Si APDs.
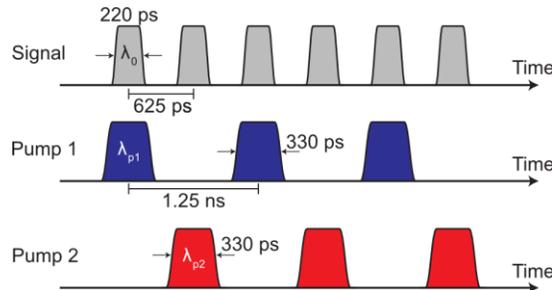

Fig. 6. Pulse timing diagram for detection of high-clock-rate signals via multi-wavelength sampling. The signal pulses have 625 ps period (1.6 GHz rate), while the two pump pulse trains each have 1.25-ns period (800 MHz rate). The pump pulse trains are staggered such that signal pulses overlap with alternating pump pulses.

We first measured the timing jitter of a single APD. This was done by sending pump and signal pulses (of FWHM 330 ps and 220 ps, respectively) to the PPLN waveguide once every 12.5 ns. With widely spaced pulses, the tails of the detected SFG can be easily distinguished (see Fig. 7a, green dots). We observed FWHM of 310 ps and full-width at 1% maximum (FW1%M) of 1.0 ns. The floor of background counts around −33 dB is due to residual pump and signal transmission from imperfect extinction of the electro-optic modulators.

The black dots in Fig. 7a show the upconverted signal with signal pulses arriving at 1.6 GHz and a continuous-wave pump. We see ISI such that adjacent time slots cannot be well distinguished. By using the dual-wavelength upconversion device and pulsing the two pumps according to the timing diagram in Fig. 6, we obtain the timing histograms shown in Fig. 8b. The effective data rate in each channel is lowered to 800 MHz, and there is much less inter-symbol interference and greater ease in distinguishing data in each channel.

As an example application for data transmission, we sent a test code sequence to the dual-wavelength upconversion detector (Fig. 8). The test sequence is encoded in the signal at λ_0 and shown in Fig. 8b, while the response histograms for channels 1 and 2 are plotted in Figs. 8a and 8c, respectively. Figure 8d shows the result of sending all the data to channel 1 (pump 1 is held continuously on); data in adjacent time slots are merged. When the signal data is "0," both channels show a small amount of feed-through (manifested as a small increase in counts at the center of the time bin), which is caused by incomplete extinction of the 1.3-μm signal intensity modulator.
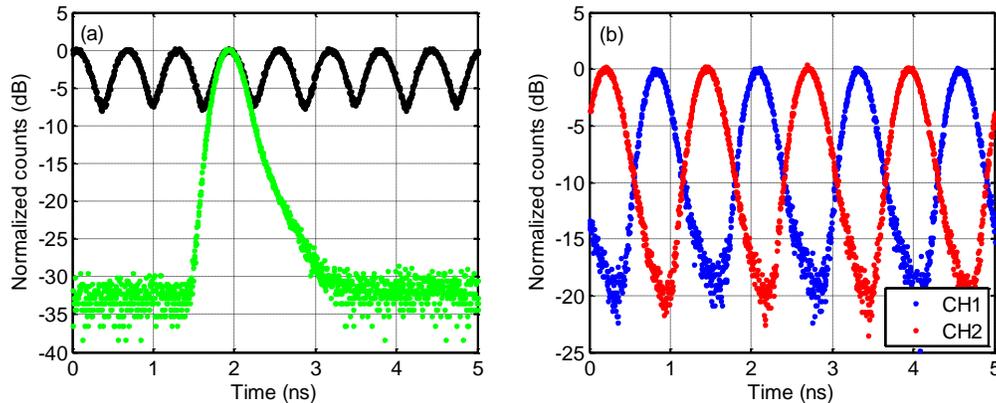

Fig. 7. (a). Single-channel, up-conversion detector response to a 1.6 GHz clock-rate pulse train showing significant inter-symbol interference (black), and response to a single pulse (green) showing FW1%M of 1.05 ns. (b) By using the dual-channel, upconversion detector and alternating channel 1 and 2 pumping, the data rate in each channel is halved and the data can be resolved.
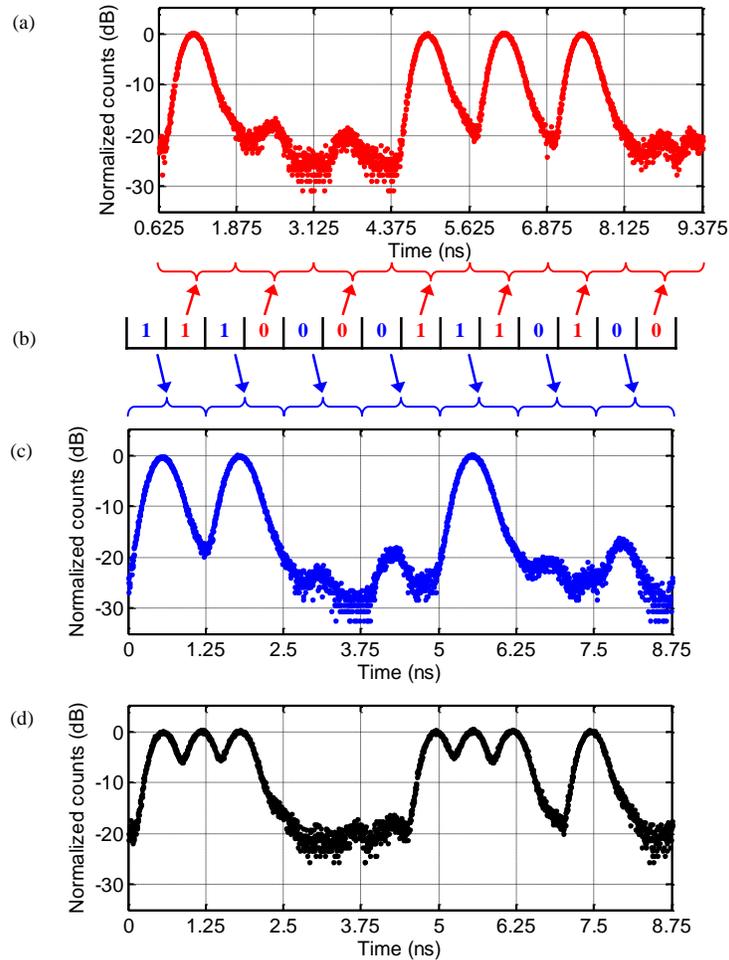
Fig. 8. Timing histogram of dual-wavelength upconversion detector for (a) Channel 1 and (c) Channel 2 to test sequence (b) encoded in the signal at λ_0. (d) Response of Channel 1 to the signal code sequence with a continuous-wave pump showing significant ISI.

5. Conclusion and future work

We have demonstrated a dual-wavelength, high-efficiency upconversion single-photon detector with extremely low dark count rates. The system is based on a PPLN waveguide with a phase-modulated QPM grating where the output light is filtered by a volume Bragg grating. We measured total-system photon detection efficiencies (dark count rates) of 25% (550 s^{-1}) and 31% (650 s^{-1}) for channels 1 and 2, respectively. We showed that the dual-channel upconversion detector can be used both as a probabilistic beamsplitter and as a deterministic switch. When used as a beamsplitter, multiple Si APDs can be used to count the upconverted photons, thereby increasing the saturation-limited count rate. With pulsed pumping, the device worked as a router that deterministically switched the output from one channel to another. We showed an increase in clock rate beyond the rate limited by the timing jitter of a single Si APD. As a beamsplitter, we expect the dual-channel device to preserve photon statistics and enable $g^{(2)}$ measurements of classical and non-classical light. With more channels, higher order temporal correlation functions may be measured using the device. When used as a router, the dual-channel device is a fast switch whose switching time is only limited by the electro-optic modulators controlling the pumps since optical frequency

conversion is instantaneous [29]. We envision this technique may be useful as a rapid switch between measurement bases in a quantum key distribution system. While we have here used two pumps with different optical frequencies to switch between two output modes, it is also possible to use different spatial modes in combination with a mode-selective device to achieve the same switching functionality [30].

Multichannel upconversion and sampling are examples of discrete time-to-frequency conversion. There has been growing interest in time-to-frequency converters for their applications in time microscopes [31–33], where ultrafast waveforms can be magnified in time such that they can be detected directly using high speed electronics. An extension of the multiple discrete wavelength sampling presented here would be to investigate continuous wavelength sampling using a chirped pump pulse (with, for example, a linearly varying instantaneous frequency as a function of time) to upconvert a weak input signal with rapid temporal variations. Each temporal slice of the input waveform is linearly mapped onto the frequency of the upconverted light. If a diffraction grating or other dispersive element is used followed by a single-photon detector array [34], one can map each temporal slice of the input waveform onto an individual detector element, enabling potentially much higher timing resolution than that provided by an individual detector element. This technique is advantageous over the single-pixel, ultrafast upconversion approach studied in Ref [27], as it can sample the entire waveform in a single shot. Such a single-shot, high-time-resolution detector system would have applications in pulse-position-modulated, weak-pulse optical communications, where the time-to-frequency converter enables narrower temporal bin widths and higher data rates.

Acknowledgments

c) K. De Greve, L. Yu, P.L. McMahon, J.S. Pelc, C.M. Natarajan, N.Y. Kim, E. Abe, S. Maier, C. Schneider, M. Kamp, S. Hofling, R.H. Hadfield, A. Forchel, A M.M. Fejer, Y. Yamamoto, "Quantum-dot spin-photon entanglement via frequency downconversion to telecom wavelength," *Nature* **491**, p. 421 (November 2012)

LETTER

Quantum–dot spin–photon entanglement via frequency downconversion to telecom wavelength

Kristiaan De Greve[1]†, Leo Yu[1]*, Peter L. McMahon[1]*, Jason S. Pelc[1]*, Chandra M. Natarajan[1,2], Na Young Kim[1], Eisuke Abe[1,3], Sebastian Maier[4], Christian Schneider[4], Martin Kamp[4], Sven Höfling[1,4], Robert H. Hadfield[2], Alfred Forchel[4], M. M. Fejer[1] & Yoshihisa Yamamoto[1,3]

Long-distance quantum teleportation and quantum repeater technologies require entanglement between a single matter quantum bit (qubit) and a telecommunications (telecom)-wavelength photonic qubit[1–5]. Electron spins in III–V semiconductor quantum dots are among the matter qubits that allow for the fastest spin manipulation[6,7] and photon emission[8,9], but entanglement between a single quantum-dot spin qubit and a flying (propagating) photonic qubit has yet to be demonstrated. Moreover, many quantum dots emit single photons at visible to near-infrared wavelengths, where silica fibre losses are so high that long-distance quantum communication protocols become difficult to implement[10]. Here we demonstrate entanglement between an InAs quantum-dot electron spin qubit and a photonic qubit, by frequency downconversion of a spontaneously emitted photon from a singly charged quantum dot to a wavelength of 1,560 nanometres. The use of sub-10-picosecond pulses at a wavelength of 2.2 micrometres in the frequency downconversion process provides the necessary quantum erasure to eliminate which-path information in the photon energy. Together with previously demonstrated indistinguishable single-photon emission at high repetition rates[11,12], the present technique advances the III–V semiconductor quantum-dot spin system as a promising platform for long-distance quantum communication.

A quantum communication network[1] will consist of stationary matter qubits and flying photonic qubits. The two key technologies for quantum communication networks are quantum teleportation from a photonic qubit to a matter qubit or vice versa, and a quantum repeater to create and store the entangled states of remote matter qubits. These two core technologies rely on the ability to create entanglement between a matter qubit and a photonic qubit over long distances, followed by a Bell state measurement that transforms the matter qubit–photonic qubit entanglement into the teleportation of a given unknown quantum state, or into matter–matter entanglement[13–18]. Matter–photon and matter–matter entanglement generation have been shown in several ionic[4,16,17] and atomic[2,5,18] systems, while matter–photon entanglement was recently observed in nitrogen-vacancy diamond colour centres[3]. However, these systems suffer from low photon collection efficiencies and relatively long optical recombination times, which can only partially be overcome by cavity-quantum electrodynamic (cavity-QED) solutions[1]. In addition, none of them use telecom-wavelength (1.5 μm) photons that would allow long-distance entanglement distribution. Combining a solid-state monolithic cavity-QED system with a fast quantum emitter[19–21] could solve the low photon yields. In the InAs quantum-dot system, subnanosecond optical recombination times have previously led to the demonstration of high single-photon rates when the quantum dots are embedded in high-quality optical cavities[8,9,20,21]. Moreover, spin control of charged InAs quantum dots was shown to be feasible on picosecond timescales

while preserving spin coherence[6,7,22], making it a promising candidate as a quantum network technology. However, spin–photon entanglement has yet to be established in this system, and its emission wavelength does not match the low-loss wavelength range of silica fibres. In this work, we address both these challenges with an ultrafast frequency downconversion technique based on a periodically poled lithium niobate (PPLN) waveguide device[23]. Its timing resolution enables demonstration of entanglement between a single InAs quantum-dot spin qubit and a photonic qubit at 910 nm, while the target wavelength (1,560 nm) would permit long-distance quantum communication.

The physical system used in our experiment is presented in Fig. 1a–d. It consists of a single electron-doped InAs quantum dot, embedded in a low-Q microcavity (see also Methods). With an external magnetic field oriented in the Voigt geometry (perpendicular to the growth direction/optical axis), two Λ-systems are formed, where an optically active, excited state is coupled to each of two ground states. The excited states are so-called trion states, as they consist of three particles: two electrons, paired into a singlet state, and an unpaired hole ($|\uparrow\downarrow\Downarrow\rangle$ and $|\uparrow\downarrow\Uparrow\rangle$). Both trion states are connected to each of the electron spin states, $|\downarrow\rangle$ and $|\uparrow\rangle$, in a Λ-configuration. These Λ-systems have been extensively studied[24], and were previously used for initialization[25] and coherent manipulation of the electron spin states[6,7,22,26]. The optical selection rules are indicated in Fig. 1a, and were verified by polarization-selective photoluminescence (Fig. 1b). In addition, initialization, rotation and measurement of the spin state of the quantum dot are realized, using all-optical techniques as reported previously[6,7] (see Fig. 1c, d and Methods). By selectively exciting one of the trion states, for example, the $|\uparrow\downarrow\Uparrow\rangle$-state, spontaneous emission decay in a Λ-system leads to entanglement between the emitted photon and the electron spin[3,4]:

$$|\psi\rangle = \frac{1}{\sqrt{2}}\left(|\uparrow\rangle \otimes |iH; \omega + \delta\omega\rangle + |\downarrow\rangle \otimes |V; \omega\rangle\right) \qquad (1)$$

Here $\delta\omega$ refers to the difference in energy (colour) of the emitted photons, determined by the electron Zeeman energy, and H and V to their polarization (see Fig. 1c); ω refers to the frequency (wavelength) of the V-polarized photon (910.10 nm). Previous coherent spin manipulation experiments[6,7] relied on a relatively large Zeeman splitting $\delta\omega$ between the respective electron spin states, both for high-fidelity spin initialization and readout, and for ultrafast coherent control of the spin through a combination of stimulated-Raman transitions and Larmor precession. In the present experiment, this energy separation is set at about $2\pi \times 17.6$ GHz (external magnetic field $B = 3$ T, Fig. 1d), leaving room for which-path information to leak out into the environment via the photon energy, which makes verification of entanglement between the polarization of the photon and the electron spin challenging. Upon detection of an emitted photon in

[1]E. L. Ginzton Laboratory, Stanford University, Stanford, California 94305, USA. [2]Scottish Universities Physics Alliance and School of Engineering and Physical Sciences, Heriot-Watt University, Edinburgh EH14 4AS, UK. [3]National Institute of Informatics, Hitotsubashi 2-1-2, Chiyoda-ku, Tokyo 101-8403, Japan. [4]Technische Physik, Physikalisches Institut, Wilhelm Conrad Röntgen Research Center for Complex Material Systems, Universität Würzburg, Am Hubland, D-97074 Würzburg, Germany. †Present address: Department of Physics, Harvard University, 17 Oxford Street, Cambridge, Massachusetts 02138, USA.
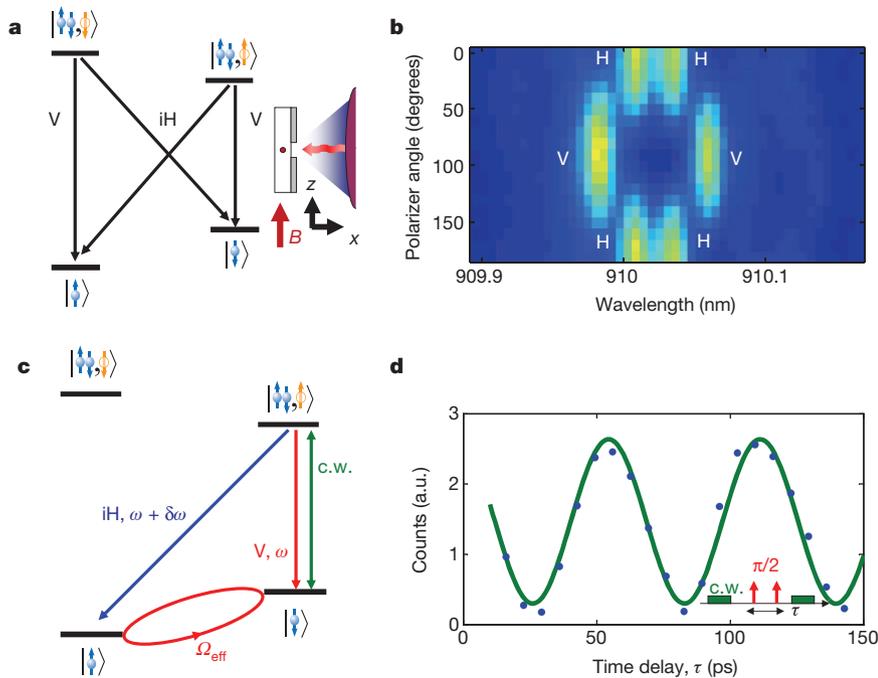*These authors contributed equally to this work.

Figure 1 | Level structure of quantum dot and spin manipulation. a, Level structure of an electron-doped quantum dot, with the magnetic field in-plane (Voigt geometry, boxed). V and H refer to linear polarizations, either perpendicular to (V) or parallel (H) to the magnetic field. Blue and orange arrows refer to the electron and (trion-) hole states, respectively. **b**, Verification (by polarization-selective magnetophotoluminescence) of the polarization selection rules of the studied electron-doped quantum dot. **c**, Level structure and optical spin manipulation scheme used. $\delta\omega$, Larmor precession frequency ($2\pi \times 17.6$ GHz for $B = 3$ T); ω, frequency of a V-polarized photon (wavelength 910.10 nm for $B = 3$ T); c.w., narrowband, continuous wave laser used for initialization and readout; Ω_{eff}, effective spin Rabi frequency resulting from manipulation by detuned ($\Delta = 300$ GHz), circularly polarized optical pulses[6,7]. **d**, Ramsey interference experiment, demonstrating coherent control of the electron spin qubit. Blue, raw data, for $\pi/2$-$\pi/2$ interference; green, least squares fit. For a 3 T magnetic field, the Larmor precession frequency $\delta\omega = 2\pi \times 17.6$ GHz. Inset, pulse scheme used.

the rotated polarization basis (say, $|\sigma^+\rangle$-photon) at time t_1, the resulting spin state evolves as follows:

$$\left|\psi_{\text{spin},\sigma^+}(t)\right\rangle = \frac{1}{\sqrt{2}}\left(e^{i\delta\omega(t-t_1)}|\uparrow\rangle - |\downarrow\rangle\right) \quad (2)$$

Owing to the large Zeeman splitting, a small uncertainty Δt_1 in the photon's arrival time can result in a large uncertainty in the phase of the spin state ($\delta\omega \times \Delta t_1$) and therefore a reduction in the entanglement visibility. Lowering the magnetic field further reduces the fidelity of the single-photon-based spin readout[6] and is therefore not a viable option in our experiment. Previous experiments in ionic[4] and NV-diamond systems[3] relied on the speed (timing jitter) of commercial single-photon detectors to fix the phase of the coherent spin precession, or, equivalently, to act as a quantum eraser[27] of the relatively small energy difference between different branches of the Λ-system (Supplementary Information). Such high bandwidth/fast detection techniques have also been employed to increase visibility in photon–photon interference experiments[12]. However, the much larger energy difference in our system requires a more advanced quantum eraser technique.

In order to tackle the large energy difference, we use a frequency downconversion technique that converts a single 910-nm photon into a single 1,560-nm photon with sub-8-ps timing resolution; this extreme timing resolution is sufficient to erase the which-path frequency information. The technique consists of mixing the single 910-nm photon with a few-picosecond pump light pulse at 2.2 µm in a PPLN waveguide device, producing a 1,560-nm photon via the process of difference-frequency generation (Methods). After narrowband filtering at 1,560 nm, the frequency-downconverted photon can be detected on a superconducting nanowire single-photon detector[28] (SNSPD) conditional on the exact overlap of the single 910-nm photon and the 2.2-µm pump pulse. The detection of the 1,560-nm photon therefore heralds a time-accurate measurement of the 910-nm photon: only if the 910-nm photon entered the PPLN waveguide exactly at the same time as the 2.2-µm pulse can a 1,560-nm photon be generated.

The system diagram of the conversion set-up is indicated in Fig. 2a. Using cross-correlation with a bright, 3-ps 910-nm pulse (Fig. 2b), we can infer a timing resolution of 8 ps or better for the PPLN waveguide device (Methods). As 8 ps correspond to an effective bandwidth of more
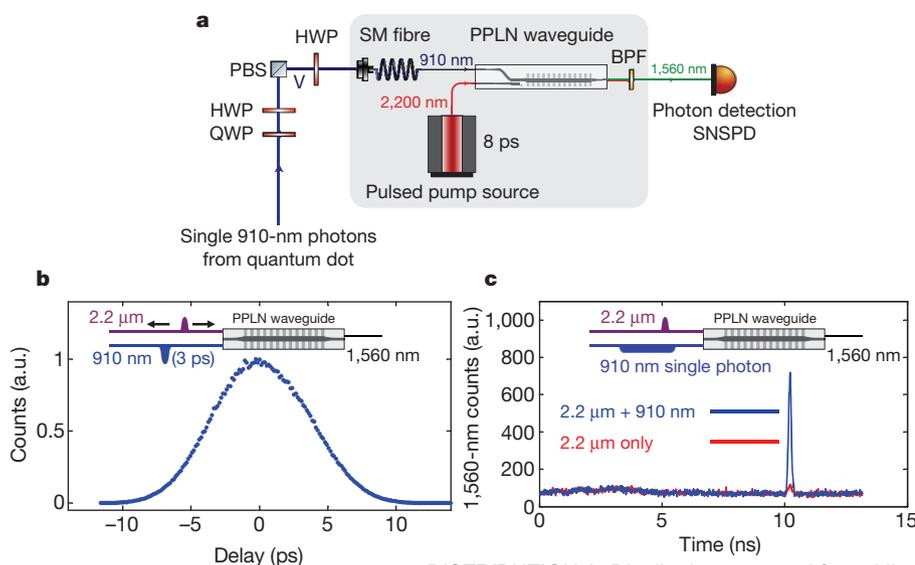

Figure 2 | Ultrafast conversion to 1,560 nm. a, Schematic overview of the conversion technique used (Methods). The 910-nm photon polarization is measured, with high timing accuracy, by a combination of a polarization analysing stage, a PPLN downconverter and an SNSPD. PBS, polarizing beamsplitter; HWP, half-wave plate; QWP, quarter-wave plate; SM, single-mode; BPF, 1,560 nm bandpass filter. **b**, Timing resolution of the 1,560-nm conversion technique, measured by cross-correlating the 2.2-µm conversion pulse with a classical, 3-ps pulse at 910 nm (inset). From these data, we can infer a sub-8-ps resolution for the arrival time of a single photon from the quantum dot. **c**, Performance of the conversion technique at single-photon levels, measured using an SNSPD. For single, 910-nm photons at the input (blue trace), the residual noise (red trace) can be seen to be well below the single-photon level (Methods). Inset, cross-correlation set-up.

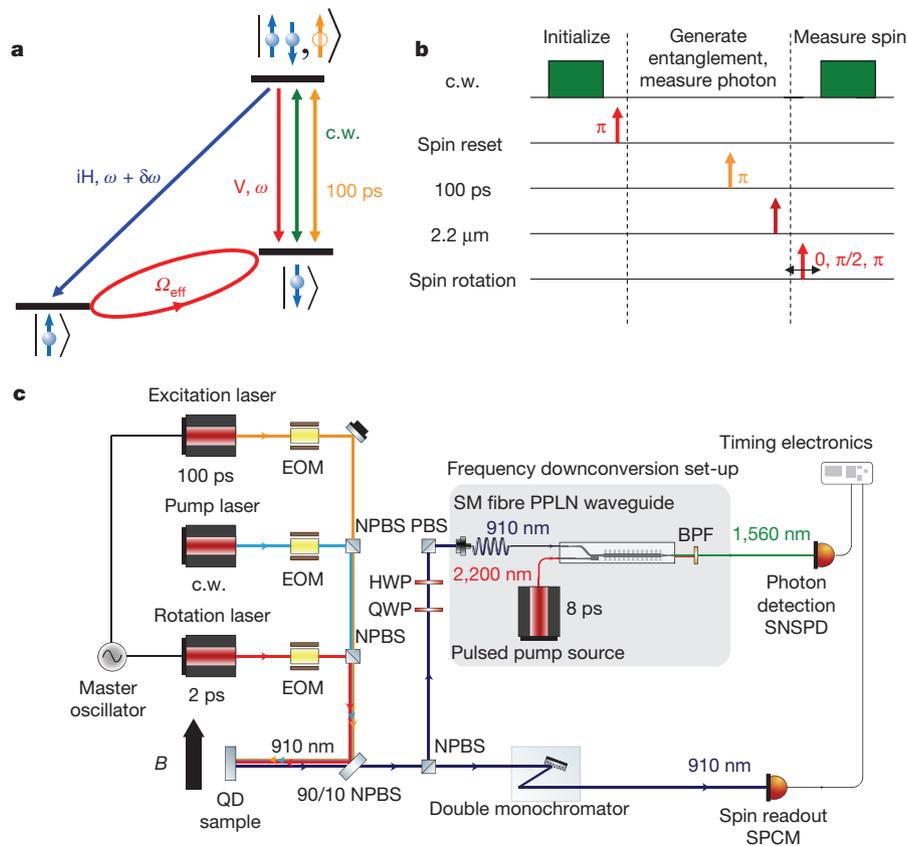DISTRIBUTION A: Distribution approved for public release.

Figure 3 | Quantum-dot manipulation scheme for spin–photon entanglement verification. a, Schematic overview of the quantum-dot manipulation techniques used in the experiment. '100 ps' indicates the resonant, 100-ps laser pulse used to excite the system into the $|{\uparrow}{\downarrow}\Uparrow\rangle$-state; 'c.w.' indicates the continuous wave (c.w.) laser used for initialization into the $|{\uparrow}\rangle$-state, and for readout of the $|{\downarrow}\rangle$-state. $\delta\omega$, Spin Larmor precession frequency; Ω_{eff}, effective spin Rabi frequency, resulting from manipulation by 3-ps, detuned optical pulses[6,7]. For the classical correlation measurements, manipulation of the spin using the H-branch was used as well, whereas the entanglement result was obtained using only V-branch pumping. **b**, Timing

diagram of the pulse sequence used in the experiment. Note the three cycles used in the experiment: initialization through optical pumping and spin rotation, generation of entanglement using 100-ps laser pulses and spontaneous emission decay, followed by ultrafast photon conversion to a telecom wavelength, and spin measurement through a combination of spin rotation (measurement basis change), optical pumping and single-photon detection. The cycle time of a single shot of the experiment was chosen to be either 39 or 52 ns. **c**, Schematic diagram of the set-up used in the experiment. EOM, electro-optic modulator; NPBS, non-polarizing beamsplitter. See text for other components.

than 100 GHz, this is more than sufficient to erase the information inherent in the Zeeman energy of 17.6 GHz at 3 T (Supplementary Information). In addition, the conversion and filtering technique results in almost noise-free signal transduction to the telecom band, as shown in Fig. 2c. We measure the polarization state of 910-nm photons using a polarization analysing stage consisting of a quarter-wave plate and a half-wave plate and a polarizer, followed by a single downconversion set-up that provides the necessary timing accuracy (filtering) in order to verify entanglement at 910 nm. The polarization selective operation of PPLN waveguides does not permit a full photonic polarization qubit at 910 nm to be directly downconverted to a polarization qubit at 1,560 nm. However, and as a straightforward extension of the work presented in this Letter, mapping the polarization qubit into a dual-rail qubit[29], using two separate time-resolved downconverters, would realize a spin-entangled 1,560-nm qubit, suitable for long-distance quantum communication[10] (Supplementary Information).

We analyse spin–photon entanglement using a combination of the time-resolved conversion technique and previously established spin initialization, manipulation and readout techniques[6,7]. Using 3-ps-long, 1-nm red-detuned optical pulses in a Ramsey interferometry set-up, we can completely control the state of any arbitrary electron spin superposition, with fidelities around 95% for the particular quantum dot used in this work (Supplementary Information). The spin state is measured using an optical pumping scheme[6,7], which is also used to initialize the system into the $|{\uparrow}\rangle$-state. Both processes emit a single

910-nm H-polarized photon that can be detected after frequency and polarization filtering from the optical pumping laser[6,7] (Fig. 3a and Methods). For a 13-ns spin interrogation time, readout and initialization fidelities of $\geq$96% can be inferred from the time-resolved emission decay, mainly limited by residual leakage of the continuous-wave laser used for optical pumping (Supplementary Information). The full control sequence of the optical pulses is indicated in Fig. 3b, and consists of three stages. First, the system is initialized into either the $|{\downarrow}\rangle$-state or the $|{\uparrow}\rangle$-state by a combination of optical pumping and spin rotation with a π-pulse. Then, a 100-ps optical π-pulse resonant with the $|{\downarrow}\rangle$–$|{\uparrow}{\downarrow}\Uparrow\rangle$-transition (or $|{\uparrow}\rangle$–$|{\uparrow}{\downarrow}\Uparrow\rangle$-transition) excites to the trion state, after which spontaneous emission occurs into the electron spin states. The difference between the spontaneous emission decay time (600 ps) and the excitation pulse duration (100 ps) allows for temporal filtering of the spontaneously emitted single photons. In addition, for the classical correlation measurements (see below), cross-polarization filtering can be used to further suppress noise from the reflection of the 100-ps excitation laser. The spontaneously emitted single photons are then sent to a polarization analysing stage, after which they are converted to 1,560 nm using the PPLN waveguide, and detected by an SNSPD. The next stage of the experiment consists of the spin analysis, which is performed through a combination of spin rotations (these implement an effective measurement basis change) and the optical pumping/readout cycle. We measure the correlations between the polarization of the 910-nm photon and the spin state through a timing histogram analysis

of the photons detected in the conversion and measurement cycles (Fig. 3c and Methods).

Using our time-resolved downconversion technique, we measure the classical (computational basis) correlations between the spin along the magnetic field axis (z), and the H–V polarization of the photon
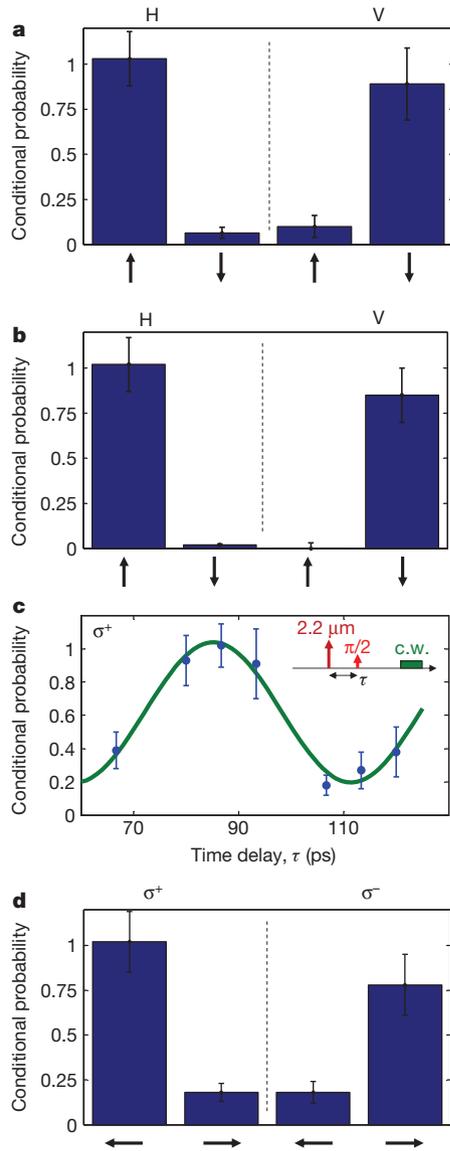

Figure 4 | Spin–photon entanglement verification. a, Classical (computational basis) spin–photon correlations, measured through downconversion to 1,560 nm. The black arrows (see also **b, d**) refer to the spin orientation in the computational (vertical arrows) or rotated (horizontal arrows) basis. **b**, Classical (computational basis) spin–photon correlations, measured at 910 nm, without downconversion. **c**, Spin–photon entanglement: on time-resolved detection of a $\sigma^{+,-}$-downconverted photon, the electron spin starts precessing due to the electron Zeeman energy (Larmor precession). By changing the arrival time of the subsequent π/2-pulse, this coherent spin precession can be mapped into a Ramsey fringe, where the population in the $|\downarrow\rangle$-state oscillates as a function of time, and depends on the helicity of the downconverted photon (the Ramsey fringes for opposite helicities are in antiphase). This oscillatory spin signal then results in an oscillatory, periodic coincidence count rate between the downconverted single photon and the spin-measurement photon. Blue, raw data from histogram analysis; green, least-squares, sinusoidal fit to the data. Inset, relative timings used. 2.2 µm indicates the 2.2-µm conversion pump pulse; π/2 shows the π/2 spin rotation pulse; c.w. indicates the continuous wave (c.w.), spin measurement laser at 910 nm. **d**, Spin–photon correlations in the rotated bases, demonstrating entanglement. Error bars, ±1 s.d. (**a**–**d**), due to Poissonian statistics ($n_{max} \approx 50$–100).

(Fig. 4a). For an H-polarized photon, we measure an excellent correlation with the $|\uparrow\rangle$-spin-state in the subsequent spin measurement cycle. Likewise, for a V-polarized photon, we see a strong correlation with the $|\downarrow\rangle$-spin-state. We can directly compare these correlations with the ones obtained without ultrafast downconversion, using a commercial single-photon detector (Fig. 4b). The results are in good agreement, and differ only due to small amounts of residual noise in the down-conversion process (Supplementary Information).

Verification of entanglement requires observation of correlations in a rotated basis of the photon polarization and the spin as well. When we measure the photon in the circular polarization basis ($|\sigma^+\rangle, |\sigma^-\rangle$), we measure the spin in the basis of $|\rightarrow\rangle = \frac{1}{\sqrt{2}}(|\uparrow\rangle + |\downarrow\rangle)$ and $|\leftarrow\rangle = \frac{1}{\sqrt{2}}(|\uparrow\rangle - |\downarrow\rangle)$. After detection of a σ^+ (σ^-)-downconverted photon at time t_1, the spin is projected into the $|\leftarrow\rangle$-state ($|\rightarrow\rangle$), which subsequently evolves in time due to Larmor precession:

$$\left|\psi_{spin}(t)\right\rangle = \frac{1}{\sqrt{2}}\left(e^{i(\delta\omega)(t-t_1)}|\uparrow\rangle \mp |\downarrow\rangle\right) \qquad (3)$$

Here $\delta\omega$ corresponds to the Zeeman frequency of $2\pi \times 17.6$ GHz. By scanning the arrival time of a π/2 spin rotation pulse in a Ramsey interferometer[6,7] (Fig. 4c and Methods) we can trace out this coherent oscillation, and verify entanglement. From the minima and maxima of these coherent oscillations, we can derive, as in Fig. 4d, the photon–spin correlations for σ^+ (σ^-) downconversion. For a particular photon polarization ($|\sigma^+\rangle, |\sigma^-\rangle$) and arrival time of the π/2 spin rotation pulse, a correlation can be measured, as expected. Subsequently changing the arrival time of the π/2-pulse by half a Larmor period results in an anticorrelation (see also Fig. 4c). Together, these results demonstrate spin–photon entanglement. We estimate the entanglement fidelity[3,4] to be 0.8 ± 0.085 (Methods and Supplementary Information), which exceeds the classical limit of 0.5 by more than three standard deviations[3,4].

Whereas our entanglement verification technique relies on time-resolved frequency conversion, resulting in filtering out only those 910-nm photons that exactly overlap with the arrival time of the 2.2-µm pump pulse, a more generic downconversion technique with a continuous wave pump laser at 2.2 µm and coincidence detection of two photons from separate quantum-dot sources could be used in future experiments in order to obtain spin–spin entanglement[17] (Supplementary Information).

We have demonstrated high-fidelity spin–photon entanglement in a single InAs quantum dot using an ultrafast downconversion technique to the lowest-loss telecom wavelength (1,560 nm). When combined with ultrafast control of InAs quantum-dot electron spins[6,7] and fast radiative decay of indistinguishable single photons from such quantum dots embedded in optical cavities[11,12,20,21], our results should enable quantum state transfer from a flying qubit to a stationary qubit or vice versa, and entanglement distribution between two remote matter qubits in long-distance quantum networks.

We note that, contemporaneously with this work, another group verified spin–energy entanglement between an InAs quantum-dot electron spin and a spontaneously emitted photon at 966 nm (ref. 30).

METHODS SUMMARY

Quantum dot and optical control. All results are obtained from a single quantum dot, emitting at 910 nm, embedded in a planar microcavity[7]. An external magnetic field in Voigt geometry splits the electron spin and trion states (Fig. 1a). A 0.68 NA aspheric lens focuses the pump and rotation lasers onto the sample. The coherent manipulation techniques are identical to those reported previously[7], with fidelities (initialization, readout, coherent rotation) around 95% or higher (Supplementary Information). After initialization, the $|\uparrow\Uparrow\rangle$-state is excited by a 100-ps mode-locked-laser pulse, synchronized with the spin-rotation laser. Photoluminescence is collected in a confocal set-up, and split into two branches. One branch is cross-polarized and sent through a double-monochromator onto a single-photon counter (SPCM) for spin-state analysis. The other branch is sent to a polarization analysing stage, after which it is sent to the downconversion set-up.

Downconversion, data acquisition and processing. The 2.2-μm light pulses needed for conversion are generated in a PPLN chip by mixing 3-ps, 911-nm pulses from the spin-rotation laser with narrowband, continuous wave 1,560-nm light. A PPLN waveguide converts 910-nm photons into 1,560-nm photons, conditional on overlap with the 2.2-μm pulses. An SNSPD subsequently detects the 1,560-nm photons. The SPCM and SNSPD signals are combined on a timing analyser, which allows for signal gating in post-processing. The noise in the conversion process is well below the single-photon level (between 4:1 and 10:1 signal-to-noise ratio). The correlation data are obtained from the coincidences between the downconverted single photons and the single photons used for spin detection, through post-processing of the data stream from the timing analyser, and normalized to uncorrelated events (Supplementary Information). The entanglement fidelity analysis follows the same procedure used in ion-trap[4] and NV-diamond[3] spin–photon entanglement experiments, and is estimated to be around 0.8 ± 0.085, well above the classical limit of 0.5.

Full Methods and any associated references are available in the online version of the paper.

1. Kimble, H. J. The quantum internet. *Nature* **453,** 1023–1030 (2008).
2. Ritter, S. *et al.* An elementary quantum network of single atoms in optical cavities. *Nature* **484,** 195–200 (2012).
3. Togan, E. *et al.* Quantum entanglement between an optical photon and a solid-state spin qubit. *Nature* **466,** 730–734 (2010).
4. Blinov, B. B., Moehring, D. L., Duan, L.-M. & Monroe, C. Observation of entanglement between a single trapped atom and a single photon. *Nature* **428,** 153–157 (2004).
5. Wilk, T., Webster, S. C., Kuhn, A. & Rempe, G. Single-atom single-photon quantum interface. *Science* **317,** 488–490 (2007).
6. Press, D., Ladd, T. D., Zhang, B. & Yamamoto, Y. Complete quantum control of a single quantum dot spin using ultrafast optical pulses. *Nature* **456,** 218–221 (2008).
7. Press, D. *et al.* Ultrafast optical spin echo in a single quantum dot. *Nature Photon.* **4,** 367–370 (2010).
8. Pelton, M. *et al.* Efficient source of single photons: a single quantum dot in a micropost microcavity. *Phys. Rev. Lett.* **89,** 233602 (2002).
9. Moreau, E. *et al.* A single-mode solid-state source of single photons based on isolated quantum dots in a micropillar. *Physica E* **13,** 418–422 (2002).
10. Takesue, H. *et al.* Quantum key distribution over a 40-dB channel loss using superconducting single-photon detectors. *Nature Photon.* **1,** 343–348 (2007).
11. Santori, C., Fattal, D., Vuckovic, J., Solomon, G. S. & Yamamoto, Y. Indistinguishable photons from a single-photon device. *Nature* **419,** 594–597 (2002).
12. Patel, R. B. *et al.* Two-photon interference of the emission from electrically tunable remote quantum dots. *Nature Photon.* **4,** 632–635 (2010).
13. Duan, L.-M., Lukin, M. D., Cirac, J. I. & Zoller, P. Long-distance quantum communication with atomic ensembles and linear optics. *Nature* **414,** 413–418 (2001).
14. Briegel, H.-J., Dür, W., Cirac, J. I. & Zoller, P. Quantum repeaters: the role of imperfect local operations in quantum communication. *Phys. Rev. Lett.* **81,** 5932–5935 (1998).
15. Yuan, Z.-S. *et al.* Experimental demonstration of a BDCZ quantum repeater node. *Nature* **454,** 1098–1101 (2008).
16. Stute, A. *et al.* Tunable ion-photon entanglement in an optical cavity. *Nature* **485,** 482–485 (2012).
17. Moehring, D. L. *et al.* Entanglement of single-atom quantum bits at a distance. *Nature* **449,** 68–71 (2007).
18. Chou, C. W. *et al.* Measurement-induced entanglement for excitation stored in remote atomic ensembles. *Nature* **438,** 828–832 (2005).
19. Faraon, A., Barclay, P. E., Santori, C., Fu, K.-M. C. & Beausoleil, R. G. Resonant enhancement of the zero-phonon emission from a colour centre in a diamond cavity. *Nature Photon.* **5,** 301–305 (2011).
20. Michler, P. *et al.* A quantum dot single-photon turnstile device. *Science* **290,** 2282–2285 (2000).
21. Santori, C., Pelton, M., Solomon, G., Dale, Y. & Yamamoto, Y. Triggered single photons from a quantum dot. *Phys. Rev. Lett.* **86,** 1502–1505 (2001).
22. Kim, D., Carter, S. G., Greilich, A., Bracker, A. S. & Gammon, D. Ultrafast optical control of entanglement between two quantum-dot spins. *Nature Phys.* **7,** 223–229 (2011).
23. Pelc, J. S., Langrock, C., Zhang, Q. & Fejer, M. M. Influence of domain disorder on parametric noise in quasi-phase-matched quantum frequency converters. *Opt. Lett.* **35,** 2804–2806 (2010).
24. Bayer, M. *et al.* Fine structure of neutral and charged excitons in self-assembled In(Ga)As/(Al)GaAs quantum dots. *Phys. Rev. B* **65,** 195315 (2002).
25. Xu, X. *et al.* Fast spin state initialization in a singly charged InAs-GaAs quantum dot by optical cooling. *Phys. Rev. Lett.* **99,** 097401 (2007).
26. Xu, X. *et al.* Optically controlled locking of the nuclear field via coherent dark-state spectroscopy. *Nature* **459,** 1105–1109 (2009).
27. Scully, M. O. & Drühl, K. Quantum eraser: a proposed photon correlation experiment concerning observation and ''delayed choice'' in quantum mechanics. *Phys. Rev. A* **25,** 2208–2213 (1982).
28. Tanner, M. G. *et al.* Enhanced telecom wavelength single-photon detection with NbTiN superconducting nanowires on oxidized silicon. *Appl. Phys. Lett.* **96,** 221109 (2010).
29. Nielsen, M. A. & Chuang, I. L. *Quantum Computation and Quantum Information* (Cambridge Univ. Press, 2000).
30. Gao, W. B., Fallahi, P., Togan, E., Miguel-Sanchez, J. & Imamoglu, A. Observation of entanglement between a quantum dot spin and a single photon. *Nature* http://dx.doi.org/10.1038/nature11573 (this issue).

Supplementary Information is available in the online version of the paper.

METHODS

Device design. The quantum-dot sample used is similar to the ones used previously to investigate ultrafast optical control and single spin echoes[7]. Compared to those experiments, the dot density was reduced, and the wavelength used was blue-shifted (910 nm). An asymmetric, low-Q cavity (10 nm FWHM, centred at 910 nm) redirects the spontaneous emission preferentially in one direction, increasing collection efficiency and reducing required peak powers for coherent control[7]. An external magnetic field (Voigt geometry, perpendicular to the optical axis) splits both the electron spin states and the excited, trion states. The resulting Λ-systems are indicated in Fig. 1a, and the polarization selection rules are verified by means of polarization-selective photoluminescence (half-wave plate and polarizing beamsplitter, Fig. 1b).

Spin control and single-photon collection. The quantum-dot device is cooled to 1.6 K inside a superconducting magnetic cryostat (Oxford Spectromag; the magnetic field used varies between $B = 3$ and 6 T). A 0.68 NA aspheric lens inside the cryostat focuses the pump and rotation lasers onto the sample, which is scanned relative to the lens by means of slip-stick piezo-electric positioners (Attocube Systems). The coherent manipulation techniques used are identical to those reported previously[7]. A narrowband c.w. laser (New Focus Velocity) is used for spin initialization and readout, resonant to the $|\downarrow\rangle$–$|\uparrow\downarrow\Uparrow\rangle$-transition (910.10 nm for a 3 T magnetic field), and switched on and off by a fibre-based EOM (EOSpace). The interrogation time is 13 ns, with an initialization and readout fidelity of about 96% or higher (Supplementary Information). Coherent spin rotations are performed in a Ramsey-interferometry set-up, using pulses from a mode-locked laser (3-ps pulse duration, centre wavelength 911 nm, Spectra-Physics Tsunami), which are delayed relative to each other through a retroreflector on a motorized stage. Individual pulses are selected through free-space EOMs (Conoptics), which are double-passed in order to increase the extinction ratio. The selective excitation of the $|\uparrow\downarrow\Uparrow\rangle$-state before spontaneous emission is realized through a combination of optical pumping into the $|\uparrow\rangle$-state, rotation by an optical π-pulse into the $|\downarrow\rangle$-state, followed by the application of a 100-ps pulse (optical π-pulse) from another mode-locked laser (Spectra-Physics Tsunami), resonant with the $|\downarrow\rangle$-$|\uparrow\downarrow\Uparrow\rangle$-transition. This laser is synchronized with the rotation laser (Spectra-Physics Lok-to-Clock system). Accurate polarization control limits the probability of excitation into the $|\uparrow\downarrow\Downarrow\rangle$-state to less than 1%. Another fibre-optic modulator allows for pulse-picking of the 100-ps excitation pulses. The single-photon photoluminescence is collected in a confocal set-up, and split into two branches by a non-polarizing beamsplitter. One branch is cross-polarized with respect to the initialization and optical pumping lasers, and sent through a double-monochromator onto a single-photon counter for spin-state analysis (Perkin-Elmer SPCM; 20% quantum efficiency, 170 Hz ungated dark count rate). The other branch is sent to a polarization analysing stage (quarter- and half-wave plate and polarizer), after which it is coupled into single-mode fibres and sent to the downconversion set-up. The polarization analysing stage is carefully calibrated, in order to account for residual birefringence in the setup. All EOMs are controlled by mutually synchronized pulse-pattern generators (76 MHz Tektronix and 10 GHz Anritsu PPG), that are themselves synchronized to the repetition rate of the mode-locked lasers. In contrast to previous experiments, no software-based lock-in technique was used. Instead, spatial, polarization, wavelength and time-filtering are used to separate reflected light from the single photons.

Downconversion set-up. The 2.2-µm light pulses needed for conversion are generated by a difference-frequency generation (DFG) process that mixes the 3-ps, 911-nm pulses from the mode-locked laser with narrowband, c.w. 1,560-nm light in an MgO-doped, PPLN chip. The 1,560-nm light is modulated by a fibre-optic modulator, and amplified by erbium-doped fibre amplifiers. After wave mixing, the residual 1,560-nm and 911-nm light is filtered out through a combination of dichroic and absorptive filters. The resulting pulse width depends on the exact power and wavelength used for the DFG process, but is measured to be between 3 and 8 ps.

A PPLN waveguide efficiently converts 910-nm, spontaneously emitted photons to 1,560-nm photons, conditional on overlap with the 2.2-µm pulses. Residual scattered light from the 910-nm and 2.2-µm branches is eliminated through a fibre-Bragg grating and a long-pass filter. The 1,560-nm photons are subsequently detected on an SNSPD, maintained at 2 K, with 14% system detection efficiency, 40-Hz ungated dark count rate and 100-ps FWHM timing jitter. Timing analysis is performed on a timing analyser (PicoQuant Hydraharp), used in time-tagged time-resolved (TTTR) mode, which allows for accurate gating of the signals of both the SPCM and the SNSPD in post-processing, thereby drastically reducing the effects of dark counts. The overall signal-to-noise ratio is limited by residual leakage of the 2.2-µm light, dark counts within the timing response of the SNSPD, and residual reflected light from the 100-ps excitation pulses, but is in general well below the single-photon level (signal-to-noise ratio ranging between 4:1 and 10:1 for the experiments described in this work). The timing of the 2.2-µm light is chosen such that the subsequent π/2-pulse arrives well within the T_2^*-dephasing time of the quantum dot; similar results can be obtained for times up to microseconds by implementing a spin echo technique to overcome shot-to-shot dephasing[7].

Data analysis and entanglement fidelity. The correlation data obtained in this work are the result of a histogram analysis, performed on the coincidence count rate between the downconverted single photons, and the single photons used for spin detection (Supplementary Information). The coincidence count rate is obtained through post-processing of the TTTR data stream, and comparing the coincidences within the same experimental run to those in subsequent, uncorrelated ones. The repetition rate is set at 39 or 52 ns, and the 0.1% single photon efficiency and time-gated frequency downconversion result in a 1,560-nm single-photon detection and entanglement generation rate of some 2–5 Hz. In combination with another 0.1% single-photon detection efficiency in order to detect the spin state, this results in an average coincidence rate of some 2–5 mHz. We emphasize that these losses are predominantly due to the inefficiency of extracting a single photon from the quantum dot, which can be significantly improved by accurate cavity design[8]. The conversion process in itself, while lossy due to the aggressive time-filtering in order to obtain good timing resolution, is rather effective, with internal quantum efficiencies estimated above 80%, and filtering losses of several dB maximum.

The entanglement fidelity analysis follows the same procedure used in the ion-trap[4] and NV-diamond[3] spin–photon entanglement experiments:

$$F \geq F_1 + F_2,$$
$$F_1 = \frac{1}{2}\left(\rho_{H\uparrow,H\uparrow} + \rho_{V\downarrow,V\downarrow} - 2\sqrt{\rho_{H\downarrow,H\downarrow}\rho_{V\uparrow,V\uparrow}}\right),$$
$$F_2 = \frac{1}{2}\left(\rho_{\sigma+\leftarrow,\sigma+\leftarrow} - \rho_{\sigma+\rightarrow,\sigma+\rightarrow} + \rho_{\sigma-\rightarrow,\sigma-\rightarrow} - \rho_{\sigma-\leftarrow,\sigma-\leftarrow}\right).$$

Here $\rho_{H\uparrow,H\uparrow}$ etc. refer to elements of the spin photon density matrix, which can be associated with the observed correlations in our experiment. For the values obtained in our work, $F_1 = 0.44 \pm 0.06$, $F_2 = 0.36 \pm 0.06$, from which we obtain a bound on the quoted fidelity: $F \geq 0.8 \pm 0.085$.

d) C. Heese, C.R. Phillips, B.W. Mayer, L. Gallmann, M.M. Fejer, U. Keller, "75 MW few-cycle mid-infrared pulses from a collinear apodized APPLN-based OPCPA," *Opt. Express* **20**, pp. 26888-94 (November 2012).

75 MW few-cycle mid-infrared pulses from a collinear apodized APPLN-based OPCPA

C. Heese,[1] C. R. Phillips,[2,*] B. W. Mayer,[1] L. Gallmann,[1] M. M. Fejer,[2] and U. Keller[1]

[1]*Department of Physics, Institute of Quantum Electronics, ETH Zurich, 8093 Zurich, Switzerland*
[2]*Edward L. Ginzton Laboratory, Stanford University, Stanford, California 94305, USA*
[*]*cphillips@phys.ethz.ch*

Abstract: We present an ultra-broadband optical parametric chirped-pulse amplification (OPCPA) system operating at 3.4 µm center wavelength with a peak power of 75 MW. The OPCPA system is split into a pre- and a power-amplifier stage. Both stages are based on apodized aperiodically poled MgO:LiNbO$_3$ (APPLN). The collinear mixing configuration allows us to manipulate the spectral phase of the output mid-infrared pulses by sending the near-infrared seed pulses through a pulse shaper. The system delivers clean 75-fs pulses with record-high 700 mW average power, corresponding to 7 µJ of pulse energy at a repetition rate of 100 kHz.

©2012 Optical Society of America

OCIS codes: (140.7090) Ultrafast lasers; (190.4970) Parametric oscillators and amplifiers; (140.3580) Lasers, solid-state.

References and links

1. A. D. Shiner, C. Trallero-Herrero, N. Kajumba, H. C. Bandulet, D. Comtois, F. Légaré, M. Giguère, J. C. Kieffer, P. B. Corkum, and D. M. Villeneuve, "Wavelength Scaling of High Harmonic Generation Efficiency," Phys. Rev. Lett. **103**(7), 073902 (2009).
2. P. Colosimo, G. Doumy, C. I. Blaga, J. Wheeler, C. Hauri, F. Catoire, J. Tate, R. Chirla, A. M. March, G. G. Paulus, H. G. Muller, P. Agostini, and L. F. DiMauro, "Scaling strong-field interactions towards the classical limit," Nat. Phys. **4**(5), 386–389 (2008).
3. K. D. Schultz, C. I. Blaga, R. Chirla, P. Colosimo, J. Cryan, A. M. March, C. Roedig, E. Sistrunk, J. Tate, J. Wheeler, P. Agostini, and L. F. DiMauro, "Strong field physics with long wavelength lasers," J. Mod. Opt. **54**(7), 1075–1085 (2007).
4. J. Tate, T. Auguste, H. G. Muller, P. Salières, P. Agostini, and L. F. DiMauro, "Scaling of Wave-Packet Dynamics in an Intense Midinfrared Field," Phys. Rev. Lett. **98**(1), 013901 (2007).
5. P. B. Corkum, "Plasma perspective on strong field multiphoton ionization," Phys. Rev. Lett. **71**(13), 1994–1997 (1993).
6. S. Baker, J. S. Robinson, C. A. Haworth, H. Teng, R. A. Smith, C. C. Chirilă, M. Lein, J. W. G. Tisch, and J. P. Marangos, "Probing Proton Dynamics in Molecules on an Attosecond Time Scale," Science **312**(5772), 424–427 (2006).
7. C. Vozzi, R. Torres, M. Negro, L. Brugnera, T. Siegel, C. Altucci, R. Velotta, F. Frassetto, L. Poletto, P. Villoresi, S. De Silvestri, S. Stagira, and J. P. Marangos, "High harmonic generation spectroscopy of hydrocarbons," Appl. Phys. Lett. **97**(24), 241103 (2010).
8. T. Fuji, N. Ishii, C. Y. Teisset, X. Gu, T. Metzger, A. Baltuška, N. Forget, D. Kaplan, A. Galvanauskas, and F. Krausz, "Parametric amplification of few-cycle carrier-envelope phase-stable pulses at 2.1 microm," Opt. Lett. **31**(8), 1103–1105 (2006).
9. G. Andriukaitis, T. Balčiūnas, S. Ališauskas, A. Pugžlys, A. Baltuška, T. Popmintchev, M.-C. Chen, M. M. Murnane, and H. C. Kapteyn, "90 GW peak power few-cycle mid-infrared pulses from an optical parametric amplifier," Opt. Lett. **36**(15), 2755–2757 (2011).
10. T. Wilhelm, J. Piel, and E. Riedle, "Sub-20-fs pulses tunable across the visible from a blue-pumped single-pass noncollinear parametric converter," Opt. Lett. **22**(19), 1494–1496 (1997).
11. A. Shirakawa, I. Sakane, M. Takasaka, and T. Kobayashi, "Sub-5-fs visible pulse generation by pulse-front-matched noncollinear optical parametric amplification," Appl. Phys. Lett. **74**(16), 2268–2270 (1999).
12. M. Ghotbi, M. Ebrahim-Zadeh, V. Petrov, P. Tzankov, and F. Noack, "Efficient 1 kHz femtosecond optical parametric amplification in BiB3O6 pumped at 800 nm," Opt. Express **14**(22), 10621–10626 (2006).
13. C. J. Fecko, J. J. Loparo, and A. Tokmakoff, "Generation of 45 femtosecond pulses at 3 µm with a KNbO3 optical parametric amplifier," Opt. Commun. **241**(4-6), 521–528 (2004).
14. G. M. Gale, G. Gallot, F. Hache, and R. Sander, "Generation of intense highly coherent femtosecond pulses in the mid infrared," Opt. Lett. **22**(16), 1253–1255 (1997).

15. U. Emmerichs, S. Woutersen, and H. J. Bakker, "Generation of intense femtosecond optical pulses near 3 µm with a kilohertz repetition rate," J. Opt. Soc. Am. B **14**(6), 1480–1483 (1997).
16. F. Tauser, F. Adler, and A. Leitenstorfer, "Widely tunable sub-30-fs pulses from a compact erbium-doped fiber source," Opt. Lett. **29**(5), 516–518 (2004).
17. C. Erny, C. Heese, M. Haag, L. Gallmann, and U. Keller, "High-repetition-rate optical parametric chirped-pulse amplifier producing 1-microJ, sub-100-fs pulses in the mid-infrared," Opt. Express **17**(3), 1340–1345 (2009).
18. O. Chalus, P. K. Bates, M. Smolarski, and J. Biegert, "Mid-IR short-pulse OPCPA with micro-Joule energy at 100kHz," Opt. Express **17**(5), 3587–3594 (2009).
19. C. Heese, C. R. Phillips, L. Gallmann, M. M. Fejer, and U. Keller, "Ultrabroadband, highly flexible amplifier for ultrashort midinfrared laser pulses based on aperiodically poled Mg:LiNbO₃," Opt. Lett. **35**(14), 2340–2342 (2010).
20. M. Bradler, C. Homann, and E. Riedle, "Mid-IR femtosecond pulse generation on the microjoule level up to 5 µm at high repetition rates," Opt. Lett. **36**(21), 4212–4214 (2011).
21. G. Cerullo and S. Silvestri, "Ultrafast optical parametric amplifiers," Rev. Sci. Instrum. **74**(1), 1–17 (2003).
22. S. Witte and K. S. E. Eikema, "Ultrafast Optical Parametric Chirped-Pulse Amplification," IEEE J. Quantum Electron. **18**(1), 296–307 (2012).
23. T. Sudmeyer, S. V. Marchese, S. Hashimoto, C. R. E. Baer, G. Gingras, B. Witzel, and U. Keller, "Femtosecond laser oscillators for high-field science," Nat. Photonics **2**(10), 599–604 (2008).
24. C. R. E. Baer, O. H. Heckl, C. J. Saraceno, C. Schriber, C. Kränkel, T. Südmeyer, and U. Keller, "Frontiers in passively mode-locked high-power thin disk laser oscillators," Opt. Express **20**(7), 7054–7065 (2012).
25. C. Heese, A. E. Oehler, L. Gallmann, and U. Keller, "High-energy picosecond Nd:YVO4 slab amplifier for OPCPA pumping," Appl. Phys. B **103**(1), 5–8 (2011).
26. A. Dubietis, G. Jonusauskas, and A. Piskarskas, "Powerful femtosecond pulse generation by chirped and strechted pulse parametric amplification in BBO crystal," Opt. Commun. **88**(4-6), 437–440 (1992).
27. C. Erny, L. Gallmann, and U. Keller, "High-repetition-rate femtosecond optical parametric chirped-pulse amplifier in the mid-infrared," Appl. Phys. B **96**(2-3), 257–269 (2009).
28. G. Imeshev, M. M. Fejer, A. Galvanauskas, and D. Harter, "Pulse shaping by difference-frequency mixing with quasi-phase-matching gratings," J. Opt. Soc. Am. B **18**(4), 534–539 (2001).
29. K. Mizuuchi, K. Yamamoto, M. Kato, and H. Sato, "Broadening of the phase-matching bandwidth in quasi-phase-matched second-harmonic generation," IEEE J. Quantum Electron. **30**(7), 1596–1604 (1994).
30. U. Kornaszewski, M. Kohler, U. K. Sapaev, and D. T. Reid, "Designer femtosecond pulse shaping using grating-engineered quasi-phase-matching in lithium niobate," Opt. Lett. **33**(4), 378–380 (2008).
31. M. Charbonneau-Lefort, B. Afeyan, and M. M. Fejer, "Optical parametric amplifiers using chirped quasi-phase-matching gratings I: practical design formulas," J. Opt. Soc. Am. B **25**(4), 463–480 (2008).
32. M. Charbonneau-Lefort, M. M. Fejer, and B. Afeyan, "Tandem chirped quasi-phase-matching grating optical parametric amplifier design for simultaneous group delay and gain control," Opt. Lett. **30**(6), 634–636 (2005).
33. M. Charbonneau-Lefort, B. Afeyan, and M. M. Fejer, "Competing collinear and noncollinear interactions in chirped quasi-phase-matched optical parametric amplifiers," J. Opt. Soc. Am. B **25**(9), 1402–1413 (2008).
34. C. R. Phillips and M. M. Fejer, "Efficiency and phase of optical parametric amplification in chirped quasi-phase-matched gratings," Opt. Lett. **35**(18), 3093–3095 (2010).
35. C. Erny, K. Moutzouris, J. Biegert, D. Kühlke, F. Adler, A. Leitenstorfer, and U. Keller, "Mid-infrared difference-frequency generation of ultrashort pulses tunable between 3.2 and 4.8 microm from a compact fiber source," Opt. Lett. **32**(9), 1138–1140 (2007).
36. C. Heese, C. R. Phillips, L. Gallmann, M. M. Fejer, and U. Keller, "Role of apodization in optical parametric amplifiers based on aperiodic quasi-phasematching gratings," Opt. Express **20**(16), 18066–18071 (2012).
37. K. W. DeLong, R. Trebino, J. Hunter, and W. E. White, "Frequency-resolved optical gating with the use of second-harmonic generation," J. Opt. Soc. Am. B **11**(11), 2206–2215 (1994).
38. C. Conti, S. Trillo, P. Di Trapani, J. Kilius, A. Bramati, S. Minardi, W. Chinaglia, and G. Valiulis, "Effective lensing effects in parametric frequency conversion," J. Opt. Soc. Amer. B **19**(4), 852 (2002).
39. J. Huang, X. P. Xie, C. Langrock, R. V. Roussev, D. S. Hum, and M. M. Fejer, "Amplitude modulation and apodization of quasi-phase-matched interactions," Opt. Lett. **31**(5), 604–606 (2006).
40. G. Stobrawa, M. Hacker, T. Feurer, D. Zeidler, M. Motzkus, and F. Reichel, "A new high-resolution femtosecond pulse shaper," Appl. Phys. B **72**(5), 627–630 (2001).

1. Introduction

Mid-infrared (MIR) pulses are of great interest for strong-field experiments, offering a possibility to study the wavelength scaling of light-matter interaction in the non-perturbative regime [1–5]. For instance, with high harmonic generation (HHG), electrons are accelerated in the electric field of one half-cycle of the laser pulse before recollision with the atom [5]. With a long wavelength, for example in the mid-infrared (MIR), acceleration takes place over a longer time interval and results in higher recollision energies at a given optical intensity.

This single aspect already illustrates the intrinsic difference between long- and short-wavelength laser-matter interactions.

A direct application of wavelength scaling in a strong-field process can be found in HHG spectroscopy [6] The measured HHG spectra can be used to derive information about electron or proton dynamics on the attosecond timescale. One difficulty for the extension of this technique to larger and more relevant molecules is the low ionization potential I_p usually found in these systems. At short optical wavelengths, saturation effects of the ionization process constrain this technique to the investigation of molecules with high I_p. This constraint can be overcome by the use of MIR laser pulses, which should enable the study of a much wider range of molecules, in particular biomolecules [7].

For efficient HHG there are constraints on both the peak intensity and total energy of the laser (as well as other system parameters). In order to make high signal-to-noise (SNR) measurements with the generated photons, it is therefore useful to move to higher repetition rates (e.g. 100 kHz) than are used in conventional chirped pulse amplification (CPA) and optical parametric CPA (OPCPA) systems, which usually operate at ≤1 kHz [8–20]. High repetition rates also enable the measurement of fast-degrading samples.

Generating the required high-intensity ultrashort pulses in the MIR is challenging due to the lack of suitable broadband gain media. OPCPA is a promising approach [21, 22], but there is a limited selection of suitable nonlinear crystals for MIR operation. Furthermore, operating an OPCPA system at high-repetition rate places stringent requirements on both the peak and average power of the pump (tens of MW and tens of W, respectively), while still requiring high stability and good beam/pulse quality. At present, the most promising pump lasers for meeting these requirements are mode-locked 1-µm diode-pumped solid-state lasers [23–25]. Developing an approach to broadband MIR OPCPA that is compatible with these lasers is therefore of great importance for the HHG applications described above.

Since the first demonstration of OPCPA [26], several approaches to obtain broad bandwidths have been explored. One way to obtain broadband OPA is to operate at wavelength- and polarization-degeneracy. For example, in Ref [8], 400-µJ, 2.1-µm, 20-fs pulses were obtained from a 1-kHz OPCPA system. However, degenerate operation constrains the wavelengths involved, limiting the range of HHG pump wavelengths that can be studied. Broadband operation can also be obtained by noncollinear OPA (NOPA) [10], but there are few suitable nonlinear crystals available in the MIR, the generated idler is spatially and angularly dispersed, and such schemes can also have the drawback of quite high experimental complexity.

If a sufficiently short signal-idler coupling distance (i.e. a high gain rate) can be obtained, broad bandwidths are possible with non-degenerate collinear OPCPA. Such high gain rates are obtained with periodically poled $MgO:LiNbO_3$. For example, in Ref [17], 1-µJ, 3.6-µm, <100-fs pulses were obtained at 100 kHz. However, the bandwidth possible with this approach is limited by the damage threshold of the crystal [27].

With the high degree of engineerability supported by quasi-phasematching (QPM) [28–30], this bandwidth limitation can be overcome while still maintaining a collinear and non-degenerate interaction. In Refs [31–34], a new approach to OPCPA based on aperiodic (chirped) QPM gratings was proposed. In this approach, there is essentially no intrinsic limit on the optical bandwidth, since a very wide range of QPM periods and crystal lengths can be reliably (lithographically) fabricated, thereby phasematching all frequencies of interest. Therefore, it is possible to utilize power-scalable 1-µm pump lasers without compromising the bandwidth of the OPA process. Additionally, the QPM grating can be engineered to tailor the spectral gain and phase over a large bandwidth [32], and high conversion efficiency is possible via adiabatic frequency conversion [34].

In Ref [19], we demonstrated the first OPCPA system based on this technique, using aperiodically poled $MgO:LiNbO_3$ (APPLN) to generate 1.5-µJ, 3.4-µm, 75-fs pulses at 100 kHz, with seed-limited pulse duration. In this paper, we present the extension of this

technique to 7-µJ energy levels by significant improvements in system and APPLN device designs. In section 2, we describe our OPCPA system and present our experimental results. In section 3 we describe the APPLN OPCPA devices, and in section 4 we provide details on the dispersion compensation scheme.
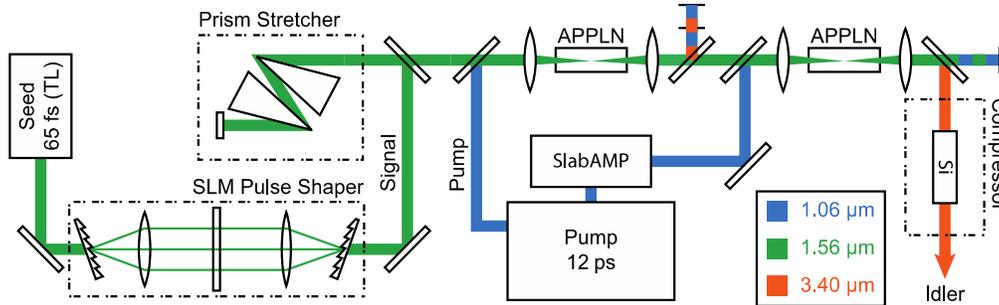
2. Experimental setup and results

Fig. 1. Optical setup of the 2-stage OPCPA delivering 75-MW pulses. After the 2nd stage, the MIR idler is extracted and compressed to 75 fs duration by propagation through 150 mm bulk silicon (90% transmission). The spectral phase of the idler can be controlled by the pulse-shaper placed in the seed beam. During the OPA process, the spectral phase of the NIR seed is transferred to the MIR idler.

Our experimental setup is shown in Fig. 1. Compared to our previous MIR source [19], we changed the seed concept [35], integrated a home-built pump laser [25] into the OPCPA, and improved the APPLN devices [36]. The amplification system consists of a pre-amplifier (denoted OPA1) and a power amplifier (denoted OPA2). With the modified seed approach, we seed OPA1 with a near-infrared (NIR) signal, and seed OPA2 with the amplified signal output of OPA1. The generated MIR idler of OPA2 is then kept and sent into the pulse compressor. In our previous system, MIR seed pulses were generated from low-energy input pulses through difference frequency generation in a fan-out QPM grating [35]. In our new system, a commercial 1.56-µm femtosecond laser is used directly as the NIR seed to OPA1, corresponding to a significant reduction in system complexity.

The most significant advantage of this NIR seeding approach is efficiency: we found a material combination which allowed for bulk compression of the MIR pulses (with 90% transmission efficiency) while still compensating for second- and third-order dispersion of the stretched pulses. This efficiency is twice that of our previous prism-based compressor design [19]. Another significant benefit of the new seed concept is that the only elements that must be placed in the output MIR idler are a collimation lens and the bulk Si compressor. All other optical components in the amplifier path are optimized and aligned at the more standard and easier to detect 1 µm pump and 1.5 µm seed wavelengths, which allows for more precise and efficient alignment of the system.

In addition, at the telecommunication seed wavelength, many well-developed optical components are available. For example, we use a spatial light modulator (SLM) for high repetition rate pulse shaping. The use of such standard components is consistent with the overall design goal for the system: We aim at developing a reliable system that is useful for strong-field physics experiments on a daily basis. The NIR seeding approach is enabled by the collinear APPLN OPCPA geometry: since both the signal and idler pulses are collinear with the pump, they are usable for subsequent experiments or amplification. In contrast, in a non-collinear configuration, a useable idler (generated wave) can only be obtained by non-trivial compensation of its spatial chirp.

The pump source for OPA1 is a turn-key industrial laser (Time-Bandwidth Products Inc., Duetto) which operates at 1.064 µm and delivers 12-ps pulses at a repetition rate of 100 kHz, with an average output power of up to 11 W. Up to 8 W of this laser is used for OPA1, while

the remaining power is sent into a home-built Nd:YVO$_4$ slab amplifier to generate the pump pulses for OPA2 [25]. This slab amplifier yields a maximum power of up to 46 W (466 µJ at 12 ps pulse duration when operating at 100 kHz).

The pulse train of the pump laser oscillator is electronically stabilized to that of the seed laser with a phase locked loop (PLL). Our locking scheme yields a residual timing jitter of less than 150 fs rms, which is very small compared to the pump and stretched seed pulse durations. By setting the phase of the PLL we can control the delay between the pulses of the two oscillators by up to ± 1 ns. This approach allows us to control the overlap of seed and pump without any moving mechanical parts.
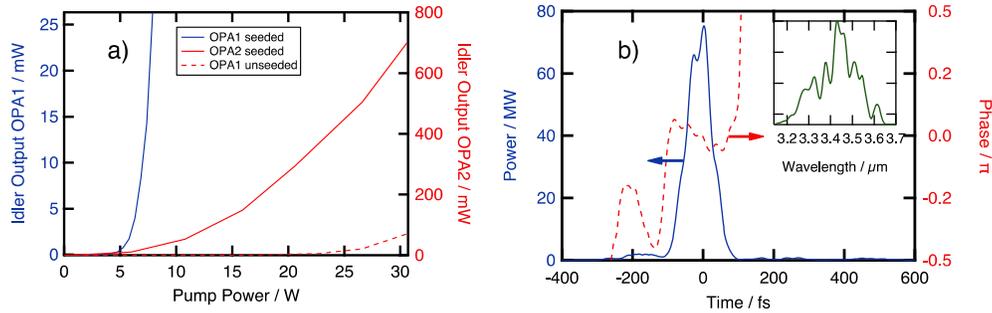

Fig. 2. (a) Pump-power dependence of OPA1 and OPA2. The maximum measured idler power after OPA1 is 26 mW (solid blue line), and there is no measurable OPG output (10 µW measurement threshold). The maximum idler power after both OPA2 and the bulk-compression stage is 700 mW, corresponding to 7 µJ (solid red line). We obtained an (over-)estimate of 72 mW for the optical parametric generation (OPG) background by blocking the seed pulses (dashed red line). This measurement is discussed further in section 3. (b) Reconstructed temporal pulse profiles from SHG-FROG after compression with 150-mm of bulk silicon. The inset shows the corresponding spectrum.

Before OPA1, the 1.56-µm seed pulses from the femtosecond fiber laser are stretched to approximately 2.6 ps by a two-prism silicon stretcher and a SLM-based pulse shaper. The holographic gratings used in this pulse shaper have a groove density of 600/mm; the dispersed pulses are collimated by an 800-mm cylindrical lens before passing through the SLM shown in Fig. 1. The energy of the stretched pulses reaching OPA1, after both the pulse shaper and the prism stretcher, is 87 pJ.

To support the required broadband output (as well as future bandwidth scaling) we use apodized, aperiodically poled MgO:LiNbO$_3$ for both OPA1 and OPA2. The QPM grating design is discussed in section 3. The pump and seed beams are collinearly overlapped in both amplification stages, with peak pump intensities of 6.8 GW/cm^2 (1/e^2 radius w = 250 µm) and 9.4 GW/cm^2 (w = 400 µm) in OPA1 and OPA2, respectively. The output idler power of the OPAs as a function of incident pump power is depicted in Fig. 2(a) (solid lines). The OPA2 curve was measured after collimation and compression, and hence shows that a final output pulse energy of 7 µJ is achieved. We characterized the output pulses using second harmonic generation (SHG) frequency resolved optical gating (FROG) [37]. The FROG-reconstructed temporal profile of the output pulses is depicted in Fig. 2(b), showing a pulse duration of 75-fs; this duration appears to be seed-limited. The corresponding power spectrum is shown as a function of wavelength in the inset.

3. Apodized APPLN amplifiers

In both amplifier stages we use 10-mm-long, 1-mm-wide, uncoated APPLN chips. The QPM chirp rate is given by κ' = -dK$_g$/dz, where K$_g$(z) is the local grating k-vector. A chirp rate of κ' = −2.5 mm^{-2} is used to achieve a broad phase-matching spectral window ranging from 2.71 to 4.24 µm. The negative chirp rate was chosen since it yielded a higher beam quality than a

positive chirp. The sign of the chirp rate can play a role in effective lensing effects which occur during the parametric frequency conversion process [38]. These and other relevant effects will be discussed in more detail in future work. Another important property of the chip is the apodization. To avoid accumulation of spectral phase ripples or other high-order phase contributions during the amplification process, the nonlinear coupling is turned on and off adiabatically (smoothly and sufficiently slowly) at the input and output ends of the QPM grating [39]. The apodization is realized by rapidly varying the poling period (poling period apodization), resulting in dephasing of the three-wave mixing process (effectively reducing the nonlinear coupling). The grating profile is depicted in Fig. 3.
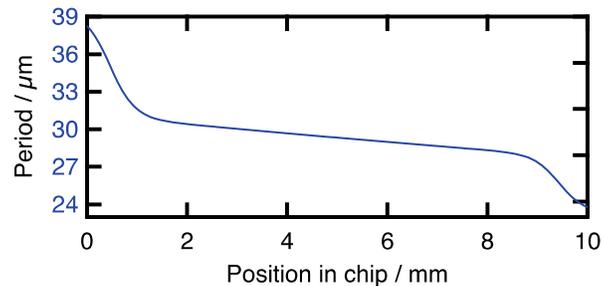

Fig. 3. Poling structure for the APPLN OPA devices used in both stages. An apodized linearly chirped QPM grating is used to ensure a smooth gain spectrum. The linear chirp rate is $\kappa' = -2.5$ mm^{-2}. The nonlinear coupling is turned on and off adiabatically at both ends, over a distance ~10% of the total length of the grating, by rapidly varying the poling period (increasing the magnitude of the chirp rate). The nominal QPM duty cycle is 50%.

With these apodized gratings, we obtain clean temporal pulse profiles after the bulk compressor, with almost all the pulse energy in the main pulse. Before designing this high-power, few-cycle OPCPA, we studied the effect of apodization on the pulse structure [36]. Without apodization the temporal structure breaks up into multiple sub-pulses, reducing peak intensity.

The focusing geometry is an important parameter of the OPCPA system design. APPLN OPAs can be affected by non-collinear gain guided modes [33]. If these modes exist, they can be amplified throughout the whole crystal, in contrast to collinear signal beams which experience gain only in the vicinity of its perfect phase-matching point [31]. Such gain guided modes are seeded by quantum noise and can therefore result in an increased optical parametric generation (OPG) background. With sufficient pump peak power that a large spot size with adequate intensity to support the collinear gain can be obtained, this gain guiding process can be suppressed at a given peak intensity, since the noncollinear beam components are dephased before they leave the large pump beam [33]. This high peak power is now available from our upgraded pump source. In the range of available pump powers we do not see a significant background from OPG. We estimated an upper limit for the OPG by blocking the seed before OPA1. The remaining output power of OPA1 is below the measurement threshold of 10 µW. When directed into OPA2, this small amount of OPG is amplified to 72 mW at full pump power of 30 W [red dashed line in Fig. 2(a)]. In the seeded case, we expect this small remaining background to be decreased substantially as a result of pump depletion.

4. Dispersion compensation

After amplification the pulses must be compressed in time. We designed the NIR pulse stretcher such that MIR pulse compression could be performed in a bulk crystal, thereby keeping the MIR losses as low as possible. During the OPA process, the spectral phase of the signal is transferred to the idler. Because both the phase and frequency shift of spectral components of the generated idler wave are inverted with respect to the signal seed wave, the

sign of the group delay dispersion (GDD) is reversed, but the sign of the third order dispersion (TOD) is maintained. Note that there are also additional contributions to the GDD and TOD of the generated idler wave due to the use of chirped QPM gratings, as discussed in [32].

Our stretching system for the 1.56-μm seed yields positive GDD and negative TOD. The 3.4-μm idler is generated with a negative GDD which is then compensated by the positive GDD of the bulk Si compressor placed after the OPCPA output. Two pieces of antireflection-coated bulk Si with a combined length of 150 mm are used. We were able to compress the 3.4-μm-pulses to 80 fs duration with a total transmission of 90% by using this seed stretching and Si bulk compressor combination.

To enable additional fine control of the dispersion, we placed a SLM-based pulse shaper in the seed beam path [40]. We used this shaper to pre-compensate the residual TOD on the idler, resulting in the seed-limited pulse duration of 75 fs shown in Fig. 2(b). More generally, with such a pulse shaper we can deliver the shortest possible pulses to an experimental target by pre-compensating for material dispersion occurring along the propagation to each specific experiment (vacuum chamber entrance windows, etc.). This approach therefore simplifies the operation of the laser for various applications.

5. Conclusion

In conclusion, we have demonstrated an OPCPA system for few-cycle pulse generation in the mid-infrared. The concept of seeding the OPCPA with the signal at 1.56 μm allows us to use standard optical components up to the 3.4 μm-idler extraction occurring after the final OPA stage. This design choice makes bulk compression with 90% efficiency possible. We achieve 75 fs pulse duration (<7 optical cycles) at 7 μJ output energy, corresponding to 700 mW of average power at a repetition rate of 100 kHz. To verify the usefulness of this source for strong-field experiments, we focused the 3.4-μm, 75 MW beam with an aspherical lens (EFL = 4 mm) into a gas target at ~100 mbar. Successful ionization of Xe, Ne and He confirms focusability to intensities $>10^{14}$ W/cm^2.

To our knowledge, this system is the first practical implementation of an OPCPA that uses apodized APPLN for the generation of clean, high-energy few-cycle pulses. By upgrading our pump source we have shown the energy scalability of the technique. In the next step we will replace our seed source in order to obtain broader bandwidths. With APPLN OPCPA devices, it should be possible significantly increase the bandwidth. With realistic improvements to the system, we therefore expect to generate few-cycle pulses with even higher energies.

Acknowledgments

e) C.R. Phillips, J.S. Pelc, M.M. Fejer, "Parametric processes in quasi-phasematching gratings with random duty cycle errors," *JOSA-B* **30**, pp. 982-93 (April 2013).

Parametric processes in quasi-phasematching gratings with random duty cycle errors

C. R. Phillips,* J. S. Pelc, and M. M. Fejer

E. L. Ginzton Laboratory, Stanford University, 348 Via Palou, Stanford, California 94305, USA
*Corresponding author: cphillips@phys.ethz.ch

Random duty cycle (RDC) errors in quasi-phase-matching (QPM) gratings lead to a pedestal in the spatial-frequency spectrum that increases the conversion efficiency for nominally phase-mismatched processes. Here, we determine the statistical properties of the Fourier spectrum of the QPM grating in the presence of RDC errors. We illustrate these properties with examples corresponding to periodic gratings with parameters typical for continuous-wave interactions, and chirped gratings with parameters typical for devices involving broad optical bandwidths. We show how several applications are sensitive to RDC errors by calculating the conversion efficiency of relevant nonlinear-optical processes. Last, we propose a method to efficiently incorporate RDC errors into coupled-wave models of nonlinear-optical interactions while still retaining only a small number of QPM grating orders.   © 2013 Optical Society of America

OCIS codes: 190.4410, 190.4360, 230.7405, 190.4970.

1. INTRODUCTION

In a wide variety of experiments using quasi-phase-matching (QPM) gratings, multiple nonlinear conversion processes can occur simultaneously, whether by design [1–8] or as a natural (and possibly parasitic) consequence of the desired device configuration [9–27]. Such parasitic processes can play an important role in many contexts, including frequency conversion of quantum states of light [8–13], optical parametric oscillators (OPOs) [14–20], optical parametric amplification (OPA) [21–23], and QPM supercontinuum generation [24–27]. The types of parasitic processes considered in this paper are nominally phase-mismatched nonlinear interactions, which, in QPM gratings with random variations in the duty cycle, can occur with efficiencies significantly higher than would be expected given an ideal QPM grating and a large phase mismatch [28,29].

In periodically or aperiodically poled lithium niobate (PPLN and APPLN, respectively), these nonidealities typically correspond to the ferroelectric domain boundaries not lying at their ideal (designed) positions [29,30]. When the errors in the domain boundary positions have stationary statistics (as is typically the case for lithographically defined QPM patterns), and in particular when these errors are independent and identically distributed (IID), they are termed random duty cycle (RDC) errors [29]. While these RDC errors usually have only a weak effect on the conversion efficiency near the QPM peak, they give rise to a "pedestal" in the spatial-frequency spectrum of the grating. Away from the phase-matching peak of the ideal structure, this QPM noise pedestal is relatively flat statistically (i.e., after averaging over an ensemble of imperfect QPM gratings), unlike the Fourier spectrum of the ideal grating (which, for example, has approximately a sinc² form for a periodic grating). This pedestal can lead to an increase in the conversion efficiency of parasitic, nominally phase-mismatched processes compared to that expected in a perfect

grating. It is therefore important to model RDC errors so that experiments can be designed that are not excessively sensitive to their effects.

In this paper, we analyze RDC errors in detail, and consider several applications where they can play a significant role. In Section 2, we first develop a general formalism for describing the QPM gratings with RDC errors, including those with arbitrary nominal duty cycle and chirp profiles. In Subsections 2.B and 2.D, we derive the statistical properties of the QPM noise pedestal itself. Our treatment readily yields results for pulsed interactions and also for backward-generated waves: these cases are discussed in Subsections 2.C and 2.E, respectively. In Section 3, we discuss the QPM noise pedestal for the cases of periodic and linearly chirped gratings. The results for these two cases will be relevant to a large fraction of QPM gratings used in practical devices.

In Section 4 we investigate a number of applications where RDC errors can play a significant (and possibly unexpected) role. We consider the following applications: dark count rates in quantum-state frequency translation, two-photon absorption (TPA) in high power optical parametric chirped pulse amplification (OPCPA), nonlinear losses in OPOs, cascaded processes in OPOs, and supercontinuum generation. This list is not intended to be exhaustive, but is representative of the importance of RDC-related effects and of how these effects can be evaluated in various different practical contexts. To analyze some of these applications, we extend the formalism of Section 2 to account for more complicated interactions, while maintaining the same overall statistical approach. For highly nonlinear interactions, however, a purely analytical approach is usually insufficient, particularly when ultrashort pulses are involved. Therefore, we also discuss in Appendix A how RDC errors could be incorporated into existing general numerical modeling tools used to simulate QPM interactions.

2. QPM GRATINGS WITH RDC ERRORS

In this section, we calculate the ensemble-averaged statistical properties of the spatial-frequency pedestal that arises due to RDC errors. We consider a three-wave difference-frequency generation (DFG) process involving monochromatic plane waves with negligible signal gain and pump depletion. Our results are directly applicable to second-harmonic generation (SHG) and sum-frequency generation (SFG), provided that depletion of the input waves can be neglected.

A. Transfer Function

Under the above assumptions, the generated idler is given by a transfer function that is related to the spatial Fourier transform (FT) of the QPM grating [31]. In this subsection, we derive this transfer function and express it in a form suitable for subsequent statistical analysis. The propagation equation for the idler envelope is given by [32]

$$\frac{dA_i}{dz} = -i\frac{\omega_i d(z)}{n_i c} A_s^* A_p e^{-i\Delta kz}, \qquad (1)$$

where subscripts (i, s, p) correspond to the idler, signal, and pump, respectively. ω_j is the carrier frequency of wave j, and n_j is the refractive index evaluated at ω_j. The envelopes A_j are defined in relation to the electric field as $E = (1/2)\sum_j A_j \exp[i(\omega_j t - k_j z)] + $ c.c. (complex conjugate), where summation is performed over $j = i$, s, p and $k_j = \omega_j n_j/c$. The phase mismatch is defined as $\Delta k = k_p - k_s - k_i$, and $d(z) = \pm d_0$ is the value of the relevant second-order nonlinear coefficient based on the $\chi^{(2)}$ tensor and the polarization directions of the interacting fields, and is inverted periodically or aperiodically in the QPM grating.

The idler field A_i can be written in a form normalized to the value it would take at the output of an ideal periodic grating, with no RDC errors, satisfying first-order QPM (for which the domain size would be given by $\Lambda_D = \pi/\Delta k$):

$$A_i = -i\frac{2L}{\pi}\frac{\omega_i d_0}{n_i c} A_s^* A_p a_i, \qquad (2)$$

where a_i is the normalized idler field and L is the length of the QPM grating. With this definition, Eq. (1) can be written as

$$\frac{da_i}{dz} = \frac{\pi}{2L}\frac{d(z)}{d_0} e^{-i\Delta kz} \equiv g(z)e^{-i\Delta kz}, \qquad (3)$$

where the normalized grating profile $g(z)$ is implicitly defined in Eq. (3), and $g(z) = 0$ for $z < 0$ and $z > L$. By integrating Eq. (3), it can be seen that the normalized idler output $a_i(L)$ is the spatial FT of $g(z)$, $\tilde{g}(k)$, evaluated at spatial frequency $k = \Delta k$. We define the FT of a function $f(x)$ as $\tilde{f}(k) \equiv \mathcal{F}[f(x)](k) = \int f(x)e^{-ikx}dx$, with tilde denoting a quantity expressed in the frequency domain. The square magnitude of $\tilde{g}$ gives the idler intensity relative to the "maximum" intensity achievable in a QPM grating of the same length, assuming that the pump and signal [or first harmonic (FH) in the case of SHG] are undepleted. By writing $g(z)$ as a sum of individual domains, $\tilde{g}(k)$ can be written as

$$\tilde{g}_{\mathbf{z}}(k) = i\frac{\pi}{2kL}\sum_{n=1}^{N}(-1)^n(e^{-ik\mathbf{z}[n]} - e^{-ik\mathbf{z}[n-1]})$$

$$= i\frac{\pi}{kL}\left[\frac{e^{-ik\mathbf{z}[0]} + (-1)^N e^{-ik\mathbf{z}[N]}}{2} + \sum_{n=1}^{N-1}(-1)^n e^{-ik\mathbf{z}[n]}\right], \qquad (4)$$

where $\mathbf{z}$ is a vector which specifies the domain boundary positions. The notation $\tilde{g}_{\mathbf{z}}$ is used to indicate the domain boundary vector $\mathbf{z}$ being considered. We refer to $\tilde{g}_{\mathbf{z}}(k)$ as the normalized transfer function.

Next, we approximate the contributions from the first and last QPM domains (those related to the positions $\mathbf{z}[0]$ and $\mathbf{z}[N]$), in order to write $\tilde{g}_{\mathbf{z}}(k)$ in a simpler form as a summation of complex exponentials. The resulting (approximate) normalized transfer function is given by

$$\tilde{g}_{\mathbf{z}}(k) \approx i\frac{\pi}{kL}\sum_{n=1}^{N}(-1)^n e^{-ik\mathbf{z}[n]}. \qquad (5)$$

Comparing Eqs. (4) and (5), we see that the approximation is perfect for an ideal grating satisfying first-order QPM, and in general its error is comparable to the contribution from a single domain.

We denote the ideal vector of domain boundary positions (those obtained in the absence of any RDC errors) as $\mathbf{z}_0$. In an ideal periodic grating, $\mathbf{z}_0[n] = n\Lambda_D$ for domain length Λ_D. For a phase-matched interaction in such an ideal periodic grating, $k = \Delta k = \pi/\Lambda_D$, in which case the summand in Eq. (5) is simply unity for each term, and so $|\tilde{g}_{\mathbf{z}_0}(\pi/\Lambda_D)| = 1$, consistent with the expected result. We assume that the components of $\mathbf{z}_0[n]$ are fixed by the nominal grating design, and that the deviations $(\mathbf{z}[n] - \mathbf{z}_0[n])$ of the domain boundaries from their ideal positions are IID. Note also that, in a real structure, the position and length of the first and last QPM domains will depend on the crystal polishing process; we neglect these and similar issues here.

B. Ensemble-Averaged Noise Pedestal and Efficiency Reduction

Following [29], we assume IID errors in the domain boundary positions. We assume a normal distribution for each of these positions with mean $\mathbf{z}_0[n]$ and variance σ_z^2, i.e., $\mathbf{z}[n] \sim \mathcal{N}(\mathbf{z}_0[n], \sigma_z^2)$. The variance in the length $l_n = \mathbf{z}[n] - \mathbf{z}[n-1]$ of each domain, σ_l^2, is related to the variance of the domain boundary positions, σ_z^2, by $\sigma_l^2 = 2\sigma_z^2$. A schematic of such RDC errors is illustrated in Fig. 1. As described in Section 1, RDC errors are typically associated with lithographically defined QPM patterns: the lithographic pattern ensures long-range order of the grating (and hence prevents period errors [29]), but any local fluctuations can lead to perturbations in the positions of the domain boundaries. After fabrication, the domains are fixed for any given grating;
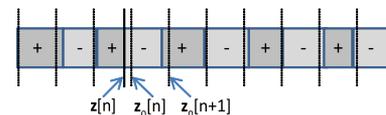

Fig. 1. (Color online) Schematic of a QPM grating with RDC errors. Vertical dashed lines indicate the ideal, equally spaced domain boundary positions. Elements of the domain boundary vectors $\mathbf{z}$ (random) and $\mathbf{z}_0$ (ideal) are indicated.

therefore, in any particular experiment, a single vector **z** applies. However, since the errors are random from one grating to the next, it is useful to calculate the expected behavior of an ensemble of devices with identically distributed errors.

As shown in [29], the ensemble-averaged mean of the normalized transfer function is given by

$$\langle \tilde{g}_{\mathbf{z}}(k) \rangle = e^{-k^2 \sigma_z^2 / 2} \tilde{g}_{\mathbf{z}_0}(k), \tag{6}$$

where the ensemble averaging is performed over random vectors **z**, and the relation

$$\langle e^{ikz} \rangle = e^{-k^2 \sigma_z^2 / 2} e^{ik\langle z \rangle} \tag{7}$$

for scalar z has been used in each term of the sum. From Eq. (6), the expected value of the transfer function is reduced compared to that of the ideal transfer function. For example, the phase-matched DFG conversion efficiency averaged over many different QPM gratings with RDC errors, given by $\langle |\tilde{g}_{\mathbf{z}}(\Delta k)|^2 \rangle$ for DFG phase mismatch Δk, would in this case be reduced by a factor $\exp(-\Delta k^2 \sigma_z^2)$ compared to first-order QPM in an ideal grating.

In addition to reducing the peak conversion efficiency, RDC errors give rise to additional spatial-frequency components far from nominal phase matching. To see this behavior we look at the ensemble-averaged value of $|\tilde{g}_{\mathbf{z}}(k)|^2$, which, with Eq. (5), is given by

$$\langle |\tilde{g}_{\mathbf{z}}(k)|^2 \rangle = \left(\frac{\pi}{kL} \right)^2 \left\langle \sum_{m=1}^{N} \sum_{n=1}^{N} (-1)^{n-m} e^{-ik(\mathbf{z}[n] - \mathbf{z}[m])} \right\rangle$$

$$= \left(\frac{\pi}{kL} \right)^2 \left[N(1 - e^{-k^2 \sigma_z^2}) \right.$$

$$\left. + e^{-k^2 \sigma_z^2} \sum_{n=1}^{N} \sum_{m=1}^{N} (-1)^{n-m} e^{-ik(\mathbf{z}_0[n] - \mathbf{z}_0[m])} \right], \tag{8}$$

where the second relation can be found by separating the first relation into terms in the summand with $m = n$ and $m \neq n$: those with $m = n$ are independent of $\mathbf{z}[n]$ and hence do not acquire an $\exp(-(k\sigma_z)^2)$ factor. The pair of summations in the second relation yields the magnitude squared of the ideal transfer function, $\tilde{g}_{\mathbf{z}_0}$ [see Eq. (5)]. Therefore, we can write Eq. (8) in a more compact and convenient form:

$$\langle |\tilde{g}_{\mathbf{z}}(k)|^2 \rangle = e^{-k^2 \sigma_z^2} |\tilde{g}_{\mathbf{z}_0}(k)|^2 + N \left(\frac{\pi}{kL} \right)^2 (1 - e^{-k^2 \sigma_z^2}), \tag{9}$$

where the second term is a noise pedestal in spatial frequency that originates from the RDC errors. We will refer to this pedestal as the QPM noise pedestal. The factor N associated with this pedestal is accurate provided that there are enough domains N that terms $O(1)$, which are missing in Eq. (5) due to the approximations made on the edge terms, can be neglected. For very thin crystals with small N, these edge terms would not be negligible.

For periodic QPM gratings with a 50% duty cycle, there is a particularly simple analytical form for the ideal transfer function when the edge terms are included. Assuming that $\mathbf{z}[n] = n\Lambda_D$ and defining $\Delta k_1 = k - \pi/\Lambda_D$, it can be shown that [33]

$$|\tilde{g}_{\mathbf{z}_0}(k)|^2 = \left[\frac{\pi}{2} \operatorname{sinc} \left(\frac{k\Lambda_D}{2} \right) \right]^2 \left[\frac{\sin(N \Delta k_1 \Lambda_D / 2)}{N \sin(\Delta k_1 \Lambda_D / 2)} \right]^2. \tag{10}$$

The first factor in square brackets represents the reduced Fourier amplitudes in higher orders of the QPM grating relative to the first-order. The second factor is a "comb of sinc's," which gives rise to tuning curves at each odd order of QPM. Equation (10) is analogous to the intensity function for multi-slit diffraction [33].

In more general cases involving aperiodic QPM designs, simple analytical solutions to $\tilde{g}_{\mathbf{z}_0}$ analogous to Eq. (10) are often unavailable. For such cases, the Fourier spectrum can be written as a sum over the harmonics of the fundamental spatial frequency of the grating. For an aperiodic grating that varies slowly enough with z that a sensible local spatial frequency can be defined, it is convenient to write this sum in terms of a local phase function $\phi(z)$ and duty cycle $D(z)$ as

$$\frac{d(z)}{d_0} \equiv \operatorname{sgn}[\cos(\phi(z)) - \cos(\pi D(z))]$$

$$\equiv (2D(z) - 1) + \sum_{\substack{m=-\infty \\ m \neq 0}}^{\infty} \frac{2 \sin(\pi m D(z))}{\pi m} \exp(im\phi(z)). \tag{11}$$

The first relation corresponds to the assumption that $d(z)/d_0 = \pm 1$, as is the case, for example, for 180 deg domains in ferroelectrics, and the second relation is a trigonometric identity. The grating phase profile $\phi(z)$ is linear in position for periodic gratings, quadratic for linearly chirped gratings, and so on. When simple closed-form expressions for the summation in Eq. (5) are not available, one can use Eq. (11) to re-express the right-hand side of Eq. (3) as a sum of the contributions from the relevant QPM orders, whose individual Fourier spectra may have simple closed-form solutions. For example, these individual Fourier spectra correspond to sinc functions for periodic gratings, and to error functions for linearly chirped gratings [31,34].

Writing $g_{\mathbf{z}}(z)$ from Eq. (3) using Eq. (11) and taking the FT results in a series of terms for the normalized transfer function. These terms are given by

$$\tilde{g}_{\mathbf{z}}^{(m)}(k) = \frac{1}{mL} \sin(\pi m D) \int_0^L \exp[i(m\phi(z') - kz')] dz', \tag{12}$$

where a constant value of $D(z)$ has been assumed; this assumption is possible because random errors in the domain boundaries can in general be represented by $\phi(z)$. $\tilde{g}_{\mathbf{z}}(k)$ is found by summing $\tilde{g}_{\mathbf{z}}^{(m)}(k)$ over all indices $m \neq 0$, and then adding the normalized transfer function $\tilde{g}_{\mathbf{z}}^{dc}(k)$ that corresponds to the zeroth-order of the QPM grating. This term is independent of $\phi(z)$ and is given by [31]

$$\tilde{g}_{\mathbf{z}}^{(dc)}(k) = \frac{\pi}{2} (2D - 1) e^{-ikL/2} \operatorname{sinc} \left(\frac{kL}{2} \right). \tag{13}$$

Equation (9) thus provides a way to evaluate the ensemble-averaged transfer function for arbitrary grating structures.

C. Transfer Function Applied to Pulsed Interactions
The normalized transfer function $\tilde{g}_{\mathbf{z}}(k)$ can be directly applied to pulsed interactions, provided that certain conditions

relating to the phase mismatch are met. For pump, signal, and idler pulses with nonoverlapping spectra, the total electric field can be written in the frequency domain as

$$\tilde{E}(z, \omega)u(\omega) = \frac{1}{2}\sum_j \tilde{A}_j(z, \omega)\exp(-ik(\omega)z), \qquad (14)$$

where $u(\omega)$ denotes the Heaviside step function, and A_j are analytic signals containing only positive Fourier components. We will always assume here that both the pump and signal propagate linearly, i.e., $\tilde{A}_j(z, \omega) = \tilde{A}_j(0, \omega)$ for $j = s$ and $j = p$; therefore, the z-arguments of A_s and A_p will be suppressed. With these envelope definitions, the evolution of each (positive) spectral component of the idler is given by [31]

$$\frac{d\tilde{A}_i(\omega)}{dz} = -i\frac{\omega d(z)}{n_i c}\int_0^\infty \tilde{A}_p(\omega + \omega')\tilde{A}_s^*(\omega')e^{-i\Delta k(\omega, \omega')z}\frac{d\omega'}{2\pi}, \quad (15)$$

where the frequency-dependent phase mismatch is given by

$$\Delta k(\omega, \omega') = k(\omega + \omega') - k(\omega) - k(\omega'). \qquad (16)$$

When analyzing pulsed interactions, we denote the carrier frequencies as ω_j for wave j, and the carrier wave vectors as $k_j = k(\omega_j)$ (assuming the same polarization for each wave). Consider a case where the signal and pump have comparable group velocities, such that the temporal walk-off of the signal and pump pulses is negligible during propagation. This condition implies that $v_s \approx v_p$, where the frequency-dependent group velocity is given by $v_g^{-1} = dk/d\omega$, and $v_j = v_g(\omega_j)$. If in addition neither the signal nor the pump pulses disperse significantly [i.e., if group velocity dispersion (GVD) is negligible over the spectral bandwidth of the pulses], the general frequency-dependent phase mismatch can be approximated as [31]

$$\Delta k(\omega, \omega') \approx k_p - k_s + \frac{\omega - \omega_i}{v_p} - k(\omega), \qquad (17)$$

which depends only on the driven idler frequency ω but not the intermediate frequency ω'. With this approximation, the integral in Eq. (15) can be simplified as a convolution. Furthermore, because each idler spectral component is driven by a particular phase mismatch, integration versus z yields a functional form proportional to $\tilde{g}_z(\Delta k(\omega))$:

$$\tilde{A}_i(\omega) = -i\frac{2L}{\pi}\frac{\omega d_0}{n(\omega)c}\tilde{g}_z(\Delta k(\omega))$$
$$\times \mathcal{F}[A_p(z = 0, t)A_s(z = 0, t)^*](\omega). \qquad (18)$$

It is useful to calculate the idler fluence W_i corresponding to this electric field, which is given by $W_i \approx (n_i\epsilon_0 c/2)\int |A_i(t)|^2 dt = (n_i\epsilon_0 c/2)\int |\tilde{A}_i(\omega)|^2 d\omega/(2\pi)$. Since each spectral component of $\tilde{A}_i$ is, in this approximation, proportional to $\tilde{g}_z(\Delta k(\omega))$, the fluence is an integral involving $\tilde{g}$ evaluated at different spatial frequencies, and, hence, these can each be ensemble averaged separately. If we assume that the dominant contribution to $\langle|\tilde{g}_z(\Delta k(\omega))|^2\rangle$ is the QPM noise pedestal over all the idler frequencies ω of interest (i.e., that we are interested in a parasitic process rather than a nominally phase-matched one), and that variations of this pedestal are small over this same frequency interval, then, with the

result for $\tilde{g}_z$ from Eq. (9) inserted into Eq. (18), the ensemble-averaged idler fluence is given by

$$\langle W_i\rangle \approx \frac{2\epsilon_0\omega_i^2 d_0^2 L\Lambda_D}{n_i c}\frac{1 - e^{-\Delta k(\omega_i)^2\sigma_z^2}}{\Delta k(\omega_i)^2\Lambda_D^2}$$
$$\times \int |A_p(z = 0, t)A_s(z = 0, t)^*|^2 dt. \qquad (19)$$

The condition that the signal and pump negligibly walk off each other does not always apply, but Eq. (19) still provides a useful estimate of the importance of parasitic processes phase matched by the QPM noise pedestal. With analogous starting assumptions, similar results can be obtained for other types of interactions, such as pulsed SHG.

D. Fluctuations in the QPM Noise Pedestal

In some experimental configurations, the fluctuations in $|\tilde{g}_z(k)|^2$ as a function of spatial frequency k, and, hence, phase matching for the corresponding optical frequency, may be important. For example, for pulsed interactions of the type discussed in Subsection 2.C, the output spectrum will fluctuate along with $\tilde{g}_z(\Delta k(\omega))$. These fluctuations can be quantified via the variance of the spatial FT of the grating. Calculation of this variance through ensemble averaging is, as with the mean, significantly simplified by approximating the contributions of the edge terms. In this subsection, we therefore assume that N is large enough that $\tilde{g}_z$ is well-approximated by Eq. (5).

By evaluating the second- and fourth-order moments $\langle|\tilde{g}_z(k)|^2\rangle$ and $\langle|\tilde{g}_z(k)|^4\rangle$, the standard deviation σ_η of the normalized transfer function can be determined. As with $\langle|\tilde{g}_z^2|\rangle$ in Eq. (8), $\langle|\tilde{g}_z^4|\rangle$ can be calculated by splitting the corresponding quadruple summation up into terms with different numbers of distinct indices, ensemble averaging, and rearranging the result in terms of $\tilde{g}_{z_0}$. After some algebra, we find that

$$\langle|\tilde{g}_z(k)|^4\rangle \approx 2N^2\left(\frac{\pi}{kL}\right)^4\left(1 - e^{-(k\sigma_z)^2}\right)^2$$
$$+ 4N\left(\frac{\pi}{kL}\right)^2(1 - e^{-(k\sigma_z)^2})e^{-(k\sigma_z)^2}|\tilde{g}_{z_0}(k)|^2$$
$$+ e^{-2(k\sigma_z)^2}|\tilde{g}_{z_0}(k)|^4. \qquad (20)$$

If we keep only the N^2 noise-pedestal term in this equation, then the standard deviation σ_η can be approximated according to

$$\sigma_\eta \approx N\left(\frac{\pi}{kL}\right)^2(1 - e^{-k^2\sigma_z^2}). \qquad (21)$$

This approximation applies for large N and values of k for which the ideal transfer function $|\tilde{g}_{z_0}(k)|^2$ is negligible. We note that the standard deviation in Eq. (21) is the same as the mean $\langle|\tilde{g}_z|^2\rangle$, as would be expected for a random walk process for the generated idler field. The magnitude of the spatial Fourier spectrum of a particular grating with RDC errors is thus with high probability within a few times the ensemble-averaged mean.

In addition to the variance, it may be important to know how rapidly the spectrum of a particular QPM grating varies with its spatial frequency. Since the rate of change in spatial frequency is related to the real-space bandwidth of the

structure (i.e., the grating length L), changes to the spatial-frequency spectrum occur over a characteristic $k \sim 2\pi/L$ scale.

E. Generation of Backward Waves

The presence of RDC errors can enhance the generation of backward waves as well as the forward waves we have considered so far. One way to approach this problem is with a transfer matrix formalism [35], in which backward waves are generated as a consequence of the nonuniformities in the nonlinear susceptibility, in particular due to the (a) periodic inversions of $d(z)$. A more straightforward approach, which is appropriate if the linear susceptibility is uniform (as is typically the case in QPM media), is to solve the evolution equation for backward wave components. For monochromatic and plane-wave idler components propagating in either the same or the opposite direction to the collinear pump and signal waves, evolution through the QPM grating is governed by the equations

$$\frac{dA_i^{(\pm)}}{dz} = \mp i \frac{\omega_i d(z)}{n_i c} A_s^* A_p e^{-i\Delta k_\pm z}, \quad (22)$$

where $\Delta k_\pm = k_p - k_s \mp k_i$. $A_i^{(\pm)}$ denotes the forward $(+)$ and backward $(-)$ components of the idler wave. Equation (22), which is a more general version of Eq. (1), can be integrated straightforwardly for both idler components. In the absence of any external idler inputs or any reflections from the input and output facets of the crystal, the result is that

$$\begin{bmatrix} a_i^{(-)}(z = 0) \\ a_i^{(+)}(z = L) \end{bmatrix} = \begin{bmatrix} \tilde{g}_{\mathbf{z}}(\Delta k_-) \\ \tilde{g}_{\mathbf{z}}(\Delta k_+), \end{bmatrix}, \quad (23)$$

where each $a_i^{(\pm)}$ is related to $A_i^{(\pm)}$ according to Eq. (2): $A_i^{(\pm)} = -i(2L/\pi)(\omega_i d_0)(n_i c)^{-1} A_s^* A_p a_i^{(\pm)}$. Equation (23) means that the idler emitted from a QPM grating with perfect antireflection (AR) coatings on the input and output facets is proportional to the normalized transfer function, evaluated at the phase mismatch associated with each direction of idler propagation (either forward or backward). In practice, the inequalities $(\Delta k_+ \sigma_z)^2 \ll 1$ and $(\Delta k_- \sigma_z)^2 \gg 1$ often apply, meaning that the QPM noise pedestal is in the approximately flat region for the forward wave, but is proportional to $1/\Delta k_-^2$ for the backward wave, based on Eq. (9). In LiNbO$_3$ for a DFG process involving a 1.064 μm pump and a 1.55 μm signal with $\sigma_z = 1$ μm, $\Delta k_- \sigma_z \approx 7.9$, while $\Delta k_+ \sigma_z \approx 0.2$.

When using AR-coated samples, Eq. (23) could, for example, be used to determine the feedback into the pump laser(s) as a result of RDC errors. However, for the remainder of this paper, we focus on the much stronger, copropagating components corresponding to $\tilde{g}(\Delta k_+)$.

3. RDC ERRORS: EXAMPLES

In order to illustrate the mean properties of QPM gratings with RDC errors determined in Subsection 2.B, in this section we evaluate the spectrum of some example uniform (periodic) and chirped (aperiodic) QPM gratings.

A. Periodic QPM Gratings

First, we consider in Fig. 2 an example periodic case with RDC errors similar to those typically observed in practice [12]. We
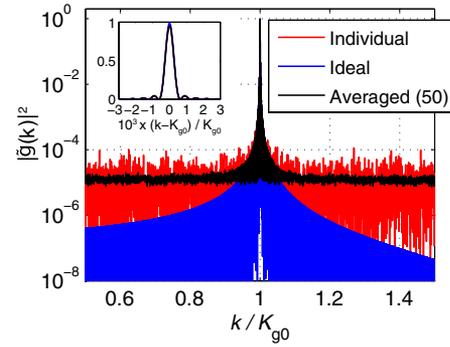

Fig. 2. (Color online) Fourier spectra $|\tilde{g}(k)|^2$ with parameters $\sigma_z = 1$ μm and a 5 cm crystal, and $K_{g0} = 2 \times 10^5$ m^{-1} ($\approx$31.4 μm period). The inset shows $|\tilde{g}(k)|^2$ on a linear scale in the vicinity of first-order QPM; the effects of RDC errors cannot be seen on this linear scale.

assume a grating of length 5 cm with nominal spatial frequency $K_g = 2 \times 10^5$ m^{-1} (period 31.4 μm, comparable to the periods required for 1.064 nm-pumped IR devices), and RDC errors $\sigma_z = 1$ μm. The red curve shows the spectrum $|\tilde{g}_\mathbf{z}(k)|^2$ for a particular example of a grating with RDC errors. The black curve shows an ensemble average over 50 such spectra. The blue curve shows the ideal transfer function $|\tilde{g}_{\mathbf{z}_0}|^2$. The inset shows the grating spectrum on a linear scale around first-order QPM. For the spatial frequencies shown, the pedestal is approximately flat. Furthermore, the ideal sinc^2-like functional form shown in the inset is almost unaffected by the RDC errors. QPM gratings with these types of RDC errors were analyzed experimentally and theoretically in [12].

To understand Fig. 2 in more detail, Eq. (10) can be rewritten in terms of the grating k-vector $K_g = \pi/\Lambda_D$ (where the nominal grating length $L = N\Lambda_D$). In the vicinity of first-order QPM ($k/K_g \approx 1$), and for RDC errors small enough that $(k\sigma_z)^2 \ll 1$, Eqs. (9) and (10) can be approximated and combined to yield [12]

$$\langle |\tilde{g}(k)|^2 \rangle \approx \frac{1}{N}(1 - e^{-k^2\sigma_z^2}) + e^{-k^2\sigma_z^2} \text{sinc}((k - K_g)L/2)^2. \quad (24)$$

In this equation, the QPM noise pedestal dominates for frequencies sufficiently detuned from the peak that the sinc^2 profile is significantly less than $1/N$ relative to its peak. For the RDC errors and QPM periods typically present in PPLN crystals [12], the prefactor $(1 - \exp(-k^2\sigma_z^2)) \sim 0.05$, thereby leading to a QPM noise pedestal of order $0.05/N$ lower than the peak of $|\tilde{g}_{\mathbf{z}_0}(k)|^2$ (i.e., the peak of the "tuning curve").

Away from first-order QPM, $\tilde{g}_\mathbf{z}$ exhibits a number of features in addition to those shown in Fig. 2. To illustrate these features, we next consider in Fig. 3 an example periodic grating with large RDC errors. We assume parameters $L = 5$ cm, $\sigma_z = 3$ μm, and grating k-vector $K_g = 2 \times 10^5$ m^{-1} (QPM period $\approx$31.4 μm). Spatial frequencies up to grating order 10 are plotted.

The solid blue curve shows the ideal sinc-like transfer function (no RDC errors). The yellow curve shows the spectrum $|\tilde{g}_\mathbf{z}(k)|^2$ for a particular example of a grating with domain boundaries $\mathbf{z}$ subject to normally distributed errors with $\sigma_z = 3$ μm. The black curve shows the analytically calculated ensemble average given by Eq. (9). Because of the large
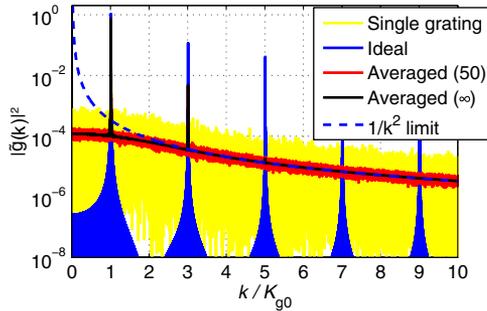
Fig. 3. (Color online) Fourier spectra for a large, 3 μm, mean error in the domain boundaries. The grating is 1 cm long and the grating k-vector is $K_g = 2 \times 10^5$ m^{-1} (QPM period ≈31.4 μm). For the red curve, the spectrum $|\tilde{g}(k)|^2$ was averaged over 50 gratings. The black curve corresponds to the analytical ensemble average from Eq. (9). The dashed blue curve shows a suitably normalized $1/k^2$ profile, which is the asymptotic functional form of the noise pedestal in Eq. (9) for large k.

assumed RDC errors, the higher-order QPM peaks are reduced substantially compared to those of the ideal grating [since $(k\sigma_z)^2$ is large at these spatial frequencies]. Furthermore, since $(k\sigma_z)^2 \ll 1$, the pedestal is not flat at high spatial frequencies; the dashed blue curve is proportional to $1/k^2$, and is scaled according to Eq. (8) so as to show the predicted asymptotic behavior of the pedestal for $|k\sigma_z|$ large enough that $\exp(-k^2\sigma_z^2) \ll 1$. Finally, the red curve shows an ensemble average over 50 spectra, showing the same features as the analytically calculated black curve.

B. Chirped QPM Gratings

In periodic QPM gratings, there is a trade-off in the grating length between efficiency and bandwidth; additionally, three-wave nonlinear interactions are subject to backconversion after reaching maximum depletion for one of the waves [36]. With chirped QPM gratings, both of these issues can be avoided simultaneously [37]. The simplest case of a chirped grating corresponds to a linear variation in grating k-vector with position. An example is shown in Fig. 4 (parameters given in the caption). The red curve shows a single spectrum $|\tilde{g}_{\mathbf{z}}|^2$, the black curve shows an ensemble average over 50 such gratings, and the blue curve shows $|\tilde{g}_{\mathbf{z}_0}|^2$.

The ideal Fourier spectrum is broadened and reduced in peak amplitude compared to that of an unchirped grating of the same length. As a result, compared to a periodic grating
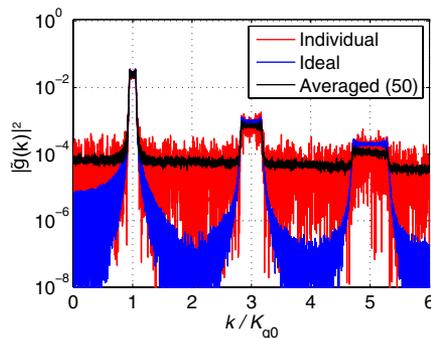

Fig. 4. (Color online) Fourier spectra for an example linearly chirped QPM grating with $\sigma_z = 1$ μm, a chirp rate of $dK_g/dz = 2.5 \times 10^6$ m^{-2}, grating length 1 cm, and mean grating k-vector $K_{g0} = 2 \times 10^5$ m^{-1}.

of the same length and subject to the same RDC errors, the magnitude of the QPM noise pedestal can be considerably closer to the peaks (or "passband") of the ideal transfer function. Additionally, since the k-space bandwidth in a (highly) chirped grating scales with the grating order, higher grating orders are closer still to the pedestal: there is an approximate $1/k^3$ scaling of $|\tilde{g}_{\mathbf{z}_0}(k)|^2$ for ideal chirped QPM gratings. This $1/k^3$ scaling originates from a factor of $1/k^2$ from Eq. (9) and a factor of $1/k$ from the k-space broadening [the $\exp(im\phi(z))$ factor for grating order m in Eq. (12)], together with Parseval's theorem.

This scaling can be seen in Fig. 4 and, as a result, $|\tilde{g}|^2$ is comparable to the QPM noise pedestal in the vicinity of fifth-order QPM: with these 1 μm RDC errors, only the first and third grating orders are above the pedestal. Note, however, that for a fixed first-order QPM conversion efficiency and a fixed spatial-frequency bandwidth of the first Fourier order of the grating, the efficiency of processes phase matched by the noise pedestal is comparable for both chirped and unchirped devices. These conditions apply in practice, given constraints on the conversion efficiency and optical bandwidth, to both chirped and unchirped gratings.

4. APPLICATIONS

In this section, we discuss some specific, representative applications in which the QPM noise pedestal is particularly important.

A. Quantum-State Frequency Translation

Second-order nonlinear interactions can be used to implement frequency conversion of quantum states of light [38,39]. With QPM technology, these quantum frequency conversion (QFC) processes can be performed efficiently with moderate-power continuous-wave (CW) sources. While QFC can in principle be noiseless [38], it has been found that, for pump wavelengths shorter than one of the quantum-state frequencies of interest, the QPM noise pedestal results in an enhancement of nominally phase-mismatched parametric fluorescence [11] and, hence, in the generation of noise photons. When photons generated by parametric fluorescence overlap spectrally with the frequency bands occupied by the signal, the ultrasensitive frequency converter cannot distinguish between the signal and noise photons, which leads to a reduction in the fidelity of the QFC process.

In a 1064 nm pumped single-photon upconversion detector for a 1.55 μm band signal, a noise count rate of approximately 8×10^5 counts/s was observed [9]. Theoretical analysis of the RDC-error-enhanced parametric fluorescence noise for this system [based on Eq. (24)] shows that the observed dark count rate is consistent with $\sigma_z \approx 3.2$ μm [11], which, in turn, is consistent with the observations of lower-than-expected conversion efficiency compared to an ideal QPM grating [9], again predicted by Eq. (24). In [12], RDC errors of $\sigma_z \approx 0.3$ μm were measured directly. A pedestal in SHG conversion efficiency was also observed, and was consistent with Eq. (24) given the measured RDC errors.

RDC error tolerances for achieving a certain conversion efficiency and dark count rate (due to parametric fluorescence) have been derived [11]; these tolerances can be quite stringent for single-photon conversion devices. Spontaneous Raman scattering is another important source of dark counts in

QFC [13]. Both these sources of dark counts can be suppressed significantly by use of a long wave pump [8].

B. Optical Parametric Chirped Pulse Amplification

RDC errors can be an important consideration in OPCPA of mid-IR pulses using $MgO:LiNbO_3$ QPM gratings. With an intense pump pulse and a sufficiently long grating, significant parasitic SHG of the pump can occur due to RDC errors. The intense second harmonic (SH) can in turn lead to TPA and subsequent strong thermal lensing and photorefractive effects, which are detrimental to the OPCPA process. To estimate the severity of this SHG-TPA process, some further analysis beyond that given in Section 2 is required. In this subsection we investigate this process, choosing parameters relevant for OPCPA based on chirped (aperiodic) gratings [21–23].

If diffractive effects are neglected, the two-photon-absorbed SH intensity is given, for small absorptions, by

$$I_{abs}(z) = \int_0^z \beta_{TPA} I_{SH}(z')^2 dz', \qquad (25)$$

where β_{TPA} is the TPA coefficient and I_{SH} is the SH intensity. It is convenient to approximate this integration as a summation over the ensemble-averaged intensities within each domain,

$$\langle I_{abs}\rangle \approx \left\langle \sum_{q=1}^{N} \Lambda_{D,q} \beta_{TPA} I_{SH}(\mathbf{z}[q])^2 \right\rangle \approx \beta_{TPA} I_{max}^2 \frac{L}{N} \left\langle \sum_{q=1}^{N} |\tilde{h}_{\mathbf{z}}^{(q)}(k)|^4 \right\rangle, \qquad (26)$$

where $\Lambda_{D,q}$ is the length of domain q. In the second form of Eq. (26), we have approximated each $\Lambda_{D,q}$ factor in the sum according to $\Lambda_{D,q} \approx \Lambda_D \equiv L/N$, on the assumption that the total range of QPM periods is relatively small. $\tilde{h}_{\mathbf{z}}^{(q)}(k)$ is the normalized SH amplitude at position $\mathbf{z}[q]$, obtained analogously to Eq. (5) as

$$\tilde{h}_{\mathbf{z}}^{(q)}(k) = \frac{\pi}{kL} \sum_{n=1}^{q} (-1)^n e^{-ik\mathbf{z}[n]}, \qquad (27)$$

and hence $\tilde{g}_{\mathbf{z}} = \tilde{h}_{\mathbf{z}}^{(N)}$. The "maximum" SH intensity, denoted I_{max}, is the SH intensity that would be predicted for a perfectly quasi-phase-matched interaction in an ideal periodic grating if pump depletion effects were neglected, and is therefore given by

$$I_{max} = \frac{n_{SH}\epsilon_0 c}{2} \left| \frac{2}{\pi} \frac{\omega_1 d_{eff}}{n_{SH} c} A_{FH}^2 L \right|^2. \qquad (28)$$

In order to evaluate Eq. (26), we need to find $\langle |\tilde{h}_{\mathbf{z}}^{(m)}|^4 \rangle$. Only slight modifications to Eq. (20) are required to account for the fact that here we are integrating only up to $\mathbf{z}[m]$, not $\mathbf{z}[N] = L$. We therefore find that

$$\langle |\tilde{h}_{\mathbf{z}}^{(m)}(k)|^4 \rangle \approx 2m^2 \left(\frac{\pi}{kL}\right)^4 (1 - e^{-(k\sigma_z)^2})^2$$
$$+ 4m \left(\frac{\pi}{kL}\right)^2 (1 - e^{-(k\sigma_z)^2}) e^{-(k\sigma_z)^2} |\tilde{h}_{\mathbf{z}_0}^{(m)}(k)|^2$$
$$+ e^{-2(k\sigma_z)^2} |\tilde{h}_{\mathbf{z}_0}^{(m)}(k)|^4. \qquad (29)$$

To estimate the SH TPA, we keep only the noise pedestal term in each $\tilde{h}_{\mathbf{z}}^{(m)}$ [the first term in Eq. (29)], under the assumption that the SHG process is highly phase mismatched. By substituting Eqs. (28) and (29) into Eq. (26), summing over the intensity absorbed within each domain, and assuming $N^3 \gg N^2$, the following expression for the total, ensemble-averaged TPA can be obtained:

$$\langle I_{abs}\rangle \approx \frac{2}{3} \beta_{TPA} I_\Lambda^2 \Lambda_D \left(\frac{L}{\Lambda_D}\right)^3 \left(\frac{\pi\sigma_z}{\Lambda_D}\right)^4 \left(\frac{1 - e^{-k^2\sigma_z^2}}{k^2\sigma_z^2}\right)^2, \qquad (30)$$

where Λ_D is the average domain length, and $I_\Lambda = I_{max}(\Lambda_D/L)^2$ is the "maximum" intensity from a single domain of size Λ_D; this latter substitution is made so that Eq. (30) gives the grating-length dependence of $\langle I_{abs}\rangle$ explicitly. For sufficiently small errors, the final factor in parentheses is equal to 1. Equation (30) indicates that I_{abs} is proportional to σ_z^4, L^3, and I_{FH}^4 (in the context of OPCPA, this FH intensity would correspond to the pump intensity); in comparing different OPCPA devices, it may be worth noting also that $I_{abs} \propto \sigma_z^4 (I_{FH}L)^4/L$.

We next evaluate Eq. (30) with relevant parameters. We assume the following system based on [21–23]: the pump wavelength is 1.064 μm, the material is $MgO:LiNbO_3$, the average domain size is $\Lambda_D = 14.94$ μm (corresponding to OPA for a 3.5 μm idler), and the crystal length is 10 mm. The SHG phase mismatch determines the spatial frequency at which Eq. (30) should be evaluated, and hence $k = 9.317$ m^{-1}. We assume RDC errors such that $\sigma_z = 1$ μm [11]. The TPA coefficient of $LiNbO_3$ at 532 nm ($\lambda_p/2$) is $\beta_{TPA} = 0.38$ cm/W [40], the effective nonlinear coefficient for 1064 nm SHG involving the d_{33} tensor element is $d_{eff} = 25.2$ pm/V [41], and the dispersion relation is given in [42]. For a first calculation, we assume a CW pump with an intensity of 10 GW/cm^2. With these parameters, we find from Eq. (30) that $\langle I_{abs}\rangle \approx 2.865$ GW/cm^2 (a remarkably large fraction of the pump).

To estimate the thermal load in the presence of a pulsed pump beam, the SH absorption must be integrated over both space and time. As in Subsection 2.C, a general procedure for such a calculation can be obtained by use of the transfer function approach of [31] (for DFG) and [43] (for SHG). In the case of SHG, provided that GVD of the FH can be neglected, the SH is driven in the frequency domain by the FT of the square of the FH envelope, $\mathcal{F}[A_{FH}(t)^2]$. Here, we can assume a pump of long enough duration that group velocity mismatch and dispersive effects are negligible, and hence the ensemble-averaged total absorbed energy at the SH is obtained by integrating the local absorbed intensity over space and time,

$$\langle U_{abs}\rangle = \langle I_{abs}^{(pk)}\rangle \iiint \bar{I}_{FH}^4(x,y,t) dxdydt, \qquad (31)$$

where $\bar{I}_{FH} \equiv I_{FH}/I_{pk}$ denotes the normalized FH intensity (maximum equal to 1) and $I_{abs}^{(pk)}$ denotes the absorbed intensity at the peak of the pulse (intensity I_{pk}). For Gaussian pulses in space and time ($1/e^2$ radius w, FWHM duration τ), the integral in Eq. (31) is given by

$$\iiint \bar{I}_1^4(x,y,t) dxdydt = \left(\frac{\pi}{8}\right)^{3/2} \frac{w^2\tau}{\sqrt{2\ln(2)}}. \qquad (32)$$

For the example considered above, $\langle I_{abs}^{(pk)} \rangle = 2.865$ GW/cm². If we assume a Gaussian pump beam with a FWHM duration of 12 ps and an energy of 300 μJ (corresponding to a beam radius of 387 μm for a peak intensity of 10 GW/cm²), Eq. (31) implies an ensemble-averaged absorbed energy of 7.18 μJ. At a repetition rate of 100 kHz (30 W pump power), this implies a thermal load of 718 mW, which is very large. Thus, SHG followed by TPA can lead to a significant thermal load on the crystal. With RDC errors of $\sigma_z = 0.5$ μm instead of 1 μm, the predicted thermal load is reduced by almost an order of magnitude, to 81 mW. Sufficient care should therefore be taken in fabricating such QPM devices to obtain submicrometer RDC errors. Note also that, with half the peak intensity (5 GW/cm²), the thermal load is reduced by a further factor of 16, to 5 mW.

C. Optical Parametric Oscillators: Nonlinear Loss

OPOs enable the generation of widely tunable and high power coherent light across the visible and infrared spectral regions [44–50]. RDC errors may play an important role in OPOs, particularly when there are high resonating intensities. In the presence of the nominal pump, signal, and idler waves (ω_p, ω_s, and ω_i, respectively) components of the nonlinear polarization are also generated at other, related frequencies, such as the SH frequencies $2\omega_j$. The most intense wave in a low-loss OPO not close to threshold is typically the resonant signal. SHG involving this wave constitutes a nonlinear loss mechanism, which for certain cases, in particular for pulsed interactions, could be significant.

Consider first a CW singly resonant OPO (SRO) case, assuming that the nonlinear losses are small and perturbative. The steady-state signal intensity, and hence the pump depletion, is determined by the number of times the pump intensity is above oscillation threshold pump intensity [18,51]; we denote this number as N_p (to distinguish between this quantity and the number of domains in the grating, N). For a low-loss cavity, the amplitude of the signal is given by the implicit relation

$$\text{sinc}^2(\Gamma_s) = N_p^{-1}, \tag{33}$$

where the pump depletion factor Γ_s is given by

$$\Gamma_s^2 = \frac{\omega_i \omega_p (2d_0/\pi)^2 |A_s|^2 L^2}{n_i n_p c^2}. \tag{34}$$

Optimal pump depletion for the SRO occurs at $N_p = (\pi/2)^2$; at this value, $\Gamma_s = \pi/2$. The SH field can be determined in the same way the idler was determined in Section 2, by substituting the value of $|A_s|$ resulting from Eq. (33) into Eq. (2) (with suitable modifications to the coupled-wave equations for SHG instead of DFG [52]) to find the "maximum" signal SH (for a phase-matched first-order QPM interaction), and then applying Eq. (8) to find the actual SH field in terms of the RDC errors. We also allow for the possibility of different tensor elements for the SHG- and OPO-gain processes (d_{SHG} and d_{OPO}, respectively), and denote the signal-SHG phase mismatch as $\Delta k_s = k(2\omega_s) - 2k(\omega_s)$. Taking the ratio of the signal and ensemble-averaged SH intensities, we arrive at the following expression for the nonlinear loss:

$$a_{NL} = \frac{\Gamma_s^2}{N} \left(\frac{\pi \sigma_z}{\Lambda_D} \right)^2 \frac{1 - e^{-\Delta k_s^2 \sigma_z^2}}{\Delta k_s^2 \sigma_z^2} \frac{n_i n_p}{n_s n_{SH}} \frac{\omega_s^2}{\omega_i \omega_p} \left(\frac{d_{SHG}}{d_{OPO}} \right)^2 \equiv \Gamma_s^2 a_0, \tag{35}$$

where we have introduced the loss term a_0 for convenience. We assume pump and signal wavelengths of 1.064 and 1.55 μm, respectively, a MgO:LiNbO₃ QPM grating operated at 150°C, $\Lambda_D \approx 15$ μm (for the nominal OPO process), and $\Delta k_s = 3.34 \times 10^5$ m⁻¹ (for the parasitic signal SHG process). Choosing the remaining parameters as $\Gamma_s = \pi/2$, $L = 5$ cm, and $\sigma_z = 1$ μm, and $d_{SHG} = d_{OPO}$, Eq. (35) yields $a_{NL} \approx 4.5 \times 10^{-3}\%$, negligible in comparison to the losses of most CW OPOs (which typically have total cavity losses of order 1% or more [15,48]).

For certain pulsed OPOs, however, the energy lost due to signal SHG may be more significant. An analogous form of Eq. (19) that applies for SHG of a pulsed signal is given by

$$\langle W_{SH} \rangle = \frac{2\epsilon_0 \omega_s^2 d_0^2 L \Lambda_D}{n_{SH} c} \frac{1 - e^{-\Delta k_s^2 \sigma_z^2}}{\Delta k_s^2 \Lambda_D^2} \int |A_s(z=0,t)^2|^2 dt. \tag{36}$$

Assuming a Gaussian resonant signal pulse, the ratio of the SH and signal fluences (and hence the nonlinear loss) can be expressed, after some algebra, as

$$a_{NL} = 2^{-1/2} \Gamma_{s,pk}^2 a_0, \tag{37}$$

where $\Gamma_{s,pk}$ is Γ_s defined in Eq. (34), evaluated at the peak intensity of the signal pulse, and a_0 is given implicitly by Eq. (35). Note that, if we also integrate over space assuming nondiffracting Gaussian beams, a total nonlinear loss of $a_{NL} = 2^{-3/2} \Gamma_{s,pk}^2 a_0$ is obtained. If the peak intensity is significantly larger than the intensity required to achieve high conversion efficiency in a CW OPO, then there will be an increase in the nonlinear loss. Furthermore, for short-pulse OPOs, the crystal length and, hence, the number of domains N appearing in Eq. (35), may be reduced substantially compared with typical CW OPO designs. If we assume $\Gamma_s = \pi$, $L = 3$ mm, $\sigma_z = 1$ μm, and consider a MgO:LiNbO₃ OPO utilizing the d_{31} tensor element for gain but with an e-wave resonant signal [17], then SHG of this signal via the d_{33} tensor element will occur in addition to the desired three-wave mixing process (amplification of the signal by the pump). Assuming values for these tensor elements based on the 1.313 μm SHG measurements in [41], and using the $2^{-3/2}$ prefactor above in calculating a_{NL}, a total nonlinear loss of $a_{NL} = 2.1\%$ is obtained. For a nominally low-loss OPO cavity, this additional loss would be very significant.

Based on the above analysis, we can conclude that, for certain short-pulse OPOs, in particular those with low losses and short crystal lengths, RDC errors can lead to a significant nonlinear loss. Nonlinear losses limit the cavity enhancement that can be achieved, and may also lead to instabilities, a reduction in conversion efficiency, and other detrimental effects (although such effects are beyond the scope of this paper).

We note also that there is another loss, denoted a_L, due to the SFG process involving the signal and pump waves ($\omega_s + \omega_p$). Although a_L can be significantly enhanced by RDC errors, this loss will be of order $a_L \sim a_{NL} a_{total}$, where a_{total} denotes the total cavity losses; this scaling arises by assuming that the signal intensity in an above-threshold OPO is of order $1/a_{total}$ times larger than the pump intensity.

Therefore, loss via signal-pump SFG should be negligible in most cases.

D. Optical Parametric Oscillators: Cascaded Processes

In addition to the signal SHG process discussed above, many other "cascaded" spectral components beyond the desired pump, signal, and idler waves can be generated in OPOs (and other nonlinear devices). For infrared OPOs, some of these cascaded components lie in the visible spectrum and can sometimes serve as a clear indication of parametric oscillation. The amount of power generated at visible wavelengths can be surprisingly high, given that the corresponding mixing processes are (usually) nominally phase mismatched. RDC errors explain how these frequencies can be generated with appreciable powers, particularly for pulsed OPOs.

As an example, consider an SRO. As discussed in Subsection 4.C, in the presence of RDC errors, a relatively intense SH can be generated by the resonant signal. This signal SH can in turn sum with the pump to yield SFG spectral components $\omega = 2\omega_s + \omega_p$; this nominally phase-mismatched SFG process can also be enhanced in the presence of RDC errors. For 1064 nm-pumped OPOs with a resonant wavelength between 1.3 and 4 μm, $\omega = 2\omega_s + \omega_p$ lies in the visible spectrum. Note that, for short-wave-resonant SROs, $\omega_s + \omega_p$ also lies in the visible and can be expected to be more efficient than the $2\omega_s + \omega_p$ spectral component. Here we consider this $2\omega_s + \omega_p$ component for several reasons: (1) it will be visible in almost any 1064 nm-pumped OPO, (2) it involves two simultaneous processes, both of which will typically be dominated by the QPM noise pedestal, and is therefore a good example to illustrate an extension of the mathematical approach of Section 2, and (3) for typical OPO parameters, this wave can actually have a small but nonnegligible power that is several orders of magnitude above the power that would be predicted in the absence of RDC errors.

To estimate the intensity of this spectral component, similar integrals to those discussed in Subsection 4.B can be performed. The equations that determine the SFG process are given by

$$\frac{dA_{\mathrm{SH}}}{dz} = -i\frac{\omega_s d(z)}{n_{\mathrm{SH}}c}A_s^2 e^{i\Delta k_s z}, \tag{38a}$$

$$\frac{dA_{\mathrm{SF}}}{dz} = -i\frac{\omega_{\mathrm{SF}}d(z)}{n_{\mathrm{SF}}c}A_p A_{\mathrm{SH}}e^{i\Delta k_{\mathrm{SFG}}z}, \tag{38b}$$

where A_p and A_s are determined by the steady-state OPO solutions. For simplicity, we assume that both A_p and A_s are z-independent (pump depletion is neglected for the purposes of calculating the SFG process).

The sum frequency (SF) is driven by the product $A_{\mathrm{SH}}(z)A_p$. Assuming A_s and A_p are known, A_{SH} can be calculated first via Eq. (38a) and substituted into Eq. (38b) to calculate A_{SF}. $|A_{\mathrm{SF}}|^2$ therefore contains many terms, which must be ensemble averaged separately, as in previous subsections. These calculations yield, after some algebra, an ensemble-averaged normalized SFG intensity given by

$$\langle|a_{\mathrm{SF}}|^2\rangle \approx \frac{1}{N^2}\left(\frac{2\pi^2}{\Delta k_{\mathrm{SFG}}\Delta k_s \Lambda_D^2}\right)^2$$
$$\times \left[1 + e^{-(\Delta k_{\mathrm{SFG}}^2 + \Delta k_s^2)\sigma_z^2} - e^{-\Delta k_s^2\sigma_z^2} - e^{-\Delta k_{\mathrm{SFG}}^2\sigma_z^2}\right], \tag{39}$$

where $\Delta k_{\mathrm{SFG}} = k(\omega_p + 2\omega_s) - k(2\omega_s) - k(\omega_p)$ (and $\Delta k_s = k(2\omega_s) - 2k(\omega_s)$). a_{SF} is normalized to the value that would be obtained if both the SFG and signal SHG processes satisfied first-order QPM in an ideal grating and pump depletion effects are neglected, and hence

$$A_{\mathrm{SH}} = -\frac{2\omega_{\mathrm{SF}}\omega_s d_0^2 L^2}{\pi^2 n_{\mathrm{SH}}n_{\mathrm{SF}}c^2}A_p(0)A_s(0)^2 a_{\mathrm{SF}}. \tag{40}$$

With Eq. (40), the ensemble-averaged SF intensity can be expressed as

$$\frac{\langle I_{\mathrm{SF}}\rangle}{I_p} = \frac{n_i^2 n_p}{n_{\mathrm{SH}}n_{\mathrm{SF}}}\left(\frac{\omega_s \omega_{\mathrm{SF}}}{\omega_i \omega_p}\right)^2 \Gamma_s^4 \bar{I}_s^2|a_{\mathrm{SF}}|^2, \tag{41}$$

where Γ_s is defined in Eq. (34) and $\bar{I}_s$ is the signal intensity normalized to its peak.

The SF intensity may be integrated over space to yield an average power. Consider a MgO:LiNbO$_3$ with crystal length 5 cm, QPM period ≈ 30 μm, pump and signal wavelengths of 1064 and 1550 nm, respectively, spot sizes of 70 μm, pump power of 10 W, and resonant signal power of 200 W. If diffraction and pump depletion effects are neglected for simplicity and RDC errors with $\sigma_z = 1$ μm are assumed, the corresponding power $P_{\mathrm{SF}} \approx 10$ μW. This is a relatively high power for a CW process involving two cascaded processes, both of which are nominally highly phase mismatched; in the absence of RDC errors and far from phase matching for both processes, the generated power would be several orders of magnitude less.

As in Subsections 4.B and 4.C, the conversion efficiency can be substantially increased for pulsed interactions, and can be estimated from Eq. (41) provided that group velocity mismatch effects can be neglected. From the Γ_s^4 dependence of $\langle I_{\mathrm{SF}}\rangle$, any increase in $\Gamma_{s,\mathrm{pk}}$ beyond $\pi/2$ for pulsed OPOs will rapidly increase the cascaded SFG efficiency.

E. Supercontinuum Generation

In supercontinuum generation [24–27], very high intensities are involved over substantial propagation lengths. As a result, RDC errors can lead to the efficient generation of sum-frequency components (2ω, 3ω, 4ω, and so on, for optical frequency ω). Depending on the particular configuration, these interactions can be viewed as useful (generating carrier envelope offset frequency signals) or as parasitic (removing energy from the FH part of the pulse and thereby reducing the rate of self-phase-modulation responsible for the continuum generation). However, the assumptions made in Subsection 2.C to model pulsed interactions do not apply (since the FH envelope changes substantially). In principle, the various nonlinear processes can be solved fully numerically with no approximations on $d(z)$. However, numerical methods typically assume a smooth grating spatial profile, with only a finite number of QPM orders. In Appendix A, we discuss how RDC errors can be sensibly incorporated into the "Fourier-filtered" propagation schemes used for pulsed interactions, by suitable perturbations of the grating phase profile $\phi(z)$ appearing in Eq. (11). The procedure we discuss should allow the parasitic processes of the types discussed in this section to be (approximately) accounted for when modeling highly nonlinear QPM devices.

5. CONCLUSIONS

In this paper, we investigated the statistical properties of QPM gratings with normally distributed errors in the boundary positions. While the use of lithographic fabrication techniques ensures the long-range order of the grating (thereby preventing QPM period errors), local fluctuations in the boundary positions are still possible. Based on Eq. (9), the resulting ensemble-averaged square-magnitude of the spatial FT of the grating, $\langle|\tilde{g}_{\mathbf{z}}(k)|^2\rangle$, can be described by the FT of the ideal grating structure with an exponential amplitude reduction factor corresponding to the variance of the domain boundary positions, plus a spatial-frequency pedestal whose mean and variance are approximately flat for small spatial frequencies k. This pedestal can enhance the conversion efficiency of nominally phase-mismatched processes.

For certain pulsed interactions, a transfer function approach can be applied, yielding a generated output optical spectrum that is proportional to the spatial-frequency spectrum of the QPM grating, with a mapping $\Delta k(\omega)$ between spatial and optical frequencies determined by the phase mismatch. For more complicated pulsed interactions, RDC errors can be incorporated into numerical simulations by perturbing the grating phase function. In addition to the effects on forward-propagating waves, we also considered the case of backward-generating waves in random QPM gratings. When reflections can be neglected, the normalized backward-generated wave has the same form as the forward wave, but evaluated at the spatial frequency associated with backward phasematching, $\Delta k_- = k_p - k_s + k_i$.

RDC errors can play an important role in a number of applications utilizing QPM gratings. We considered several example device configurations, including QFC, OPCPA, and OPOs. For systems involving high intensities (where RDC errors can lead to high conversion efficiency of parasitic processes), very low intensities (where only a small RDC-error-induced enhancement in parasitic nonlinear processes can scatter too much light into wavelength ranges of interest), and low-loss cavities (where RDC-enhanced nonlinear loss mechanisms limit the achievable cavity enhancement), RDC errors can be a critical consideration. For some applications, RDC-related parasitic processes can be suppressed by system design, while, for other applications, improvements in QPM fabrication are required. Our analysis allows RDC errors and their effects to be understood analytically and modeled numerically, and should therefore be of use in a wide range of applications.

APPENDIX A: RDC ERRORS IN PULSED SYSTEMS

As discussed in Section 4, RDC errors can be particularly important in pulsed systems, where the intensities can be much higher than in CW systems. When the two input pulses for a SFG or DFG process experience negligible depletion and have long enough durations that group velocity walk-off and GVD effects between those two pulses can be neglected, the analysis of Subsection 2.C applies, and the generated field can be expressed in terms of $\tilde{g}_{\mathbf{z}}(\Delta k(\omega))$. However, often depletion and dispersion effects cannot be approximated in this way. In these situations, equations governing the nonlinear interaction must often be solved numerically.

One way to solve these equations is to propagate the electric field through each successive QPM domain individually, accounting for the discrete reversals in the sign of $d(z)$. However, this layer-by-layer approach differs significantly from the numerical methods often used to model pulsed QPM interactions, in which the grating is first expanded in a (local) Fourier series given in Eq. (11), and only the dominant (slowly varying, strongly interacting) terms in the series are retained [26,53].

An alternative way to describe RDC errors mathematically is by a perturbation of the grating phase $\phi(z)$ appearing in Eq. (11), since a change in this phase corresponds to a shift in the domain boundary positions. For a given nonideal QPM structure, there are an infinite number of possible $\phi(z)$ profiles for which Eq. (11) is satisfied. Of these profiles, we would (ideally) choose the one(s) for which $\exp(i\phi(z))$ has the narrowest spatial-frequency bandwidth, so that the relevant properties and statistics of the grating can be described by a small number of harmonic terms in Eq. (11). Rather than select this ideal but unknown choice for a given grating, here we discuss heuristic choices of $\phi(z)$ that maintain the important properties of the QPM noise pedestal.

To analyze phase profiles $\phi(z)$ with random perturbations, we define $\phi_0(z)$ to be the phase profile of the ideal structure, such that the random phase perturbation is given by

$$\delta\phi(z) \equiv \phi(z) - \phi_0(z). \tag{A1}$$

Each time $\phi(z)$ passes through $\pi/2$ or $3\pi/2$ corresponds to a reversal in the sign of $d(z)$. To avoid artificially introducing extra domains via $\delta\phi$, $\phi(z)$ should be increasing, i.e., $d\phi/dz > 0$. Although this assumption could be violated for large enough $\delta\phi(z)$, one way to maintain the monotonicity of $\phi(z)$ (with high probability) is by limiting the magnitude and rate of variation of $\delta\phi(z)$. We note that a somewhat similar issue applies when assuming normally distributed discrete RDC errors defined by $\delta z_n \equiv \mathbf{z}[n] - \mathbf{z}_0[n]$ when calculating $\tilde{g}_{\mathbf{z}}(k)$, as in Section 2: with normally distributed errors, there is a finite probability that $|\delta z_n| > \Lambda_D$ (which would lead to unphysical situations, such as domains with negative length). When dealing with large RDC errors, other statistical assumptions could be made in order to avoid these types of issues.

The shift δz_n in domain boundary n due to RDC errors is given, implicitly, by $\phi(z_{n0} + \delta z_n) - \phi_0(z_{n0}) = 0$. This condition can be re-written as

$$\delta\phi(z_{n0} + \delta z_n) = -(\phi_0(z_{n0} + \delta z_n) - \phi_0(z_{n0})) \approx -K_g(z)\delta z_n, \tag{A2}$$

where the latter relation assumes a constant or slowly varying grating k-vector $K_g(z)$, where $K_g(z) \equiv d\phi_0/dz$. The phase profile should share (approximately) the statistical properties of δz_n; at a fixed z, $\delta\phi(z)$ should thus be normally distributed, and $\delta\phi(z)$ should be negligibly correlated with $\delta\phi(z + \delta x)$ for $|\delta x| > \pi K_g(z)^{-1}$ (to ensure independent domain boundary errors).

Phase profiles with the these properties can be constructed with a Gaussian filter of white noise. Consider a filter with form $h(z) \propto \exp(-(z/w)^2)$ with spatial width w. The resulting standard deviation of the phase $\delta\phi(z)$ after filtering is given by
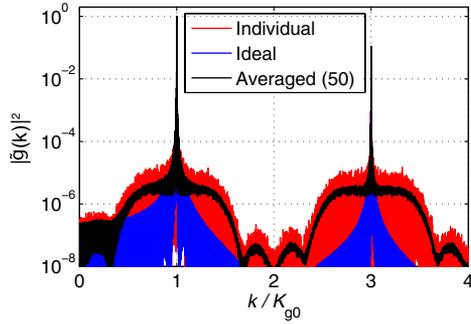
Fig. 5.   (Color online) Fourier spectrum arising from domain boundary variations defined by a grating phase perturbation $\delta\phi(z)$ defined by applying a sinc filter to white noise.

$\sigma_{\delta\phi}$. Based on the above considerations, the parameter w must satisfy

$$\sigma_{\delta\phi} \ll K_g w \ll \pi, \tag{A3}$$

where the first condition leads to the monotonicity of $\phi(z)$, and the second condition leads to weak correlations between neighboring domains. Equation (44) can be satisfied only for small RDC errors (i.e., small $\sigma_{\delta\phi}$).

The assumption of normally distributed RDC errors may not always be accurate. Furthermore, the statistical properties of the QPM noise pedestal might sometimes be less important than generating a noise pedestal that has the correct magnitude, extends over the relevant spatial-frequency region (defined by the optical frequencies involved), and can be applied to numerical simulations. In such cases, use of a non-Gaussian filter may be more expeditious. For example, consider a sinc filter with spatial-frequency extent $2K_g$. With $\delta\phi(z)$ determined via convolution with this filter, the Fourier spectrum of each QPM order, $\tilde{g}_z^{(m)}(k)$ [Eq. (12)], extends over a range $2K_g$; summing over all QPM orders, a reasonably flat QPM noise pedestal is produced. This sinc filter yields a noise pedestal at all spatial frequencies after summing over all grating orders, while only requiring a single grating order to be included for any given nonlinear interaction (i.e., the odd-integer value of m that minimizes $|mK_g - \Delta k_{\mathrm{opt}}|$, where Δk_{opt} represents the phase mismatch of the process being modeled).

When a narrow spectral region of the QPM noise pedestal is of interest, a corresponding narrower bandwidth spatial filter for $\phi(z)$ might be used; this case is illustrated in Fig. 5. Although the $\delta\phi(z)$ corresponding to this approximately band-limited noise power spectrum violates the assumed statistical independence of the QPM domains, the reduction in required spatial resolution compared to the Gaussian filter is substantial. In general, provided that a smooth and continuous $\phi(z)$ can be specified for any individual numerical simulation, useful descriptions of RDC errors can be incorporated efficiently and straightforwardly into standard numerical models of pulsed nonlinear interactions in QPM media.

ACKNOWLEDGMENTS

REFERENCES

1. S. Zhu, Y. Zhu, and N. Ming, "Quasi-phase-matched third-harmonic generation in a quasi-periodic optical superlattice," Science **278**, 843–846 (1997).
2. K. Fradkin-Kashi and A. Arie, "Multiple-wavelength quasi-phase-matched nonlinear interactions," IEEE J. Quantum Electron. **35**, 1649–1656 (1999).
3. K. Fradkin-Kashi, A. Arie, P. Urenski, and G. Rosenman, "Multiple nonlinear optical interactions with arbitrary wave vector differences," Phys. Rev. Lett. **88**, 023903 (2001).
4. M. Baudrier-Raybaut, R. Haidar, P. Kupecek, P. Lemasson, and E. Rosencher, "Random quasi-phase-matching in bulk polycrystalline isotropic nonlinear materials," Nature **432**, 374–376 (2004).
5. M. Asobe, O. Tadanaga, H. Miyazawa, Y. Nishida, and H. Suzuki, "Multiple quasi-phase-matched device using continuous phase modulation of $\chi^{(2)}$ grating and its application to variable wavelength conversion," IEEE J. Quantum Electron. **41**, 1540–1547 (2005).
6. R. Lifshitz, A. Arie, and A. Bahabad, "Photonic quasicrystals for nonlinear optical frequency conversion," Phys. Rev. Lett. **95**, 133901 (2005).
7. G. Porat, Y. Silberberg, A. Arie, and H. Suchowski, "Two photon frequency conversion," Opt. Express **20**, 3613–3619 (2012).
8. J. S. Pelc, Q. Zhang, C. R. Phillips, L. Yu, Y. Yamamoto, and M. M. Fejer, "Cascaded frequency upconversion for high-speed single-photon detection at 1550 nm," Opt. Lett. **37**, 476–478 (2012).
9. M. A. Albota and F. C. Wong, "Efficient single-photon counting at 1.55 μm by means of frequency upconversion," Opt. Lett. **29**, 1449–1451 (2004).
10. C. Langrock, E. Diamanti, R. V. Roussev, Y. Yamamoto, M. M. Fejer, and H. Takesue, "Highly efficient single-photon detection at communication wavelengths by use of upconversion in reverse-proton-exchanged periodically poled LiNbO$_3$ waveguides," Opt. Lett. **30**, 1725–1727 (2005).
11. J. S. Pelc, C. Langrock, Q. Zhang, and M. M. Fejer, "Influence of domain disorder on parametric noise in quasi-phase-matched quantum frequency converters," Opt. Lett. **35**, 2804–2806 (2010).
12. J. S. Pelc, C. R. Phillips, D. Chang, C. Langrock, and M. M. Fejer, "Efficiency pedestal in quasi-phase-matching devices with random duty-cycle errors," Opt. Lett. **36**, 864–866 (2011).
13. J. S. Pelc, L. Ma, C. R. Phillips, Q. Zhang, C. Langrock, O. Slattery, X. Tang, and M. M. Fejer, "Long-wavelength-pumped upconversion single-photon detector at 1550 nm: performance and noise analysis," Opt. Express **19**, 21445–21456 (2011).
14. J. Kiessling, R. Sowade, I. Breunig, K. Buse, and V. Dierolf, "Cascaded optical parametric oscillations generating tunable terahertz waves in periodically poled lithium niobate crystals," Opt. Express **17**, 87–91 (2009).
15. C. R. Phillips, J. S. Pelc, and M. M. Fejer, "Continuous wave monolithic quasi-phase-matched optical parametric oscillator in periodically poled lithium niobate," Opt. Lett. **36**, 2973–2975 (2011).
16. A. Henderson and R. Stafford, "Spectral broadening and stimulated Raman conversion in a continuous-wave optical parametric oscillator," Opt. Lett. **32**, 1281–1283 (2007).
17. J. E. Schaar, K. L. Vodopyanov, and M. M. Fejer, "Intracavity terahertz-wave generation in a synchronously pumped optical parametric oscillator using quasi-phase-matched GaAs," Opt. Lett. **32**, 1284–1286 (2007).
18. C. R. Phillips and M. M. Fejer, "Stability of the singly resonant optical parametric oscillator," J. Opt. Soc. Am. B **27**, 2687–2699 (2010).
19. D. T. Reid, "Ultra-broadband pulse evolution in optical parametric oscillators," Opt. Express **19**, 17979–17984 (2011).
20. C. R. Phillips and M. M. Fejer, "Adiabatic optical parametric oscillators: steady-state and dynamical behavior," Opt. Express **20**, 2466–2482 (2012).
21. C. Heese, C. R. Phillips, L. Gallmann, M. M. Fejer, and U. Keller, "Ultrabroadband, highly flexible amplifier for ultrashort midinfrared laser pulses based on aperiodically poled Mg:LiNbO$_3$," Opt. Lett. **35**, 2340–2342 (2010).

22. C. Heese, C. R. Phillips, L. Gallmann, M. M. Fejer, and U. Keller, "Role of apodization in optical parametric amplifiers based on aperiodic quasi-phasematching gratings," Opt. Express **20**, 18066–18071 (2012).

23. C. Heese, C. R. Phillips, B. W. Mayer, L. Gallmann, M. M. Fejer, and U. Keller, "75 MW few-cycle mid-infrared pulses from a collinear apodized APPLN-based OPCPA," Opt. Express **20**, 26888–26894 (2012).

24. T. Fuji, J. Rauschenberger, A. Apolonski, V. S. Yakovlev, G. Tempea, T. Udem, C. Gohle, T. W. Haensch, W. Lehnert, M. Scherer, and F. Krausz, "Monolithic carrier-envelope phase-stabilization scheme," Opt. Lett. **30**, 332–334 (2005).

25. C. Langrock, M. M. Fejer, I. Hartl, and M. E. Fermann, "Generation of octave-spanning spectra inside reverse-proton-exchanged periodically poled lithium niobate waveguides," Opt. Lett. **32**, 2478–2480 (2007).

26. C. R. Phillips, C. Langrock, J. S. Pelc, M. M. Fejer, I. Hartl, and M. E. Fermann, "Supercontinuum generation in quasi-phase-matched waveguides," Opt. Express **19**, 18754–18773 (2011).

27. C. R. Phillips, C. Langrock, J. S. Pelc, M. M. Fejer, J. Jiang, M. E. Fermann, and I. Hartl, "Supercontinuum generation in quasi-phase-matched $LiNbO_3$ waveguide pumped by a Tm-doped fiber laser system," Opt. Lett. **36**, 3912–3914 (2011).

28. S. Helmfrid and G. Arvidsson, "Influence of randomly varying domain lengths and nonuniform effective index on second-harmonic generation in quasi-phase-matching waveguides," J. Opt. Soc. Am. B **8**, 797–804 (1991).

29. M. M. Fejer, G. A. Magel, D. H. Jundt, and R. L. Byer, "Quasi-phase-matched second harmonic generation: tuning and tolerances," IEEE J. Quantum Electron. **28**, 2631–2654 (1992).

30. G. Rosenman, K. Garb, A. Skliar, M. Oron, D. Eger, and M. Katz, "Domain broadening in quasi-phase-matched nonlinear optical devices," Appl. Phys. Lett. **73**, 865–867 (1998).

31. G. Imeshev, M. M. Fejer, A. Galvanauskas, and D. Harter, "Pulse shaping by difference-frequency mixing with quasi-phase-matching gratings," J. Opt. Soc. Am. B **18**, 534–539 (2001).

32. R. W. Boyd, *Nonlinear Optics*, 3rd ed (Academic, 2008).

33. M. Born, E. Wolf, and A. B. Bhatia, *Principles of Optics: Electromagnetic Theory of Propagation, Interference and Diffraction of Light* (Cambridge University, 1999).

34. M. Charbonneau-Lefort, B. Afeyan, and M. M. Fejer, "Optical parametric amplifiers using chirped quasi-phase-matching gratings I: practical design formulas," J. Opt. Soc. Am. B **25**, 463–480 (2008).

35. D. S. Chemla and J. Zyss, *Nonlinear Optical Properties of Organic Molecules and Crystals* (Academic, 1987).

36. J. A. Armstrong, N. Bloembergen, J. Ducuing, and P. S. Pershan, "Interactions between light waves in a nonlinear dielectric," Phys. Rev. **127**, 1918–1939 (1962).

37. C. R. Phillips and M. M. Fejer, "Efficiency and phase of optical parametric amplification in chirped quasi-phase-matched gratings," Opt. Lett. **35**, 3093–3095 (2010).

38. P. Kumar, "Quantum frequency conversion," Opt. Lett. **15**, 1476–1478 (1990).

39. S. Tanzilli, W. Tittel, M. Halder, O. Alibart, P. Baldi, N. Gisin, and H. Zbinden, "A photonic quantum information interface," Nature **437**, 116–120 (2005).

40. R. DeSalvo, A. Said, D. Hagan, E. Van Stryland, and M. Sheik-Bahae, "Infrared to ultraviolet measurements of two-photon absorption and n_2 in wide bandgap solids," IEEE J. Quantum Electron. **32**, 1324–1333 (1996).

41. I. Shoji, T. Kondo, A. Kitamoto, M. Shirane, and R. Ito, "Absolute scale of second-order nonlinear-optical coefficients," J. Opt. Soc. Am. B **14**, 2268–2294 (1997).

42. O. Gayer, Z. Sacks, E. Galun, and A. Arie, "Temperature and wavelength dependent refractive index equations for MgO-doped congruent and stoichiometric $LiNbO_3$," Appl. Phys. B **91**, 343–348 (2008).

43. G. Imeshev, A. Galvanauskas, D. Harter, M. A. Arbore, M. Proctor, and M. M. Fejer, "Engineerable femtosecond pulse shaping by second-harmonic generation with Fourier synthetic quasi-phase-matching gratings," Opt. Lett. **23**, 864–866 (1998).

44. R. G. Smith, J. E. Geusic, H. J. Levinstein, J. J. Rubin, S. Singh, and L. G. Van Uitert, "Continuous optical parametric oscillation in $Ba_2NaNb_5O_{15}$," Appl. Phys. Lett. **12**, 308–310 (1968).

45. R. L. Byer, M. K. Oshman, J. F. Young, and S. E. Harris, "Visible CW parametric oscillator," Appl. Phys. Lett. **13**, 109 (1968).

46. S. T. Yang, R. C. Eckardt, and R. L. Byer, "Continuous-wave singly resonant optical parametric oscillator pumped by a single-frequency resonantly doubled Nd:YAG laser," Opt. Lett. **18**, 971–973 (1993).

47. L. E. Myers and W. R. Bosenberg, "Periodically poled lithium niobate and quasi-phase-matched optical parametric oscillators," IEEE J. Quantum Electron. **33**, 1663–1672 (1997).

48. A. Henderson and R. Stafford, "Low threshold, singly-resonant CW OPO pumped by an all-fiber pump source," Opt. Express **14**, 767–772 (2006).

49. M. J. McCarthy and D. C. Hanna, "All-solid-state synchronously pumped optical parametric oscillator," J. Opt. Soc. Am. B **10**, 2180–2190 (1993).

50. G. J. Hall, M. Ebrahimzadeh, A. Robertson, G. P. A. Malcolm, and A. I. Ferguson, "Synchronously pumped optical parametric oscillators using all-solid-state pump lasers," J. Opt. Soc. Am. B **10**, 2168–2179 (1993).

51. S. T. Yang, R. C. Eckardt, and R. L. Byer, "Power and spectral characteristics of continuous-wave parametric oscillators: the doubly to singly resonant transition," J. Opt. Soc. Am. B **10**, 1684–1695 (1993).

52. R. Eckardt and J. Reintjes, "Phase matching limitations of high efficiency second harmonic generation," IEEE J. Quantum Electron. **20**, 1178–1187 (1984).

53. M. Conforti, F. Baronio, C. De Angelis, M. Marangoni, and G. Cerullo, "Theory and experiments on multistep parametric processes in nonlinear optics," J. Opt. Soc. Am. B **28**, 892–895 (2011).

f) C.R. Phillips, C. Langrock, D. Chang, Y.W. Lin, L. Gallmann, "Apodization of chirped quasi-phasematching devices," *JOSA-B* **30**, pp. 1551-68 (June 2013).

Apodization of chirped quasi-phasematching devices

C. R. Phillips,[1,2,]* C. Langrock,[1] D. Chang,[1] Y. W. Lin,[1] L. Gallmann,[2] and M. M. Fejer[1]

[1]*Edward L. Ginzton Laboratory, Stanford University, Stanford, California 94305, USA*
[2]*Department of Physics, Institute of Quantum Electronics, ETH Zurich, Zurich 8093, Switzerland*
*Corresponding author: cphillips@phys.ethz.ch

Chirped quasi-phasematching (QPM) optical devices offer the potential for ultrawide bandwidths, high conversion efficiencies, and high amplification factors across the transparency range of QPM media. In order to properly take advantage of these devices, apodization schemes are required. We study apodization in detail for many regimes of interest, including low-gain difference frequency generation (DFG), high-gain optical parametric amplification (OPA), and high-efficiency adiabatic frequency conversion (AFC). Our analysis is also applicable to second-harmonic generation, sum frequency generation, and optical rectification. In each case, a systematic and optimized approach to grating construction is provided, and different apodization techniques are compared where appropriate. We find that nonlinear chirp apodization, where the poling period is varied smoothly, monotonically, and rapidly at the edges of the device, offers the best performance. We consider the full spatial structure of the QPM gratings in our simulations, but utilize the first order QPM approximation to obtain analytical and semi-analytical results. One application of our results is optical parametric chirped pulse amplification; we show that special care must be taken in this case to obtain high gain factors while maintaining a flat gain spectrum.   © 2013 Optical Society of America

OCIS codes: (190.4360) Nonlinear optics, devices; (230.7405) Wavelength conversion devices; (190.4970) Parametric oscillators and amplifiers; (320.7080) Ultrafast devices.
http://dx.doi.org/10.1364/JOSAB.30.001551

1. INTRODUCTION

Chirped (aperiodic) quasi-phasematching (QPM) gratings have received attention for various optical frequency conversion schemes, including difference frequency generation (DFG), optical parametric amplification (OPA), sum frequency generation (SFG), optical parametric oscillators (OPOs), and many other applications [1–23]. Their main role so far has been to broaden the phasematching bandwidth compared to conventional periodic QPM gratings, without the need to use short crystals with reduced conversion efficiency, tighter focusing, or higher intensities. This broadening can be understood through a simple spatial frequency argument: due to dispersion, there is a mapping between phasematched frequency and grating *k*-vector; in chirped QPM gratings, the grating *k*-vector is swept smoothly over the range of interest, thereby broadening the spatial Fourier spectrum of the grating and hence the phasematching bandwidth.

For continuous wave (cw) interactions involving the generation of a weak wave from two undepleted waves, the generation of the output wave can be described in terms of the spatial Fourier transform of the QPM grating evaluated at the spatial frequency corresponding to the phase mismatch associated with the three-wave interaction [2]. This type of interaction corresponds, for example, to negligible pump depletion and low signal amplification in OPA, or to second-harmonic generation (SHG) with negligible pump depletion. Since the nonlinear polarization is abruptly turned on at the edges of the nonlinear crystal, this QPM transfer function exhibits an interference effect associated with the corresponding high spatial frequency components. Such a spectral ripple is highly undesirable in most applications.

In order to remove the spectral ripple, apodization techniques may be employed to bring some measure of the effective nonlinearity smoothly to zero [1,24–27]. Several schemes have been proposed, including deleted domains, duty cycle variation, waveguide tapering [24], the use of nonlinear chirp profiles [1], and step-chirp designs [26].

In the context of apodization, we take linearity to mean that the output wave of interest is linear in the nonlinear coefficient $d(z)$. In many cases of practical interest, the assumption of linearity does not hold. For example, in high-gain OPA employing chirped QPM gratings, apodization is particularly important [1]. Furthermore, relatively recently it has been shown that saturated nonlinear interactions in chirped QPM gratings can exhibit high efficiencies due to an adiabatic following process [7,8]. As a result of this process, for three-wave mixing (TWM) processes involving input pump and signal waves and a generated idler wave, the ratio of pump output and input intensities approaches 0 with respect to both the input signal and pump intensities, i.e., approaches 100% pump depletion. This behavior, termed adiabatic frequency conversion (AFC), occurs for interactions that are both plane wave and monochromatic, provided that the QPM grating is sufficiently chirped.

In this paper, we study apodization for various different types of operating regimes of interest to chirped QPM devices, including low-gain and low-efficiency interactions such as DFG, high-gain OPA interactions, and even AFC. We show how apodization profiles can be constructed systematically, and how their construction can be connected with the underlying structure of the TWM process in an intuitive way. This approach enables high performance, limited only by the

inherently discrete QPM grating structure. We analyze all of the designs presented in detail numerically, in particular taking into account the full nonlinear evolution of the coupled waves in the actual discrete QPM structure (as opposed to assuming a simplified first order QPM interaction). Our study will enable the continued development of many different chirped QPM devices and technologies.

In Section 2, we establish the CWEs that will be used in the remaining sections. In Section 3, we solve these equations for the simple case of DFG in a chirped QPM grating, highlighting the connection between these solutions and the eigenmodes of the relevant CWE. In Section 4, we determine and compare apodization profiles for the linear cases [corresponding to DFG, SFG, SHG, optical rectification (OR), etc.]. In Section 5, we consider the case of high-gain OPA in chirped QPM devices, and establish and compare apodization techniques. In Section 6, we introduce AFC, and show in detail how these interactions can be analyzed and understood using the geometrical analysis of TWM processes developed in [28]. In Section 7, we develop apodization procedures for AFC via this geometrical analysis. We give an example apodization profile designed for the case of a moderate-gain, high-pump-depletion OPA device. Our results show that for all of the above types of interactions, and particularly for OPA and AFC, nonlinear chirp apodization offers significant advantages over other approaches, such as deleted domain apodization (DDA). Last, we conclude and discuss several important practical aspects of our results in Section 8.

2. COUPLED WAVE EQUATIONS

In this section, we introduce the equations governing arbitrary TWM processes in QPM devices. We consider plane wave, quasi-cw interactions, for which each signal frequency mixes with a single pump and idler frequency. Even for non-cw interactions, this assumption is very useful for studying TWM processes, for example, in optical parametric chirped pulse amplification (OPCPA) systems.

A. Three-Wave Mixing

In the quasi-cw approximation, the evolution of the electric field in the QPM grating is given by the coupled wave equations (CWEs) [29]:

$$\frac{dA_i}{dz} = -i\frac{\omega_i d_0}{n_i c}\bar{d}(z)A_s^* A_p e^{-i\Delta k_0 z}, \tag{1a}$$

$$\frac{dA_s}{dz} = -i\frac{\omega_s d_0}{n_s c}\bar{d}(z)A_i^* A_p e^{-i\Delta k_0 z}, \tag{1b}$$

$$\frac{dA_p}{dz} = -i\frac{\omega_p d_0}{n_p c}\bar{d}(z)A_i A_s e^{+i\Delta k_0 z}, \tag{1c}$$

where subscripts i, s, and p denote quantities associated with the idler, signal, and pump envelopes, respectively. The normalized nonlinear coefficient $\bar{d}(z)$ is defined in terms of the spatially varying nonlinear coefficient $d(z)$ as $\bar{d}(z) = d(z)/d_0$, where d_0 is the nonlinear coefficient in the unmodulated material. ω_j is the angular optical frequency of wave j (these satisfy $\omega_p = \omega_i + \omega_s$), and n_j is refractive index of wave j. The material phase mismatch Δk_0 is given by

$\Delta k_0 = k_p - k_s - k_i$, where $k_j = \omega_j n_j/c$ is the wavevector for wave j. The electric field envelopes A_j are assumed here for simplicity to contain only a single frequency component, and are defined such that the total electric field is given by

$$E(z, t) = \frac{1}{2}\sum_j A_j(z)\exp[i(\omega_j t - k_j z)] + \text{c.c.}, \tag{2}$$

where c.c. denotes complex conjugate.

Note that when pulsed interactions are analyzed within the quasi-cw limit, a set of CWEs similar to Eqs. (1) should be found, and expressed in the frequency domain, since the coupling coefficients $(\omega_j d_0)/(n_j c)$ and phase mismatch Δk are frequency dependent.

B. Quasi-Phasematching

Equations (1) apply for arbitrary spatial profiles of the nonlinear coefficient $d(z)$, provided that backward waves can be neglected. In a QPM grating, $d = \pm d_0$. Because of this constraint, it is possible to write arbitrary QPM grating profiles in a Fourier series:

$$\bar{d}(z) \equiv \frac{d(z)}{d_0} = \text{sgn}[\cos(\phi_G(z)) - \cos(\pi D(z))] \tag{3a}$$

$$= (2D(z) - 1) + \sum_{\substack{m = -\infty \\ m \neq 0}}^{\infty} \frac{2\sin(\pi m D(z))}{\pi m}\exp(im\phi_G(z)), \tag{3b}$$

where $D(z)$ and $\phi_G(z)$ are the grating duty cycle and phase functions, respectively. Often, $D(z) \approx 0.5$ by design, due to QPM fabrication limitations [30], minimization of photorefractive effects [31–33], and also in order to maximize the amplitude of the first Fourier order ($m = \pm 1$) in Eq. (3), but we consider more general cases here. In chirped QPM gratings, the phase function can be expressed as

$$\phi_G(z) = \phi_G(z_i) + \int_{z_i}^{z} K_g(z')dz', \tag{4}$$

where $K_g(z)$ is the smooth and continuous local grating k-vector (or local spatial frequency), and $\phi_G(z_i)$ is a chosen initial phase. z_i and z_f denote the positions of the input and output ends of the grating. Note that we do not assume $z_i = 0$, and therefore the $\exp(-ik_j z)$ phase factors in Eq. (2) must be accounted for in determining the *input* envelopes $A_j(z_i)$ given a known input electric field $E(z_i, t)$.

In an interaction where only one Fourier order of the QPM grating is close to the phasematching condition, $\bar{d}(z)$ can be approximated by considering only the $\pm m$th terms in Eq. (3b). In particular, for a first order QPM interaction, Eqs. (1) become

$$\frac{dA_i}{dz} = -i\kappa_i(z)A_s^* A_p e^{-i\phi_1(z)}, \tag{5a}$$

$$\frac{dA_s}{dz} = -i\kappa_s(z)A_i^* A_p e^{-i\phi_1(z)}, \tag{5b}$$

$$\frac{dA_p}{dz} = -i\kappa_p(z)A_iA_s e^{+i\phi_1(z)}. \tag{5c}$$

In these equations, the coupling coefficients $\kappa_j(z)$ are given by

$$\kappa_j(z) = \frac{\omega_j d_0}{n_j c}\frac{2}{\pi}\sin(\pi D(z)), \tag{6}$$

and the accumulated phase mismatch $\phi_1(z)$ is given by

$$\phi_1(z) = \phi_1(z_i) + \int_{z_i}^{z}\Delta k_1(z')\mathrm{d}z', \tag{7}$$

where the local phase mismatch is given by

$$\Delta k_m(z) = k_p - k_s - k_i - mK_g(z), \tag{8}$$

for integer m (the QPM order), and $\phi_1(z_i)$ corresponds to the relative phase between the three envelopes and their driving terms at the input of the device. Usually, one of the envelopes is initially zero, and in such cases $\phi_1(z_i)$ has no effect on the dynamics. The first order QPM approximation is often very accurate in practical situations, as we will show later in this paper.

C. Normalized Coupled Wave Equations

For the purposes of analysis and numerical simulations, it is often useful to normalize Eqs. (5). The photon flux of wave j is proportional to $(n_j/\omega_j)|A_j|^2$. Motivated by energy conservation, and in particular by the Manley–Rowe relations, we introduce dimensionless envelopes a_j whose square magnitudes are proportional to these photon fluxes. These envelopes are implicitly defined with

$$A_j = \sqrt{\frac{\omega_j}{n_j}}\sqrt{\sum_n \frac{n_n}{\omega_n}|A_{n0}|^2}\, a_j. \tag{9}$$

In these definitions, A_{n0} is the envelope of wave n at the input to the grating. With these definitions, Eqs. (5) become

$$\frac{da_i}{dz} = -ig(z)\gamma a_s^* a_p e^{-i\phi_1(z)}, \tag{10a}$$

$$\frac{da_s}{dz} = -ig(z)\gamma a_i^* a_p e^{-i\phi_1(z)}, \tag{10b}$$

$$\frac{da_p}{dz} = -ig(z)\gamma a_i a_s e^{+i\phi_1(z)}, \tag{10c}$$

where $g(z) = \sin(\pi D(z))$, and the coupling coefficient γ is given by

$$\gamma = \sqrt{\frac{\omega_i\omega_s\omega_p}{n_i n_s n_p}}\sqrt{\sum_j \frac{n_j}{\omega_j}|A_{j0}|^2}\frac{2d_0}{\pi c}. \tag{11}$$

$\phi_1(z)$ is defined in Eq. (7). The input conditions for Eqs. (10) satisfy, in all cases,

$$\sum_j |a_j(z_i)|^2 = 1. \tag{12}$$

Furthermore, we could also introduce a dimensionless propagation coordinate $\zeta = \gamma z$; however, for clarity we work with physical units instead. An analogous set of normalized CWEs could be obtained, accounting for the full spatial dependence of the QPM grating [$\bar{d}(z) = \pm 1$]. The only differences would be substituting $g(z) \to \pi\bar{d}(z)/2$, and $\phi_1(z) \to \Delta k_0 z$ [see Eqs. (1)].

3. LOW-GAIN, LOW-DEPLETION DEVICES

To begin our study, we first consider cases in which only the generated idler wave in Eqs. (10) changes substantially; the other two envelopes propagate linearly, i.e., without depletion, amplification, or nonlinear phase shifts, and hence are constant. This type of configuration, while quite simple, is applicable to many different types of devices, and can help guide intuition for more complicated cases. We will always assume in this paper that one of the waves is zero at the input of the grating. For definiteness we choose this to be the idler wave, but our results apply to other cases, with minor modifications.

The generated wave, found by integrating Eq. (1a), can be expressed as

$$A_i(z_f) = -i\frac{\omega_i d_0}{n_i c}A_s^* A_p F[\bar{d}(z)](\Delta k_0), \tag{13}$$

where the $\mathcal{F}$ denotes the Fourier transform, defined as $\mathcal{F}[f(z)](k) = \int_{-\infty}^{\infty}f(z)\exp(-ikz)\mathrm{d}z$. Eq. (13) holds for arbitrary QPM structures, for which $\bar{d}(z) = \pm 1$ within the interval $[z_i, z_f]$ and $\bar{d}(z) = 0$ elsewhere. An important consequence of this Fourier transform relation is that in a device of finite length, the idler spectrum acquires a ripple, due to interference associated with the abrupt changes in $\bar{d}(z)$ at z_i and z_f. The same argument applies if we consider only the first Fourier order of the grating, as in Eqs. (5) and (10). In Section 4, we discuss apodization functions to suppress such spectral ripples. In this section, we show solutions for the particular case of a linearly chirped QPM grating, and use that solution to introduce a heuristic for constructing apodization functions for general chirped QPM gratings.

A. Analytical Solution

For a linearly chirped grating, given by $K_g(z) = K_g(z_i) - \Delta k'(z - z_i)$ for constant chirp rate $\Delta k'$. In this case, the phase $\phi_1(z)$ in Eqs. (10) is given by

$$\phi_1(z) = \phi_1(z_i) + \frac{\Delta k'}{2}[(z - z_{\mathrm{pm}})^2 - (z_i - z_{\mathrm{pm}})^2], \tag{14}$$

where z_{pm} is the phasematched point, satisfying $K_g(z_{\mathrm{pm}}) = \Delta k_0$. Assuming $\phi_1(z_i) = 0$ and a constant QPM duty cycle [$g(z) = g_0 = $ constant for $z_i \leq z \leq z_f$], we integrate Eq. (10a) to obtain a normalized output idler field under the first order QPM approximation. The result is

$$a_i(z) = -\frac{1}{2}a_s^* a_p e^{i\pi/4}e^{i\Delta k'(z_{pm}-z_i)^2/2}\sqrt{\frac{2\pi\gamma^2 g_0^2}{\Delta k'}}$$
$$\times \left[\mathrm{erf}\left(\sqrt{2}e^{i\pi/4}\sqrt{\Delta k'}(z_{\mathrm{pm}} - z_i)\right)\right.$$
$$\left. + \mathrm{erf}\left(\sqrt{2}e^{i\pi/4}\sqrt{\Delta k'}(z - z_{\mathrm{pm}})\right)\right], \tag{15}$$

where erf is the error function. Based on Eq. (15), the generated idler (at $z = z_f$) exhibits a significant ripple in amplitude and phase as a function of z_{pm}, and hence as a function of phase mismatch Δk_0 (based on the mapping between Δk_0 and z_{pm}), and thus on optical frequency ω (based on the mapping between Δk_0 and ω). A mathematically simple way to suppress this ripple is by extending the QPM grating length L to infinity, i.e., $z_i \to -\infty$ and $z_f \to +\infty$. In these limits, the (asymptotic) output idler field is given by

$$a_i^{(L \to \infty)} = \left\{ -i\sqrt{\frac{2\pi\gamma^2 g_0^2}{|\Delta k'|}} e^{-i\pi \, \mathrm{sgn}(\Delta k')/4} e^{\left[i\frac{\Delta k'}{2}(z_{pm}-z_i)^2\right]} \right.$$
$$\left. + \frac{\gamma g_0}{\Delta k_1(z_f)} e^{\left[i\frac{\Delta k'}{2}((z_{pm}-z_i)^2 - (z_f - z_{pm})^2)\right]} - \frac{\gamma g_0}{\Delta k_1(z_i)} \right\} a_s^* a_p,$$

$$(16)$$

where $\Delta k(z_f)^{-1} \to 0$ as $z_f \to \infty$, and similarly $\Delta k(z_i)^{-1} \to 0$ as $z_i \to -\infty$. The second and third terms in this equation, whose phase oscillates rapidly compared to that of the first term, eventually vanish, yielding a magnitude that is independent of z_{pm} (and hence frequency). In this case, the nonlinear interaction is turned on and off smoothly by the gradual transition from large to small phase mismatch; the result is an apodized interaction.

Further insight can be gained by examining Eq. (10a). In the case of a constant grating duty cycle and a constant, finite phase mismatch, Eq. (10a) supports idler eigenmodes: solutions whose magnitude is independent of z. We define these eigenmodes in the general case [with varying $g(z)$ and $\Delta k(z)$, but still maintaining the assumption of constant signal and pump envelopes] as

$$a_i^{(eig)}(z) = \frac{\gamma g(z)}{\Delta k_1(z)} a_s^* a_p e^{-i\phi_1(z)}.   (17)$$

If $\Delta k(z)$ and $g(z)$ are constant, this eigenmode is a solution to Eq. (10a). Based on Eq. (16), we also define the "zeroth-order" idler as $a_i^{(0)} = -i\sqrt{2\pi\gamma^2 g_0^2/|\Delta k'|} a_s^* a_p e^{-i\pi \, \mathrm{sgn}(\Delta k')/4}$. With these definitions, Eq. (16) can be written in the following form:

$$a_i^{(L \to \infty)}(z_f) = a_i^{(0)} e^{-i\phi_1(z_{pm})} + a_i^{(eig)}(z_f) - a_i^{(eig)}(z_i),   (18)$$

with spectral ripples essentially originating from the nonzero values of the idler eigenmode at the input and output ends of the device ($a_i^{(eig)}(z_i)$ and $a_i^{(eig)}(z_f)$, respectively). This form usually applies even for gratings with monotonic but spatially varying chirp rates and can, in these more general cases, be understood via the stationary phase approximation [34]. Apodization can thus be viewed as reducing the magnitude of idler eigenmode to zero (or close to zero) sufficiently slowly. The connection between eigenmodes of the TWM interaction and apodization is quite general, and even applies for other, more complicated types of interactions [7], as we discuss in Section 7. Such eigenmodes are also connected with the cascaded phase shifts acquired during phase mismatched $\chi^{(2)}$ interactions [35]. To illustrate Eq. (18) and its accuracy, we show in Fig. 1 the propagation of the idler as a function of z for a particular linearly chirped grating.
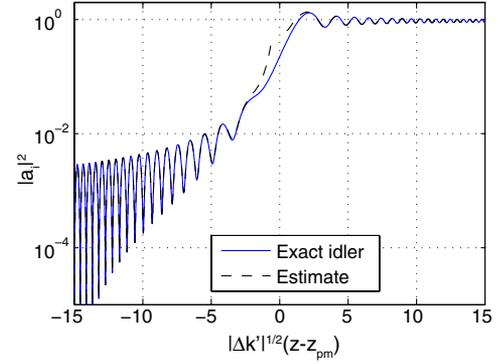

Fig. 1. Evolution of the idler a_i in a linearly chirped QPM grating, for a DFG interaction. The solid (blue) line shows the numerical solution of Eq. (10a), corresponding to (and indistinguishable from) the analytical solution given by Eq. (15). The dashed (black) line shows the asymptotic solution corresponding to Eq. (18). A normalized propagation coordinate, given by $\xi = \sqrt{|\Delta k'|}(z - z_{pm})$, is used. The idler in each curve is normalized to $|a_i^{(0)}|^2$ [defined by Eqs. (16) and (18)]. The dashed (black) curve shows $[a_i^{(eig)}(z) - a_i^{(eig)}(z_i)]$ for $\xi < -0.5$, and $[a_i^{(eig)}(z) - a_i^{(eig)}(z_i) + a_i^{(0)} \exp(-i\phi_1(z_{pm}))]$ for $\xi > 0.5$. The input, phasematching, and output points correspond to $\xi = -15$, $\xi = 0$, and $\xi = 15$, respectively. Because of the way the figure has been normalized, there are no other free parameters in the calculation.

B. Adiabaticity Heuristic

In this subsection, we will use Eqs. (17) and (18) to develop a heuristic criterion by which apodization profiles can be constructed. These apodization regions will be appended to the ends of a nominal grating profile (e.g., linearly chirped); we illustrate different types of apodization in Section 4.

The essential idea is to impose changes in $g(z)$ and $\Delta k_1(z)$ such that the ratio $g(z)/|\Delta k_1(z)| \ll 1$ at $z = z_i$ and $z = z_f$, and for this change to be slow enough that the idler eigenmodes Eq. (17) are still accurate local solutions to Eq. (10a). Inspecting Eq. (17), away from z_{pm}, the eigenmodes have a slowly varying amplitude and rapidly varying phase. Our heuristic is to maintain this structure (phase varying much more rapidly than relative changes in amplitude), which leads to the condition

$$\left| \left(\frac{\gamma g}{\Delta k_1}\right)^{-1} \frac{d}{dz}\left(\frac{\gamma g}{\Delta k_1}\right) \right| \ll \left| \frac{d}{dz}(e^{-i\phi_1}) \right|.   (19)$$

In a QPM device supporting a wide spectral bandwidth, this condition must be met for all the spectral components of interest, and hence for all values of z_{pm}, at all positions z within both the input and output apodization profiles. Evaluating the derivatives in Eq. (19) and replacing the $\ll$ by $\leq \epsilon$ for "small" $\epsilon > 0$, we thus find, within the apodization regions,

$$\max_\omega \left\{ \left| \frac{1}{g}\frac{dg}{dz} - \frac{1}{\Delta k_1}\frac{d\Delta k_1}{dz} \right| - \epsilon |\Delta k_1| \right\} \leq 0,   (20)$$

where maximization with respect to ω is performed over the spectral range of interest. This equation can be used to construct differential equations for apodization profiles in which $K_g(z)$, $g(z)$, or both, or a related quantity, are varied nonlinearly with position. In Section 4, we consider specific apodization examples based on this adiabaticity equation.

$$K_g(z) = \begin{cases} K_- + [\epsilon s_c(z - z_{b,-}) + (K_{b,-} - K_-)^{-1}]^{-1} & \text{for } K_g(z) < K_{b,-}. \\ K_{\text{nom}}(z) & \text{for } K_{b,-} \leq K_g(z) \leq K_{b,+}. \\ K_+ + [\epsilon s_c(z - z_{b,+}) + (K_{b,+} - K_+)^{-1}]^{-1} & \text{for } K_g(z) > K_{b,+}. \end{cases} \tag{25}$$

4. QPM APODIZATION TECHNIQUES

In this section, we use Eq. (20) to construct apodization regions for nominally chirped QPM devices, and compare different apodization techniques. We assume that there is a nominal, unapodized chirp profile $K_{\text{nom}}(z)$ that has already been chosen, and show how to determine apodization profiles that are appended to the ends of this nominal profile in order to suppress the spectral ripples that would otherwise occur.

A. Nonlinear Chirp (NLC) Apodization

First, we consider nonlinear chirp apodization (NLCA). In this case, there is a constant duty cycle, $dg/dz = 0$, but a spatially varying chirp rate $d\Delta k_1/dz$. Therefore, Eq. (20) can be written as

$$s_c \frac{dK_g}{dz} = \epsilon \min_\omega \{[\Delta k_0(\omega) - K_g(z)]^2\}, \tag{21}$$

where $s_c = -\text{sgn}(\Delta k')$ is the sign of the grating chirp rate, and we have replaced the $\leq$ with = (assuming that the inequality is strict for the extrema of the spectrum). Eq. (21) can be expressed in a more explicit form by distinguishing between the input and output ends of the grating, and by treating K_g as the integration variable rather than z (which is possible since we assume monotonic chirp functions):

$$s_c \frac{dK_g}{dz} = \begin{cases} \epsilon[K_- - K_g]^2 & \text{if } \Delta k(z,\omega) > 0, \\ \epsilon[K_+ - K_g]^2 & \text{if } \Delta k(z,\omega) < 0, \end{cases} \tag{22}$$

where $K_- = \min_\omega[\Delta k_0(\omega)]$ and $K_+ = \max_\omega[\Delta k_0(\omega)]$ (with min and max performed over the frequency range of interest). Within each apodization region, Eq. (22) can be solved analytically, yielding the following implicit equation:

$$\frac{1}{K_g(z) - K_\pm} - \frac{1}{K_{b,\pm} - K_\pm} = \epsilon s_c(z - z_{b,\pm}), \tag{23}$$

where $z_{b,\pm}$ and $K_{b,\pm}$ represent boundary conditions. These boundary conditions can be determined from the fact that we append apodization regions to a nominal QPM profile, under the assumption that K_g and dK_g/dz must be continuous at the apodization boundaries. These boundaries are therefore the points at which the chirp rate in Eq. (22) equals the nominal chirp rate. Explicitly, for a nominal profile $K_{\text{nom}}(z)$ and chirp rate $dK_{\text{nom}}/dz \equiv K_{\text{nom},z}$, $z_{b,\pm}$ and $K_{b,\pm}$ are the solutions to the following equations:

$$K_{\text{nom},z}(z_{b,\pm}) = \epsilon s_c[K_\pm - K_{b,\pm}]^2, \tag{24a}$$

$$K_{b,\pm} = K_{\text{nom}}(z_{b,\pm}). \tag{24b}$$

Given the solution to Eq. (24), we can now specify the full form of the grating:

Note that the equation for $K_g(z)$ in the apodization regions diverges with respect to z. Therefore, for a real grating, initial and final values of $K_g(z)$ must be chosen. In choosing these values, we must bear in mind that the final values of $\gamma(\omega)g(z)/\Delta k_1(z,\omega)$ determine the fidelity of the apodization, but only to the extent that the first order QPM contribution ($m = 1$) dominates. The existence of other QPM orders means that, eventually, increases in Δk no longer suppress spectral ripple. In an extreme case of $K_g(z)$ passing through phasematching for third-order QPM, for example, the spectral ripple could actually be made worse. The limits on $K_g(z)$ are thus determined by a trade-off between apodization fidelity, fabrication constraints, higher-order-QPM contributions, and potentially other issues as well. We expect that in most practical cases, these issues will not substantially limit the performance of the apodized device. Note also that, in a practical device, it may be useful to reduce the chirp rate at the edges of the grating so that the range of $K_g(z)$ is not sensitive to changes in crystal length that occur during polishing. We discuss this further in Subsection 8.B.

In Subsections 4.B and 4.C, we discuss two other apodization techniques. In Subsection 4.D, we show example apodization profiles and corresponding idler spectra (Fig. 2).

B. Duty Cycle Apodization

Another approach to suppressing spectral ripples is by apodizing $g(z)$ instead of Δk_1. In principle, changes in $g(z)$ can be implemented via changes in the QPM duty cycle $D(z)$. Therefore, we refer to this approach as duty cycle apodization (DCA). For this case, we can again assume a known, nominal chirp function (e.g., a linear chirp), and substitute this function into Eq. (20). Analogously to Eq. (21), we find the following differential equation for $g(z)$, suitable for a finite and monotonic nominal chirp rate:

$$s_{g'} \frac{1}{g} \frac{dg}{dz} = \min_\omega \left\{ -s_{g'} \frac{1}{\Delta k_0(\omega) - K_g(z)} \frac{dK_g}{dz} \right. $$
$$\left. \times \left[1 - \sqrt{1 + \epsilon^2 \frac{(\Delta k_0 - K_g(z))^4}{(dK_g/dz)^2}} \right] \right\}, \tag{26}$$

where $s_{g'} = \text{sgn}(dg/dz)$. This equation can be used to determine $g(z)$ in a similar way to the NLCA case discussed in Subsection 4.A, but we omit the mathematical details here.

C. Deleted Domain Apodization

In lithographic poling, it is often challenging in practice to obtain a custom duty cycle function, due to the dynamics of the poling process [30], particularly for MgO:LiNbO$_3$ poling [36]. Instead, the voltage waveform used for poling is usually chosen to yield as close to a 50% duty cycle as possible. Such gratings are also advantageous in order to suppress photorefractive

effects [31], including recently identified pyroelectrically induced beam distortions [32,33].

If duty cycle modulation is not possible, a continuously varying first order QPM coefficient $g(z)$ cannot be achieved. An alternative approach is to use a discrete approximation to the desired continuous $g(z)$ profile, as demonstrated in [24]. In this scheme, QPM domains are "deleted" (not inverted) in order to reduce the effective duty cycle of the grating, averaged over many periods. Therefore, we call this approach deleted domain apodization (DDA). To express this approach mathematically, we assume that the grating has N periods with center positions z_n and length $l_n (n = 1, …, N)$, and either 50% ($g_n = 1$) or 0% ($g_n = 0$) duty cycle. The spatial profile of the grating is then given by

$$\bar{d}(z) = 1 - \sum_n 2g_n \Pi_{l_n/2}(z - z_n), \qquad (27)$$

where $\Pi_l(z)$ is the rectangle function (with width l and center 0). The integral of $(1 - \bar{d})$ should then be a good approximation to the target profile $g(z)$:

$$\sum_n g_n \int_{z_i}^z 2\Pi_{l_n/2}(z' - z_n)\mathrm{d}z' \approx \int_{z_i}^z g(z')\mathrm{d}z'. \qquad (28)$$

A simple way to obtain each g_n from this approximate relation is to initially assume $g_n = 1$, and then reverse the sign of g_{n+1} whenever, for a position $z \approx z_n + l_n/2$, the left hand side of Eq. (28) exceeds the right hand side.

D. Comparison and Discussion

In this subsection, we compare the three apodization techniques described in Subsections 4.A–4.C (NLCA, DCA, and DDA, respectively). We choose an example with the following parameters. The grating center spatial frequency $K_{g0} = 3 \times 10^2$ mm^{-1} (≈ 21 µm period), nominal length $L_{\text{nom}} = 10$ mm, nominal bandwidth $\Delta k_{\text{BW}} = 20$ mm^{-1}, and positive chirp rate $\Delta k' = +\Delta k_{\text{BW}}/L_{\text{nom}} = 2$ mm^{-2}. Apodization profiles are found via the preceding differential equations, and we choose $\epsilon = 0.5$ in each case (for $\epsilon > 1$, the apodization fidelity decreases). For the NLCA example, the range of k-vectors, $|K_g(z_f) - K_g(z_i)| = 200$ mm^{-1}, and the apodized grating length is $L = z_f - z_i = 14$ mm. For the DCA and DDA examples, $g(z_f) = g(z_i) = 0.052$, and the apodized grating length is $L = z_f - z_i = 16$ mm. The resulting idler spectrum for phase mismatches in the vicinity of first order QPM is shown in Fig. 2. The NLCA profile is found according to Eq. (25); the DCA profile according to Eq. (26), and the DDA example is determined from the DCA profile combined with Eq. (28).

The NLCA and DCA cases show the best ripple suppression, while the DDA case still has a substantial ripple in this example. The NLCA ripple is limited by the range of QPM periods and presence of higher order QPM terms. In cases where precise control of the duty cycle is not possible over a wide range of periods, even orders of the grating will contribute as well, so second-order QPM contributions represent one possible limiting factor for the NLCA approach. These issues are difficult to quantify in general, so we have restricted the example to a range of $K_g(z)$ far from higher-order QPM. The DCA ripple will be limited by the range of duty cycles that can be fabricated reliably. This range is typically quite restricted,
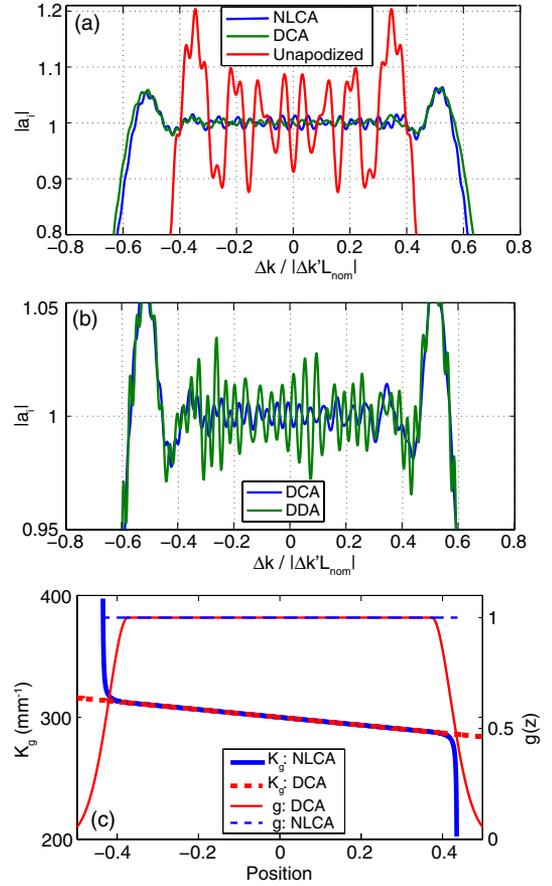

Fig. 2. Apodization examples for DFG, calculated numerically via Eq. (1a), using the full $\bar{d} = \pm 1$ grating structure. (a) Nonlinear chirp apodization (NLCA), (b) duty cycle apodization (DCA), (c) deleted domain apodization (DDA) with a domain profile determined from the DCA example in (b). The parameters are given in the text.

and therefore the high performance of the DCA example may not be achievable in practice. Furthermore, the length of the apodization region will usually be longer for DCA compared with NLCA.

While DDA is not limited by duty cycle fabrication issues, the DDA example exhibits poorer performance than DCA, due to the non-negligible k-space bandwidth, compared to the nominal grating k-vector. Consequently, the implicit assumption of a small change in relative phase between the idler and its driving polarization between the remaining undeleted domains does not hold. More specifically, to achieve a low effective nonlinearity, there must be a large gap between undeleted domains. Since all of the spectral components of interest are phase mismatched in the apodization regions for a chirped grating, this gap can correspond to a large relative phase shift between the idler and its driving polarization. Such large phase shifts likely prevent the interference that would, for the case of a smooth duty cycle modulation, (almost) completely suppress the input and output eigenmodes (and hence the spectral ripples). This issue is particularly important for gratings with a broad k-space bandwidth, such as the example shown in Fig. 2. On the other hand, for periodic QPM gratings, such as those discussed in [24], the underlying assumption of a slowly varying relative phase holds very well, and DDA is effective in such cases.

Since DCA is challenging in terms of fabrication and DDA exhibits reduced performance, the NLCA approach will be favorable in most chirped QPM-grating cases. These conclusions are especially valid in more complicated interactions involving high gain or pump depletion. An example of the poorer performance of DDA compared with NLCA in a high-gain interaction is shown in Section 5.

In each of the above apodization approaches, the absolute scale of the amplitude ripple remaining in the apodized device is determined by fabrication and QPM constraints, such as the presence of higher-order QPM contributions, and is independent of grating length. In contrast, the scale of the "zeroth-order" term [$a_i^{(0)}$ in Eq. (18)] increases with grating length for a given bandwidth, since in a longer device the chirp rate can be reduced. Therefore, the relative scale of the ripples is reduced in longer devices. Note, however, that the range of group delays associated with any remaining spectral ripples is not reduced, and may increase.

5. OPTICAL PARAMETRIC AMPLIFICATION

We now turn our attention to high-gain and high-efficiency devices. In this section, we consider chirped QPM OPA. Such devices have several advantageous properties, including the potential for high gain, almost arbitrary gain bandwidth, tailorable gain and phase spectra, and high conversion efficiency [1,4,5,7]. They have been used in a mid-infrared OPCPA system, enabling broad bandwidth, high power, and high-repetition rate operation [9,10].

A critical consideration in obtaining high-fidelity amplification from these devices is apodization. Without apodization, there is a pronounced ripple in gain and phase; this ripple can be much more severe than in the linear cases (e.g., DFG), due to the high gain involved. The presence of such a ripple can be explained heuristically by the abrupt turn-on and turn-off of nonlinear coupling between the signal and idler fields at the edges of the device, in analogy to the simpler case of DFG. Here, we build on the theoretical work presented in [1] to show how optimal OPA apodization profiles can be constructed. Our approach is similar in spirit to the one presented in Section 4 for DFG apodization.

A. Overview of Chirped QPM OPA

We first give a brief theoretical description of chirped QPM OPA interactions, under the assumption of a cw (or quasi-cw) pump wave, which is undepleted and much stronger than the signal and idler waves ($|a_i| \ll |a_p|$ and $|a_s| \ll |a_p|$). In this case, the amplification of each signal spectral component (and corresponding idler component) is governed by Eqs. (10a) and (10b). By defining new envelopes b_j according to $a_j(z) = g(z)^{1/2} \exp[-i\phi_1(z)/2]b_j(z)$ for $j = i$ and $j = s$, the following second-order equation can be obtained from Eqs. (10a) and (10b) [1]:

$$\frac{d^2 b_s}{dz^2} + Q(z)b_s, \tag{29}$$

where the "potential" $Q(z)$ is given by

$$Q = -(\gamma g)^2 + \frac{1}{2}\frac{d}{dz}\left(\frac{g'}{g}\right) - \frac{i\Delta k'}{2} - \frac{1}{4}\left(\frac{g'}{g} - i\Delta k\right)^2, \tag{30}$$

where $f' = df/dz$ for function $f(z)$. This potential is position dependent (via $g(z)$ and $K_g(z)$) and frequency dependent (via $\gamma(\omega)$ and $\Delta k_0(\omega)$).

Equation (29), which is in standard form, is amenable to complex Wentzel–Kramers–Brillouin (WKB) analysis. This analysis yields several important results for device operation [1]. In particular, for smoothly chirped gratings, the signal intensity gain can be approximated according to

$$\ln(G_s(\omega)) \approx 2 \int_{z_i}^{z_f} \mathrm{Re}\sqrt{[g(z)\gamma(\omega)]^2 - \left[\frac{\Delta k_0(\omega) - K_g(z)}{2}\right]^2}\, dz, \tag{31}$$

which, in the case of a constant grating chirp rate ($\Delta k' = \partial \Delta k/\partial z$) and a 50% duty cycle ($g = 1$), yields $G_s = \exp(2\pi\gamma^2/|\Delta k'|)$ for spectral components within the gain bandwidth. Equation (31) shows that gain occurs for each spectral component ω over the spatial region for which the signal-idler coupling, $g(z)\gamma(\omega)$, is sufficiently large compared with the phase mismatch, $\Delta k(z,\omega) = \Delta k_0(\omega) - K_g(z)$. Outside this spatial region, the signal and idler waves are oscillatory. The points where the integrand in Eq. (31) is zero are called turning points. The gain bandwidth can be determined from Eq. (31) as the range of frequencies for which both turning points lie within the grating. For the case of a linear grating chirp, this bandwidth is given implicitly as the range of frequencies ω whose phase mismatch $\Delta k_0(\omega)$ lies within the following range:

$$\left\{\omega : (\Delta k_0(\omega) - K_{g0}) \in \left[-\frac{|\Delta k' L|}{2} + 2\gamma(\omega), +\frac{|\Delta k' L|}{2} - 2\gamma(\omega)\right]\right\}, \tag{32}$$

for center grating k-vector K_{g0}.

Outside the gain region, the waves are oscillatory versus position, leading to fluctuations of the output waves versus frequency, and consequently a ripple in the output spectrum (since the oscillations of different spectral components have different phase). These properties are illustrated in Fig. 3, where we show the propagation of a single spectral component. The figure shows both an unapodized and an apodized case. Apodized and unapodized gain spectra are shown later, in Fig. 4, after we have discussed an apodization scheme.

B. Apodization Constraint for Chirped QPM OPA

The oscillatory behavior shown in Fig. 3 can be understood as interference associated with the two complex WKB global asymptotic solutions of Eqs. (29) (see, for example, the appendices of [1]). The role played by these global solutions in the context of amplitude oscillations is twofold: first, the assumed input conditions to the device (zero idler, finite signal) imply that the signal consists of a complex linear superposition of these two global solutions. Second, the global solutions themselves are oscillatory. Given such oscillations, frequency-dependent changes in the phasematched point lead to oscillations in the gain spectrum.

These spectral oscillations can be suppressed by suppressing oscillations in the WKB solutions, which is achieved by the condition $|\nu(z)| \gg 1$ for $z = z_i$ and $z = z_f$, where ν is defined as
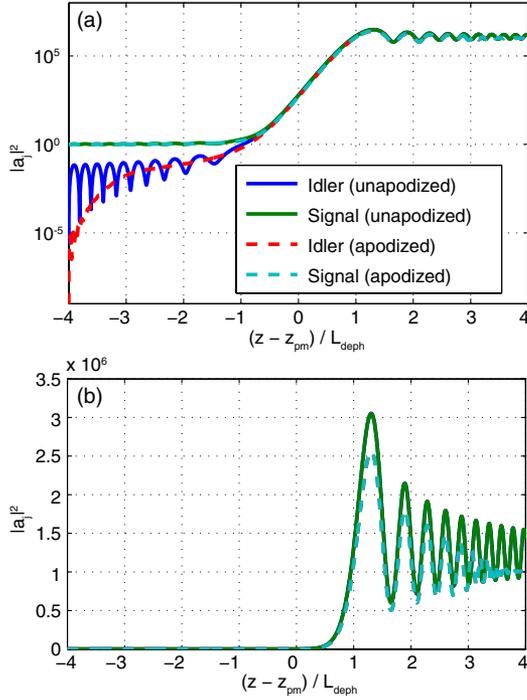
Fig. 3. Propagation example for OPA in a linearly chirped QPM grating, showing the signal and idler as a function of normalized position. The gain factor $\lambda_R = 2.2$. The position has been normalized to the dephasing length, $L_{\rm deph} = 2\gamma/|\Delta k'|$. The normalized grating length is given by $L/L_{\rm deph} = 8$. The phasematching point $z_{\rm pm}$ is located at the middle of the grating. The dashed lines show the evolution of the signal and idler in a apodized grating with the same parameters; oscillations in $a_i(z)$ and $a_s(z)$ near $z = z_i$ and $z = z_f$ are suppressed in this case. For this example, we apodize via the chirp rate and duty cycle simultaneously to reveal the idler evolution under idealized input conditions; (b) shows the fields on a linear scale to better indicate how the oscillations are suppressed near the output of the grating in the apodized case, but not the unapodized case; the signal and idler magnitudes are indistinguishable on this linear scale due to the high gain involved.

$$\nu(z) \equiv \frac{\Delta k_1(z)}{2\gamma g(z)}. \tag{33}$$

The $|\nu(z_i)| \gg 1$ condition ensures that the input conditions correspond to one of the two global solutions (very small contribution from the other solution) [Eqs. (C4) and (C5) of [1]]. The $|\nu(z_f)| \gg 1$ condition suppresses ripples on this global solution [Eq. (C3) of [1]].

These conditions are also quite closely related to the idler eigenmodes of Eq. (17). Indeed, for large phase mismatches, Eqs. (10a and 10b) support two *local* signal-idler eigenmodes whose amplitudes would be constant with respect to position in the case of a constant and large phase mismatch and constant duty cycle. These eigenmodes may be determined by substituting $a_i = a_{i0} \exp(i \int_{z_i}^{z} \phi_i(z')\mathrm{d}z')$ and $a_s = a_{s0} \exp(i \int_{z_i}^{z} \phi_s(z')\mathrm{d}z')$ into Eqs. (10a and 10b), neglecting derivatives of $a_{j0}(z)$, and solving for $\phi_i(z)$, $\phi_s(z)$, and $|a_{s0}(z)/a_{i0}(z)|^2$. While these eigenmodes are not solutions to Eqs. (10a and 10b) in the case of a varying phase mismatch, they provide some insight into the more complicated dynamics supported by the WKB solutions described above.

For large phase mismatches, one of these two eigenmodes has a small signal component, while the other has a small idler
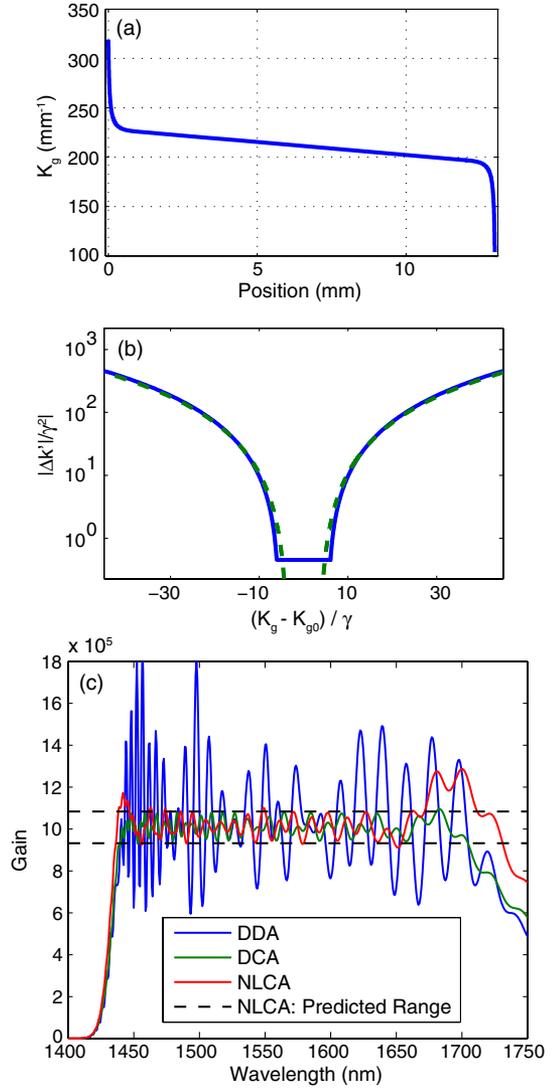

Fig. 4. Chirped-QPM OPA apodization examples. (a) Grating k-vector profile for a NLCA example, (b) normalized grating chirp rate corresponding to (a), and (c) signal gain spectrum. The dashed lines in (b) show $\min((\Delta k_1/\gamma_0)^2)\epsilon$, with minimization performed with respect to signal wavelength (restricted to the target gain bandwidth that spans the 1450–1650 nm range). This figure indicates that the optimal normalized chirp rate in the apodization region approximately satisfies $|\Delta k'| = \min(\Delta k_1^2)\epsilon$. The dashed lines in (c) indicate analytical estimates of the fluctuations in the gain due to the finite value of $|\gamma_0/\Delta k_1|$ at the ends of the grating, as described in the text. The gain spectra for DCA and corresponding DDA examples are also shown in (c), for comparison.

component. The rate of signal-phase accumulation, $\varphi_s(z)$, differs between these two eigenmodes, leading to amplitude oscillations unless the signal and idler fields correspond to only one of the eigenmodes. In the limit where $\nu(z_i)^{-1} = 0$, the input conditions (zero idler) are matched to one of the two eigenmodes, thereby suppressing ripples near the start of the grating [region $z_i \leq z \ll z_{\rm pm}$ of the apodized example in Fig. 3] since the magnitude of this eigenmode varies slowly as ν is decreased, but does not vary over the fast Δk^{-1} length scale associated with the local phase mismatch Δk. Note that the different length-scales in phase-mismatched TWM interactions have been analyzed using multiple-scale analysis in [37].

After the amplification region ($z \gg z_{\mathrm{pm}}$), the fields can be thought of as consisting of a linear combination of the two local eigenmodes. In the limit where $\nu(z_f)^{-1} = 0$, the signal-component of one of the two eigenmodes is brought to zero at the end of the grating, thereby suppressing signal-amplitude oscillations [region $z_{\mathrm{pm}} \ll z \leq z_f$ of the apodized example in Fig. 3].

The $|\nu(z_i)|^{-1} = 0$ and $|\nu(z_f)|^{-1} = 0$ conditions can be achieved, in principle, by extending the nominal grating chirp profile to infinity. In practice, this condition can be achieved (with high fidelity) by apodization. In performing such apodization, $|\nu(z)|$ in Eq. (33) should be increased slowly enough that the local WKB solutions remain accurate; if $\nu(z)$ is changed too rapidly, there will be coupling between the two asymptotic solutions of Eqs. (10), again leading to interference. As such, a sufficient criterion is to maintain the validity of the WKB approximation within the apodization regions. This condition corresponds, for an individual spectral component ω, to the following inequality [38]:

$$\left| \frac{dQ}{dz} \frac{1}{Q^{3/2}} \right| \leq \epsilon, \qquad (34)$$

for "small" ϵ. This condition should be maintained for all spectral components of interest [i.e., all within the amplification bandwidth associated with Eq. (31)].

C. Nonlinear Chirp Apodization for OPA

In this subsection we use Eq. (34) to determine apodization profiles for undepleted-pump, chirped QPM OPAs. As before, we start from a nominal grating design, such as a linear chirp profile. Apodization regions are then appended to this nominal design, with the grating k-vector and duty cycle properly matched at the joining points. With Eq. (34), these apodization regions can be made as short as possible. This condition will help with meeting any maximum grating length constraints. In the context of OPAs, an even greater benefit is that optimized apodization profiles will ensure that parasitic effects, such as pump SHG and other unwanted processes, can be avoided or suppressed in the apodization regions by having a chirp rate that is as high as possible within as short a length as possible.

Equation (34) yields an implicit differential equation in z which, as stated, is difficult to solve. A much simpler equation is obtained by writing $g(z)$ and the chirp rate $K_z \equiv dK_g/dz$ as functions of K_g, and integrating versus K_g. This approach is possible because we assume that $K_g(z)$ is monotonic, and $g(z)$ is monotonic within each individual apodization region. For notational convenience, in the following analysis we suppress the g subscript on K_g. We mainly consider NLCA rather than DCA or DDA for the reasons discussed in Subsection 4.D, and therefore assume that $g(z)$ is constant versus position. For simplicity, we also assume that $\gamma(\omega) = \gamma_0$ is frequency-independent, although in practice this assumption is not necessary.

With the above assumptions, the following equation can be obtained from Eqs. (30) and (34):

$$\left(\frac{dK_z}{dK} \right)^2 \leq \min_{\Delta k_0} \left\{ \frac{4\epsilon^2}{K_z^2} \left| \left(\frac{\Delta k}{2} \right)^2 - \gamma_0^2 + i \frac{K_z}{2} \right|^3 - \Delta k^2 \right\}$$
$$\equiv \min_{\Delta k_0} \{ f(\Delta k_0, K, K_z) \}, \qquad (35)$$

where $\Delta k(z, \omega) = \Delta k_0(\omega) - K(z)$. The minimization in Eq. (35) with respect to $\Delta k_0(\omega)$ is performed over the desired amplification bandwidth of the device. The function f has been introduced as a shorthand to identify the dependence of the inequality on Δk_0 (and hence on optical frequency).

Close to the turning points satisfying $\Delta k_0 - K = \pm 2\gamma_0$, $f(\Delta k_0, K, K_z)$ is negative (unless ϵ is chosen to be too large, e.g., $\epsilon \gg 1$), which means that $|dQ/dz| > \epsilon |Q^{3/2}|$. If we move far enough from these turning points (toward the edges of the nominal grating profile) then equality is obtained. We wish to find a pair of grating k-vectors at which to begin the apodization region; these are denoted $K_{\mathrm{apod},s}$ and $K_{\mathrm{apod},e}$ for the start-regions and end-regions of the grating, respectively. These will be the k-space points at which inequality in Eq. (35) is satisfied for the whole spectral range of interest. The minimization in Eq. (35) will correspond to either the minimum or maximum value of $\Delta k_0(\omega)$ across this spectral range. Beyond these k-vectors, it is possible to chirp the grating more rapidly while still satisfying Eq. (34). We therefore assume that the inverse grating profile, $z(K)$, corresponds to a nominal chirp profile $z_{\mathrm{nom}}(K)$ for K between $K_{\mathrm{apod},s}$ and $K_{\mathrm{apod},e}$, and is determined via Eq. (35) outside this region.

Based on the above discussion, we first determine $K_{\mathrm{apod},s}$ and $K_{\mathrm{apod},e}$ by solving the following pair of equations:

$$\min_{\Delta k_0} \{ f(\Delta k_0, K_{\mathrm{apod},j}, K_{z,\mathrm{nom}}) \} = \left(\frac{dK_{z,\mathrm{nom}}}{dK} \right)^2, \qquad (36a)$$

$$\min_{\Delta k_0} [|\Delta k_0 - K_{\mathrm{apod},j}|] \geq 2\gamma_0, \qquad (36b)$$

for $j = s$ and $j = e$, where subscript "nom" denotes the nominal grating profile. For a linearly chirped grating, $K_{z,\mathrm{nom}}(K)$ is constant. Eq. (36a) arises from Eq. (35), while Eq. (36b) ensures that the $K_{\mathrm{apod},j}$ lie outside the amplification region for all of the spectral components involved.

It is convenient to define the k-space domain of the nominal grating:

$$\mathrm{dom}(K_{\mathrm{nom}}) = \{ K : \min_j(K_{\mathrm{apod},j}) \leq K \leq \max_j(K_{\mathrm{apod},j}) \}. \qquad (37)$$

We now use $K_{\mathrm{apod},j}$ to find the entire grating profile by first solving the following equations for $K(z)$ and $K_z(K)$:

$$K(z) = K_{\mathrm{nom}}(z), K \in \mathrm{dom}(K_{\mathrm{nom}}), \qquad (38a)$$

$$\frac{dK_z}{dK} = s_{K_z} \min_{\Delta k_0}(\sqrt{f}), K \notin \mathrm{dom}(K_{\mathrm{nom}}), \qquad (38b)$$

where $s_{K_z} = \mathrm{sgn}(dK_{z,\mathrm{nom}}/dK)$, and with the initial conditions for Eq. (38b) given by

$$K_z(K_{\mathrm{apod},j}) = K_{z,\mathrm{nom}}(K_{\mathrm{apod},j}). \qquad (39)$$

Equations (38a) and (38b) yield $K_z(K)$ over the entire grating spatial frequency profile. We can thus determine $z(K)$ by

$$z(K) = \int_{K_i}^{K_f} K_z(K)^{-1} \mathrm{d}K, \qquad (40)$$

and then invert this function to find $K_g(z)$.

An example implementation of this design procedure is shown in Fig. 4. For this example, we select a specific experimental configuration. We assume an MgO:LiNbO$_3$ OPA device at 150 °C, designed to amplify signal components between 1450 and 1650 nm using a narrow-bandwidth 1064 nm pump. The corresponding range of idler wavelengths is 3000–4000 nm. For illustration purposes, we assume a nondispersive coupling coefficient γ, with $\gamma(\omega) = \gamma_0$. We choose a gain coefficient $\lambda_{R,p} = \gamma_0^2/|\Delta k'| = 2.2$. The range of phase mismatches corresponding to the signal bandwidth is $\Delta k_{\mathrm{BW}} \approx 16.6$ mm^{-1}. This value originates from the material phase mismatches of $\Delta k = 219.7$ and 203.1 mm^{-1} for signal wavelengths of 1450 and 1650 nm, respectively. According to Eq. (31), a linear chirp rate $\Delta k'$ and nominal grating length L_{nom} satisfying $|\Delta k' L_{\mathrm{nom}}| = \Delta k_{\mathrm{BW}} + 4\gamma_0$ are required in order to fully amplify this bandwidth. Therefore, given values of L_{nom}, Δk_{BW}, and $\lambda_{R,p}$, the values of γ_0 and $|\Delta k'|$ can be determined. Here, we choose $L_{\mathrm{nom}} = 10$ mm, which yields $\gamma_0 \approx 2.4$ mm^{-1} and $\Delta k' = \pm 2.62$ mm^{-2}.

To construct an apodization profile, we assume a positive chirp rate ($\Delta k' > 0$), a symmetric grating profile, set $\epsilon = 1$, and solve Eq. (38). It is useful to introduce a parameter δ to describe the range of grating k-vectors,

$$\left| \frac{K_g(z_f) - K_g(z_i)}{2\gamma} \right| \le \delta, \qquad (41)$$

where we choose $\delta = 45$ for the present example. This value is chosen to yield large values of $|\nu|$ defined in Eq. (33) at the ends of the device, while still remaining far from higher-order QPM. For our example, $K_g(z_i) \approx 319.5$ mm^{-1} and $K_g(z_f) \approx 103.3$ mm^{-1}.

The k-vector profile is shown in Fig. 4(a). In Fig. 4(b), the grating chirp rate is compared to Δk^2, illustrating that optimal normalized chirp rate is approximately proportional to the square of the minimum phase mismatch. The output gain spectrum as a function of wavelength is shown in Fig. 4(c). We show DCA and DDA examples for comparison to the NLCA case. For each of these simulations, we assume the full grating structure ($\bar{d} = \pm 1$) and integrate Eqs. (1) numerically, for each spectral component, within each successive QPM domain.

The finite value of δ^{-1} defined above as well as higher-order QPM contributions result in a ripple in the gain for the NLCA example. Under the assumption of a first order QPM interaction, the ripple is such that $|\ln(G_s) - 2\pi\lambda_{R,p}| \le 4\delta^{-1}$ for frequencies within the amplification region [1]. In a real grating, there are also small contributions from the other orders of the QPM grating. The dashed black lines in Fig. 4 are bounds on the gain ripple found by analytically summing *all* such contributions, showing excellent agreement with the full numerical NLCA simulations. The gain spectra for the DCA and DDA examples are also included. The DCA example was specified heuristically, with an amplitude profile determined via hyperbolic tangent functions; it shows comparable performance to NLCA, but requires large modulation of the QPM duty cycle. The DDA example was derived from the DCA example, and shows a significant reduction in apodization

quality compared with both DCA and NLCA. For these DCA and DDA examples, the chirp rate is linear. Note that with no apodization, the ripple is huge, with gain varying by a factor of 4 across the passband (from $\approx 0.5 \times 10^6$ to $\approx 2 \times 10^6$).

6. ADIABATIC FREQUENCY CONVERSION

We next consider adiabatic frequency conversion (AFC). This type of interaction can occur in chirped QPM gratings when the coupling between the three waves is sufficiently strong, and enables high pump conversion efficiency across a very broad range of phase mismatches and intensities. In this section, we first show how AFC can be analyzed and understood in general TWM configurations. In Section 7, we develop an apodization procedure for AFC devices via an approach similar to the DFG and OPA cases considered above.

In AFC, instead of reaching a maximum at a certain input intensity, the pump depletion can increase monotonically with respect to the input intensity of either the pump or signal wave, or both [7,8]. Rather than back-convert after the point of maximum pump depletion, the fields adiabatically follow a local nonlinear eigenmode that evolves with the grating period. If the grating is sufficiently chirped, then at the input to the device, the relevant eigenmode corresponds to zero idler (i.e., to the input conditions), while at the output this eigenmode corresponds to zero pump (the desired output condition of full pump depletion). This adiabatic following process is possible provided that the coupling rate γ between the fields is strong enough (at a given chirp rate $\Delta k'$), or if the chirp rate is slow enough (at a given coupling rate). The required coupling rate also depends on the input conditions, as we will discuss.

Before considering AFC and nonlinear eigenmodes in more detail, we discuss in Subsection 6.A a reformulation of Eqs. (10) based on [28], in which TWM interactions are described geometrically. This geometric analysis provides many insights into the structure of various TWM processes, especially AFC, as we will show.

A. Geometric Analysis of Three-Wave Mixing Interactions

In [28], the geometrical analysis was motivated by the Hamiltonian structure of the TWM equations. Furthermore, [28] considered general QPM interactions, corresponding to $\bar{d} = \pm 1$. Here, we briefly recapitulate the formulation given in more detail in [28], and give the modifications required for first order QPM interactions.

First, reduced field variables X, Y, and Z can be defined according to

$$X + iY = a_i a_s a_p^* e^{i\phi_1(z)}$$
$$Z = |a_p|^2, \qquad (42)$$

The phase of $X + iY$ specifies the relative phase between the envelopes a_j and their driving polarizations in the CWEs [Eqs. (10)], and hence the direction of energy transfer. The remaining variable Z specifies the pump photon flux. These variables can be treated as specifying a real-valued "position" vector $\mathbf{W}$ in an abstract 3-space, defined as

$$\mathbf{W} = [X, Y, Z]^T. \qquad (43)$$

During propagation, $\mathbf{W}$ evolves according to the evolving complex envelopes a_j, but is constrained to lie on a surface whose

shape is determined by the input conditions. This surface is given by the implicit relation $\varphi = 0$, where

$$\varphi = X^2 + Y^2 - Z(Z - K_{\text{ip}})(Z - K_{\text{sp}}),\qquad(44)$$

and where the constants K_{ip} and K_{sp} are Manley–Rowe invariants, given by

$$K_{jp} = |a_j|^2 + |a_p|^2,\qquad(45)$$

for $j = i$ and $j = s$. With the envelope definitions and input conditions considered here, with zero input idler, $K_{\text{sp}} = 1$ and $K_{\text{ip}} = |a_p(z_i)|^2 \leq 1$. It is convenient to introduce a parameter ρ describing the ratio of input photon fluxes: $\rho \equiv |a_s(z_i)/a_p(z_i)|^2$. For cases with an input signal that is much larger than the pump ($\rho \gg 1$, and hence $0 \leq Z \leq K_{\text{ip}} \ll 1$), $\varphi = 0$ is (approximately) a sphere. For other input conditions ($\rho \not\gg 1$), the conserved surface $\varphi = 0$ is not spherical, but remains closed and convex [28].

The evolution of W is given by

$$\frac{d\mathbf{W}}{d(\gamma z)} = \nabla H \times \nabla \varphi,\qquad(46)$$

where $\nabla = [\partial/\partial X, \partial/\partial Y, \partial/\partial Z]^T$, and where the local Hamiltonian H, which is discussed in more detail in [28], can be expressed as

$$H = gX + \frac{\Delta k}{2\gamma}(Z - (K_{\text{ip}} + K_{\text{sp}})).\qquad(47)$$

This local Hamiltonian is position-dependent in the case of a chirped QPM grating. Eq. (46) implies that $\mathbf{W}$ is constrained to remain on the implicit surface $\varphi = 0$, since the "force" acting on $\mathbf{W}$ is perpendicular to the local surface normal $\nabla\varphi$.

B. Solution for Uniform QPM Gratings

The geometrical approach of [28], an important result of which is reproduced in Eq. (46), greatly simplifies the interpretation of many TWM problems. For example, during propagation in a uniformly phasematched medium, $\mathbf{W}$ is constrained to lie on the intersection between a plane ($H = \text{constant}$) and a convex surface ($\varphi = 0$), and hence on a ring (or a single point). The distance required to fully traverse the ring is the period associated with the Jacobi-elliptic analytical solutions of the there-wave mixing problem, derived in [39]. Much of the complicated structure of these analytical solutions can thus be visualized with this geometrical construction.

Furthermore, Eq. (46) reveals the existence of the local nonlinear eigenmodes discussed above. The existence of such eigenmodes is well known [35], but the geometric description provides a particularly convenient framework for their study, and the interpretation of their role in spatially nonuniform structures, such as chirped gratings.

These eigenmodes, which we denote as $\mathbf{W}_m$, satisfy $d\mathbf{W}/dz = 0$, and hence correspond to the two points for which ∇H is normal to the surface $\varphi = 0$ (the points where $\nabla\varphi$ is in the same direction as $\pm\nabla H$). Because $\varphi = 0$ is closed and convex, there are two and only two such points. These eigenmodes can also be viewed as generalizations of the

eigenmodes we discussed in Subsections 3.A and 5.B for the specific cases of DFG and OPA, respectively.

To illustrate the nonlinear eigenmodes and the evolution of $\mathbf{W}$, we show in Fig. (5) a propagation example for a uniformly phasematched device. In this example, the black arrow points in the direction of ∇H; its location has been chosen so that the point where it touches the conserved surface $\varphi = 0$ corresponds to a nonlinear eigenmode. Since the medium is uniform (constant g and Δk_1, and other QPM orders are neglected), this eigenmode is fixed, and hence represents a true eigenmode of the TWM interaction. In a chirped device, the direction of ∇H, and hence the local nonlinear eigenmode $\mathbf{W}_m$, would be swept from the top to the bottom of $\varphi = 0$ as $\nu = \Delta k_1/(2\gamma g)$ [see Eq. (33)] is swept from $\pm\nu \gg 1$ to $\mp\nu \gg 1$.

C. Solution for Chirped QPM Gratings

We next consider the AFC solutions supported by chirped QPM gratings, for which the reduced field vector $\mathbf{W}(z)$ can follow the nonlinear eigenmodes $\mathbf{W}_m(z)$. Since $\mathbf{W}_m = [X_m \;\; Y_m \;\; Z_m]^T$ are points where $\nabla H \times \nabla\varphi = 0$, they can be found, for any given value of ν, by solving the following set of equations:
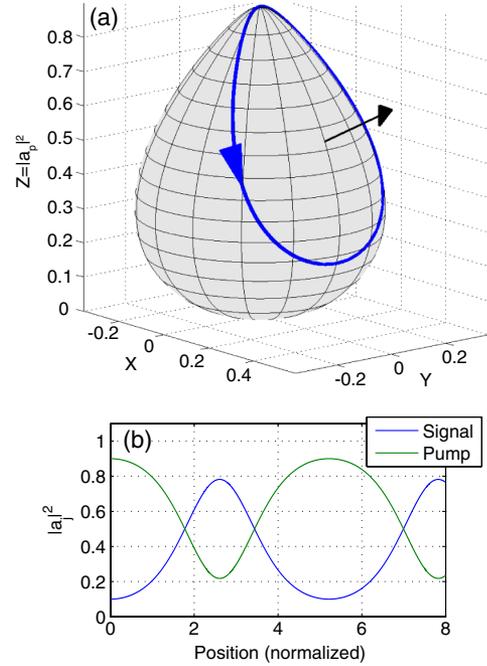

Fig. 5. (a) Solution to an example TWM problem, visualized with the geometric description of [28] [and Eq. (46) in particular]. The parameters for this example are $K_{\text{ip}} = |a_p(z_i)|^2 = 0.9$, $g = 1$ (50% duty cycle), and $\Delta k_1/\gamma = 1$. The surface shown is $\varphi = 0$, and the curve (blue) represents the trajectory of $\mathbf{W}$. Since Δk_1 and g are both constant in this example, the curve lies on a plane $H = \text{constant}$. $\mathbf{W}$ is initially at the top of the surface ($Z \equiv |a_p|^2 = K_{\text{ip}} = 0.9$), and the direction of $\mathbf{W}$ (with increasing z) is shown by the blue arrow on the curve. The direction of ∇H is also shown (black arrow). The point where this arrow touches the surface is a nonlinear eigenmode associated with the chosen parameters (i.e., a point where ∇H is in the direction of the surface normal to $\varphi = 0$, $\nabla\varphi$). In this unchirped example, the field vector $\mathbf{W}$ orbits around the fixed eigenmode $\mathbf{W}_m$. In (b), the photon fluxes $|a_j|^2$ are shown for comparison. One period of these fluxes corresponds to a complete traversal of the blue curve in (a); position is normalized to γ, defined in Eq. (11).

$$\varphi = 0, \tag{48a}$$

$$\frac{\partial \varphi}{\partial Z} = \nu \frac{\partial \varphi}{\partial X}, \tag{48b}$$

$$Y = 0, \tag{48c}$$

where Eq. (48a) ensures that the eigenmode is consistent with the input conditions, and Eqs. (48b) and (48c) follow from the forms of ∇H and $\nabla \varphi$.

Because $\varphi = 0$ is convex for all input conditions, the eigenmodes always evolve through chirped QPM gratings in a similar way. The relevant nonlinear eigenmode initially corresponds to low idler energy, and is swept smoothly (by changing g and Δk_1) to one corresponding to low pump energy. If the sweep rate is slow enough (conditions for which are discussed in Subsection 7.A), the fields follow this eigenmode, and as a result most of the pump energy is transferred to the signal and idler waves. To parameterize the solutions

for linearly chirped gratings, we introduce normalized coupling factors $\lambda_R = \gamma^2/|\Delta k'|$, $\lambda_{R,p} = (1 + \rho)^{-1}\gamma^2/|\Delta k'|$, and $\lambda_{R,s} = (1 + 1/\rho)^{-1}\gamma^2/|\Delta k'|$. For an undepleted-pump OPA ($\rho \to 0$), the signal gain is given by $|a_s(z_f)/a_s(z_i)|^2 = \exp(2\pi\lambda_{R,p})$ [1]. For a constant-signal DFG or SFG interaction ($\rho \to \infty$), the pump depletion is given by $|a_p(z_f)/a_p(z_i)|^2 = \exp(-2\pi\lambda_{R,s})$ [8].

To illustrate the AFC process, we show in Fig. 6 the trajectory of the reduced field vector $\mathbf{W}$ (solid lines) and the local nonlinear eigenmode $\mathbf{W}_m$ (dashed lines) for four example cases, with the following parameters: (b) $\lambda_{R,s} = 1$ and $K_{ip} = 10^{-3}$, (c) $\lambda_{R,s} = 2$ and $K_{ip} = 10^{-3}$, (e) $\lambda_{R,p} = 2$ and $K_{ip} = 0.9$, and (f) $\lambda_{R,p} = 10$ and $K_{\mathrm{ip}} = 0.9$. The structure of $\varphi = 0$ is shown in Figs. 6(a) and 6(d) for the input conditions $K_{ip} = 10^{-3}$ (0.1% of input photons in the pump, 99.9% in the signal) and $K_{ip} = 0.9$ (90% of input photons in the pump, 10% in the signal), respectively.

For both choices of K_{ip}, the adiabatic following process requires a large coupling factor λ_R; for smaller λ_R, a ripple in the components of $\mathbf{W}$ [solid lines in Figs. 6(b), 6(c), 6(e), and 6(f)]
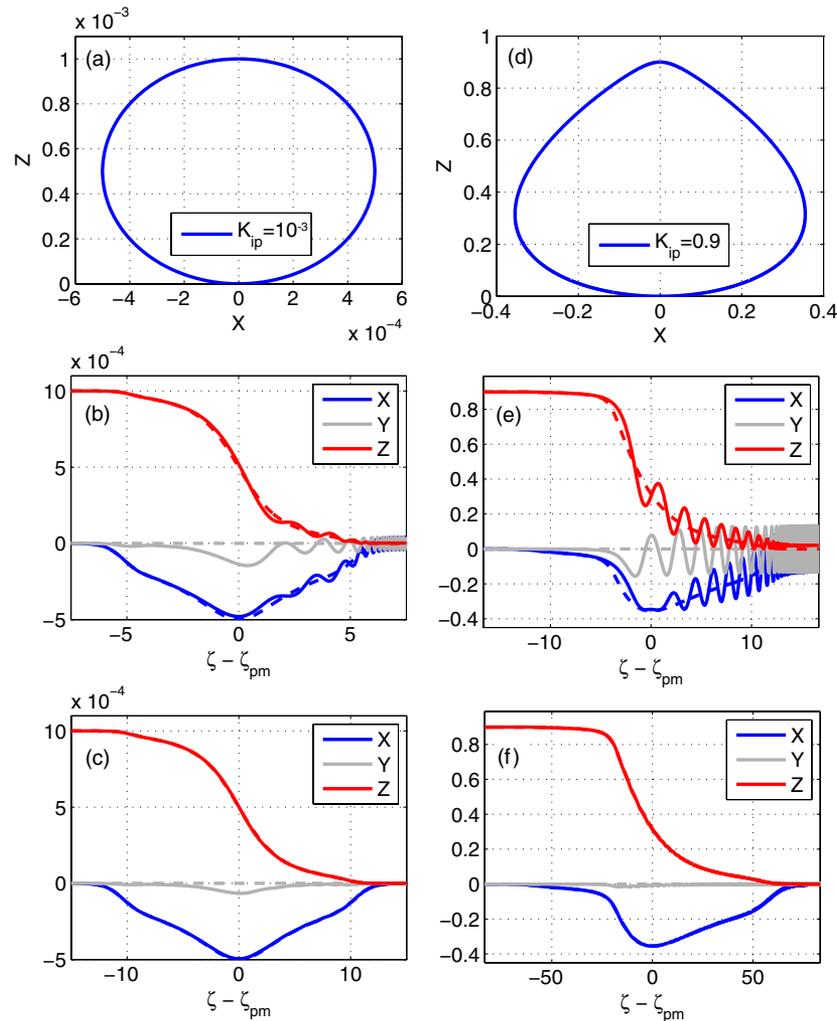

Fig. 6. Propagation of field vector $\mathbf{W}$ and eigenmode vector $\mathbf{W}_m$ [the solid and dashed lines, respectively, in (b), (c), (e), and (f)], illustrating the adiabatic following process arising from Eq. (46). The left column is for $K_{\mathrm{ip}} \equiv |a_p(z_i)|^2 = 10^{-3}$ (strong input signal), while the right column is for $K_{\mathrm{ip}} = 0.9$ (strong input pump). The first row [(a) and (d)] are cuts through the surface $\varphi = 0$ in the plane $Y = 0$, corresponding to these two input conditions. The second and third rows show the evolution of the field vectors (versus coordinate $\zeta = \gamma z$) under these input conditions, for two different coupling factors: $\lambda_{R,s} = (1, 2)$ for (b) and (c), respectively, and $\lambda_{R,p} = (2, 10)$ for (e) and (f), respectively. In (b), (c), (e) and (f), the x curve is on the bottom, y in the middle, and z on the top.

around $\mathbf{W}_m$ (dashed lines) is introduced. Such ripples occur when the chirp rate is too rapid for the fields to follow the local eigenmode; they are thus indications of nonadiabaticity. For the strong-signal case ($K_{ip} = 10^{-3}$), the amplitude of these ripples scales as $\exp(-2\pi\lambda_{R,s})$; for the strong-pump case ($K_{ip} = 0.9$) the behavior is more complicated, but a fast decay of the ripple amplitude with respect to $\lambda_{R,p}$ is still obtained at large $\lambda_{R,p}$. At larger values of the coupling factors, the fields $\mathbf{W}$ can be seen in Fig. 6 to follow the local eigenmode $\mathbf{W}_m$ more closely (the ripple amplitude is reduced).

A ripple in $\mathbf{W}(z)$ also occurs if the fields are not launched properly into the input eigenmode, i.e., if $|\nu(z_i)|$ is not large enough: unless $|\nu(z_i)|^{-1} = 0$, the input conditions ($|a_i(z_i)| = 0$) are different from that of the input eigenmode ($|a_i| \neq 0$). These ripples are not noticeable in Fig. 6 because we have introduced an apodization profile to ensure that $|\nu(z_i)|$ and $|\nu(z_f)|$ are very large.

7. ADIABATIC FREQUENCY CONVERSION: APODIZATION

A. Adiabaticity Condition Based on Geometric Picture
The AFC solutions illustrated in Subsection 6.C are obtained for all input conditions provided that the grating is sufficiently chirped, and the chirp rate is sufficiently slow. In order to make use of these solutions in a practical setting, it is important to determine how rapidly the grating can be chirped while still maintaining adiabaticity. In this section, we determine a heuristic constraint for the QPM chirp rate. If this constraint is satisfied, then the adiabatic following process can occur (with a certain fidelity).

As ν is varied (by changing Δk_1, g or both), the local eigenmode $\mathbf{W}_m$ changes, but always remains in the X–Z plane (since $Y_m = 0$). When the reduced field vector $\mathbf{W}$ is in the X–Z plane, each of the envelopes a_j is $\pm\pi/2$ radians out of phase with its driving term in Eq. (10), which implies that $d|a_j|/dz = 0$; this is why $\mathbf{W}_m$ lies in the X–Z plane. Further physical insight into the meaning of this X–Z plane can be gained by considering an unchirped device: $\mathbf{W}$ passes through the X–Z plane at points where the direction of energy flow changes (e.g., at points where the pump is fully depleted, just before the onset of back-conversion).

In order for adiabatic following to occur, the reduced variable Z must keep up with the corresponding component Z_m of the local eigenmode, and hence it is necessary that

$$\frac{dZ}{dz} \approx \frac{dZ_m}{dz}. \tag{49}$$

To satisfy this condition, $\mathbf{W}$ must be sufficiently separated from the X–Z plane: from the form of $d\mathbf{W}/dz$ [Eq. (46)], $dZ/d(\gamma z) = 2gY$, and therefore the required magnitude of Y increases with dZ_m/dz, while dZ_m/dz increases with the chirp rate.

Since $\varphi = 0$ is convex, an angle $\theta_\parallel$ in the X–Z plane associated with the local eigenmode can be defined according to

$$\tan(\theta_\parallel) = \left.\frac{\partial\varphi/\partial Z}{\partial\varphi/\partial X}\right|_{\mathbf{W}=\mathbf{W}_m} = \nu, \tag{50}$$

To see why the latter equality holds, recall that $\nu = \Delta k/(2\gamma g)$, $Y_m = 0$, and that the eigenmodes $\mathbf{W}_m$ are points for which

$\nabla\varphi = [\,\partial\varphi/\partial X \quad \partial\varphi/\partial Y \quad \partial\varphi/\partial Z\,]$ is parallel or antiparallel to $\nabla H = [\,g \quad 0 \quad \Delta k/(2\gamma)\,]$. Based on the curvature of $\varphi = 0$, an angle $\theta_\perp$ associated with the value of Y can be defined according to

$$Y = R_\perp(\mathbf{W}_m)\sin(\theta_\perp), \tag{51}$$

where $R_\perp$ is the local radius of curvature (RoC) of the surface in the direction perpendicular to the X–Z plane. In order for the interaction to be adiabatic, we expect that the condition $|\theta_\perp| \ll 1$ must be satisfied in addition to $dZ/dz \approx dZ_m/dz$, since in the limit of an infinitely slow chirp rate, $Y \to 0$ and hence $\theta_\perp \to 0$. Additionally, this angular condition implies a small relative separation of the fields from the local eigenmode, in analogy to conventional adiabatic following processes [40].

With the conditions $|\theta_\perp| \ll 1$ and $dZ/dz = dZ_m/dz$, it is possible to obtain a heuristic constraint on the chirp rate required for the adiabatic following process that in turn can be used to construct apodization profiles. To obtain this constraint, first consider the local curvatures of $\varphi = 0$. Formulas for the curvatures of surfaces specified by implicit equations are given in [41]. We denote the in-plane (X–Z plane) curvature as $k_\parallel$ (RoC $R_\parallel = -k_\parallel^{-1}$), and the curvature in the orthogonal direction as $k_\perp$ (RoC $R_\perp = -k_\perp^{-1}$). After some algebra it can be shown that, at $\mathbf{W}_m$, these curvatures are given by

$$k_\parallel = -\frac{2}{|\nabla\varphi|}\frac{\bar{G}(Z_m) + \nu^2}{1 + \nu^2}, \tag{52a}$$

$$k_\perp = -\frac{2}{|\nabla\varphi|}, \tag{52b}$$

where the parameter $\bar{G}(Z)$ is given by

$$\bar{G}(Z) = 1 + K_{ip} - 3Z. \tag{53}$$

Given $\mathrm{sgn}(\nu(z_i))$, the relevant local eigenmode and hence $k_\parallel$ and $k_\perp$ are functions of only ν.

An expression for the evolution of the local eigenmode is also required. With Eqs. (48a) and (48c), X_m can be expressed in terms of Z_m. Substituting this result into Eq. (48b), an implicit equation for Z_m is obtained, of the form $f(Z_m(\nu), \nu) = 0$ for function f. By taking the derivative of this $f = 0$ equation with respect to ν, it can be shown that

$$\frac{dZ_m}{d\nu} = -\mathrm{sgn}\left(\frac{d\nu}{dz}\right)\frac{|\nabla\varphi|}{2(\bar{G}(Z_m) + \nu^2)(1 + \nu^2)^{1/2}}, \tag{54}$$

where the sgn prefactor assumes $\nu(\zeta)$ is monotonic. With the above relations and the condition $dZ_m/dz = dZ/dz$, the inequality $|\theta_\perp| \ll 1$ can be expressed as

$$\left|\frac{d}{d(\gamma z)}\left(\frac{\Delta k}{2\gamma g}\right)\right| \ll 2gq(\nu), \tag{55}$$

where the function $q(\nu)$ is defined as

$$q(\nu) = (1 + \nu^2)^{1/2}(\bar{G}(Z_m(\nu)) + \nu^2). \tag{56}$$

Equation ([55](#)) is the required adiabaticity condition that we will use to determine AFC apodization profiles. The right hand side is a function only of ν, and hence of Δk_1 and g. It is interesting to note that, if we define a new propagation coordinate $\Xi = \int_{z_i}^{z} \sqrt{(2\gamma g(z'))^2 + \Delta k_1(z')^2}\,dz'$, then Eq. ([55](#)) can be expressed in an intuitive, purely geometrical form:

$$\left| \frac{d\theta_\parallel}{d\Xi} \right| \ll \frac{k_\parallel}{k_\perp}. \tag{57}$$

The form of Ξ arises from Eq. ([46](#)): the rate of change of $\mathbf{W}_m$ has an overall scaling with $|\nabla H| = \sqrt{(\gamma g)^2 + (\Delta k/2)^2}$.

We have also found that the fidelity of Eq. ([55](#)) is consistent with the values of the output pump depletion predicted by numerical simulations of the CWEs for well-apodized gratings operating in the highly nonlinear, highly saturated regime, as a function of the coupling factor $\lambda_R = \gamma^2/|\Delta k'|$ that we defined in Subsection [6.C](#). Such consistency helps to support the use of Eq. ([55](#)) as an adiabaticity criterion for constructing apodization profiles and for estimating how slow the chirp must be in order for adiabatic following to occur.

Further insight can be gained by considering the region around $|\nu| \approx 1$. In the undepleted-pump limit (in which adiabatic following does not occur), the signal is amplified in the region where $|\nu| < 1$ [1]. Since this limit can be described accurately by the complex WKB method, the points $|\nu| = 1$ are referred to as turning points. For small signal input compared to the pump (small ρ), the turning point closest to the input side of the grating is also an important point in the adiabatic following process: as K_{ip} is increased toward unity ($\rho \to 0$), the ratio $k_\parallel/k_\perp \to 0$ near this turning point, and hence, in order to maintain adiabaticity, the chirp rate must be very slow, based on Eq. ([57](#)). Physically, the signal must experience a large enough gain to begin depleting the pump over a small region near $|\nu| = 1$ in order to follow the eigenmode. The geometrical explanation for this requirement, provided by Eq. ([57](#)), is that the rate at which the eigenmode is swept in the X–Z plane, and hence the required value of Y, scales with $k_\parallel^{-1}$, while the deviation of the angle $\theta_\perp$ from zero scales (for a given value of Y) with $k_\perp$.

B. AFC Apodization Procedure

We will design apodization profiles such that adiabaticity is maintained, as in previous sections. As before, we also assume that there is a known nominal grating profile to which we append apodization regions. For the reasons discussed in Subsection [4.D](#), we consider NLCA and not DCA or DDA, and therefore assume $g = 1$. If a range of spectral components are present, then ν and $\mathbf{W}_m$ depend on both frequency and position. Based on Eq. ([55](#)) and assuming $g = 1$, we can obtain the following equation for the grating chirp rate within the apodization regions:

$$\left| \frac{dK_g}{dz} \right| = 2\epsilon\gamma^2 \min_{\omega}[q(\nu(z,\omega))], \tag{58}$$

where $\nu(z,\omega) = [\Delta k_0(\omega) - K_g(z)]/(2\gamma(\omega))$ is defined in Eq. ([33](#)), $q(\nu)$ is defined in Eq. ([56](#)), and minimization is performed over the spectral range of interest. When $q(\nu)$ is small,
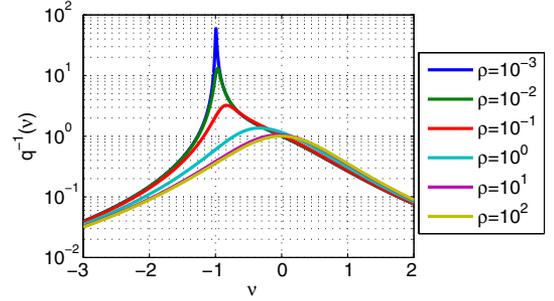

Fig. 7. $q(\nu)^{-1}$ [q defined in Eq. ([56](#)), ν defined in Eq. ([33](#))], shown for several values of ρ, assuming a positively chirped grating. For small ρ, the maximum of q^{-1} occurs near the first turning point ($|\nu| = 1$) and diverges as $\rho \to 0$.

a slow grating chirp rate is required. We show in Fig. [7](#) the form of $q(\nu)^{-1}$ for several values of ρ: for small ρ, the minimum of q becomes very small, necessitating a very slow chirp rate.

Based on Fig. [7](#) and for a positive QPM chirp rate, the minimum of q is between $\nu = -1$ (obtained for the high-gain OPA limit) and $\nu = 0$ (for the strong-signal, weak-pump DFG limit). Consider positions z for which $\nu(z,\omega)$ is outside of this interval at the edges of the nominal grating profile for all frequencies ω of interest. At these positions, $q(\nu)$ is smallest for the spectral component(s) for which $|\nu|$ is smallest. The apodization regions will begin at points for which this condition holds.

In this section, we will use subscripts $-$ and $+$ to denote the input and output apodization regions, respectively. For a given value of ϵ, we wish to find apodization boundaries $z_{i,\pm}$ for which $\nu(z_{i,\pm},\omega)$ lies outside the interval described above for all ω in the spectral range of interest, and for which Eq. ([58](#)) is satisfied for the nominal grating profile. The spectral components for which $|\nu|$ is smallest at these apodization boundaries are denoted $\omega_\pm$, and hence satisfy $|\nu(z_{i,\pm},\omega_\pm)| = \min_\omega(|\nu(z_{i,\pm}),\omega)|$. The corresponding values of ν are given by $\nu_{i,\pm} = \nu(z_{i,\pm},\omega_\pm)$. Thus for $z = z_{i,\pm}$ and $K_g(z) = K_{\mathrm{nom}}(z)$, Eq. ([58](#)) is satisfied, and the relevant frequency is $\omega = \omega_\pm$.

We now introduce position-dependent but frequency-independent variables derived from ν according to

$$\nu_\pm(z) = \frac{\Delta k_0(\omega_\pm) - K_g(z)}{2\gamma g(z)}, \tag{59}$$

that satisfy $\nu_\pm(z_{i,\pm}) = \nu_{i,\pm}$. $\nu_\pm(z)$ are substituted into Eq. ([58](#)) to yield a differential equation,

$$\left| \frac{d\nu_\pm}{dz} \right| = \epsilon\gamma q(\nu_\pm), \tag{60}$$

that can be solved straightforwardly by numerically integrating with respect to $\nu_\pm$. Given $\nu_\pm(z)$, the grating profile $K_g(z)$ is determined via Eq. ([59](#)).

C. AFC Apodization Example

In this subsection, we apply the procedure described in Subsection [7.B](#) to construct an apodization profile for an AFC device. We choose $\rho = 0.2$, corresponding to a case

with a strong pump and moderate-strength signal, in order to illustrate that AFC, and our apodization approach, is effective even when substantial signal gain occurs. We choose a nominally linear grating chirp profile, with $\lambda_R = \gamma^2/|\Delta k'| = 5$, and select $\epsilon = 1/(2\lambda_R)$ so that the apodization regions are 'as adiabatic' as the nominal profile. As in previous sections, we select a nominal grating profile sufficient to support a bandwidth from 1450 to 1650 nm with a 1064 nm pump wavelength, assume a MgO:LiNbO$_3$ device and, in this case, fix $\gamma = \gamma_0 = 3.5 \times 10^3$. The apodization regions are found by solving Eq. (60), as described above, for chosen initial and final values $K_g(z_i)$ and $K_g(z_f)$, respectively.

The simulation is shown in Fig. 8. The pump depletion as a function of signal wavelength is shown in Fig. 8(a) for apodized (NLCA) and unapodized cases. For the apodized case, a very high pump depletion is maintained over the entire target spectrum. In the unapodized case, only a moderate efficiency is predicted, and there are substantial fluctuations in efficiency over the target spectrum. The apodized grating profile is shown in Fig. 8(b), indicating that the apodization regions take up only a relatively small fraction of the device's total length, as in our preceding examples. In practice, achieving high conversion efficiencies will involve a trade-off involving achievable input parameters, amplification of quantum noise, and suppression of unwanted parasitic effects, such as pump SHG [42]. In particular, to achieve a high conversion efficiency at moderate coupling factor λ_R, the ratio of signal and pump photon fluxes at the input the device, ρ, should not be too small. This trade-off between λ_R, ρ, and efficiency was considered in [7].
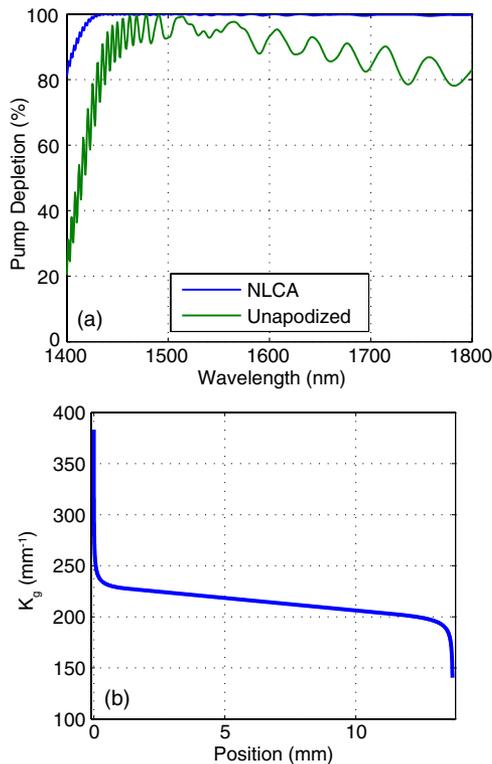

Fig. 8.   AFC apodization example, with $\rho = 0.2$ and $\lambda_R = 5$. The remaining parameters are given in the text. (a) Pump depletion versus signal wavelength for apodized and unapodized cases, (b) grating profile $K_g(z)$.

8. DISCUSSION AND CONCLUSIONS

A. Summary

In this paper, we have considered apodization of chirped QPM gratings in detail. Without apodization, such devices exhibit a substantial ripple in spectral amplitude and phase, which is highly disadvantageous to many applications.

We studied most of the main operation regimes of interest. These regimes include the linear regimes of DFG, SFG, SHG, OR, etc., in which only the generated wave is changing substantially; the case of high-gain OPA, in which there is only minor pump depletion; and the case of AFC, in which all of the waves change substantially but remain close to the position-dependent and frequency-dependent nonlinear eigenmode of the TWM process throughout the device. In each of these cases, the structure of the eigenmodes of the unchirped QPM interaction play an important role. We showed, for all of these operating regimes, how apodization profiles can be constructed systematically in order to reach performance limited only by inherent discretization associated with the QPM grating structure. We did not consider SHG with non-negligible pump depletion, but the geometrical analysis of Sections 6 and 7 could be applied to that case as well, and hence we expect adiabatic SHG to occur in properly apodized QPM gratings. We will consider this SHG case and its applications in future work.

We considered different types of apodization, including nonlinear chirp apodization (NLCA), QPM duty cycle apodization (DCA), and deleted-domain apodization (DDA). In principle, comparable performance is achieved by NLCA and DCA. However, DCA is challenging in terms of QPM fabrication since all the domains typically must be created in a single poling event, and the dynamics governing the domain sizes are complicated and difficult to control. Furthermore, DCA typically requires a somewhat larger apodization region. The DDA approach exhibits substantially reduced performance, that we showed for the cases of DFG and OPA. While DDA is well suited to long, unchirped QPM devices, it exhibits poorer performance for chirped QPM devices due to the broad spatial frequency bandwidth of the grating. For the above reasons, we believe that NLCA will usually be the best method of apodizing all types of chirped QPM devices. This conclusion is consistent with our experimental findings [10]. Furthermore, NLCA has the potential to be the least susceptible to photorefractive damage related issues due to its 50% duty cycle [31–33].

In designing apodization profiles, we made sure to maintain the nominal or desired profile of the device for the spectral range of interest. This approach means that nominal grating profiles supporting favorable properties, such as a broad bandwidth or an engineered group delay spectrum, can first be designed [4] and then apodization regions can be appended systematically in order to achieve the desired performance with optimal fidelity. For the case of AFC, this involved constructing a systematic approach to visualizing such devices based on the elegant geometrical description of TWM processes introduced in [28]. Our analysis showed how to both understand and design general AFC devices, even when substantial signal gain and pump depletion are involved simultaneously. The geometrical description also shows clearly why it is difficult to achieve high gain and efficiency simultaneously in AFC devices.

When simulating the QPM designs presented, we used full nonlinear CWEs of the actual discrete QPM grating structures,

without restricting our analysis to the first order QPM approximation. These simulations thus established that the first order QPM approximation is indeed very accurate, even for the more complicated cases of OPA and AFC.

B. QPM Fabrication Considerations

In simulations not shown, we tested the dependence of the devices on the fabrication resolution by "snapping" all of the domain boundaries to a fixed grid of a chosen spacing. We found for the examples presented here (center period ≈ 30 μm) that even for a grid spacing of up to 1 μm, there is almost no change in device performance. This result means that the typical fabrication grids of 0.1 μm used in lithographic poling are more than sufficient, even for devices with a shorter range of QPM periods. It should be noted, however, that unavoidable random duty cycle (RDC) errors in the QPM grating can enhance the efficiency of unwanted parasitic effects and should not be ignored [42,43].

We emphasize that our procedure for constructing the QPM grating from a designed phase and duty cycle profile, given in Eq. (3), in general makes the device insensitive to the discrete nature of the QPM domains, since it ensures that the higher spatial frequencies of the grating are always separated by an integer number of "carrier frequencies" of the grating, and therefore have minimal overlap with the first Fourier order.

For fabricating apodized gratings, it is important to note that there is typically some uncertainty in the actual crystal length due to variations in the amount of material lost during polishing. Unless care is taken, these fluctuations could end up removing the most highly phase mismatched parts of the device, since the grating period is increased very rapidly over a short distance at the edges of the grating. One way to resolve this issue is by having an unpoled gap between the ends of the crystal and the ends of the designed grating. However, such unpoled regions will introduce an additional spectral ripple and can be very disadvantageous in the context of photore-fractive effects, as mentioned above [31–33]. Instead, one could make simple modifications to the apodization proce-dures presented here to ensure a slow chirp rate at the edges of the grating (i.e., the chirp rate is first increased rapidly, then decreased again near the edges of the grating, while still sat-isfying the required inequalities and maintaining a monotonic $K_g(z)$ profile). In this way, the range of spatial frequencies present on the device can be made insensitive to the polishing process.

If there is a single poling event, and if it can be assumed that the domains are independent of each other and their position on the wafer, then the local duty cycle will be determined by the local period. This period dependence of the duty cycle could, in principle, be accounted for in the design, at least to the extent that it is known. One could express the duty cycle D as a function of grating k-vector K_g, and substitute the resulting form $g(K_g(z))$ into the inequalities we discussed. Since these subtleties are determined mainly by QPM fabrica-tion issues rather than QPM device physics, we did not discuss them in detail here, but they could be accounted for with minor extensions of the methods presented.

C. Spatiotemporal Apodization

In this paper, we have not considered solitons and solitary waves either in the spatial or temporal domain [44]. AFC offers the potential for high conversion efficiency across a nonuniform spatial and temporal profile, but parasitic processes associated with overdriving the center of the beams present a potential limitation of this approach. There-fore, some applications could benefit significantly from approaches, such as adiabatic soliton evolution [45]. Since many of our results draw on concepts of local eigenmodes, they are likely to apply to such interactions as well, but analy-sis of these cases is beyond the scope of this paper. Instead, based on practical considerations, we have used plane wave models in order to obtain results that are not reliant on or strongly constrained by diffractive effects. Nonetheless, care should be taken in order to avoid excessive excitation of three-wave modulation instabilities that can be associated with three-wave nonlinear eigenmodes [44]; these and other spatial effects relevant to the design of highly nonlinear chirped QPM devices will be the subject of future work.

An alternative way of viewing such spatiotemporal effects is as a means of QPM apodization. That is, to have beams or pulses that are initially nonoverlapping in space or time, re-spectively, and fully walk across each other's spatial or tem-poral profiles as they propagate through the nonlinear crystal. In this way, components generated by mixing between these two beams/pulses will be apodized, since the interaction is smoothly turned on and off via walk-off. In principle, one could also use beams that diffract strongly within the crystal so that the intensities are low at the input and output ends and increase slowly toward the focus.

A drawback of such schemes is that they could strongly influence the desired interaction, or change it entirely. We have found, for example, that excessive group velocity walk-off can lead to additional spectral ripples in nonlinear chirped QPM interactions, such as AFC. Furthermore, walk-off based schemes will necessitate significantly longer crys-tals at a given optical intensity, and hence will exacerbate any unwanted parasitic effects that scale with the device length. Therefore, while spatiotemporal apodization schemes may find use in some contexts, we have not considered them in detail here.

One case that is of interest and can be suitably engineered is waveguide-coupling-based apodization, as discussed in [24]. Having the two input waves initially in different waveguides and then adiabatically coupled to each other is analogous, in this context, to a smooth modulation of $g(z)$ from ≈ 0 to ≈ 1, and therefore may be of continued interest for wave-guide-based apodization, particularly since DDA, the pre-ferred approach from [24] for apodizing periodic gratings, is less suited to chirped QPM devices. For example, one could imagine combining a NLCA scheme with a waveguide-coupling-based amplitude apodization to further suppress spectral ripples beyond the limits imposed here by the discrete nature of the QPM grating.

D. Conclusions

The difficulty in fabricating duty-cycle-modulated QPM gra-tings, combined with the high versatility of chirped QPM gra-tings, means that such devices will continue to play a central role in QPM technology. In addition to efficient frequency conversion, our apodization techniques could be applied to efficiently excite nonlinear eigenmodes at a chosen finite phase mismatch; for example, in the context of cascaded $\chi^{(2)}$

interactions. The systematic study of device operation and apodization we have presented here should therefore be of critical importance to the continued development of QPM technology and its applications.

ACKNOWLEDGMENT

REFERENCES

1. M. Charbonneau-Lefort, B. Afeyan, and M. M. Fejer, "Optical parametric amplifiers using chirped quasi-phase-matching gratings I: practical design formulas," J. Opt. Soc. Am. B **25**, 463–480 (2008).
2. G. Imeshev, M. M. Fejer, A. Galvanauskas, and D. Harter, "Pulse shaping by difference-frequency mixing with quasi-phase-matching gratings," J. Opt. Soc. Am. B **18**, 534–539 (2001).
3. G. Imeshev, M. A. Arbore, M. M. Fejer, A. Galvanauskas, M. Fermann, and D. Harter, "Ultrashort-pulse second-harmonic generation with longitudinally nonuniform quasi-phase-matching gratings: pulse compression and shaping," J. Opt. Soc. Am. B **17**, 304–318 (2000).
4. M. Charbonneau-Lefort, M. M. Fejer, and B. Afeyan, "Tandem chirped quasi-phase-matching grating optical parametric amplifier design for simultaneous group delay and gain control," Opt. Lett. **30**, 634–636 (2005).
5. M. Charbonneau-Lefort, B. Afeyan, and M. M. Fejer, "Competing collinear and noncollinear interactions in chirped quasi-phase-matched optical parametric amplifiers," J. Opt. Soc. Am. B **25**, 1402–1413 (2008).
6. L. Gallmann, G. Steinmeyer, U. Keller, G. Imeshev, M. M. Fejer, and J. Meyn, "Generation of sub-6 fs blue pulses by frequency doubling with quasi-phase-matching gratings," Opt. Lett. **26**, 614–616 (2001).
7. C. R. Phillips and M. M. Fejer, "Efficiency and phase of optical parametric amplification in chirped quasi-phase-matched gratings," Opt. Lett. **35**, 3093–3095 (2010).
8. H. Suchowski, V. Prabhudesai, D. Oron, A. Arie, and Y. Silberberg, "Robust adiabatic sum frequency conversion," Opt. Express **17**, 12731–12740 (2009).
9. C. Heese, C. R. Phillips, B. W. Mayer, L. Gallmann, M. M. Fejer, and U. Keller, "75 MW few-cycle mid-infrared pulses from a collinear apodized APPLN-based OPCPA," Opt. Express **20**, 26888–26894 (2012).
10. C. Heese, C. R. Phillips, L. Gallmann, M. M. Fejer, and U. Keller, "Role of apodization in optical parametric amplifiers based on aperiodic quasi-phasematching gratings," Opt. Express **20**, 18066–18071 (2012).
11. C. Heese, C. R. Phillips, L. Gallmann, M. M. Fejer, and U. Keller, "Ultrabroadband, highly flexible amplifier for ultrashort midinfrared laser pulses based on aperiodically poled Mg:LiNbO₃," Opt. Lett. **35**, 2340–2342 (2010).
12. C. R. Phillips, L. Gallmann, and M. M. Fejer, "Design of quasiphasematching gratings via convex optimization," Opt. Express **21**, 10139–10159 (2013).
13. C. Langrock, M. M. Fejer, I. Hartl, and M. E. Fermann, "Generation of octave-spanning spectra inside reverse-proton-exchanged periodically poled lithium niobate waveguides," Opt. Lett. **32**, 2478–2480 (2007).
14. C. R. Phillips, C. Langrock, J. S. Pelc, M. M. Fejer, I. Hartl, and M. E. Fermann, "Supercontinuum generation in quasi-phase-matched waveguides," Opt. Express **19**, 18754–18773 (2011).
15. C. R. Phillips, C. Langrock, J. S. Pelc, M. M. Fejer, J. Jiang, M. E. Fermann, and I. Hartl, "Supercontinuum generation in quasi-phase-matched LiNbO₃ waveguide pumped by a Tm-doped fiber laser system," Opt. Lett. **36**, 3912–3914 (2011).
16. M. Conforti, F. Baronio, and C. De Angelis, "Nonlinear envelope equation for broadband optical pulses in quadratic media," Phys. Rev. A **81**, 053841 (2010).
17. K. A. Tillman, D. T. Reid, D. Artigas, J. Hellström, V. Pasiskevicius, and F. Laurell, "Low-threshold femtosecond optical parametric oscillator based on chirped-pulse frequency conversion," Opt. Lett. **28**, 543–545 (2003).
18. K. A. Tillman and D. T. Reid, "Monolithic optical parametric oscillator using chirped quasi-phase matching," Opt. Lett. **32**, 1548–1550 (2007).
19. C. R. Phillips and M. M. Fejer, "Adiabatic optical parametric oscillators: steady-state and dynamical behavior," Opt. Express **20**, 2466–2482 (2012).
20. C. R. Phillips and M. M. Fejer, "Stability of the singly resonant optical parametric oscillator," J. Opt. Soc. Am. B **27**, 2687–2699 (2010).
21. T. W. Neely, L. Nugent-Glandorf, F. Adler, and S. A. Diddams, "Broadband mid-infrared frequency upconversion and spectroscopy with an aperiodically poled LiNbO₃ waveguide," Opt. Lett. **37**, 4332–4334 (2012).
22. Y. Deng, A. Schwarz, H. Fattahi, M. Ueffing, X. Gu, M. Ossiander, T. Metzger, V. Pervak, H. Ishizuki, T. Taira, T. Kobayashi, G. Marcus, F. Krausz, R. Kienberger, and N. Karpowicz, "Carrier-envelope-phase-stable, 1.2 mJ, 1.5 cycle laserpulses at 2.1 μm," Opt. Lett. **37**, 4973–4975 (2012).
23. V. J. Hernandez, C. V. Bennett, B. D. Moran, A. D. Drobshoff, D. Chang, C. Langrock, M. M. Fejer, and M. Ibsen, "104 MHz rate single-shot recording with subpicosecond resolution using temporal imaging," Opt. Express **21**, 196–203 (2013).
24. J. Huang, X. P. Xie, C. Langrock, R. V. Roussev, D. S. Hum, and M. M. Fejer, "Amplitude modulation and apodization of quasi-phase-matched interactions," Opt. Lett. **31**, 604–606 (2006).
25. T. Umeki, M. Asobe, Y. Nishida, O. Tadanaga, K. Magari, T. Yanagawa, and H. Suzuki, "Widely tunable 3.4 μm band difference frequency generation using apodized $\chi^{(2)}$ grating," Opt. Lett. **32**, 1129–1131 (2007).
26. A. Tehranchi and R. Kashyap, "Design of novel unapodized and apodized step-chirped quasi-phase matched gratings for broadband frequency converters based on second-harmonic generation," J. Lightwave Technol. **26**, 343–349 (2008).
27. A. Bostani, A. Tehranchi, and R. Kashyap, "Engineering of effective second-order nonlinearity in uniform and chirped gratings," J. Opt. Soc. Am. B **29**, 2929–2934 (2012).
28. G. G. Luther, M. S. Alber, J. E. Marsden, and J. M. Robbins, "Geometric analysis of optical frequency conversion and its control in quadratic nonlinear media," J. Opt. Soc. Am. B **17**, 932–941 (2000).
29. R. W. Boyd, *Nonlinear Optics*, 3rd ed. (Academic, 2008).
30. G. D. Miller, "Periodically poled lithium niobate: modeling, fabrication, and nonlinear-optical performance," Ph.D. dissertation (Stanford University, 1998).
31. M. Taya, M. C. Bashaw, and M. M. Fejer, "Photorefractive effects in periodically poled ferroelectrics," Opt. Lett. **21**, 857–859 (1996).
32. J. R. Schwesyg, M. Falk, C. R. Phillips, D. H. Jundt, K. Buse, and M. M. Fejer, "Pyroelectrically induced photorefractive damage in magnesium-doped lithium niobate crystals," J. Opt. Soc. Am. B **28**, 1973–1987 (2011).
33. C. R. Phillips, J. S. Pelc, and M. M. Fejer, "Continuous wave monolithic quasi-phase-matched optical parametric oscillator in periodically poled lithium niobate," Opt. Lett. **36**, 2973–2975 (2011).
34. C. M. Bender and S. A. Orszag, *Advanced Mathematical Methods for Scientists and Engineers I: Asymptotic Methods and Perturbation Theory*, Vol. **1** (Springer, 1999).
35. G. I. Stegeman, D. J. Hagan, and L. Torner, "$\chi^{(2)}$ cascading phenomena and their applications to all-optical signal processing, mode-locking, pulse compression and solitons," Opt. Quantum Electron. **28**, 1691–1740 (1996).
36. H. Steigerwald, F. Luedtke, and K. Buse, "Ultraviolet light assisted periodic poling of near-stoichiometric, magnesium-doped lithium niobate crystals," Appl. Phys. Lett. **94**, 032906 (2009).
37. C. Conti, S. Trillo, P. Di Trapani, J. Kilius, A. Bramati, S. Minardi, W. Chinaglia, and G. Valiulis, "Effective lensing effects in parametric frequency conversion," J. Opt. Soc. Am. B **19**, 852–857 (2002).
38. R. B. White, *Asymptotic Analysis of Differential Equations* (World Scientific, 2005).

39. J. A. Armstrong, N. Bloembergen, J. Ducuing, and P. S. Pershan, "Interactions between light waves in a nonlinear dielectric," Phys. Rev. **127**, 1918–1939 (1962).

40. M. D. Crisp, "Adiabatic-Following approximation," Phys. Rev. A **8**, 2128–2135 (1973).

41. R. Goldman, "Curvature formulas for implicit curves and surfaces," Comput. Aided Geom. Des. **22**, 632–658 (2005).

42. C. R. Phillips, J. S. Pelc, and M. M. Fejer, "Parametric processes in quasi-phasematching gratings with random duty cycle errors," J. Opt. Soc. Am. B **30**, 982–993 (2013).

43. J. S. Pelc, C. R. Phillips, D. Chang, C. Langrock, and M. M. Fejer, "Efficiency pedestal in quasi-phase-matching devices with random duty-cycle errors," Opt. Lett. **36**, 864–866 (2011).

44. A. V. Buryak, P. D. Trapani, D. V. Skryabin, and S. Trillo, "Optical solitons due to quadratic nonlinearities: from basic physics to futuristic applications," Phys. Rep. **370**, 63–235 (2002).

45. S. Ashihara, J. Nishina, T. Shimura, and K. Kuroda, "Soliton compression of femtosecond pulses in quadratic media," J. Opt. Soc. Am. B **19**, 2505–2510 (2002).

g) G.L. Shentu, J.S. Pelc, X.D. Wang, Q.C. Sun, M.Y. Zheng, M.M. Fejer, Q. Zhang, J.W. Pan, "Ultralow noise up-conversion detector and spectrometer for the telecom band," *Opt. Express* **21**, pp. 13986-13991 (June 2013).

Ultralow noise up-conversion detector and spectrometer for the telecom band

Guo-Liang Shentu,[1] Jason S. Pelc,[2] Xiao-Dong Wang,[3] Qi-Chao Sun,[1] Ming-Yang Zheng,[1] M. M. Fejer,[2] Qiang Zhang,[1] and Jian-Wei Pan[1]

[1]*Shanghai Branch, National Laboratory for Physical Sciences at Microscale and Department of Modern Physics, University of Science and Technology of China, Shanghai, 201315, China*
[2]*Edward L. Ginzton Laboratory, Stanford University, Stanford, California 94305, USA*
[3]*College of Physics and Electronic Engineering of Northwest Normal University, Lanzhou, 730070, China*
[*]*qiangzh@ustc.edu.cn*

Abstract: We demonstrate up-conversion single-photon detection for the 1550-nm telecommunications band using a PPLN waveguide, long-wavelength pump, and narrowband filtering using a volume Bragg grating. We achieve total-system detection efficiency of around 30% with noise at the dark-count level of a Silicon APD. Based on the new detector, a single-pixel up-conversion infrared spectrometer with a noise equivalent power of -142 dBm Hz$^{-1/2}$ was demonstrated, which was as good as a liquid nitrogen cooled CCD camera.

© 2013 Optical Society of America

OCIS codes: (190.7220) Upconversion; (190.4410) Nonlinear optics, parametric processes; (270.5570) Quantum detectors.

References and links

1. R. H. Hadfield, "Single-photon detectors for optical quantum information applications," Nat. Photonics **3**(12), 696–705 (2009).
2. H. Takesue, S. W. Nam, Q. Zhang, R. H. Hadfield, T. Honjo, K. Tamaki, and Y. Yamamoto, "Quantum key distribution over a 40-dB channel loss using superconducting single-photon detectors," Nat. Photonics **1**(6), 343–348 (2007).
3. D. Stucki, N. Walenta, F. Vannel, R. T. Thew, N. Gisin, H. Zbinden, S. Gray, C. R. Towery, and S. Ten, "High rate, long-distance quantum key distribution over 250 km of ultra-low loss fibres," New J. Phys. **11**(7), 075003 (2009).
4. Y. Liu, T. Y. Chen, J. Wang, W. Q. Cai, X. Wan, L. K. Chen, J. H. Wang, S. B. Liu, H. Liang, L. Yang, C. Z. Peng, K. Chen, Z. B. Chen, and J. W. Pan, "Decoy-state quantum key distribution with polarized photons over 200 km," Opt. Express **18**(8), 8587–8594 (2010).
5. S. Wang, W. Chen, J. F. Guo, Z. Q. Yin, H. W. Li, Z. Zhou, G. C. Guo, and Z. F. Han, "2 GHz clock quantum key distribution over 260 km of standard telecom fiber," Opt. Lett. **37**(6), 1008–1010 (2012).
6. A. R. Dixon, Z. L. Yuan, J. F. Dynesl, A. W. Sharpe, and A. J. Shields, "Gigahertz decoy QKD with 1Mbit/s secure key rate," Opt. Express **16**, 18790–18979 (2008).
7. Q. Zhang, H. Takesue, T. Honjo, K. Wen, T. Hirohata, M. Suyama, Y. Takiguchi, H. Kamada, Y. Tokura, O. Tadanaga, Y. Nishida, M. Asobe, and Y. Yamamoto, "Megabits secure key rate quantum key distribution," New J. Phys. **11**(4), 045010 (2009).
8. N. Namekata, H. Takesue, T. Honjo, Y. Tokura, and S. Inoue, "High-rate quantum key distribution over 100 km using ultra-low-noise, 2-GHz sinusoidally gated InGaAs/InP avalanche photodiodes," Opt. Express **19**(11), 10632–10639 (2011).
9. ID Quantique Inc, Geneva, Switzerland, "id100ID210/ID220 SERIES SELECTION GUIDE," http://www.idquantique.com/images/stories/PDF/id220-single-photon-counter/id220-specs.pdf.
10. P. Kumar, "Quantum frequency conversion," Opt. Lett. **15**(24), 1476–1478 (1990).
11. A. P. Vandevender and P. G. Kwiat, "High efficiency single photon detection via frequency up-conversion," J. Mod. Opt. **51**, 1433–1445 (2004).
12. C. Langrock, E. Diamanti, R. V. Roussev, Y. Yamamoto, M. M. Fejer, and H. Takesue, "Highly efficient single-photon detection at communication wavelengths by use of upconversion in reverse-proton-exchanged periodically poled LiNbO$_3$ waveguides," Opt. Lett. **30**(13), 1725–1727 (2005).
13. M. A. Albota and F. N. C. Wong, "Efficient single-photon counting at 1.55 microm by means of frequency upconversion," Opt. Lett. **29**(13), 1449–1451 (2004).
14. R. T. Thew, H. Zbinden, and N. Gisin, "Tunable upconversion photon detector," Appl. Phys. Lett. **93**(7), 071104 (2008).

15. H. Kamada, M. Asobe, T. Honjo, H. Takesue, Y. Tokura, Y. Nishida, O. Tadanaga, and H. Miyazawa, "Efficient and low-noise single-photon detection in 1550 nm communication band by frequency upconversion in periodically poled LiNbO3 waveguides," Opt. Lett. **33**(7), 639–641 (2008).

16. J. S. Pelc, L. Ma, C. R. Phillips, Q. Zhang, C. Langrock, O. Slattery, X. Tang, and M. M. Fejer, "Long-wavelength-pumped upconversion single-photon detector at 1550 nm: performance and noise analysis," Opt. Express **19**(22), 21445–21456 (2011).

17. H. Dong, H. Pan, L. Yao, E. Wu, and H. Zeng, "Efficient single-photon frequency upconversion at 1.06 μm with ultralow background counts," Appl. Phys. Lett. **93**(7), 071101 (2008).

18. J. S. Pelc, P. S. Kuo, O. Slattery, L. Ma, X. Tang, and M. M. Fejer, "Dual-channel, single-photon upconversion detector at 1.3 μm," Opt. Express **20**(17), 19075–19087 (2012).

19. P. S. Kuo, J. S. Pelc, O. Slattery, Y. S. Kim, M. M. Fejer, and X. Tang, "Reducing noise in single-photon-level frequency conversion," Opt. Express **38**, 1310–1312 (2013).

20. Q. Zhang, C. Langrock, M. M. Fejer, and Y. Yamamoto, "Waveguide-based single-pixel up-conversion infrared spectrometer," Opt. Express **16**(24), 19557–19561 (2008).

21. L. Ma, O. Slattery, and X. Tang, "Experimental study of high sensitivity infrared spectrometer with waveguide-based up-conversion detector," Opt. Express **17**(16), 14395–14404 (2009).

22. M. T. Rakher, L. Ma, O. Slattery, X. Tang, and K. Srinivasan, "Quantum transduction of telecommunications-band single photons from a quantum dot by frequency upconversion," Nat. Photonics **4**(11), 786–791 (2010).

23. Princeton Instruments, "Spectroscopy Cameras PyLoN," *http://www.piacton.com/Uploads/Princeton/Documents/Datasheets/Princeton_Instruments_PyLoN-IR_RevN2_9_23_12.pdf*.

24. All pump power mentioned below is measured by a power meter after the DM.

25. P. A. Jansson, *Deconvolution of Images and Spectra* (Academic Press, 1997), Chap. 14.

26. L. Ma, O. Slattery, and X. Tang, "Single photon frequency up-conversion and its applications," Phys. Rep. **521**(2), 69–94 (2012).

27. H. Takesue, "Erasing distinguishability using quantum frequency up-conversion," Phys. Rev. Lett. **101**(17), 173901 (2008).

28. R. Ikuta, Y. Kusaka, T. Kitano, H. Kato, T. Yamamoto, M. Koashi, and N. Imoto, "Wide-band quantum interface for visible-to-telecommunication wavelength conversion," Nat Commun **2**, 1544 (2011).

29. S. Zaske, A. Lenhard, C. A. Keßler, J. Kettler, C. Hepp, C. Arend, R. Albrecht, W. M. Schulz, M. Jetter, P. Michler, and C. Becher, "Visible-to-telecom quantum frequency conversion of light from a single quantum emitter," Phys. Rev. Lett. **109**(14), 147404 (2012).

30. J. S. Pelc, L. Yu, K. De Greve, P. L. McMahon, C. M. Natarajan, V. Esfandyarpour, S. Maier, C. Schneider, M. Kamp, S. Höfling, R. H. Hadfield, A. Forchel, Y. Yamamoto, and M. M. Fejer, "Downconversion quantum interface for a single quantum dot spin and 1550-nm single-photon channel," Opt. Express **20**(25), 27510–27519 (2012).

31. S. Tanzilli, W. Tittel, M. Halder, O. Alibart, P. Baldi, N. Gisin, and H. Zbinden, "A photonic quantum information interface," Nature **437**(7055), 116–120 (2005).

1. Introduction

Single-photon detectors (SPD) operating in the 1.55-μm telecom band are a core part of quantum communication over optical fiber [1]. Currently, SPD performance limits the transmission distance and key rate of fiber based quantum key distribution (QKD) [2–8].

Current telecom band commercial SPDs based on InGaAs/InP avalanche photodiodes (APDs) suffer from low efficiency about 10% and large dark-count rate of 10^3 count per second (cps) [9]. In contrast, the efficiency of Silicon APD working in the visible to NIR windows is up to 65% and the dark count rate is can be lower than 100 cps. Up-conversion detectors [10–14] utilizing sum-frequency generation (SFG) in periodically poled lithium niobate (PPLN) waveguide or bulk crystals can convert the telecom-band photons into the near infrared window and then detect them with a Silicon APD. The detection efficiency of PPLN waveguide-based up-conversion detectors can be higher than 40% [12]. However, for early implementations pumped at short pump wavelengths, the noise count rate of the detector reached 10^5 cps [12, 13]. Monochromator based filtering has been exploited to decrease the noise. However, due to the low throughput of the monochromator, the detection efficiency also reduced dramatically [15].

Noise in up-conversion detectors mainly comes from spontaneous parametric down conversion (SPDC) and spontaneous Raman scattering (SRS) when the strong pump goes through the waveguide. A recent experiment demonstrated that a long wave pump can suppress both spontaneous processes [16,17] without dramatically reducing the detection

efficiency. Here, we combine the long wave pump and a high efficiency narrow-band filter, volume Bragg grating (VBG) [18, 19].

Meanwhile, based on up-conversion detector, up-conversion spectrometer has been invented to measure the infrared spectrum, whereby the pump wavelength is tuned and the phase-matching acceptance bandwidth of the upconverter acts as a frequency selective element [20]. The spectrometer had a noise equivalent power (NEP) of −128 dBm Hz$^{-1/2}$ [21] and found an immediate application in testing quantum dot with a wavelength of 1.3 μm [22]. Based on our up-conversion detector, we improved the NEP by one order of magnitude due to noise reduction, i.e. −142 dBm Hz$^{-1/2}$, which is as good as the liquid nitrogen cooled CCD camera based spectrometer [23]. Furthermore, the narrow-band VBG helps to improve our spectrometer's resolution into 0.16 nm.

2. Upconversion detector

We fabricated PPLN waveguides via the reverse proton exchange technique. The waveguides are 52-mm long and are poled with a quasi-phase-matching (QPM) period of 19.6μm. The waveguides incorporated mode filters designed to match the mode size of SMF-28 optical fiber and were fiber pigtailed with coupling losses of approximately 0.7 dB, and had a total fiber-to-output-facet throughput of −1.5 dB for the telecom band signal. The waveguides were antireflection coated to avoid interference fringes and improve the system throughput.

A schematic of our experimental setup is shown in Fig. 1. We used a single longitudinal mode Thulium fiber laser (TDFL) and amplifier (TDFA) manufactured by AdValue Photonics (Tucson, AZ) as the pump source for this experiment. The laser amplifier emits an average power of approximately 800 mW with a wavelength of 1950 nm. The pump-laser power was controlled by adjusting the pump current of TDFA, and noise emission from the pump laser was blocked using a 1.55-μm/1.9-μm wavelength division multiplexer (WDM).
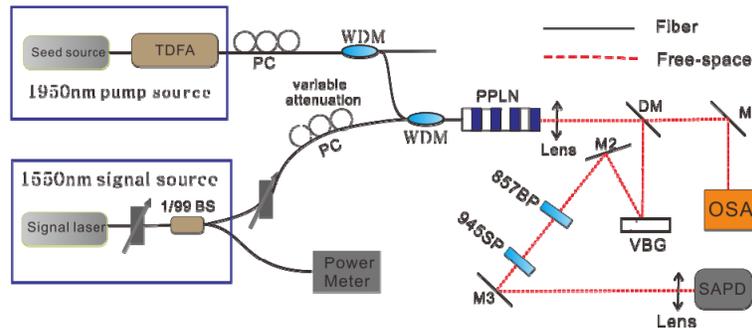

Fig. 1. Schematic of the noise-free up-conversion single photon detector. BS: beam splitter, M1-M3: mirrors.

A cw, single-frequency, tunable telecom-band external cavity diode laser (ECDL) provided the signal at a wavelength of 1.55 μm. We used a variable attenuator, a 1/99 tap coupler and a calibrated detector to monitor the input signal power. The signal was combined with the pump in another 1.55-μm/1.9-μm WDM and coupled into the PPLN waveguide through the fiber pigtail. The waveguide only supports TM-polarized light so the polarizations of both the pump and the signal are controlled by polarization controllers (PCs) respectively before entering the waveguide. A Peltier cooler based temperature-control system is used to keep the waveguide's temperature at 56°C to maintain the phase-matching condition.

The generated SFG photons are collected by an AR-coated objective lens, and are separated from the pump by a dichroic mirror (DM). The residual pump is transmitted through the DM and analyzed by an optical spectrum analyzer (OSA). A 945nm short pass filter (SPF) and a 857nm band pass filter (BPF) are used to block the second and higher order

harmonic of the pump. A VBG with a 95% reflection efficiency is exploited to further suppress the noise from SRS. In our setup, VBG filter's spectral bandwidth is 0.05 nm at a center wavelength tunable near 864nm (full width at half maximum), corresponding to a bandwidth of 0.16 nm at the signal wavelength, which is narrower than our waveguide's acceptance bandwidth of 0.5 nm, which helps to reduce the SRS noise. Finally, the SFG photons are collected and detected by a Silicon APD (SAPD), whose detection efficiency is up to 45% at 860 nm and dark count rate is 25 cps.

The experimental result is shown in Fig. 2(a). We tune the pump power by adjusting the variable attenuator and record the detection efficiency and noise count rates. When the pump power is set at 58 mW [24], the detection efficiency was 28.6%, with a noise count rate of 100 cps. When the pump power is set at 20 mW, the noise is reduced to to 25 cps, while the detection efficiency is still 15%. This performance is achieved by combining the long-wave pump and VBG narrow band filtering techniques. In order to show the contribution of each technique, we also measure the dark count and efficiency curve without VBG. We change the VBG with a prism, which is a standard configuration [12] and cannot reduce the SRS noise. The result is shown in Fig. 2(b).
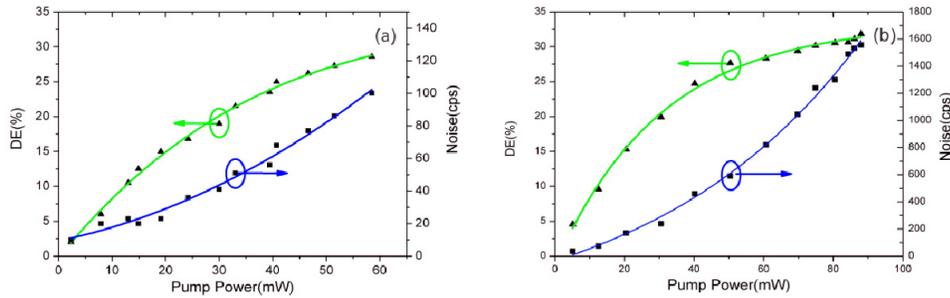
Fig. 2. The detection efficiency (green line, triangle) and noise count rate (blue line, square) versus pump power, which is measured just after the waveguide. (a) with VBG, (b) without VBG.

3. Spectrometer

Previous research utilized the PPLN waveguide's acceptance bandwidth as a filter in the frequency domain [20,21]. Scanning the pump wavelength, the center wavelength of this filter, allows us to trace out the spectrum of the signal light. In order to realize the up-conversion spectrometer, we slightly changed the setup in Fig. 1 by replacing the 1950 nm seed fiber laser with a 1.9-μm band tunable ECDL. By adjusting the grating inside the 1.9-μm band ECDL, the emission spectrum of pump could be scanned from 1920 nm to 1980 nm, and thus the spectral range of the up-conversion spectrometer is from 1532.9 nm to 1570.9 nm.

One of the advantages of our spectrometer is its low NEP ($NEP = \hbar \upsilon \sqrt{2D} / \eta$). Here, η represents detection efficiency and D represents dark count rate. In our experiment, we set the pump power at 30 mW and the detection efficiency, dark count rate and NEP are 20%, 60 Hz and −142 dBm, respectively.

In previous experiments, the resolution of the spectrometer is determined by the spectral acceptance of the PPLN waveguide [20,21]. Here, our spectrometer's resolution is decided by the VBG's spectral bandwidth for the signal wavelength, 0.16 nm. A point to note here is that the upconverted wavelength will change with different signal wavelength. For measurements of signals over total bandwidth greater than 3.09 nm, the angle of the VBG must be adjusted such that its reflection resonance tracks the changing upconverted wavelength. This can be achieved by mounting the VBG on a motorized rotation stage.

In order to test our up-conversion spectrometer, we used the light from a 1.55-μm multimode laser diode as the signal for the spectral measurements. The experimental results are shown in Fig. 3(a). We first took a spectral measurement (shown in dark solid line) of the 1.5-μm laser diode using the commercial OSA when the output power of the laser diode was −15 dBm. Before injecting the signal into the up-conversion spectrometer, we set the input signal power to −98.9 dBm, corresponding to approximately 1 million photons per second, by adjusting the tunable attenuator. We set the pump power at 30 mW and scan the pump laser and achieve a raw spectrum as shown in Fig. 3(a) (red dot line) [21]. Then we use a standard Jansson-Van Cittert iteration deconvolution method [25] with VBG's spectral curve (shown in the Fig. 3(c)) [21] to achieve the real spectrum (green dotted line). The number of iterations in our deconvolution process is one hundred.
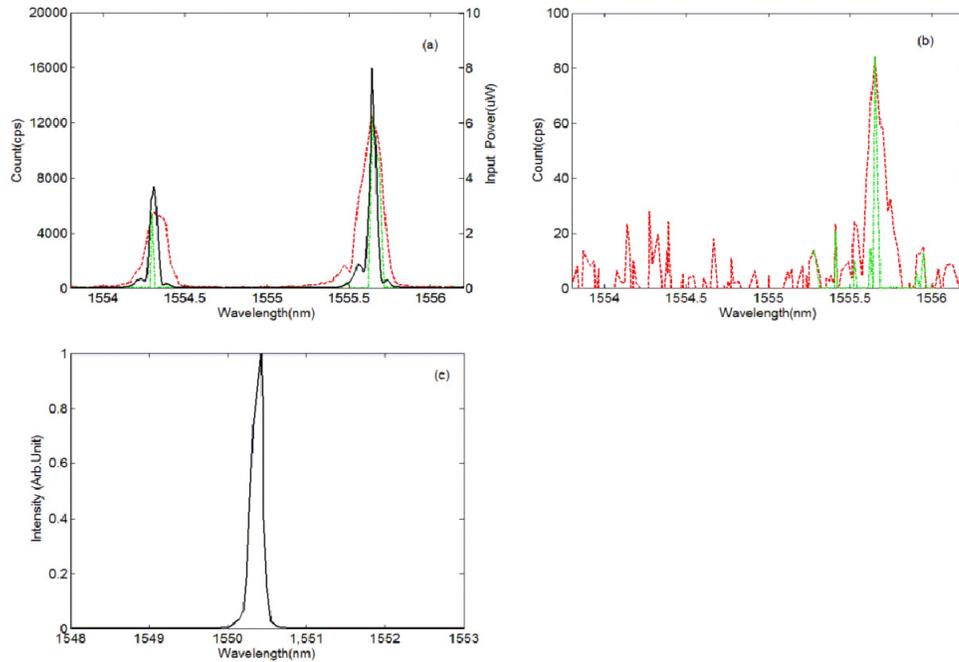
Fig. 3. Spectrum detected by the OSA (dark solid line), raw spectrum (red dot line), deconvolved spectrum (green dotted line) by up-conversion spectrometer. (a) Input signal power of −110 dBm. (b) Input signal power of −135 dBm. (c) Reflection spectrum from the VBG. Double-Y axis is used in (a). Left Y axis represents the number of photon detection events for the up-conversion spectrometer, while right Y axis represents the optical intensity measured by OSA.

In order to verify the NEP of our up-conversion spectrometer, the peak of the spectrum was still measured well down to an input power of −135 dBm and the spectrum was Fig. 3(b).

4. Conclusion

We utilized a long-wavelength pump and VBG filter to achieve a high efficiency and ultralow noise up-conversion single photon detector. The new detector can be directly used in a QKD system to improve its performance. Based on the detector, we demonstrate an up-conversion spectrometer with a NEP of −142 dBm $Hz^{-1/2}$ and a resolution of 0.16 nm. Moreover, the ultralow noise frequency conversion technique can find other important applications [26], for example, erasing the frequency difference between two photons to enable interference measurements [27] and bridging the quantum memory with the telecom band wavelength [23,28–31].

Acknowledgment

This work has been supported by the National Fundamental Research Program (under Grant No. 2011CB921300 and 2011CBA00300), the NNSF of China, the CAS, and the Shandong Institute of Quantum Science & Technology Co., Ltd. J.S.P. and M.M.F. acknowledge the U.S. AFOSR for their support under Grant No. FA9550-09-1-0233.

h) K. De Greve, P.L. McMahon, L. Yu, J.S. Pelc, C. Jones, C.M. Natarajan, N.Y. Kim, E. Abe, S. Maier, C. Schneider, M. Kamp, S. Hofling, R.H. Hadfield, A. Forchel, M.M. Fejer, Y. Yamamoto, "Complete tomography of a high-fidelity solid-state entangled spin-photon qubit pair," *Nature Communications* **4**, art. 2228 (July 2013)

ARTICLE

Complete tomography of a high-fidelity solid-state entangled spin–photon qubit pair

Kristiaan De Greve[1,*,†], Peter L. McMahon[1,*], Leo Yu[1], Jason S. Pelc[1], Cody Jones[1], Chandra M. Natarajan[1,2], Na Young Kim[1], Eisuke Abe[1,3,†], Sebastian Maier[4], Christian Schneider[4], Martin Kamp[4], Sven Höfling[1,4], Robert H. Hadfield[5], Alfred Forchel[4], M.M. Fejer[1] & Yoshihisa Yamamoto[1,3]

Entanglement between stationary quantum memories and photonic qubits is crucial for future quantum communication networks. Although high-fidelity spin–photon entanglement was demonstrated in well-isolated atomic and ionic systems, in the solid-state, where massively parallel, scalable networks are most realistically conceivable, entanglement fidelities are typically limited due to intrinsic environmental interactions. Distilling high-fidelity entangled pairs from lower-fidelity precursors can act as a remedy, but the required overhead scales unfavourably with the initial entanglement fidelity. With spin–photon entanglement as a crucial building block for entangling quantum network nodes, obtaining high-fidelity entangled pairs becomes imperative for practical realization of such networks. Here we report the first results of complete state tomography of a solid-state spin–photon-polarization-entangled qubit pair, using a single electron-charged indium arsenide quantum dot. We demonstrate record-high fidelity in the solid-state of well over 90%, and the first (99.9%-confidence) achievement of a fidelity that will unambiguously allow for entanglement distribution in solid-state quantum repeater networks.

[1] E. L. Ginzton Laboratory, Stanford University, Stanford, California 94305, USA. [2] Scottish Universities Physics Alliance and School of Engineering and Physical Sciences, Heriot-Watt University, Edinburgh EH14 4AS, UK. [3] National Institute of Informatics, Hitotsubashi 2-1-2, Chiyoda-ku, Tokyo 101-8403, Japan. [4] Technische Physik, Physikalisches Institut, Wilhelm Conrad Röntgen Research Center for Complex Material Systems, Universität Würzburg, Am Hubland, D-97074, Würzburg, Germany. [5] School of Engineering, University of Glasgow, Glasgow G12 8QQ, UK. * These authors contributed equally to this work. † Present address: Harvard University, Department of Physics, 17 Oxford Street, Cambridge, Massachusetts 02138, USA (K.D.G.); RIKEN Center for Emergent Matter Science (CEMS), Wako, Saitama 351-0198, Japan (E.A.). Correspondence and requests for materials should be addressed to K.D.G. (email: kdegreve@stanford.edu) or to P.L.M. (email: pmcmahon@stanford.edu).

Over the past two decades, entanglement between remote quantum systems has had a key role within the nascent field of quantum information[1,2], particularly so in quantum communication. Not only can entangled states be used for the generation of unconditionally secure cryptographic keys[1]; an entangled pair of quantum systems can be used as a resource to teleport quantum states[3]. In addition, entanglement is self-propagating: under certain, well-understood conditions, two pairs of entangled states can be used to generate a new pair, by performing joint Bell-state measurements[4] on one state of each pair—in a process known as entanglement swapping[5]. This process can be used to generate remote entanglement between stationary quantum memories that never interacted, by performing a probabilistic, partial Bell-state measurement through two-photon interference of the photonic part of two entangled pairs, each consisting of the quantum memory and a photonic qubit[6]. The resulting state from the post-selective process is one in which the quantum memories are entangled. Using such a scheme, in combination with local Bell-state measurements, gives rise to a quantum relay, where entanglement propagates along a chain of nodes[7,8]. Quantum repeaters, built in this way, are crucial for developing long-distance quantum communication networks[9–11]. Such schemes rely on the generation and/or existence of high-fidelity entangled states and intermediate Bell-state measurement; as otherwise errors would propagate and quickly make the end states fully mixed (classical). Perfect entanglement and Bell-state measurement, of course, do not exist in practice. The canonical solution to this problem, entanglement purification[12–14], consists of the distillation of high-fidelity entangled states out of lower-fidelity precursors. The combination of entanglement purification with a quantum relay of remotely entangled quantum memories is the essence of a quantum repeater[7,8], where many parallel, sacrificial links are used to generate remote entanglement in a nested protocol that combines entanglement purification with entanglement swapping. The number of parallel links required depends, in a nonlinear way, on the initial fidelity of the entangled pairs[8], and deteriorates rapidly with decreasing initial state fidelity. This immediately leads to a particular conundrum: although high-fidelity entanglement and quantum operations have been demonstrated for well-isolated systems such as trapped ions[15–17] and atoms[10,11], such systems do not lend themselves easily to the sort of large-scale parallelism that would be required to overcome their residual errors. Conversely, in the solid-state, where massive parallelism appears more realistic, the fidelity of quantum memory–photon entanglement in nitrogen-vacancy diamond[18] and optically active quantum dots[19–21] has so far remained rather poor, which would require ever-larger overheads in terms of parallelism to correct for the local imperfections.

In this work, we present results from a solid-state spin–photon entanglement setup that we previously[21] used to demonstrate a proof-of-principle, and with which we placed a bound on entanglement fidelity of $F > 0.8$. We have optimized the setup, and now demonstrate, via full state tomography (which has not been previously reported for any solid-state spin–photon experiment at optical frequencies[20–21]), a record-high solid-state spin–photon entanglement fidelity, with levels approaching, or in some cases surpassing, reported ion–photon[15,17] and atom–photon[22,23] entanglement fidelities.

Results

Spin–photon entanglement via optimized quantum erasure.
We use a single InAs quantum dot electron spin as the stationary qubit[24,25] (see Fig. 1a). A magnetic field in the Voigt geometry (in-plane, perpendicular to the growth direction, $B = 3$ T) provides a natural quantization axis, and allows for optical initialization[26] and ultrafast, high-fidelity optical control[25]. In addition, interference between the spontaneous emission decay pathways in the resulting Λ-systems results in entanglement between the spin and the photon[19–21], see Fig.1b. The large magnetic field results in a Zeeman energy splitting, $\delta\omega$, of $2\pi \times 17.6$ GHz. Conversely, the equivalent frequency difference between the H- and V-polarized branches of the spontaneous emission decay, $\delta\omega$, can result in frequency-which-path information leaking out to the environment[21,19]. By mixing a short gating pulse with the single photon in a nonlinear crystal (a periodically poled lithium niobate (PPLN) waveguide[21,27], see Fig. 1c), we can postselect for the photon's exact arrival time, with sub-8 ps timing resolution and with negligible background noise. The bandwidth of this detection scheme, about 100 GHz, greatly exceeds the frequency-which-path information of 17.6 GHz; this scheme is therefore inherently incapable of distinguishing the frequency difference, resulting in quantum erasure. As the timing resolution is not infinite, the environment can nevertheless still obtain some partial information, yielding a theoretical fidelity bound of about 95%. The quantum dot manipulation scheme and the system diagram are indicated in Fig. 1d,e. We first initialize the system by a 13-ns optical pumping pulse[25,26]. Then, a 100-ps optical π-pulse excites the quantum dot into the $|\uparrow\downarrow\Uparrow\rangle$-state, after which spontaneous emission results in spin-polarization entanglement.

Complete tomography of the spin–photon entangled qubit pair.
We perform joint, time-resolved measurements on the polarization state of the photon (polarization analysing stage in Fig. 1e), and the spin state. The latter can be measured by a combination of a few-picoseconds, high-fidelity, all-optical spin rotation pulse[25,28] and another optical pumping pulse to read out the spin in its computational ($|\downarrow\rangle, |\uparrow\rangle$) basis. Together, this allows us to perform complete state tomography of the entangled spin–photon-polarization qubit pair[29,30], and enables us to compare the experimentally obtained entangled state with the theoretical, ideal spin-polarization entangled state (assuming no errors and perfect frequency quantum erasure—see Supplementary Note 1):

$$|\Psi_{\text{ideal}}\rangle = \frac{1}{\sqrt{2}}(|\uparrow\rangle \otimes |iH\rangle + |\downarrow\rangle \otimes |V\rangle). \tag{1}$$

In quantum state tomography, one aims to reconstruct the density matrix, $\rho_{\text{reconstructed}}$ of the experimentally obtained quantum state by means of a set of linearly independent measurements[29,30]. This density matrix approaches the theoretical one, $\rho_{\text{ideal}} = |\Psi_{\text{ideal}}\rangle\langle\Psi_{\text{ideal}}|$, with the difference vanishing in the limit of arbitrarily small errors in both the generation process and the measurement performed to reconstruct the density matrix.

For a two-qubit system, and assuming proper normalization, a minimum of 15 linearly independent measurements is required to reconstruct the density matrix: $\rho_{\text{reconstructed}} = 1/4 \times \sum_{i,j} r_{i,j}\sigma_i \otimes \sigma_j$, where σ_i, σ_j refer to the Pauli operators of the respective qubits ($\sigma_0 = I$, the identity operator). As the Pauli operators are the generators of quantum mechanical qubit rotations, the coefficients $r_{i,j} = \text{Tr}[\rho_{\text{reconstructed}}\sigma_i \otimes \sigma_j]$ are related to the joint measurement of both qubits after applying single qubit rotations on both of them[29]. In particular, the joint measurement is calculated through comparing the coincidence counts between our spin and photon measurement devices, and comparing them to the coincidences obtained in different, uncorrelated events. For our photonic polarization qubit, we measure both in the {H,V} computational basis, and in two rotated bases, by means of our polarization analysing stage: $\{\sigma^+ = (H + iV)/\sqrt{2}, \sigma^- = (H - iV)/\sqrt{2}\}$ and $\{D^+ = (H + V)/\sqrt{2}, D^- = (H - V)/\sqrt{2}\}$.
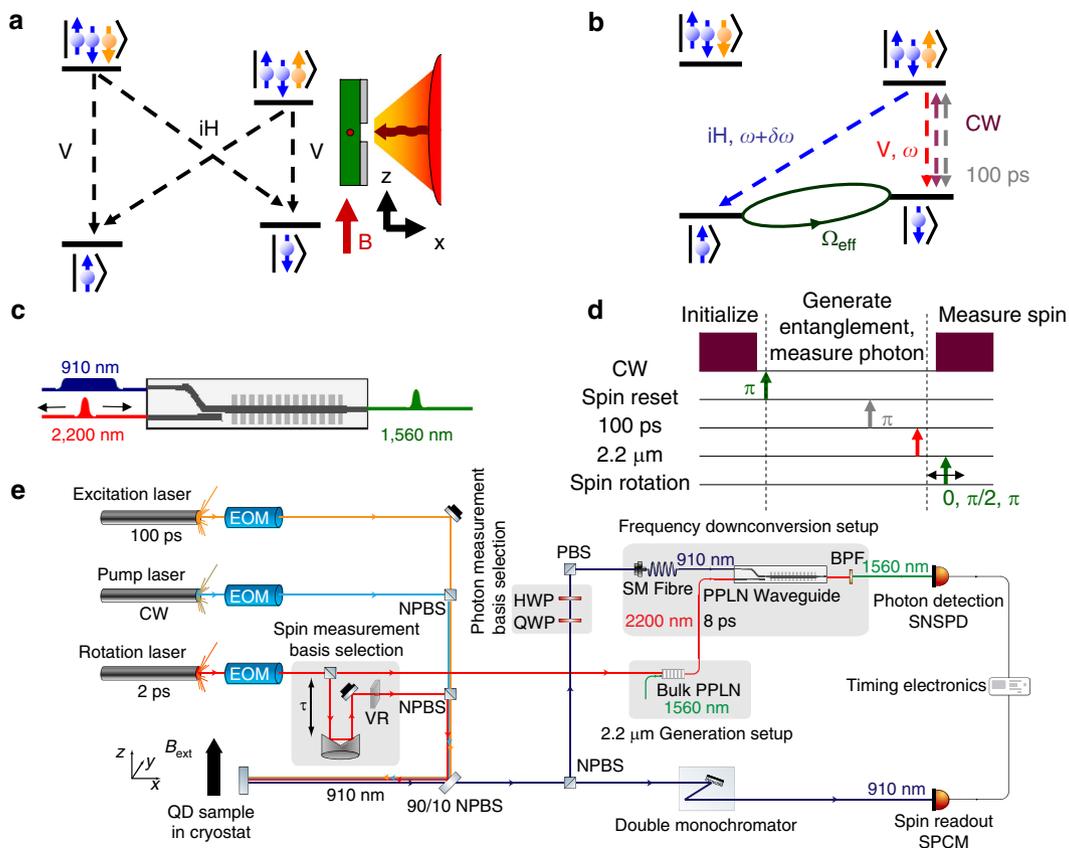
Figure 1 | Outline and setup of the spin–photon entanglement experiment. (a) Level structure of an electron-doped quantum dot, with the magnetic field in-plane (Voigt geometry, see inset). V and H refer to linear polarizations, either perpendicular to (V) or parallel (H) to the magnetic field. (**b**) Excitation and manipulation used in the experiment. See text for details. CW: continuous-wave laser, used for spin initialization and read-out. 100 ps: 100 ps laser pulse used for trion excitation. $\delta\omega$: Zeeman energy splitting ($2\pi \times 17.6\,GHz$). Ω_{eff}: effective spin-Rabi frequency of the detuned coherent-spin rotation laser. (**c**) Schematic overview of the time-resolved conversion process. A few-ps, 2.2-µm gate pulse converts a single 910-nm photon to a 1560-nm photon with picosecond timing resolution in a periodically poled lithium niobate waveguide. The resulting timing resolution acts as a quantum eraser for frequency-which-path information present in the spontaneous emission decay from the Λ-system, permitting high-fidelity spin-polarization entanglement to be measured. (**d**) Timing and pulse scheme used for generating and verifying spin–photon entanglement. (**e**) Schematic overview of the experimental apparatus. EOM: electro-optic modulator; VR: variable retarder; H(Q)WP: half-(quarter-)waveplate; (N)PBS: (non-)polarizing beamsplitter; PPLN: periodically poled lithium niobate; QD: quantum dot; SM: single-mode; BPF: bandpass filter.

For the spin qubit, we change the measurement basis by applying a rotation pulse (π or $\pi/2$) with the appropriate delay to change the rotation axis[25]; the bases we measure in are: $\{\downarrow, \uparrow\}$, $\{\leftarrow_x = (\uparrow - \downarrow)/\sqrt{2}, \rightarrow_x = (\uparrow + \downarrow)/\sqrt{2}\}$, $\{\leftarrow_y = (\uparrow - i\downarrow)/\sqrt{2}, \rightarrow_y = (\uparrow + i\downarrow)/\sqrt{2}\}$. Each coincidence measurement results in a conditional probability, using which the $r_{i,j}$ can be computed. From the 36 potential joint measurement settings resulting from these states, we choose a subset of 16 (15 + 1), that are linearly independent, which results in a straightforward, direct reconstruction of an initially unnormalized density matrix using the above definition and arithmetic manipulation—see Supplementary Note 2. Normalization of the density matrix then follows from a simple division by the trace, as suggested by James et al.[30].

The result of this direct reconstruction is indicated in Fig. 2, where we compare the thus obtained density matrix with the ideal one. The overlap with the ideal state, $\langle \Psi_{ideal} | \rho_{reconstructed} | \Psi_{ideal} \rangle$ yields a fidelity of 92.7%. However, due to measurement errors, this density matrix is non-physical (non-positive); in particular, one of the eigenvalues is negative: -0.19.

MLE reconstruction of the spin–photon density matrix. This drawback of direct reconstruction is commonly avoided by using a different reconstruction procedure. It is possible to enforce a physical, positive-semi-definite density matrix as an output, and to use a maximum likelihood estimation (MLE) procedure to find a density matrix that is most compatible with the experimental data[30]. Using numerical optimization, density matrices $\rho_{MLE} = T^\dagger T / \mathrm{Tr}(T^\dagger T)$ that form a best fit with the measurement results are sought. Such density matrices are properly normalized (have trace = 1), are strictly non-negative and Hermitian, and can therefore be regarded as physical[30] (see Supplementary Note 3).

Figure 3 shows the density matrix obtained from the MLE procedure. The fidelity is calculated using the same definition as for the direct reconstruction: $F_{MLE} = \langle \Psi_{ideal} | \rho_{MLE} | \Psi_{ideal} \rangle$. The non-zero measurement uncertainties (Poissonian counting statistics[21]) imply that the fidelity of the reconstructed state will also have an uncertainty associated with it. To quantify this uncertainty, we calculated the MLE-reconstruction for a range of possible input measurements, randomly sampled from the distribution of the possible measurement results, using a Monte Carlo method—see Supplementary Note 3. The resulting histogram (probability distribution) of the calculated fidelity is indicated in Fig. 3c, where 100,000 simulated noisy measurement results are used to calculate the MLE-obtained fidelity. We obtain a mean fidelity of 92.1% (median: 92.7%), with a standard
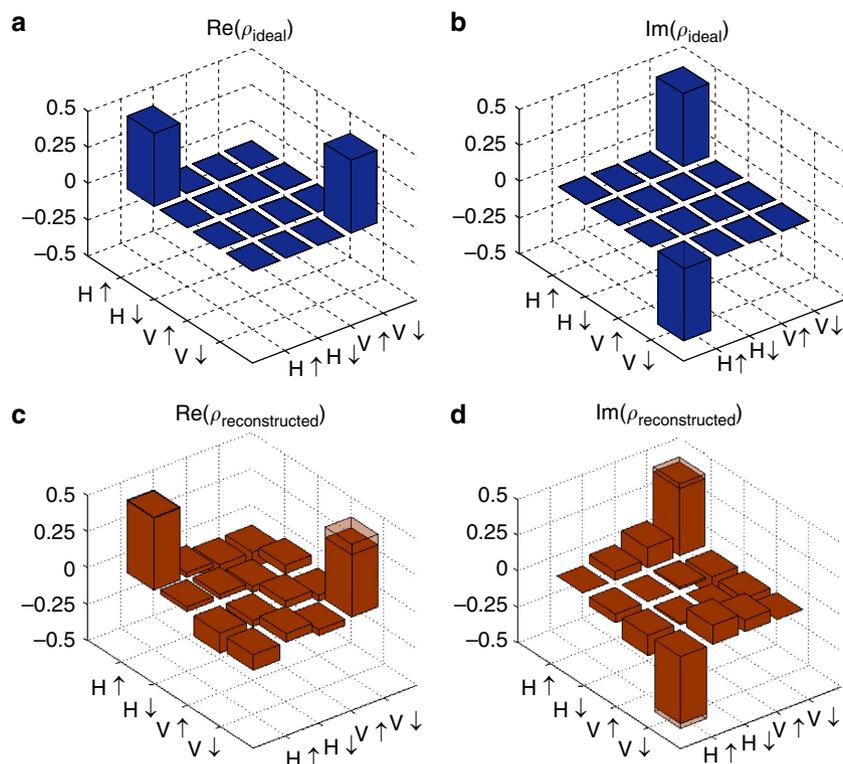
DISTRIBUTION A: Distribution approved for public release.

Figure 2 | Direct density matrix reconstruction. (**a**) Real part of the density matrix of the ideal spin–photon entangled state, $\rho_{ideal} = |\Psi_{ideal}\rangle \otimes \langle\Psi_{ideal}|$. (**b**) Imaginary part of the density matrix of the ideal spin–photon entangled state, $\rho_{ideal} = |\Psi_{ideal}\rangle \otimes \langle\Psi_{ideal}|$. (**c**) Real part of the reconstructed density matrix $\rho_{reconstructed}$, overlayed on the ideal density matrix (shaded box). (**d**) Imaginary part of the reconstructed density matrix $\rho_{reconstructed}$, overlayed on the ideal density matrix (shaded box).
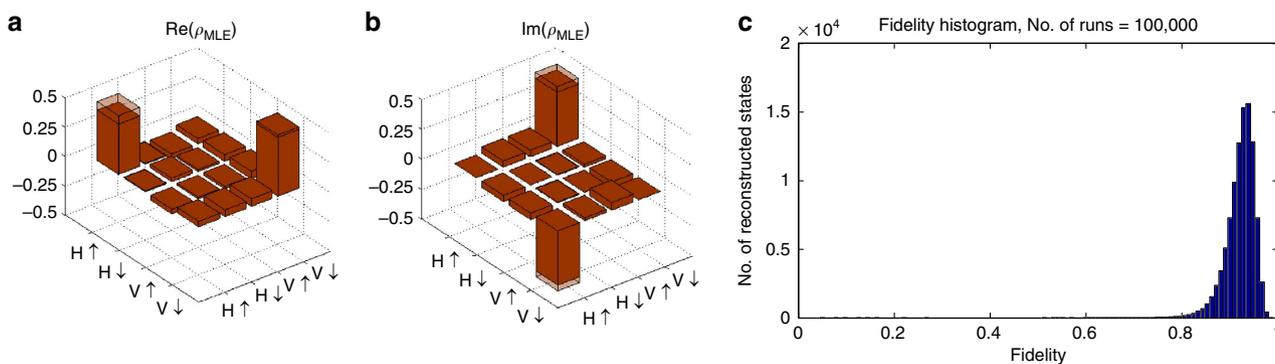
Figure 3 | Density matrix reconstruction through least-squares estimation. (**a**) Real part of the density matrix obtained using the MLE procedure described in the text. The ideal density matrix (ρ_{ideal}) is overlayed (shaded box). (**b**) Imaginary part of the density matrix obtained using the MLE procedure described in the text. The ideal density matrix (ρ_{ideal}) is overlayed (shaded box). (**c**) Histogram (100,000 runs) of the obtained fidelities using the MLE-reconstruction, taking into account the experimental uncertainties. The mean and median fidelities are over 92%, with standard errors of about 3.2%.

deviation of 3.2%. The theoretical upper bound, determined by the timing resolution of the time-resolved conversion technique[21], is around 95%, and is therefore close to being satisfied; residual errors in the pulse control of the spins account for most of the remaining difference (see Supplementary Note 1). Using the same methods, we calculated a concurrence of 0.908 (s.d.: 0.051), a tangle of 0.826 (s.d.: 0.086), an entanglement of formation of 0.87 (s.d.: 0.069) and a linear entropy of 0.107 (s.d.: 0.06).

Discussion

The entanglement fidelity becomes critically important if one intends to connect such multiple matter–light quantum interfaces

to make a quantum repeater[7,8]. For each link in a repeater network, the photons from two spin–photon pairs interfere to produce a spin–spin Bell-state[16], where the spin qubits are stored in separate repeater nodes at either end of the channel (see Fig. 4a). The repeater node would have two or more photon-based interfaces to communication links and local quantum gates between spins and spin-state read-out in each repeater node transfer information through the network. To overcome errors, these local operations could also distil a high-fidelity Bell-state (say $F \geq 0.995$) from multiple lower-fidelity pairs of entangled qubits[13].

When two spin–photon pairs with fidelity F_{sp} interfere, the resulting spin–spin entanglement fidelity F_{ss} is lower-bounded by $F_{ss} \geq (F_{sp})^2$, assuming perfect interference between the photons.
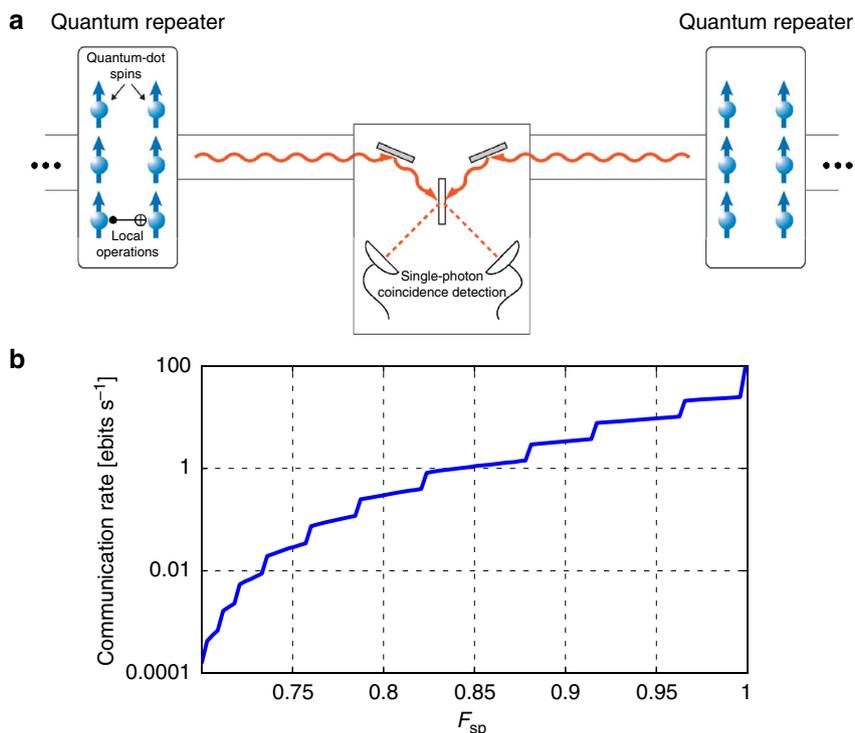
Figure 4 | Quantum dot spin–photon entangled pairs for quantum repeaters. (**a**) A schematic diagram of a quantum repeater based on optical quantum dots. When a spin–photon pair is generated, the spin is stored in the repeater node, whereas the photon is sent into the communication channel. Two such photons from different repeater nodes interfere to (probabilistically) produce spin–spin entanglement between two repeaters. (**b**) Plot of the simulated net communication rate of entangled spin–spin pairs after consumption (in purification) of 'raw' spin–photon states and EPR-Bell-pairs (Einstein-Podolsky-Rosen) suitable for use in the network. Entanglement distillation consumes many raw pairs generated at $F_{ss} = F_{sp}^2 + (1/3)(1 - F_{sp})^2$ (assuming depolarizing noise). As F_{sp} approaches the threshold 0.71 from above, the net communication rate goes to zero. The communication rate in entangled bits per second (ebits s^{-1}) is calculated, assuming spin–photon pairs interfering at a rate of 100 s^{-1}. The final spin–spin entanglement fidelity is at least 0.995.

Furthermore, it is known that entanglement distillation of EPR-Bell-states (Einstein-Podolsky-Rosen) has a 'threshold' lower bound of $F_{ss} > 0.5$ to increase fidelity at the output[13]. From this simple ansatz, we can draw two conclusions. First, and again assuming perfect photonic interference, using two spin–photon entangled pairs with measured fidelity $F_{sp} > 1/\sqrt{2} \approx 0.71$ will always result in a spin–spin entangled pair with fidelity $F_{ss} > 0.5$, which is above the threshold for purification. Conversely, for spin–photon fidelities below 0.71, it is not generally true that such a purifiable spin–spin entangled pair can be created. Although some lower-fidelity spin–photon states result in spin–spin entangled states that can be purified, more information about the particular state (via the knowledge of the full density matrix) would be required–see Supplementary Discussion. In this sense, 0.71 can be seen as an unconditional threshold for the spin–photon entanglement fidelity—a sufficient condition for scalability. To the best of our knowledge, this experiment is the first one in any solid-state system to unambiguously demonstrate (at the 99.9% confidence level) a spin–photon fidelity above this threshold.

Second, and more importantly, the efficiency of entanglement distillation, which directly has an effect on the communication rate, increases as $F_{sp} \rightarrow 1$. This effect can be seen clearly by the simulation results in Fig. 4b. Here we calculate the average net communication rate of high-fidelity ($F \geq 0.995$) spin–spin entangled pairs by distillation from noisy spin–photon Bell states[8]. If one compares the performance of the two systems starting from $F_{sp} = 0.9$ versus $F_{sp} = 0.8$, the former has a higher

communication rate by a factor of 10, illustrating the dramatic effect of improved spin–photon entanglement fidelity. For our experiment, the Monte Carlo uncertainty analysis used revealed that our spin–photon state has a fidelity above the threshold of $1/\sqrt{2}$ with 99.9% certainty, and that our entangled state has a fidelity greater than 0.9 with 81.4% certainty (Supplementary Table S1).

In conclusion, we demonstrated a full tomographic analysis of high-fidelity spin–photon entanglement in a solid-state system using InAs quantum dots. The resulting fidelity would allow for efficient distillation of purified entangled states, and represents a milestone in the quest to build quantum networks.

Methods

InAs quantum dot device. We used a Si-δ-doped quantum dot (QD) sample, similar to previous devices[21]. The dot density was reduced, and the emission blue-shifted (910 nm). We obtained excellent collection efficiency by means of an asymmetric, low-Q cavity (10 nm full width at half maximum, centred at 910 nm) that reduces photon loss from the spontaneous emission into the substrate. An external magnetic field perpendicular to the growth direction (Voigt geometry) splits the electron spin states as well as the excited, trion states. Figure 1a indicates the resulting Λ-systems, and the polarization selection rules were verified by means of polarization-selective photoluminescence (half-waveplate and polarizing beamsplitter)[25,28]. We screened the device and selected those quantum dots with the cleanest selection rules, to suppress residual errors.

Experimental setup. A superconducting magnetic cryostat (Oxford Spectromag; the magnetic field used was varied between $B = 3$ and 6 T) cooled the devices to a base temperature of 1.5 K. A 0.68-NA aspheric lens inside the cryostat focused the

pump and rotation lasers onto the sample, which was scanned relative to the lens by means of slip-stick piezo-electric positioners (Attocube Systems). We used similar coherent manipulation techniques as those reported previously[25]. A narrowband continous-wave-laser (New Focus Velocity) was used for spin initialization and read-out, resonant to the $|\downarrow\rangle$-$|\uparrow\downarrow\Uparrow\rangle$-transition (910.10 nm for a 3-T magnetic field); fibre-based electro-optic modulators (EOM, EOspace) were used to switch the laser light on and off. We used a Ramsey-interferometry setup for coherent spin rotations, using pulses from a modelocked laser (3 ps pulse duration, centre wavelength 911 nm, Spectra-Physics Tsunami), which were delayed relative to each other through a retroreflector on a motorized stage. Pulse-picking was realized using free-space EOMs (Conoptics), which were double-passed to increase the extinction ratio. The selective excitation of the $|\uparrow\downarrow\Uparrow\rangle$-state prior to spontaneous emission was realized through a combination of optical pumping into the $|\uparrow\rangle$-state, rotation by an optical π-pulse into the $|\downarrow\rangle$-state, followed by the application of a 100-ps pulse (optical π-pulse) from another, synchronized, modelocked laser (Spectra-Physics Tsunami with Lok-to-Clock system), resonant with the $|\downarrow\rangle$-$|\uparrow\downarrow\Uparrow\rangle$-transition. Pulse-picking of the 100-ps excitation pulses required another fibre-optic modulator. For the single-photon photoluminescence, we built a confocal setup, split into two branches by a non-polarizing beamsplitter. One branch was cross-polarized with respect to the initialization and optical pumping lasers, and sent through a double-monochromator onto a single-photon counter for spin-state analysis (Perkin-Elmer single-photon counting module; 20% quantum efficiency, 170 Hz ungated dark count rate). The other branch was sent to a polarization analysing stage (quarter- and half-waveplate and polarizer), after which it was coupled into single-mode fibres and sent to the downconversion setup. We carefully calibrated the polarization analysing stage, to account and compensate for residual birefringence in the setup. All EOMs were controlled by mutually synchronized pulse-pattern generators (76 MHz Tektronix and 10 GHz Anritsu PPG), themselves synchronized to the repetition rate of the modelocked lasers. Spatial, polarization, wavelength and time-filtering sufficed for separating reflected light from the single photons.

Quantum erasure via frequency conversion. For the 2.2-µm light pulses needed for conversion, we used a difference-frequency generation process that mixed the 3-ps, 911-nm pulses from the modelocked laser with narrowband, continous-wave 1560-nm light in an MgO-doped, PPLN chip. The 1560-nm light was modulated by a fibre-optic modulator, and amplified by erbium-doped fibre amplifiers. The residual 1560-nm and 911-nm light was filtered out through a combination of dichroic and absorptive filters. The resulting pulse width depended on the exact power and wavelength used for the difference-frequency generation process, but was measured to be between 3 and 8 ps.

Conditional on exact temporal overlap, a PPLN waveguide efficiently converted 910-nm, spontaneously emitted photons to 1560-nm photons. To eliminate residual noise from the 910 nm and 2.2 µm branches, we installed a fibre-Bragg grating and a long-pass filter. The 1560-nm photons were subsequently detected on a superconducting nanowire single-photon detector, maintained at 2 K, with 14% system detection efficiency, 40-Hz ungated dark count rate and 100-ps full width at half maximum timing jitter. Timing analysis was performed on a timing analyser (Hydraharp, PicoQuant GmbH), used in time-tagged time-resolved mode, which allows for accurate gating of the signals of both the single-photon counting module and the superconducting nanowire single-photon detector in post-processing, thereby drastically reducing the effects of dark counts. The timing of the 2.2-µm light was chosen such that the subsequent π/2-pulse arrives after 70–100 ps, which is well within the T_2^*-dephasing time of the quantum dot (1.5 ns), though spin-echo techniques could be used to overcome this limitation.

Correlation analysis. The correlation data that were used in the tomographic reconstruction algorithms, were the result of a histogram analysis, performed on the coincidence count rate between the downconverted single photons, and the single photons used for spin detection. The coincidence count rate was obtained through post-processing of the time-tagged time-resolved datastream, and comparing the coincidences within the same experimental run to those in subsequent, uncorrelated ones. The repetition rate is set at 39 or 52 ns, and the 0.1% single-photon efficiency and time-gated frequency downconversion resulted in a 1560-nm single-photon detection and entanglement generation rate of approximately 2–5 Hz. In combination with another 0.1% single-photon detection efficiency to detect the spin state (this efficiency is the result of all losses between the QD and the detector, including efficiency of collecting a photon from the QD into the optical path; losses from subsequent spatial, polarization and frequency filtering, finite detector quantum efficiency), this resulted in an average coincidence rate of approximately 2–5 mHz. We emphasize that these losses are predominantly due to the inefficiency of extracting a single photon from the quantum dot, which could be significantly improved by accurate cavity design. The conversion process in itself, although lossy due to the aggressive time-filtering to obtain good timing resolution, was rather effective, with internal quantum efficiencies estimated above 80%, and filtering losses of several dB maximum.

References

1. Ekert, A. K. Quantum cryptography based on Bell's theorem. *Phys. Rev. Lett.* **67,** 661–663 (1991).
2. Bennett, C. H., Brassard, G. & Mermin, N. D. Quantum cryptography without Bell's theorem. *Phys. Rev. Lett.* **68,** 557–559 (1992).
3. Bennett, C. H., Brassard, G., Crépeau, C. R., Jozsa, Peres, A. & Wootters, W. K. Teleporting an unknown quantum state via dual classical and Einstein-Podolsky-Rosen channels. *Phys. Rev. Lett.* **70,** 1895–1899 (1993).
4. Bell, J. S. On the Einstein Podolsky Rosen paradox. *Physics* **1,** 195–200 (1964).
5. Zukowski, M., Zeilinger, A., Horne, M. A. & Ekert, A. K. 'Event-Ready-Detectors' Bell Experiment via Entanglement Swapping. *Phys. Rev. Lett.* **71,** 4287–4290 (1993).
6. Duan, L.-M., Lukin, M. D., Cirac, J. I. & Zoller, P. Long-distance quantum communication with atomic ensembles and linear optics. *Nature* **414,** 413–418 (2001).
7. Briegel, H.-J., Dür, W., Cirac, J. I. & Zoller, P. Quantum repeaters: The role of imperfect local operations in quantum communication. *Phys. Rev. Lett.* **81,** 5932–5935 (1998).
8. Dür, W., Briegel, H.-J., Cirac, J. I. & Zoller, P. Quantum repeaters based on entanglement purification. *Phys. Rev. A* **59,** 169–181 (1999).
9. Kimble, H. J. The quantum internet. *Nature* **453,** 1023–1030 (2008).
10. Hofmann, J. *et al.* Heralded Entanglement Between Widely Separated Atoms. *Science* **337,** 72–75 (2012).
11. Ritter, S. *et al.* An elementary quantum network of single atoms in optical cavities. *Nature* **484,** 195–200 (2012).
12. Bennett, C. H., Bernstein, H. J., Popescu, S. & Schumacher, B. Concentrating partial entanglement by local operations. *Phys. Rev. A* **53,** 2046–2052 (1996).
13. Bennett, C. H. *et al.* Purification of noisy entanglement and faithful teleportation via noisy channels. *Phys. Rev. Lett.* **76,** 722–725 (1996).
14. Bennett, C. H., DiVincenzo, D. P., Smolin, J. A. & Wooters, W. K. Mixed state entanglement and quantum error correction. *Phys. Rev. A* **54,** 3824–3851 (1996).
15. Blinov, B. B., Moehring, D. L., Duan, L.-M. & Monroe, C. Observation of entanglement between a single trapped atom and a single photon. *Nature* **428,** 153–157 (2004).
16. Moehring, D. L. *et al.* Entanglement of single-atom quantum bits at a distance. *Nature* **449,** 68–71 (2007).
17. Stute, A. *et al.* Tunable ion-photon entanglement in an optical cavity. *Nature* **485,** 482–485 (2012).
18. Togan, E. *et al.* Quantum entanglement between an optical photon and a solid-state spin qubit. *Nature* **466,** 730–734 (2010).
19. Schaibley, J. R. *et al.* Demonstration of quantum entanglement between a single quantum dot electron spin and a photon. *Phys. Rev. Lett.* **110,** 167401 (2013).
20. Gao, W. B., Fallahi, P., Togan, E., Miguel-Sanchez, J. & Imamoğlu, A. Entanglement between a quantum-dot-spin and a single-photon. *Nature* **491,** 426–430 (2012).
21. De Greve, K. *et al.* Quantum-dot spin-photon entanglement via frequency downconversion to telecom wavelength. *Nature* **491,** 421–425 (2012).
22. Volz, J. *et al.* Observation of entanglement of a single photon with a trapped atom. *Phys. Rev. Lett.* **96,** 030404 (2006).
23. Wilk, T., Webster, S. C., Kuhn, A. & Rempe, G. Single-atom single-photon quantum interface. *Science* **317,** 488–490 (2007).
24. Berezovsky, J., Mikkelsen, M. H., Stoltz, N. G., Coldren, L. A. & Awschalom, D. D. Picosecond coherent optical manipulation of a single electron spin in a quantum dot. *Science* **320,** 349–352 (2008).
25. Press, D., Ladd, T. D., Zhang, B. & Yamamoto, Y. Complete quantum control of a single quantum dot spin using ultrafast optical pulses. *Nature* **456,** 218–221 (2008).
26. Xu, X. *et al.* Fast spin state initialization in a singly charged InAs-GaAs quantum dot by optical cooling. *Phys. Rev. Lett.* **99,** 097401 (2007).
27. Pelc, J. S. *et al.* Downconversion quantum interface for a single quantum dot spin and 1550-nm single-photon channel. *Opt. Express* **20,** 27510–27519 (2012).
28. De Greve, K. *et al.* Ultrafast coherent control and suppressed nuclear feedback of a single quantum dot hole qubit. *Nat. Phys.* **7,** 872–878 (2011).
29. Nielsen, M. A. & Chuang, I. L. *Quantum Computation and Quantum Information* (Cambridge University Press, 2000).
30. James, D. F. V., Kwiat, P. G., Munro, W. J. & White, A. G. Measurement of qubits. *Phys. Rev. A* **64,** 052312 (2001).

Author contributions

S.M., C.S., M.K. and S.H. grew and fabricated the samples. K.D.G. and P.L.M. designed the experiment. K.D.G., P.L.M., J.S.P., L.Y., C.M.N. and N.Y.K. performed the optical experiments. K.D.G., P.L.M. and C.J. performed the theoretical analysis. J.S.P. designed and fabricated the PPLN waveguides. J.S.P. and L.Y. developed the 2.2-μm setup and the 1560-nm filtering design. CMN and RHH packaged, characterized and set up the superconducting nanowire single-photon detectors . Y.Y., M.M.F. and A.F. guided the work. K.D.G. and P.L.M. wrote the manuscript with input from all authors.

Additional information

Supplementary Information accompanies this paper at http://www.nature.com/naturecommunications

Competing financial interests: The authors declare no competing financial interests.

Reprints and permission information is available online at http://npg.nature.com/reprintsandpermissions/

How to cite this article: De Greve, K. *et al.* Complete tomography of a high-fidelity solid-state entangled spin–photon qubit pair. *Nat. Commun.* 4:2228 doi: 10.1038/ncomms3228 (2013).

i) G.L. Shentu, Q.C. Sun, X. Jiang, X.D. Wang, J.S. Pelc, M.M. Fejer, Q. Zhang, J.W. Pan, "217 km long distance photon-counting optical time-domain reflectometry based on ultra-low noise up-conversion single photon detector," *Opt. Express* **21**, pp. 24674-79 (Oct. 2013).

217 km long distance photon-counting optical time-domain reflectometry based on ultra-low noise up-conversion single photon detector

Guo-Liang Shentu,[1,5] **Qi-Chao Sun,**[1,2,5] **Xiao Jiang,**[1,5] **Xiao-Dong Wang,**[1,3] **Jason S. Pelc,**[4] **M. M. Fejer,**[4] **Qiang Zhang,**[1,*] **and Jian-Wei Pan**[1]

[1]*Shanghai Branch, National Laboratory for Physical Sciences at Microscale and Department of Modern Physics,*
University of Science and Technology of China, Shanghai, 201315, China
[2]*Department of Physics, Shanghai Jiao Tong University, Shanghai, 200240, China*
[3]*College of Physics and Electronic Engineering of Northwest Normal University, Lanzhou, 730070, China*
[4]*Edward L. Ginzton Laboratory, Stanford University, Stanford, California, 94305, USA*
[5]*These authors contributed equally to this work*

*qiangzh@ustc.edu.cn

Abstract: We demonstrate a photon-counting optical time-domain reflectometry with 42.19 dB dynamic range using an ultra-low noise up-conversion single photon detector. By employing the long-wave pump technique and a volume Bragg grating, we achieve a noise equivalent power of -139.7 dBm/$\sqrt{\text{Hz}}$ for our detector. We perform the OTDR experiments using a fiber of length approximate 217 km, and show that our system can identify defects along the entire fiber length in a measurement time of 13 minutes.

© 2013 Optical Society of America

OCIS codes: (190.7220) Upconversion; (120.4825) Optical time domain reflectometry; (270.5570) Quantum detectors.

References and links

1. M. K. Barnoski and S. M. Jensen, "Fiber waveguides-novel technique for investigating attenuation characteristics," Appl. Opt. **15**, 2112–2115 (1976).
2. S. D. Personick, "Photon probe-optical-fiber time-domain reflectometer," Bell Syst. Tech. J. **56**, 355–366 (1977).
3. F. Scholder, J. D. Gautier, M. Wegmuller, and N. Gisin, "Long-distance OTDR using photon counting and large detection gates at telecom wavelength," Opt. Commun. **213**, 57–61 (2002).
4. M. Wegmuller, F. Scholder, and N. Gisin, "Photon-counting OTDR for local birefringence and fault analysis in the metro environment," J. Lightwave Technol. **22**, 390 (2004).
5. P. Eraerds, M. Legré, J. Zhang, H. Zbinden, and N. Gisin, "Photon counting OTDR: Advantages and limitations," J. Lightwave Technol. **28**, 952–964 (2010).
6. E. Diamanti, C. Langrock, M. M. Fejer, Y. Yamamoto, and H. Takesue, "1.5 μm photon-counting optical time-domain reflectometry with a single-photon detector based on upconversion in a periodically poled lithium niobate waveguide," Opt. Lett. **31**, 727–729 (2006).
7. J. Hu, Q. Zhao, X. Zhang, L. Zhang, X. Zhao, L. Kang, and P. Wu, "Photon-counting optical time-domain reflectometry using a superconducting nanowire single-photon detector," J. Lightwave Technol. **30**, 2583–2588 (2012).
8. C. Schuck, W. H. P. Pernice, X. Ma, and H. X. Tang, "Optical time domain reflectometry with low noise waveguide-coupled superconducting nanowire single-photon detectors," Appl. Phys. Lett. **102**, 191104 (2013).

9. M. Legre, R. Thew, H. Zbinden, and N. Gisin, "High resolution optical time domain reflectometer based on 1.55 μm up-conversion photon-counting module," Opt. Express **15**, 8237–8242 (2007).

10. G.-L. Shentu, J. S. Pelc, X.-D. Wang, Q.-C. Sun, M.-Y. Zheng, M. M. Fejer, Q. Zhang, and J.-W. Pan, "Ultralow noise up-conversion detector and spectrometer for the telecom band," Opt. Express **21**, 13986–13991 (2013).

11. H. Takesue, E. Diamanti, C. Langrock, M. M. Fejer, and Y. Yamamoto, "1.5- μm single photon counting using polarization-independent up-conversion detector," Opt. Express **14**, 13067–13072 (2006).

12. S. A.Castelletto, I. P. Degiovanni, V. Schettini, and A. L.Migdall, "Reduced deadtime and higher rate photon-counting detection using a multiplexed detector array," J. Mod. Opt. **54**, 337-352 (2007)

1. Introduction

Optical time-domain reflectometry (OTDR) is a commonly used measurement technique for fiber network diagnosis. By detecting the Rayleigh backscattered light of a pulse launched into fiber under test (FUT), one can get information about the attenuation properties, loss and refractive index changes in the FUT [1, 2]. Conventional OTDRs using linear photodetectors are widely used, but their performance is limited by the high noise equivalent power (NEP) of the p-i-n or avalanche photodiodes used in these systems. Photon-counting OTDRs (ν-OTDR), which employ single photon detectors instead, have been the subject of increased attention, becauase they offer better sensitivity, superior spatial resolution, an inherent flexibility in the trade-off between acquisition time and spatial precision, and the absence of the dead zones.

Several ν-OTDR systems have been demonstrated with InGaAs/InP avalanche photodiode (APD) operated in Geiger-mode [3, 4]. But in these demonstrations, the InGaAS/InP APDs used suffer from noise issues caused by large dark current and after pulsing [5]. Time gated operation of the detectors is used in these ν-OTDR measurements to reduce the noise. However, a consequence of time gated operation is that it only allows part of the fiber to be measured at a time, so the measurement time is longer than that using free running detectors by almost 3-order of magnitude [6]. Recently, ν-OTDRs based on free running superconducting single photon detectors (SSPD) have been reported [7, 8]. Thanks to the low NEP of SSPD, which is about -140.97 dBm$/\sqrt{\text{Hz}}$, a dynamic range of 37.4 dB is achieved in a total measurement time of about 10 minutes [8]. However, the superconducting nanowire is operated in a bulky liquid helium cryostat to reduce the thermal noise. Up-conversion single photon detectors that consist of a frequency upconversion stage in a nonlinear crystal followed by detection using a silicon APD (SAPD), provide an elegant room-temperature free-running single-photon detection technology, and have been successfully applied in ν-OTDR systems [6, 9]. Recent results include a two-point resolution of 1 cm [9] and a measurement time more than 600 times shorter [6]. But these systems are not appropriate for long-distance fiber measurements, for the NEP of these up-conversion single photon detectors is about 2-order of magnitude larger than that of the SSPD. The high NEP means that much longer measurement times are required to obtain the same signal-to-noise (SNR) ratio at the end of the ν-OTDR trace.

In a recent paper, we demonstrated an ultra-low noise up-conversion single photon detector by using long-wavelength pump technology, and a volume Bragg grating (VBG) as a narrow band filter to suppress the noise[10]. The up-conversion single photon detector we used in the experiment has a NEP of about -139.7 dBm$/\sqrt{\text{Hz}}$. Here, we employ the ultra-low noise up-conversion single photon detector and a high peak power pulsed laser, and present a ν-OTDR over fiber of 217 km length. With measurement time of 13 minutes, we achieve a dynamic range of 42.19 dB. The distance resolution of our system is about 10 cm; while the two-point resolution is about 100 m.

2. Experimental Setup

The experimental setup is shown in Fig. 1. Laser pulses with central wavelength of 1549.87 nm are launched into the FUT through an optical circulator. The peak power can be adjusted using
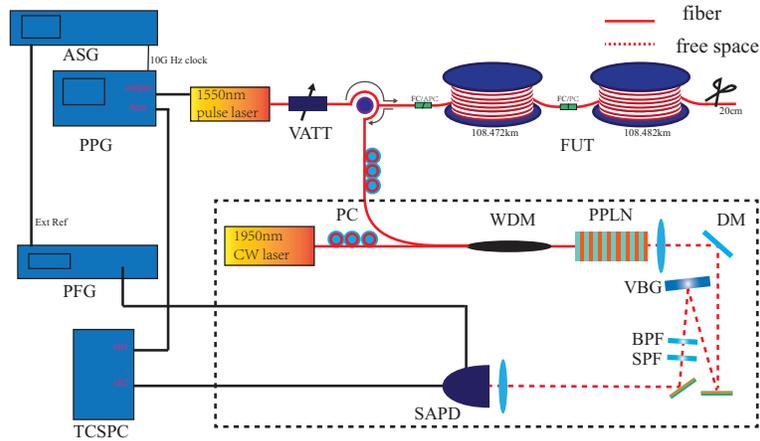
Fig. 1. Schematic of the experimental setup. ASG: analog signal generator, PPG: pulse pattern generator, PFG: pulse function arbitrary noise generator, TCSPC: time correlated single-photon counting system, VATT: variable optical attenuator, Circ: optical circulator, FUT: fiber under test, DM: dichroic mirror, PC: polarization controller, SPF: 945 nm short pass filter, BPF: 857 nm band pass filter, VBG: volume Bragg grating.

a variable optical attenuator (VATT). The FUT consists of two fiber spools of length 108.47 km and 108.48 km sequentially. The back scattered light is coupled into the third port of the circulator, and then detected by the ultra-low noise up-conversion single photon detector. The output of SAPD is fed into a time correlated single-photon counting system (TCSPC), which is operated in time-tagged time-resolved (TTTR) mode.

An analog signal generator acts as a clock of the whole ν-OTDR system by feeding a 10 GHz signal into "clock in" plug of a pulse pattern generator (PPG), and a 10 MHz signal as external reference of a pulse function arbitrary noise generator (PFG). The PPG's output is used to control the pulse laser, while its auxiliary output connected with TCSPC module to provide a 20 MHz synchronized clock. The output of PFG is used to switch the SAPD off temporarily during a repetition period of laser pulse, when we need to measure the FUT by sections.

The up-conversion single photon detector we used for this experiment, shown in the dash box of Fig. 1, is fully described in [10]. The signal light and 1952.39 nm pump laser are combined by a 1950 nm/1550 nm WDM and coupled into the z-cut PPLN waveguide through the fiber pigtail. A polarization controller is used to adjust the pump laser to the TM mode, for the PPLN waveguide only supports Type-0 (ee $\rightarrow$ e) phase matching. A Peltier temperature controller is used to keep the waveguide's temperature at 60.8 °C to maintain the phase-matching of the sum frequency generation (SFG) process. The generated SFG photons are collected by an AR-coated objective lens, and separated from the pump by a dichroic mirror (DM). A VBG, a 945 nm short pass filter (SPF) and a 857 nm band pass filter (BPF) are used to suppress the noise. Finally, the SFG photons are collected and detected by a SAPD. The dark count rate of the SAPD we used is about 60 Hz. Thanks to the long-wavelength pump and the narrow band VBG filter, we can suppress the dark count rate of the up-conversion single photon detector to 80 Hz while the detection efficiency is 15%, which corresponds to an NEP of about -139.7 dBm/$\sqrt{\text{Hz}}$. This condition is set as the operation point in our experiment.
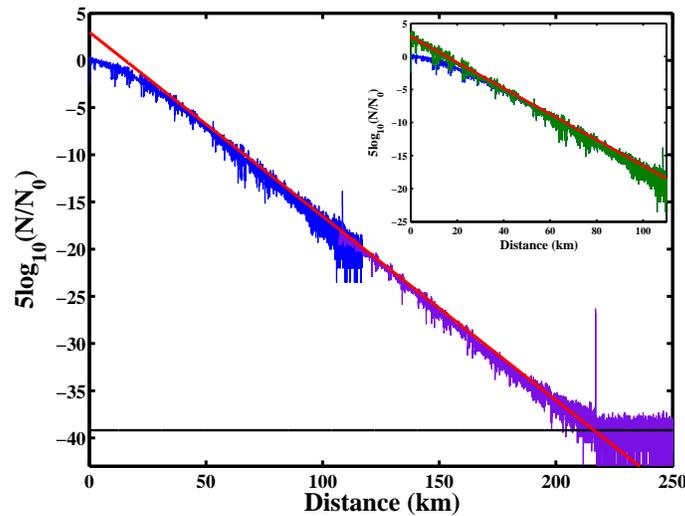
Fig. 2. Measurement of optical fiber of 217 km length performed by our ν-OTDR system. The pulse width is 1 μs. N is the counts of back scattered photons, N_0 is the count at the the initial point of the trace. The blue trace and violet trace are obtained in the first step and the second step of measurement, respectively. The position of the two peaks, 108.47203 km and 216.95422 km, coincides with the length of the two fiber spools. The black horizontal line shows the RMS noise level of the trace,which is about -39.19 dB. The intersection and slope of the extrapolated trace (red line) are 3 dB and 0.195 dB/km, respectively. The inset shows the comparison between the corrected trace (green) and the trace measured directly (blue).

3. Long distance ν-OTDR Application

In long distance ν-OTDR applications, if the pulse extinction ratio is poor and there is still light in the pulse interval, the back scattered photons of the light will cause non-negligible noise. Therefore the laser pulse extinction ratio is also crucial for a good signal noise ratio. To take advantage of the our low NEP of up-conversion detector, we expect the noise to be below the noise level of the detector. This requires a extremely high pulse extinction ratio of more than 100 dB. This is achieved by providing a small reversed bias voltage to the laser diode; we have confirmed that the emission between laser pulses is below our detection limit . The maximum peak power of our laser pulse is about 23 dBm. The repetition frequency is chosen according to the length of FUT. For a 217 km-long fiber, the round trip time of laser pulses in it is 2.14 ms. So the repetition frequency of the laser pulse must be lower than 452 Hz and in our experiment, we set the laser pulse repetition frequency at 400 Hz. The pulse width of the laser is set at 1 μs.

The measurement is divided into two steps. The repetition frequency and pulse width are unchanged in the two steps. In the first step, we attenuated the peak power to about 5 dBm and perform a 3minute ν-OTDR measurement. Due to the fiber loss, the counts of back scattered photons become smaller than the detector noise at about 120 km of the FUT. We only record the $0-120$ km ν-OTDR trace of FUT in the first step. And then, we manually adjust the laser peak power to 23 dBm, and perform a 10 minutes measurement of the remaining fiber. Because the peak power is high, there will be a great amount of photons reflected by the input surface and backscattered by the initial several kilometers of the FUT. To protect the SAPD, we apply a TTL signal to the SAPD gate input. The frequency of the signal is 400 Hz and the duty cycle

of the signal is 60%. The low TTL level is applied to the SAPD gate input to switch it off after the pulses are launched into the FUT. Thus, we only get the v-OTDR trace from 100 km to the end of FUT in the second step. The two sections are jointed into one according to their time delays, as shown in Fig. 2.

The up-conversion single photon detector in the experiment is polarization dependent. The strong fluctuation of the v-OTDR trace in Fig. 2 corresponds to the polarization state revolution when the light propagates through the fiber, and can be used to study the polarization properties of fiber. The polarization induced fluctuation can be eliminated by using a polarization scrambler [9] or a polarization independent up-conversion single photon detector [11]. The cross talk and Fresnel reflection of the optical circulator will induce a very high peak in the v-OTDR trace, which is not useful for diagnosing the FUT. Furthermore, the high peak will induce a following dip in the v-OTDR trace due to the dead time of SAPD and TCSPC. In order to avoid this, we adjust the high peak's polarization so that it has a very low probability to be recorded by our polarization dependent OTDR.

In Fig. 2, N is the counts of back scattered photons, N_0 is the count at the the initial point of the trace. Thus $10\log_{10}(N/N_0)$ represents the total loss in the round trip of the fiber. As is common in OTDR experiments, we plot $5\log_{10}(N/N_0)$, which represent single-pass loss through the fiber. The dead time of the SAPD used in the experiment is about $T_d = 60$ ns, during which, the photons will not be recorded successfully. So the measured counting rate is smaller than the actual one. Here we utilize a standard way to make the correction [12]. So when the measurement time $T \gg T_d$, the counting rate registered per time bin reduces to $C_r(t)T = C_{act}(t)T - C_{act}(t)T\sum C_r(t')$, where $C_r(t)$ is the registered counting rate per time bin, $C_{act}(t)$ is the actual counting rate without dead time effect and the summation means the total counting rate of time bins of time interval $[t - T_d, t]$. The actual counts can be corrected as $C_{act}(t)T = \frac{C_r(t)T}{1-\sum C_r(t')}$. It is obvious that the difference between measured and true actual counting rate is small when the counting rate is very low. In the first step of our experiment, the count rate is more than 7×10^5 Hz for the beginning of the v-OTDR trace. As shown in inset of Fig. 2, we correct the measurement trace (with a color of blue) with the above formula and the achieved trace (with a color of green) coincidences with the extrapolated trace (with a color of red) obtained by a linear fit of measured trace. The slope of the extrapolated trace indicates the attenuation of fiber of 0.195 dB/km. The intersection of the extrapolated trace is the actual value of the trace at the initial point, which is about 3 dB. The trace of experiment can be distinguished from the noise obviously at the end of the fiber. The root mean square (RMS) noise level is calculated from the data at the tails of the trace. The dynamic range is about 42.19 dB, which is determined by the difference between the intersection of the extrapolated trace and the RMS noise level.

One important parameter of OTDR is the distance resolution. It is the ability of the OTDR to locate a defect along the FUT, especially, the ability to locate the end of the FUT. The timing jitter of the detector Δt determines the distance resolution ΔL. The distance resolution can be estimated as $\Delta L = v_g \Delta t / 2$, where v_g is the group velocity of light in fiber. From our detector timing jitter of 500 ps we compute a distance resolution of approximately 5 cm. In order to demonstrate the spatial resolution experimentally, we cut 20 cm fiber off at the end of the second fiber spool, and perform the experiment again as described above. The last reflection peaks of the two v-OTDR traces are shown in Fig. 3. As shown in the Fig., the laser pulse is not broadened after transmitting through 217 km fiber. The leading edges of the two peaks, as shown in inset of Fig. 3, are separated with a 20 cm distance which coincides with the length of the cutting off fiber. According to the Fig., the experimental distance resolution is about 10 cm, which is larger than the expected resolution of 5 cm. The difference is caused by the fluctuation of the counts, which can be improved by extending the measurement time. Note that
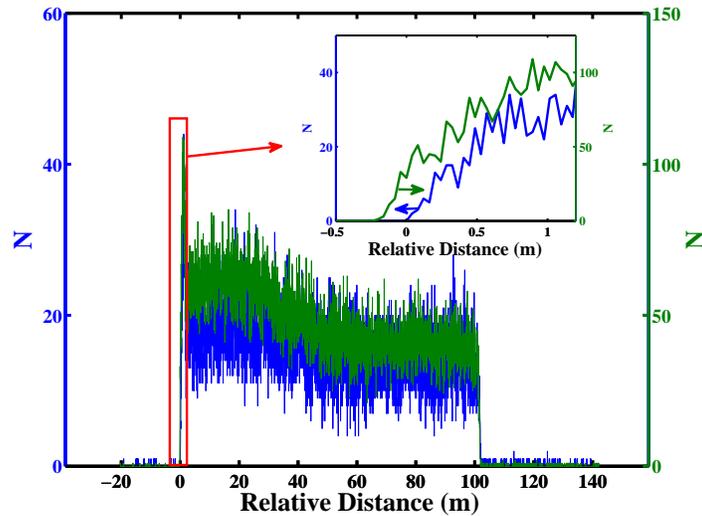
Fig. 3. Counts of last reflection peaks of ν-OTDR trace of the 217 km fiber (blue line) and after the 20 cm fiber is cut off at the end (green line), which are represented by the right y-axis and left y-axis, respectively. The amplitude of the two peaks are different because the cutting surfaces of fiber end are not identical. The inset shows the enlarged view of the leading edge of the two peaks.

the distance resolution is different than the two-point resolution, which is minimum distance between the defects that can be discriminated. The two-point resolution we can achieve is about 100 m, which is determined by the 1 μs pulse width we used in our experiment. Using shorter pulses will improve two-point resolution. But meanwhile, shorter pulses with a constant peak power means less photons in the pulse, which will decrease the measuring range and resolution.

4. Conclusion

In conclusion, we have presented the implementation of a ν-OTDR over 217 km-long optical fiber. It is based on an ultra-low noise up-conversion single photon detector, and the NEP of the detector is suppressed to -139.7 dBm/$\sqrt{\text{Hz}}$ by using long-wavelength pump technology and a VBG as a narrow band filter. We also use laser pulses of 23 dBm peak power to reduce the measurement time. This apparatus can achieve a dynamic range of 42.19 dB and distance resolution of about 10 cm at the distance of 217 km in measurement time of 13 minutes.

j) B.W. Mayer, C.R. Phillips, L. Gallmann, M.M. Fejer, U. Keller, "Sub-four-cycle laser pulses directly from a high-repetition-rate optical parametric chirped-pulse amplifier at 3.4 μm," *Opt. Lett.* **38**, pp. 4265-68 (Nov. 2013)

Sub-four-cycle laser pulses directly from a high-repetition-rate optical parametric chirped-pulse amplifier at 3.4 μm

B. W. Mayer,[1,*] C. R. Phillips,[1,2] L. Gallmann,[1] M. M. Fejer,[2] and U. Keller[1]

[1]*Department of Physics, Institute for Quantum Electronics, ETH Zurich, Zurich 8093, Switzerland*

[2]*Edward L. Ginzton Laboratory, Stanford University, Stanford, California 94305, USA*

Corresponding author: mayerb@phys.ethz.ch

We generate sub-four-cycle pulses (41.6 fs) with 12 μJ of pulse energy in the mid-infrared spectral range (center wavelength 3.4 μm) from a high-repetition-rate, collinear three-stage optical parametric chirped-pulse amplifier (OPCPA) operating at 50 kHz. Apodized aperiodically poled MgO:LiNbO$_3$ crystals with a negative chirp rate are employed as gain media to achieve ultrabroadband phase-matching while minimizing optical parametric generation. The seed pulses are obtained via a 1.56 μm femtosecond fiber laser, which is spectrally broadened in a dispersion-shifted telecom fiber to support 1000 nm bandwidth idler pulses in the mid-infrared.   © 2013 Optical Society of America

OCIS codes: (140.0140) Lasers and laser optics; (190.4970) Parametric oscillators and amplifiers; (190.7110) Ultrafast nonlinear optics.
http://dx.doi.org/10.1364/OL.38.004265

Recent developments in the generation of higher-order harmonics (HHG) show a clear trend towards the application of coherent and bright light sources operating at long wavelengths, enabling the generation of XUV- or multi-hundred-electron volt (eV) and even kiloelectron volt (keV) soft x-ray pulses [1,2]. Long-wavelength ultrashort laser pulses thus enable new capabilities for multidimensional spectroscopy and studies on atomic and molecular dynamics [3–6], in both the mid-infrared and XUV regions. To achieve high signal-to-noise ratios in the sensitive detection schemes used for many applications, light sources with high average photon flux are needed. In particular, higher repetition rates than those of conventional Ti:sapphire-based systems (which mainly operate in the few-kilohertz regime) are strongly favored. The development of suitable optical parametric amplifier (OPA)- and optical parametric chirped-pulse amplifier (OPCPA)-based sources is progressing rapidly, with reported systems operating at central wavelengths near 1.8 μm [7–9], 2 μm [10–12], 3 μm [13,14], 3.4 μm [15,16], and 4 μm [17].

In this Letter, we present a collinear, high-repetition-rate, mid-infrared OPCPA system operating at a center wavelength of 3.4 μm based on aperiodically poled lithium niobate (APPLN) OPA devices. The collinear interaction in such quasi-phase-matching (QPM) devices in contrast to noncollinear phase-matching in bulk crystals gives an idler output without an angular chirp. Compared with our previous work [16], this new system has been fully redesigned to account for recent developments in the theory of these devices [18,19], and to suppress parasitic spatial effects [20]. The new system design solves the seed bandwidth limitations of our previous system [16], greatly reduces optical parametric generation (OPG), and maintains good quantum conversion efficiency (≈24.5%) of the final OPA stage.

The new system delivers sub-four-cycle pulses [41.6 fs full width at half-maximum (FWHM)], without being limited by the damage threshold of the gain crystals, or by the bandwidth of the seed pulses provided by our fiber laser (in contrast to our previous result [16]). In particular, we show for the first time, to the best of our knowledge, the bandwidth capabilities of aperiodically poled MgO:LiNbO$_3$ amplification devices by demonstrating 1000-nm-wide gain while maintaining compressible output idler pulses.

In such aperiodic (or chirped) QPM gratings, the grating *k* vector is swept smoothly and monotonically through phase-matching for all of the spectral components of interest. Signal and idler spectral components experience gain in the vicinity of their local phasematching points. A unique aspect of this approach to OPCPA is that the gratings can support almost arbitrary phase-matching bandwidths with the potential for customized gain profiles [21,22], good conversion efficiencies [18,23], and access to bandwidths beyond those possible with conventional birefringent phase-matching techniques without operating at the crystal damage threshold. Furthermore, the system complexity is kept at a minimum by the collinear nature of the OPCPA chain. These properties make our approach an excellent route towards relatively compact systems offering intense few-cycle mid-infrared pulses for attosecond science.

Our OPCPA system is shown schematically in Fig. 1. We first generate a broadband seed source around
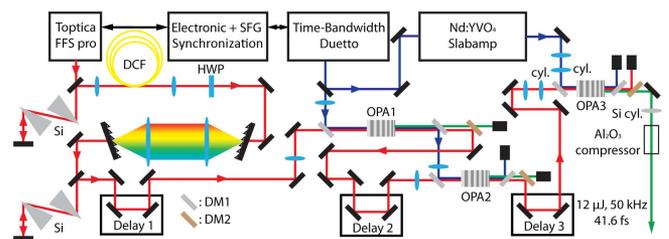

Fig. 1.   Schematic overview of the mid-infrared OPCPA setup. DM, dichroic mirror; DM1, reflective 1064 nm/transmissive 1560 and 3400 nm; DM2, reflective 1560 nm/transmissive 3400 nm.

© 2013 Optical Society of America

1.56 μm, amplify this pulse in the OPCPA chain, and extract the generated idler pulse after the final OPCPA stage. As the primary seed source for the system, we use a mode-locked femtosecond fiber laser operating at $\lambda = 1.56$ μm with a bandwidth corresponding to 65-fs transform limited pulse energy of 3.1 nJ at 80 MHz repetition rate (250 mW average power). Since our goal is to generate few-cycle infrared idler pulses, we first need to generate the required seed bandwidth in the near-infrared spectral range before seeding the OPCPA system. For this purpose, the pulses are first compressed to their transform limit via a pair of silicon prisms in a double-pass configuration. For our new spectral broadening system, the pulses are collimated with a pair of standard lenses and then coupled into a 1-m-long dispersion-shifted (DS) telecom fiber (DCF3, Thorlabs Inc.) with a zero-dispersion wavelength of ≈1.6 μm. This fiber operates in the normal dispersion regime, in contrast to the anomalous dispersion regime, which can be utilized for soliton pulse compression. The initially compressed input pulse is thus spectrally broadened while it is temporally dispersed through the fiber. This configuration avoids the modulation instability regime while still utilizing convenient off-the-shelf telecom fiber technology.

At the output of the spectral broadening fiber, the seed pulse supports more than 250 nm of signal bandwidth. To provide an OPCPA seed, the polarization of the spectrally broadened pulse is optimized with a half-wave plate (HWP) and then stretched by a $4f$ pulse shaper in a double-pass configuration. The pulse shaper consists of two metallic plane folding mirrors, two plane-concave cylindrical mirrors with a radius of curvature (ROC) of −800 mm, and two holographic transmission gratings with 600 lines/mm. The gratings exhibit a single-pass efficiency of greater than 85% at the design wavelength of 1.55 μm. A double-pass configuration of a subsequently arranged pair of silicon prisms provides the third-order dispersion (TOD) required to compress the final output pulses.

The spectrum after the $4f$ pulse shaper and the pair of silicon prisms is shown in Fig. 2(a) ("seed" curve, black solid line). The pulse energy available to seed the first OPCPA stage (depicted as OPA1 in Fig. 1) is 92.5 pJ. The spectral ripples seen in Fig. 2(a) originate from the imperfect pulse profile used to seed the DS fiber: while spectral broadening in the positive dispersion regime can in principle provide smooth output spectra, in our case, the pulses are already partially distorted by the nonlinear broadening that also occurs in the erbium-doped fiber amplifiers (EDFAs) of the fiber laser system itself. We confirmed this conclusion via numerical modeling of the spectral broadening process in the DS fiber using standard techniques [24,25], assuming the frequency resolved optical gating (FROG)- reconstructed pulses emitted by the fiber laser as input to the model. During the OPA process, any modulations of the seed spectrum are transferred to the generated idler spectrum.

The primary pump source for our OPCPA system is an industrial laser (Time-Bandwidth-Products Inc., Duetto) operating at 1.064 μm and delivering 12 ps pulses at a repetition rate of 50 kHz and average output power of up to 10 W. The output of this laser is split in two parts. One
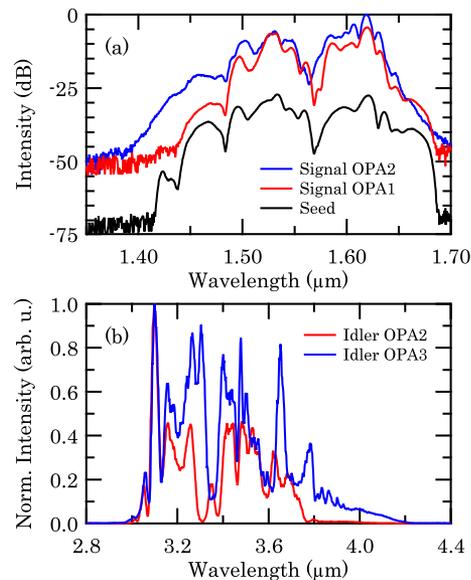

Fig. 2. (a) Signal spectra. Spectra of the seed (black line) and the amplified signal after OPA1 and OPA2, respectively (red and blue lines). An offset has been added to the seed curve for clarity. (b) Normalized mid-infrared idler spectra after OPA2 (red) and OPA3 (blue), respectively.

part is further amplified by a Nd:YVO$_4$ Innoslab-type amplifier [26], to provide a higher-power pump for the final OPA stage. The remaining part is collinearly overlapped with the seed in OPA1 via a dichroic mirror, denoted DM1 in Fig. 1 (transmissive for the seed at 1560 nm and reflective for the pump at 1064 nm). The average pump power reaching OPA1 is 5.7 W (113 μJ), and it is focused to a spot size of 315 μm ($1/e^2$ radius), corresponding to an intensity of 4.9 GW/cm^2. The pump output after the uncoated OPA1 crystal is split from the signal and idler outputs by another dichroic mirror DM1. In the new layout of our OPCPA chain, this pump is then reused to seed OPA2, providing a power of 3.8 W. The pump is refocused in OPA2 to an intensity of 6.7 GW/cm^2 ($1/e^2$ radius of 220 μm) and collinearly overlapped with the signal output of OPA1 (~1.56 μm), which is split from the idler by dichroic mirror DM2 after the first amplification stage. The gain of the preamplification part of the system (i.e., between the OPA1 input and the OPA3 input) corresponds to 42.8 dB.

The spectra of the seed and the amplified signals are shown in Fig. 2(a). Note that the amplified spectra also contain the unamplified 80 MHz background from the seed source. With respect to these spectra, there is evidence of gain narrowing, due to the non-flat-top pump temporal profile, reducing the amplification for signal spectral components below 1.475 μm and above 1.625 μm.

The third and final amplification stage, denoted OPA3, is pumped by the output of our Innoslab amplifier [26]. The pump power reaching the OPA3 crystal is 15.2 W, corresponding to 304 μJ. The signal output of OPA2 is used as the seed for this stage, and the generated mid-infrared idler around $\lambda = 3.4$ μm is extracted afterwards as the final output of the system. Dichroic mirrors DM1 and DM2 are used to combine and split up the waves.

In OPA3, we use a moderate peak intensity of the pump so as to not drive the crystal too strongly. A consequence

of pumping the crystal too strongly is the onset of beam fanning, likely due to photorefractive effects driven by parasitic green light, which is generated primarily due to random duty cycle variations in the QPM grating [19]. To use all of the available pump power in the 1-mm-aperture APPLN devices, we use elliptical foci for the pump and signal beams. To obtain the required beam sizes, we employ both spherical and cylindrical lenses (indicated by "cyl." in Fig. 1), forming one spherical and one cylindrical telescope. The pump beam is focused to an intensity of 4.4 GW/cm^2 ($1/e^2$ width of 700 µm in the horizontal dimension corresponding to the direction of the crystal c axis, $1/e^2$ width of 1700 µm in the vertical dimension). The resulting idler spectra of OPA2 and OPA3 are shown in Fig. 2(b). The spectra are measured with an imaging grating spectrometer.

In all stages we use newly designed uncoated MgO:LiNbO$_3$ crystals, each having an 11-mm long, 1-mm by 3-mm wide, apodized APPLN grating design with a chirp rate of $\kappa = -2.5$ mm^{-2} (corresponding to a decreasing period versus position) in order to achieve a broad phase-matching in a spectral window spanning the 3 to 4 µm spectral range. Concerning apodization, we have studied the importance of apodization profiles for such chirped QPM devices experimentally [27], and have recently shown how they can be implemented systematically for a wide range of parametric interactions [18].

For idler compression after OPA3, we utilize propagation through a bulk medium. Our compressor consists of a 50-mm long rod of coated sapphire, with the length chosen as a trade-off between efficiency and gain narrowing in the preamplifier OPCPA stages. Note that adjustment of the dispersion compensation primarily takes place on the seed pulse in the near-infrared spectral range. Due to the phase-reversal properties of OPA, the even-order spectral phase components of the idler inherit, approximately, the even-order components of the seed spectral phase with a flipped sign, whereas the sign of odd-order components of the idler phase is not flipped [21]. The combination of the applied seed phase, which utilizes the 4f pulse shaper and pair of silicon prisms described above, and idler propagation through the bulk sapphire after the final OPA stage enables compensation of the idler spectral phase up to fourth order. With this approach, we were able to compress the chirped 3.4 µm pulses to 41.6 fs (sub-four-cycles), with 12 µJ of pulse energy after collimation and compression. The compressed pulses were characterized with mid-infrared second-harmonic generation (SHG)-FROG, as shown in Fig. 3. With respect to the retrieved spectrum, we believe the discrepancy compared to the measured spectrum originates from the spectral dependence of SHG conversion efficiency and beamsplitter characteristics over the large bandwidth supported by the idler spectrum. However, the 68.8 fs FWHM of the autocorrelation signal provides additional evidence for the sub-four-cycle duration of our pulses.

It is important to note that inside the APPLN grating, the generated idler power is approximately 948 mW ($\approx$19 µJ). This value was calculated when accounting for all linear losses encountered from the optical elements after OPA3, including Fresnel losses from the end facet of the uncoated APPLN grating. We estimate a corresponding internal conversion efficiency (number
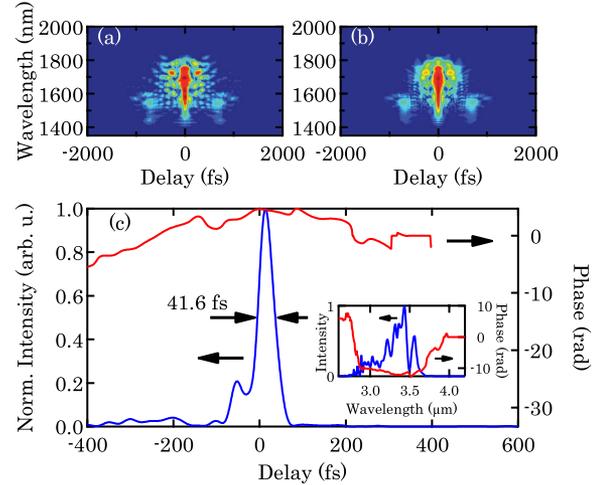

Fig. 3. (a) Measured SHG-FROG spectrogram of the compressed 41.6 fs mid-infrared pulse. The FROG error for a grid size of 512 by 386 points is 0.0116. (b) Retrieved spectrogram and (c) retrieved temporal intensity and phase. The inset shows the retrieved spectrum and spectral phase.

of idler photons at the end of the QPM grating divided by the number of pump photons at the input) of 24.5%. With respect to the overall gain in the system, the net amplification between the OPA3 input and compressor output corresponds to 11.8 dB.

In order to develop a working OPCPA system using APPLN devices, several important design constraints must be met that go beyond using QPM gratings to support a sufficient phase-matching bandwidth. For example, with a given phase-matching bandwidth and OPA gain, the noncollinear gain guided modes discussed in [20] can be fully suppressed with a sufficient pump peak power, thereby suppressing excess OPG. By the design of the system layout and the APPLN gratings, the presence of OPG has been minimized. Specifically, by operating our system at 50 kHz and reusing the OPA1 transmitted pump for OPA2, we are able to satisfy this pump peak power constraint in each stage, and also ensure sufficient seed power for OPA3 without excessively saturating OPA1 and OPA2.

The remaining OPG background was characterized first by measuring the idler output power while operating the amplification chain in an unseeded configuration and also by a spectral characterization of the OPG. The spectra of the amplified idler (seeded case) and the OPG (unseeded case) are shown in Fig. 4. Note the different scales for the idler spectrum of OPA3 and the idler OPG spectrum. In both cases the amount of amplified quantum noise accounts for less than 2.5% of the total idler power, and this value represents an overestimate of the actual OPG in the seeded system. This value is a substantial improvement compared to the background in our previous OPCPA system [16] and to reported OPG levels of other comparable systems [10–12]. To the best of our knowledge, this is the lowest OPG background within output pulses delivered by a high-repetition-rate, mid-infrared OPCPA reported so far, and proves that the excess quantum noise amplification discussed in [20] for this type of gain medium can be fully suppressed by appropriate system design.
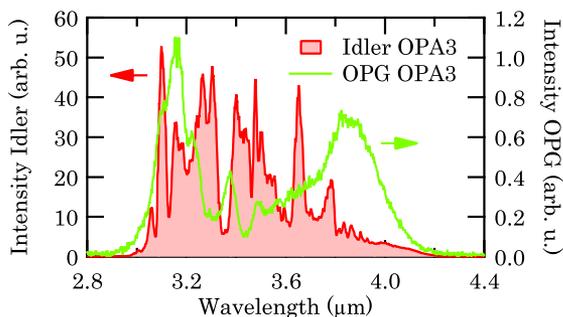
Fig. 4. OPG spectrum for the unseeded case of the amplifier chain in comparison to the idler spectrum of OPA3. Note the different scales for the idler and OPG spectrum. The power contained by the area under the green OPG curve accounts for less than 2.5% of the total amount of idler power.

In addition to redesigning the OPCPA stages to minimize OPG while improving bandwidth and maintaining conversion efficiency, the sign of the pulse chirp was also flipped (we now use a sapphire compressor instead of a silicon compressor [16]). This change was made in order to optimize the OPCPA temporal dynamics. Furthermore, in addition to being more convenient experimentally, seeding the power amplifier stage (OPA3) with the signal rather than the idler helps to suppress unwanted processes such as idler SHG. The details of this and other subtle aspects of our system design are beyond the scope of this Letter, and will be discussed further in future work.

In conclusion, we have demonstrated a 50 kHz, midinfrared light source delivering 41.6 fs record-short pulses directly from such a high-repetition-rate OPCPA at 3.4 µm central wavelength. The system provides a compressed pulse energy of 12 µJ. Additionally, good internal conversion efficiency of 24.5% was achieved and the OPG background was minimized by the redesign of the seeding and amplification scheme. The internal conversion efficiency is an indication that the power amplifier stage OPA3 is operating in a strongly saturated regime, with the potential to eventually access the fully saturated adiabatic frequency conversion limit [18]. So far, we are using 1-mm by 3-mm wide APPLN gratings. In recent years, wide-aperture samples have become available [28], allowing QPM technology to support very high energies. In combination with new developments in high-power ultrafast amplifiers [29,30], this technology should enable high-power and high-repetition-rate few-cycle pulse generation in the mid-infrared.

References

1. C. Trallero-Herrero, C. Jin, B. E. Schmidt, A. D. Shiner, J.-C. Kieffer, P. B. Corkum, D. M. Villeneuve, C. D. Lin, F. Légaré, and A. A. T. Le, J. Phys. B **45**, 011001 (2012).
2. T. Popmintchev, M.-C. Chen, D. Popmintchev, P. Arpin, S. Brown, S. Ališauskas, G. Andriukaitis, T. Balčiunas, O. D. Mücke, A. Pugzlys, A. Baltuška, B. Shim, S. E. Schrauth, A. Gaeta, C. Hernández-García, L. Plaja, A. Becker, A. Jaron-Becker, M. M. Murnane, and H. C. Kapteyn, Science **336**, 1287 (2012).
3. C. T. Middleton, P. Marek, P. Cao, C.-C. Chiu, S. Singh, A. M. Woys, J. J. de Pablo, D. P. Raleigh, and M. T. Zanni, Nat. Chem. **4**, 355 (2012).
4. M. Yang, Ł. Szyc, J. Dreyer, E. T. J. Nibbering, and T. Elsaesser, J. Phys. Chem. A **114**, 12195 (2010).
5. P. Hamm and M. T. Zanni, *Concepts and Methods of 2D Infrared Spectroscopy* (Cambridge University, 2011).
6. P. Colosimo, G. Doumy, C. I. Blaga, J. Wheeler, C. Hauri, F. Catoire, J. Tate, R. Chirla, A. M. March, G. G. Paulus, H. G. Muller, P. Agostini, and L. F. DiMauro, Nat. Phys. **4**, 386 (2008).
7. C. Li, D. Wang, L. Song, J. Liu, P. Liu, C. Xu, Y. Leng, R. Li, and Z. Xu, Opt. Express **19**, 6783 (2011).
8. B. E. Schmidt, A. D. Shiner, P. Lassonde, J.-C. Kieffer, P. B. Corkum, D. M. Villeneuve, and F. Légaré, Opt. Express **19**, 6858 (2011).
9. M. Bradler, C. Homann, and E. Riedle, "Broadband difference frequency mixing between visible and near-infrared pulses for few-cycle pulse generation with stable carrier-envelope phase," Appl. Phys. B (to be published).
10. T. Fuji, N. Ishii, C. Y. Teisset, X. Gu, T. Metzger, A. Baltuška, N. Forget, D. Kaplan, A. Galvanauskas, and F. Krausz, Opt. Lett. **31**, 1103 (2006).
11. X. Gu, G. Marcus, Y. Deng, T. Metzger, C. Teisset, N. Ishii, T. Fuji, A. Baltuska, R. Butkus, V. Pervak, H. Ishizuki, T. Taira, T. Kobayashi, R. Kienberger, and F. Krausz, Opt. Express **17**, 62 (2009).
12. Y. Deng, A. Schwarz, H. Fattahi, M. Ueffing, X. Gu, M. Ossiander, T. Metzger, V. Pervak, H. Ishizuki, T. Taira, T. Kobayashi, G. Marcus, F. Krausz, R. Kienberger, and N. Karpowicz, Opt. Lett. **37**, 4973 (2012).
13. C. J. Fecko, J. J. Loparo, and A. Tokmakoff, Opt. Commun. **241**, 521 (2004).
14. M. Hemmer, A. Thai, M. Baudisch, H. Ishizuki, T. Taira, and J. Biegert, Chin. Opt. Lett. **11**, 013202 (2013).
15. C. Heese, C. R. Phillips, L. Gallmann, M. M. Fejer, and U. Keller, Opt. Lett. **35**, 2340 (2010).
16. C. Heese, C. R. Phillips, B. W. Mayer, L. Gallmann, M. M. Fejer, and U. Keller, Opt. Express **20**, 26888 (2012).
17. G. Andriukaitis, T. Balciunas, S. Alisauskas, A. Pugzlys, A. Baltuska, T. Popmintchev, M.-C. Chen, M. M. Murnane, and H. C. Kapteyn, Opt. Lett. **36**, 2755 (2011).
18. C. R. Phillips, C. Langrock, D. Chang, Y. W. Lin, L. Gallmann, and M. M. Fejer, J. Opt. Soc. Am. B **30**, 1551 (2013).
19. C. R. Phillips, J. S. Pelc, and M. M. Fejer, J. Opt. Soc. Am. B **30**, 982 (2013).
20. M. Charbonneau-Lefort, B. Afeyan, and M. M. Fejer, J. Opt. Soc. Am. B **25**, 1402 (2008).
21. M. Charbonneau-Lefort, B. Afeyan, and M. M. Fejer, J. Opt. Soc. Am. B **25**, 463 (2008).
22. C. R. Phillips, L. Gallmann, and M. M. Fejer, Opt. Express **21**, 10139 (2013).
23. G. Porat and A. Arie, J. Opt. Soc. Am. B **30**, 1342 (2013).
24. J. M. Dudley, G. Genty, and S. Coen, Rev. Mod. Phys. **78**, 1135 (2006).
25. C. R. Phillips, C. Langrock, J. S. Pelc, M. M. Fejer, I. Hartl, and M. E. Fermann, Opt. Express **19**, 18754 (2011).
26. C. Heese, A. E. Oehler, L. Gallmann, and U. Keller, Appl. Phys. B **103**, 5 (2011).
27. C. Heese, C. R. Phillips, L. Gallmann, M. M. Fejer, and U. Keller, Opt. Express **20**, 18066 (2012).
28. H. Ishizuki and T. Taira, Opt. Express **20**, 20002 (2012).
29. P. Russbueldt, T. Mans, J. Weitenberg, H. D. Hoffmann, and R. Poprawe, Opt. Lett. **35**, 4169 (2010).
30. T. Eidam, S. Hanf, E. Seise, T. V. Andersen, T. Gabler, C. Wirth, T. Schreiber, J. Limpert, and A. Tünnermann, Opt. Lett. **35**, 94 (2010).

k) G.L. Shentu, X.X. Xia, Q.C. Sun, J.S. Pelc, M.M. Fejer, Q. Zhang, J.W. Pan, "Upconversion detection near 2 μm at the single photon level," *Opt. Lett.* **38**, pp. 4985-87 (Dec. 2013)

Upconversion detection near 2 μm at the single photon level

Guo-Liang Shentu,[1] Xiu-Xiu Xia,[1] Qi-Chao Sun,[1,2] Jason S. Pelc,[3] M. M. Fejer,[3] Qiang Zhang,[1,*] and Jian-Wei Pan[1]

[1]*Shanghai Branch, National Laboratory for Physical Sciences at Microscale and Department of Modern Physics, University of Science and Technology of China, Shanghai 201315, China*

[2]*Department of Physics, Shanghai Jiao Tong University, 800 Dongchuan Road, Shanghai 200240, China*

[3]*Edward L. Ginzton Laboratory, Stanford University, Stanford, California 94305, USA*

*Corresponding author: qiangzh@ustc.edu.cn

We have demonstrated upconversion detection at the single photon level in the 2 μm spectral window using a pump wavelength near 1550 nm, a periodically poled lithium niobate (PPLN) waveguide, and a volume Bragg grating (VBG) to reduce noise. We achieve a system photon detection efficiency of 10%, with a noise count rate of 24,500 counts per second, competitive with other 2 μm single photon detection technologies. This detector has potential applications in environmental gas monitoring, life science, and classical and quantum communication.   © 2013 Optical Society of America

OCIS codes: (190.7220) Upconversion; (190.4410) Nonlinear optics, parametric processes; (270.5570) Quantum detectors.

http://dx.doi.org/10.1364/OL.38.004985

The detection of weak infrared signals at wavelengths near 2 μm is an enabling technology in fields such as environmental gas monitoring and life science [1–3], as many important chemical compounds have fundamental absorption bands located in this wavelength range due to vibrational or rotational transitions [3,4]. For example, CO_2 has an absorption band near 2 μm, the line strength of which is at least 70 times bigger than the absorption band located near 1.6 μm [5]. Therefore, the measurements of CO_2's absorption at the 2 μm band can increase the altitude resolution compared with the 1.6 μm band, and is more suitable for the lower troposphere [5]. However, traditional mid-infrared detection systems are not sensitive enough for those applications. In environmental gas monitoring, a detection sensitivity at least on the order of ~1 ppm (parts per million) is desired for CO_2, to define spatial gradients from which sources and sinks can be derived and quantified, as well as annual increases in its rate of concentration [5]; whereas, CO requires a detection sensitivity equivalent to ~100 ppb (parts per billion) [6]. Monitoring warming gases with detection sensitivity at these levels can advance the study of global warming and its influences for life on Earth [7]. In life science, the on-line detection of several chemical compounds in exhaled human breath may help doctors with disease evaluation and non-invasive treatments. For example, exhaled NO can be utilized as a biomarker for asthma [8], however, it requires a detection sensitivity at the level of ~1 ppb. Also, exhaled ammonia is a potential non-invasive indicator for liver [9] and kidney function, as well as peptic ulcer diseases.

Furthermore, hollow core-photonic bandgap fibers (HC-PBGF) have been proposed to provide a 100-fold enhancement of the overall capacity of broadband core networks; recent results suggest that the lowest propagation losses occur at wavelengths near 2 μm [10].

In summary, it can be seen that many fields can benefit from single photon detection at the 2–15 μm wavelength region. However, of the broadly employed InGaAs/InP avalanche photodiodes (APDs) to detect near infrared single photons, to the best of our knowledge no commercial detectors exist for wavelengths longer than 1.7 μm. Although commercial superconducting single photon detectors (SSPDs) exist, reported detection efficiencies (DE) are approximately 3% at a temperature of 2 K [11]. Furthermore, SSPD's applications are limited due to for the need for bulky cryogenic cooling and exquisite temperature control. We have, therefore, expanded the application of frequency upconversion detectors [12–18] to the 2 μm band. In frequency upconversion, signal photons interact with a strong pump in a PPLN waveguide to produce converted photons in the visible to near-infrared region, which can be detected by a Silicon APD (SAPD) with a high DE and low dark count rates (DCRs).

In this Letter, we have demonstrated a room temperature single photon upconversion detector at the 2 μm band, with a detection efficiency of approximately 10%.

We fabricated PPLN waveguides via the reverse proton exchange technique [19]; the waveguides are 52 mm long and are poled with a quasi-phase-matching (QPM) period of 19.6 μm. The waveguides were designed with single mode filters to match the SMF-28 single mode optical fiber, with a fiber pigtail at the input, and were antireflection-coated to avoid interference effects and improve system throughput. A schematic of our experimental setup is shown in Fig. 1. A cw, single-frequency, tunable telecom-band external cavity diode laser (ECDL) and an erbium-doped fiber amplifier (EDFA) were utilized as the pump source for this experiment. The pump produced a maximum average power of approximately 1 W. The pump was filtered using a 1550 nm/1950 nm wavelength division multiplexer (WDM), a 1550 nm/980 nm WDM and a manually tunable optical filter to remove amplified spontaneous emission noise, and other spurious output. A 1/99 beam splitter (BS) was utilized to monitor the pump power.
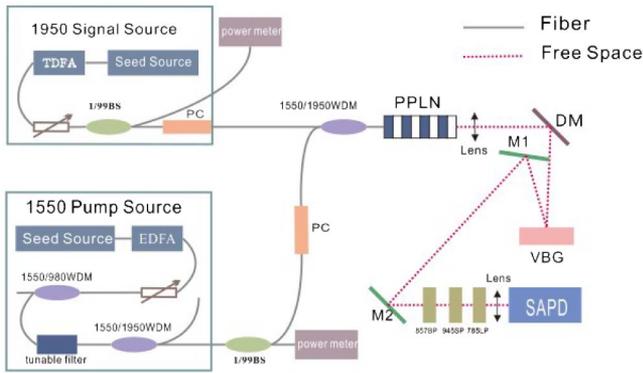
Fig. 1.   Schematic of the upconversion single photon detector at 2 μm. BS, beam splitter; M1-M2, mirrors.

Fig. 2.   DE (purple triangles) and noise count rate (blue squares) versus pump power. DE is fitted.

A single longitudinal mode thulium fiber laser (TDFL) and amplifier (TDFA) were employed as the signal sources near 1950 nm. Then, a variable attenuator, five spliced 1/99 BSs, and a thermal power meter with a sensitivity of 1 μW, were utilized to control and monitor the input signal power. The total input photon number and time gate were set as 1 MHz and 1 ns, respectively. Therefore, the average photon number per time gate was 10^{-3}. The signal was combined with the pump in a 1550 nm/1950 nm WDM. The polarization of both signal and pump fields were aligned to the TM mode of the PPLN waveguide using polarization controllers. Also, a Peltier cooler-based temperature control system was employed to keep the waveguide's temperature at 60°C, thereby maintaining the phase-matching condition. The signal, pump, and SFG wavelengths are 1950, 1550, and 864 nm, respectively.

The phase-matching bandwidth of our waveguide was 0.3 nm, which was mainly decided by the length of the QPM gratings. To increase the bandwidth, one can reduce the length of the waveguide, or fabricate a chirped one.

At the waveguide output, the sum-frequency generation (SFG) photons were separated from the pump by a dichroic mirror (DM) after being collected by an AR-coated objective. A 945 nm short-pass filter (SPF), a 785 nm long-pass filter (LPF), and a 857 nm BPF were then used to block the second and higher order harmonics of the pump. Additionally, we used a volume Bragg grating (VBG) [18,20] with a 95% reflection efficiency and a 0.05 nm bandwidth to further suppress noise generated in the waveguide. Finally, the SFG photons were collected and detected by a SAPD, which had a DE of approximately 45% at 860 nm, with the DCRs around 25 cps.

The main experimental results are shown in Fig. 2. We tuned the pump power by adjusting the variable attenuator and recorded DE and noise count rates at each tuned pump power point. The DE is calculated by dividing the number of detected counts after noise count rate subtraction and detector linearity correction by the number of signal photons before the WDM. When the pump power was set at 300 mW, the DE was 10.25%, with a noise count rate of 24,500 cps. DE data is fitted with a sine square function [14], while the noise count rate is fitted with a polynomial curve to guide the eye.

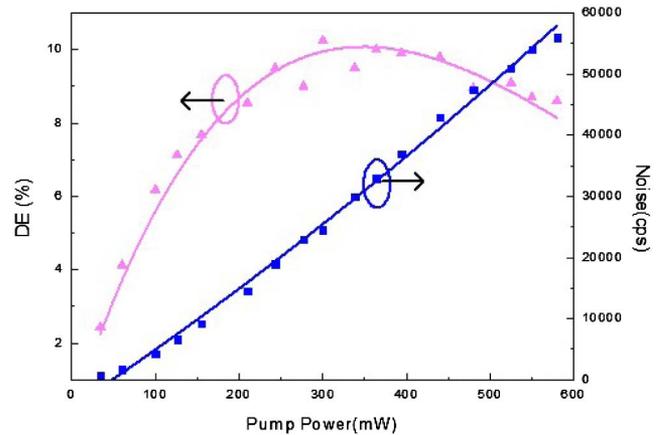The PPLN waveguide had a total fiber-to-output-facet throughput of 4.5 dB for the 2 μm signal. The losses in the combination WDM and free space light were measured as 1 dB and 0.8 dB, respectively. In combination with SAPD's DE, which is approximately 45%, the theoretical DE should be around 10%, which is consistent with our measurement.

To ascertain the conversion efficiency of the signal photons in the PPLN waveguide in our experiment, we measured the depletion [21] of the input signal as a function of the pump power by coupling the light exiting the waveguide into an optical spectrum analyzer (OSA) and comparing the observed signal levels when the pump is turned on, versus off. A signal depletion level of 23.5 dB was observed, corresponding to an internal conversion efficiency of 99.6%. Our measurement of the signal depletion, in logarithmic units, is shown in Fig. 3. The experimental data fits the theory [21] very well.

The noise is mainly due to spontaneous Raman scattering (SRS). SRS can produce photons either redshifted or blueshifted from the pump as Stokes or anti-Stokes sidebands, generated with an intensity ratio determined by a Boltzmann factor owing to the thermal occupation of phonons [17]. The ratio of the rate R_{aS} of anti-Stokes Raman photons for a medium pumped at ω_a to Stokes photons R_S for a medium pumped at ω_b, with $\omega_b - \omega_a = \Delta\omega$, is given by
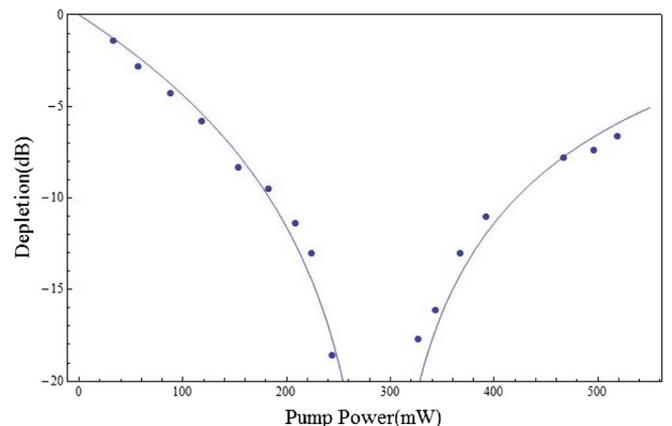

Fig. 3.   Signal depletion versus pump power.

$$\frac{R_{aS}}{Rs} = \left(\frac{\omega_b}{\omega_a}\right)^3 \exp\left[-\frac{h\Delta\omega}{2\pi kT}\right]. \qquad (1)$$

It was shown in [14] that, for an upconversion detector with $\lambda_p = 1.32$ μm and $\lambda_1 = 1.55$ μm, the ratio of noise counts is consistent with this Boltzmann factor when the roles of the signal and pump are interchanged. In our experiment, the noise count rate was near 150 at the DE peak power when the pump and signal were interchanged, and the ratio calculated from Eq. (1) was approximately 150. Therefore, a noise count rate of 24,500 cps at the DE peak is reasonable.

We have demonstrated the upconversion detection near the 2 μm band with reasonable DCRs and a relatively high DE compared with existing single photon detectors at this wavelength, which has potential applications in many fields. To further improve the performance of this detector, we can employ long wavelength pump [17] and cascade frequency conversion to reduce the noise, as well as increasing the DE. A narrower band VBG could continue to reduce the noise. Note that the fiber coupling in the experiment was optimized for 1550 nm not 1950 nm. Therefore, it is possible to redesign the mode filter to attain ~1 dB input coupling losses.

Note added in proofs: We note that related experiment has been reported in Ref. [22].

References

1. M. N. Abedin, M. G. Mlynczak, and T. F. Refaat, Proc. SPIE **7808**, 78080V1 (2010).
2. S. S. Kim, C. Young, B. Vidakovic, S. G. A. Gabram-Mendola, C. W. Bayer, and B. Mizaikoff, IEEE Sens. J. **10**, 145 (2010).
3. M. R. McCurdy, Y. Bakhirkin, G. Wysocki, R. Lewicki, and F. K. Tittel, J. Breath Res. **1**, 014001 (2007).
4. G. Ehret, C. Kiemle, M. Wirth, A. Amediek, A. Fix, and S. Houweling, Appl. Phys. B **90**, 593 (2008).
5. R. T. Menzies and D. M. Tratt, Appl. Opt. **42**, 6569 (2003).
6. J. Li, U. Parchatka, R. Königstedt, and H. Fischer, Opt. Express **20**, 7590 (2012).
7. J. Houghton, Rep. Prog. Phys. **68**, 1343 (2005).
8. D. Bukstein, M. Kraft, A. H. Liu, and S. P. Peters, J. Allergy Clin. Immunol. **118**, S1 (2006).
9. C. Shimamoto, I. Hirata, and K. Katsu, Hepato-gastroenterology **47**, 443 (2000).
10. P. J. Roberts, F. Couny, H. Sabert, B. J. Mangan, D. P. Williams, L. Farr, M. W. Mason, A. Tomlinson, T. A. Birks, J. C. Knight, and P. St. J. Russell, Opt. Express **13**, 236 (2005).
11. Superconducting Nanotechnology, Moscow, Russia, "Super-conducting single-photon detector," http://scontel.ru/images/detectors/sspd_data.pdf.
12. P. Kumar, Opt. Lett. **15**, 1476 (1990).
13. A. P. Vandevender and P. G. Kwiat, J. Mod. Opt. **51**, 1433 (2004).
14. C. Langrock, E. Diamanti, R. V. Roussev, Y. Yamamoto, M. M. Fejer, and H. Takesue, Opt. Lett. **30**, 1725 (2005).
15. M. A. Albota and F. N. C. Wong, Opt. Lett. **29**, 1449 (2004).
16. R. T. Thew, H. Zbinden, and N. Gisin, Appl. Phys. Lett. **93**, 071104 (2008).
17. J. S. Pelc, L. Ma, C. R. Phillips, Q. Zhang, C. Langrock, O. Slattery, X. Tang, and M. M. Fejer, Opt. Express **19**, 21445 (2011).
18. G. L. Shentu, J. S. Pelc, X. D. Wang, Q. C. Sun, M. Y. Zheng, M. M. Fejer, Q. Zhang, and J. W. Pan, Opt. Express **21**, 13986 (2013).
19. K. R. Parameswaran, R. K. Route, J. R. Kurz, R. V. Roussev, M. M. Fejer, and M. Fujimura, Opt. Lett. **27**, 179 (2002).
20. P. S. Kuo, J. S. Pelc, O. Slattery, Y. S. Kim, M. M. Fejer, and X. Tang, Opt. Lett. **38**, 1310 (2013).
21. J. S. Pelc, G. L. Shentu, Q. Zhang, M. M. Fejer, and J. W. Pan, Phys. Rev. A **86**, 033827 (2012).
22. X. Gu, K. Huang, H. Pan, E. Wu, and H. Zeng, Laser Phys. Lett. **10**, 055401 (2013).

l).. C.R. Phillips, B.W. Mayer, L. Gallmann, M.M. Fejer, U. Keller, "Design constraints of optical parametric chirped pulse amplification based on chirped quasi-phase-matching gratings," *Opt. Express* **22**, pp. 9627-58, (April 2014).

Design constraints of optical parametric chirped pulse amplification based on chirped quasi-phase-matching gratings

C. R. Phillips,[1,2,*] **B. W. Mayer,**[1] **L. Gallmann,**[1,3] **M. M. Fejer,**[2] **and U. Keller**[1]

[1]*Department of Physics, Institute of Quantum Electronics, ETH Zurich, 8093 Zurich, Switzerland*
[2]*Edward L. Ginzton Laboratory, Stanford University, Stanford, California 94305,USA*
[3]*Institute of Applied Physics, University of Bern, 3012 Bern, Switzerland*
[*]*cphillips@phys.ethz.ch*

Abstract: Chirped quasi-phase-matching (QPM) gratings offer efficient, ultra-broadband optical parametric chirped pulse amplification (OPCPA) in the mid-infrared as well as other spectral regions. Only recently, however, has this potential begun to be realized [1]. In this paper, we study the design of chirped QPM-based OPCPA in detail, revealing several important constraints which must be accounted for in order to obtain broad-band, high-quality amplification. We determine these constraints in terms of the underlying saturated nonlinear processes, and explain how they were met when designing our mid-IR OPCPA system. The issues considered include gain and saturation based on the basic three-wave mixing equations; suppression of unwanted non-collinear gain-guided modes; minimizing and characterizing nonlinear losses associated with random duty cycle errors in the QPM grating; avoiding coincidentally-phase-matched nonlinear processes; and controlling the temporal/spectral characteristics of the saturated nonlinear interaction in order to maintain the chirped-pulse structure required for OPCPA. The issues considered place constraints both on the QPM devices as well as the OPCPA system. The resulting experimental guidelines are detailed. Our results represent the first comprehensive discussion of chirped QPM devices operated in strongly nonlinear regimes, and provide a roadmap for advancing and experimentally implementing OPCPA systems based on these devices.

© 2014 Optical Society of America

References and links

1. B. W. Mayer, C. R. Phillips, L. Gallmann, M. M. Fejer, and U. Keller, "Sub-four-cycle laser pulses directly from a high-repetition-rate optical parametric chirped-pulse amplifier at 3.4 μm," Opt. Lett. **38**, 4265–4268 (2013).
2. M. Charbonneau-Lefort, B. Afeyan, and M. M. Fejer, "Optical parametric amplifiers using chirped quasi-phase-matching gratings I: practical design formulas," J. Opt. Soc. Am. B **25**, 463–480 (2008).
3. M. Charbonneau-Lefort, B. Afeyan, and M. M. Fejer, "Competing collinear and noncollinear interactions in chirped quasi-phase-matched optical parametric amplifiers," J. Opt. Soc. Am. B **25**, 1402–1413 (2008).
4. C. Heese, C. R. Phillips, L. Gallmann, M. M. Fejer, and U. Keller, "Ultrabroadband, highly flexible amplifier for ultrashort midinfrared laser pulses based on aperiodically poled Mg:LiNbO$_3$," Opt. Lett. **35**, 2340–2342 (2010).

5. C. Heese, C. R. Phillips, B. W. Mayer, L. Gallmann, M. M. Fejer, and U. Keller, "75 MW few-cycle mid-infrared pulses from a collinear apodized APPLN-based OPCPA," Opt. Express **20**, 26888–26894 (2012).

6. C. R. Phillips and M. M. Fejer, "Efficiency and phase of optical parametric amplification in chirped quasi-phase-matched gratings," Opt. Lett. **35**, 3093–3095 (2010).

7. H. Suchowski, V. Prabhudesai, D. Oron, A. Arie, and Y. Silberberg, "Robust adiabatic sum frequency conversion," Opt. Express **17**, 12731–12740 (2009).

8. C. R. Phillips, C. Langrock, D. Chang, Y. W. Lin, L. Gallmann, and M. M. Fejer, "Apodization of chirped quasi-phasematching devices," J. Opt. Soc. Am. B **30**, 1551–1568 (2013).

9. G. Porat and A. Arie, "Efficient, broadband, and robust frequency conversion by fully nonlinear adiabatic three-wave mixing," J. Opt. Soc. Am. B **30**, 1342–1351 (2013).

10. O. Yaakobi, M. Clerici, L. Caspani, F. Vidal, and R. Morandotti, "Complete pump depletion by autoresonant second harmonic generation in a nonuniform medium," J. Opt. Soc. Am. B **30**, 1637–1642 (2013).

11. H. Suchowski, P. R. Krogen, S.-W. Huang, F. X. Kärtner, and J. Moses, "Octave-spanning coherent mid-IR generation via adiabatic difference frequency conversion," Opt. Express **21**, 28892-28901 (2013).

12. C. R. Phillips, L. Gallmann, and M. M. Fejer, "Design of quasi-phasematching gratings via convex optimization," Opt. Express **21**, 10139–10159 (2013).

13. K. A. Tillman, D. T. Reid, D. Artigas, J. Hellström, V. Pasiskevicius, and F. Laurell, "Low-threshold femtosecond optical parametric oscillator based on chirped-pulse frequency conversion," Opt. Lett. **28**, 543–545 (2003).

14. K. A. Tillman and D. T. Reid, "Monolithic optical parametric oscillator using chirped quasi-phase matching," Opt. Lett. **32**, 1548–1550 (2007).

15. L. Gallmann, G. Steinmeyer, U. Keller, G. Imeshev, M. M. Fejer, and J. Meyn, "Generation of sub-6-fs blue pulses by frequency doubling with quasi-phase-matching gratings," Opt. Lett. **26**, 614–616 (2001).

16. G. Imeshev, M. M. Fejer, A. Galvanauskas, and D. Harter, "Pulse shaping by difference-frequency mixing with quasi-phase-matching gratings," J. Opt. Soc. Am. B **18**, 534–539 (2001).

17. D. Artigas and D. T. Reid, "Efficient femtosecond optical parametric oscillators based on aperiodically poled nonlinear crystals," Opt. Lett. **27**, 851–853 (2002).

18. Y. Deng, A. Schwarz, H. Fattahi, M. Ueffing, X. Gu, M. Ossiander, T. Metzger, V. Pervak, H. Ishizuki, T. Taira, T. Kobayashi, G. Marcus, F. Krausz, R. Kienberger, and N. Karpowicz, "Carrier-envelope-phase-stable, 1.2 mJ, 1.5 cycle laser pulses at 2.1 μm," Opt. Lett. **37**, 4973–4975 (2012).

19. M. Conforti, F. Baronio, and C. D. Angelis, "From femtosecond infrared to picosecond visible pulses: temporal shaping with high-efficiency conversion," Opt. Lett. **32**, 1779–1781 (2007).

20. Ł. Kornaszewski, M. Kohler, U. K. Sapaev, and D. T. Reid, "Designer femtosecond pulse shaping using grating-engineered quasi-phase-matching in lithium niobate," Opt. Lett. **33**, 378–380 (2008).

21. C. Langrock, M. M. Fejer, I. Hartl, and M. E. Fermann, "Generation of octave-spanning spectra inside reverse-proton-exchanged periodically poled lithium niobate waveguides," Opt. Lett. **32**, 2478–2480 (2007).

22. T. W. Neely, L. Nugent-Glandorf, F. Adler, and S. A. Diddams, "Broadband mid-infrared frequency upconversion and spectroscopy with an aperiodically poled LiNbO$_3$ waveguide," Opt. Lett. **37**, 4332–4334 (2012).

23. V. J. Hernandez, C. V. Bennett, B. D. Moran, A. D. Drobshoff, D. Chang, C. Langrock, M. M. Fejer, and M. Ibsen, "104 MHz rate single-shot recording with subpicosecond resolution using temporal imaging," Opt. Express **21**, 196–203 (2013).

24. T. Umeki, M. Asobe, Y. Nishida, O. Tadanaga, K. Magari, T. Yanagawa, and H. Suzuki, "Widely tunable 3.4 μm band difference frequency generation using apodized $\chi^{(2)}$ grating," Opt. Lett. **32**, 1129–1131 (2007).

25. A. Bostani, A. Tehranchi, and R. Kashyap, "Engineering of effective second-order nonlinearity in uniform and chirped gratings," J. Opt. Soc. Am. B **29**, 2929–2934 (2012).

26. A. Shirakawa, I. Sakane, M. Takasaka, and T. Kobayashi, "Sub-5-fs visible pulse generation by pulse-front-matched noncollinear optical parametric amplification," Appl. Phys. Lett. **74**, 2268–2270 (1999).

27. D. Herrmann, L. Veisz, R. Tautz, F. Tavella, K. Schmid, V. Pervak, and F. Krausz, "Generation of sub-three-cycle, 16 TW light pulses by using noncollinear optical parametric chirped-pulse amplification," Opt. Lett. **34**, 2459–2461 (2009).

28. B. E. Schmidt, A. D. Shiner, P. Lassonde, J.-C. Kieffer, P. B. Corkum, D. M. Villeneuve, and F. Légaré, "CEP stable 1.6 cycle laser pulses at 1.8 μm," Opt. Express **19**, 6858–6864 (2011).

29. G. Andriukaitis, T. Balciunas, S. Aliauskas, A. Puglys, A. Baltuka, T. Popmintchev, M. Chen, M. M. Murnane, and H. C. Kapteyn, "90 GW peak power few-cycle mid-infrared pulses from an optical parametric amplifier," Opt. Lett. **36**, 2755–2757 (2011).

30. C. Li, D. Wang, L. Song, J. Liu, P. Liu, C. Xu, Y. Leng, R. Li, and Z. Xu, "Generation of carrier-envelope phase stabilized intense 1.5 cycle pulses at 1.75 μm," Opt. Express **19**, 6783–6789 (2011).

31. J. Rothhardt, S. Demmler, S. Hädrich, J. Limpert, and A. Tünnermann, "Octave-spanning OPCPA system delivering CEP-stable few-cycle pulses and 22 W of average power at 1 MHz repetition rate," Opt. Express **20**, 10870–10878 (2012).

32. S. Witte and K. Eikema, "Ultrafast optical parametric chirped-pulse amplification," Selected Topics in IEEE J. Quant. Electron. **18**, 296–307 (2012).

33. G. Cerullo and S. De Silvestri, "Ultrafast optical parametric amplifiers," Review of Scientific Instruments **74**,

1–18 (2003).

34. F. Krausz and M. Ivanov, "Attosecond physics," Rev. Mod. Phys. **81**, 163–234 (2009).

35. P. Colosimo, G. Doumy, C. I. Blaga, J. Wheeler, C. Hauri, F. Catoire, J. Tate, R. Chirla, A. M. March, G. G. Paulus, H. G. Muller, P. Agostini, and L. F. DiMauro, "Scaling strong-field interactions towards the classical limit," Nature Physics **4**, 386–389 (2008).

36. A. Cavalieri, N. Müller, T. Uphues, V. Yakovlev, A. Baltuška, B. Horvath, B. Schmidt, L. Blümel, R. Holzwarth, S. Hendel, M. Drescher, U. Kleineberg, P. M. Echenique, R. Kienberger, F. Krausz, and U. Heinzmann, "Attosecond spectroscopy in condensed matter," Nature **449**, 1029–1032 (2007).

37. A. N. Pfeiffer, C. Cirelli, M. Smolarski, D. Dimitrovski, M. Abu-Samha, L. B. Madsen, and U. Keller, "Atto-clock reveals natural coordinates of the laser-induced tunnelling current flow in atoms," Nature Physics **8**, 76–80 (2011).

38. T. Rohwer, S. Hellmann, M. Wiesenmayer, C. Sohrt, A. Stange, B. Slomski, A. Carr, Y. Liu, L. M. Avila, M. Kalläne *et al.*, "Collapse of long-range charge order tracked by time-resolved photoemission at high momenta," Nature **471**, 490–493 (2011).

39. C. T. Middleton, P. Marek, P. Cao, C.-c. Chiu, S. Singh, A. M. Woys, J. J. de Pablo, D. P. Raleigh, and M. T. Zanni, "Two-dimensional infrared spectroscopy reveals the complex behaviour of an amyloid fibril inhibitor," Nature chemistry **4**, 355–360 (2012).

40. T. Popmintchev, M.-C. Chen, D. Popmintchev, P. Arpin, S. Brown, S. Alisauskas, G. Andriukaitis, T. Balciunas, O. D. Mcke, A. Pugzlys, A. Baltuska, B. Shim, S. E. Schrauth, A. Gaeta, C. Hernndez-Garca, L. Plaja, A. Becker, A. Jaron-Becker, M. M. Murnane, and H. C. Kapteyn, "Bright coherent ultrahigh harmonics in the keV X-ray regime from mid-infrared femtosecond lasers," Science **336**, 1287–1291 (2012).

41. P. Russbueldt, T. Mans, J. Weitenberg, H. D. Hoffmann, and R. Poprawe, "Compact diode-pumped 1.1 kW Yb:YAG Innoslab femtosecond amplifier," Opt. Lett. **35**, 4169–4171 (2010).

42. T. Eidam, S. Hanf, E. Seise, T. V. Andersen, T. Gabler, C. Wirth, T. Schreiber, J. Limpert, and A. Tünnermann, "Femtosecond fiber CPA system emitting 830 w average output power," Opt. Lett. **35**, 94–96 (2010).

43. C. Heese, C. R. Phillips, L. Gallmann, M. M. Fejer, and U. Keller, "Role of apodization in optical parametric amplifiers based on aperiodic quasi-phasematching gratings," Opt. Express **20**, 18066–18071 (2012).

44. C. Heese, A. E. Oehler, L. Gallmann, and U. Keller, "High-energy picosecond Nd:YVO4 slab amplifier for OPCPA pumping," Applied Physics B **103**, 5–8 (2011).

45. M. Conforti, F. Baronio, and C. De Angelis, "Nonlinear envelope equation for broadband optical pulses in quadratic media," Physical Review A **81**, 053841 (2010).

46. C. R. Phillips, C. Langrock, J. S. Pelc, M. M. Fejer, I. Hartl, and M. E. Fermann, "Supercontinuum generation in quasi-phasematched waveguides," Opt. Express **19**, 18754–18773 (2011).

47. D. T. Reid, "Ultra-broadband pulse evolution in optical parametric oscillators," Opt. Express **19**, 17979–17984 (2011).

48. C. R. Phillips, C. Langrock, J. S. Pelc, M. M. Fejer, J. Jiang, M. E. Fermann, and I. Hartl, "Supercontinuum generation in quasi-phase-matched LiNbO$_3$ waveguide pumped by a Tm-doped fiber laser system," Opt. Lett. **36**, 3912–3914 (2011).

49. M. Kolesik and J. V. Moloney, "Nonlinear optical pulse propagation simulation: from maxwell's to unidirectional equations," Physical Review. E **70**, 036604 (2004).

50. C. R. Phillips, J. S. Pelc, and M. M. Fejer, "Parametric processes in quasi-phasematching gratings with random duty cycle errors," J. Opt. Soc. Am. B **30**, 982–993 (2013).

51. R. A. Baumgartner and R. Byer, "Optical parametric amplification," Quantum Electronics, IEEE Journal of **15**, 432–444 (1979).

52. M. Charbonneau-Lefort, B. Afeyan, and M. M. Fejer, "Theory and simulation of gain-guided noncollinear modes in chirped quasi-phase-matched optical parametric amplifiers," J. Opt. Soc. Am. B **27**, 824–841 (2010).

53. O. Gayer, Z. Sacks, E. Galun, and A. Arie, "Temperature and wavelength dependent refractive index equations for MgO-doped congruent and stoichiometric LiNbO$_3$," Appl. Phys. B: Lasers Opt. **91**, 343–348 (2008).

54. I. Shoji, T. Kondo, A. Kitamoto, M. Shirane, and R. Ito, "Absolute scale of second-order nonlinear-optical coefficients," J. Opt. Soc. Am. B **14**, 2268–2294 (1997).

55. R. DeSalvo, A. Said, D. Hagan, E. Van Stryland, and M. Sheik-Bahae, "Infrared to ultraviolet measurements of two-photon absorption and n_2 in wide bandgap solids," IEEE J. Quant. Electron. **32**, 1324–1333 (1996).

56. O. Beyer, D. Maxein, K. Buse, B. Sturman, H. T. Hsieh, and D. Psaltis, "Investigation of nonlinear absorption processes with femtosecond light pulses in lithium niobate crystals," Phys. Rev. E **71**, 056603 (2005).

57. P. Reckenthaeler, D. Maxein, T. Woike, K. Buse, and B. Sturman, "Separation of optical Kerr and free-carrier nonlinear responses with femtosecond light pulses in LiNbO$_3$ crystals," Physical Review B **76**, 195117 (2007).

58. J. R. Schwesyg, M. Falk, C. R. Phillips, D. H. Jundt, K. Buse, and M. M. Fejer, "Pyroelectrically induced photorefractive damage in magnesium-doped lithium niobate crystals," J. Opt. Soc. Am. B **28**, 1973–1987 (2011).

59. M. Charbonneau-Lefort, B. Afeyan, and M. M. Fejer, "Optical parametric amplifiers using nonuniform quasi-phase-matched gratings. II. space-time evolution of light pulses," J. Opt. Soc. Am. B **25**, 683–700 (2008).

60. R. Schiek, "Nonlinear refraction caused by cascaded second-order nonlinearity in optical waveguide structures," J. Opt. Soc. Am. B **10**, 1848–1855 (1993).

61. H. Ishizuki and T. Taira, "Half-joule output optical-parametric oscillation by using 10-mm-thick periodically poled mg-doped congruent linbo3," Opt. Express **20**, 20002–20010 (2012).
62. D. S. Hum, R. K. Route, and M. M. Fejer, "Quasi-phase-matched second-harmonic generation of 532 nm radiation in 25°-rotated, x-cut, near-stoichiometric, lithium tantalate fabricated by vapor transport equilibration," Opt. Lett. **32**, 961–963 (2007).
63. F. Druon, M. Hanna, G. Lucas-Leclin, Y. Zaouter, D. Papadopoulos, and P. Georges, "Simple and general method to calculate the dispersion properties of complex and aberrated stretchers-compressors," J. Opt. Soc. Am. B **25**, 754–762 (2008).
64. M. Charbonneau-Lefort, M. M. Fejer, and B. Afeyan, "Tandem chirped quasi-phase-matching grating optical parametric amplifier design for simultaneous group delay and gain control," Opt. Lett. **30**, 634–636 (2005).
65. C. Lynch, D. Bliss, T. Zens, A. Lin, J. Harris, P. Kuo, and M. Fejer, "Growth of mm-thick orientation-patterned GaAs for IR and THz generation," Journal of Crystal Growth **310**, 5241–5247 (2008).
66. C. R. Phillips, J. Jiang, C. Mohr, A. C. Lin, C. Langrock, M. Snure, D. Bliss, M. Zhu, I. Hartl, J. S. Harris, M. E. Fermann, and M. M. Fejer, "Widely tunable midinfrared difference frequency generation in orientation-patterned gaas pumped with a femtosecond tm-fiber system," Opt. Lett. **37**, 2928–2930 (2012).
67. J. Kiessling, R. Sowade, I. Breunig, K. Buse, and V. Dierolf, "Cascaded optical parametric oscillations generating tunable terahertz waves in periodically poled lithium niobate crystals," Opt. Express **17**, 87–91 (2009).
68. R. Sowade, I. Breunig, I. Camara Mayorga, J. Kiessling, C. Tulea, V. Dierolf, and K. Buse, "Continuous-wave optical parametric terahertz source," Opt. Express **17**, 22303 (2009).
69. C. R. Phillips, J. S. Pelc, and M. M. Fejer, "Continuous wave monolithic quasi-phase-matched optical parametric oscillator in periodically poled lithium niobate," Opt. Lett. **36**, 2973–2975 (2011).
70. C. R. Phillips and M. M. Fejer, "Adiabatic optical parametric oscillators: steady-state and dynamical behavior," Opt. Express **20**, 2466–2482 (2012).
71. K. Vodopyanov, "Optical THz-wave generation with periodically-inverted GaAs," Laser & Photonics Reviews **2**, 11–25 (2008).
72. H. Jang, G. Strömqvist, V. Pasiskevicius, and C. Canalias, "Control of forward stimulated polariton scattering in periodically-poled KTP crystals," Opt. Express **21**, 27277–27283 (2013).

1. Introduction

Quasi-phase-matching (QPM) has been an enabling technology for many frequency conversion schemes and their applications. An important advantage of QPM over conventional birefringent phase-matching (BPM) is the additional capability to design frequency converters having desired properties, such as a broad bandwidth with a custom amplitude or phase profile, while still utilizing the largest nonlinear coefficient of the QPM material. Such capabilities have been made possible by lithographic fabrication techniques, which enable accurate construction of non-uniform QPM gratings containing a wide range of spatial frequency content. Chirped QPM gratings, in which the grating k-vector is varied smoothly and monotonically through the length of the device, have proven to be particularly useful in ultrafast optics, since the corresponding phase-matching bandwidth can be made almost arbitrarily large while maintaining a smooth spectral phase profile.

Chirped QPM gratings have been widely deployed in frequency conversion schemes involving second-harmonic generation (SHG), difference frequency generation (DFG), sum frequency generation (SFG), optical parametric oscillators (OPOs), and related applications [1–25]. Their main role historically has been to broaden the phase-matching bandwidth compared to conventional periodic QPM gratings, without the need to use short crystals with reduced conversion efficiency, tighter focusing, higher intensities, operation close to the damage threshold, or other potential drawbacks. Quite recently, new applications of chirped QPM gratings have emerged, in particular high-gain optical parametric amplification (OPA) [1–6], and high-efficiency adiabatic frequency conversion (AFC) [6–11]. Together, these processes reveal the possibility of achieving essentially arbitrary-bandwidth, high-efficiency optical parametric chirped pulse amplification (OPCPA) within the transparency window of QPM media, while simultaneously suppressing gain-narrowing effects [12]. Such an approach is an important tool for OPA and OPCPA development [1,18,26–33], as well as for the emergent field of attosecond science [34–40], offering high-intensity few-cycle pulse generation at high repetition rates and

in new wavelength regions from comparatively simple and collinear experimental geometries, utilizing power-scalable 1-μm pump lasers [41, 42]. This potential has motivated the development of our mid-IR OPCPA system, which has most recently enabled generation of sub-four-cycle pulses in the mid-IR directly from the OPCPA output [1].

While obtaining arbitrary phase-matching bandwidth is a relatively straightforward process of fabricating a structure with the required range of QPM periods, achieving high-quality ultra-broadband OPA or OPCPA is much more challenging, owing in particular to subtle additional effects which emerge due to the high intensities and strongly nonlinear interactions involved. Indeed, broadband operation in this case requires careful control of the ultrafast dynamics of a nonlinear, spatially inhomogeneous medium. Understanding and manipulating the associated physical processes is very important for the continued advancement of such devices.

In this paper, we examine in detail several nonlinear processes which occur in high-gain and strongly-saturated QPM interactions, and thereby determine the design constraints which must be met by OPCPA systems based on chirped QPM devices to avoid such effects while still supporting broad bandwidths and good conversion efficiency. Throughout the paper, we discuss these constraints in the context of our high repetition rate mid-IR OPCPA system, in particular to explain how we arrived at our most recent OPCPA result [1], which yielded almost a factor of 2 shorter pulse duration compared to our result from a year earlier [5, 43], and promises further improvements in the near future. The physics, design constraints, and system design procedures we develop will be applicable to OPCPA, AFC interactions, and to strongly nonlinear parametric systems in general, especially those involving spatially inhomogeneous phase-matching media.

The paper is arranged as follows. In section 2, we introduce the experimental OPCPA setup reported in [1], explaining its characteristic features. In section 3, we show the fundamental properties of OPA and AFC in chirped QPM devices, as well as corresponding OPCPA design guidelines. In section 4, we discuss transverse beam effects, in particular the existence of gain-guided modes and their suppression in the context of OPCPA. In section 5, we consider random duty cycle (RDC) errors in QPM structures, and the role these imperfections can have on OPCPA performance. In section 6, we examine additional, unwanted mixing processes supported by the $\chi^{(2)}$ nonlinearity, and show how these can be suppressed. In section 7, we describe the effects of group velocity mismatch on saturated chirped-QPM interactions, and the corresponding implications for pulse chirping in order to avoid deleterious effects. With the analysis from the above sections in hand, in section 8 we collect the key OPCPA design constraints, further explain their implications and application to the mid-IR OPCPA system described in section 2, and discuss the results. In appendix B, we provide for convenience a summary of the definitions used in the paper.

2. Experimental system

In this section, we give a brief description of the mid-IR OPCPA system described Ref. [1], in order to motivate and give context to the OPCPA design study performed in this paper. Our system is shown schematically in Fig. 1.

The primary seed laser for the system is a 1.56-μm femtosecond fiber laser (Toptica FFS) which produces 65-fs pulses at 80 MHz and an average power of 250 mW (3.1 nJ). We spectrally broaden this source using a dispersion-shifted telecom fiber (Thorlabs DCF3) to provide > 200-nm bandwidth (corresponding to >1000-nm bandwidth for the 3.4-μm idler), before chirping to few-ps durations via a pair of silicon prisms and a 4f pulse shaper in order to provide a suitable OPCPA seed. This chirping configuration was chosen with compression of the final 3.4-μm idler output of the OPCPA chain in mind. The seed energy reaching the OPCPA chain is 92.5 pJ. The primary pump laser is a 1.064-μm industrial laser (Time-Bandwidth Prod-
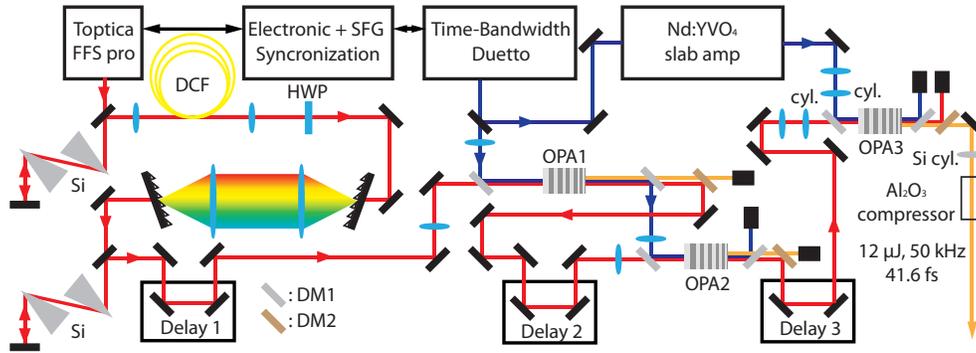
Fig. 1. Schematic overview of the mid-infrared OPCPA setup. DM: dichroic mirrors. DM1: reflective 1064 nm / transmissive 1560 nm & 3400 nm, DM2: reflective 1560 nm / transmissive 3400 nm. The OPA2 and OPA3 amplification stages are seeded by the 1560-nm signal output beams from OPA1 and OPA2, respectively; the 3400-nm idler output beams from OPA1 and OPA2 are discarded. For OPA3, the signal output is discarded, and the idler output is compressed in a bulk sapphire rod.

ucts Duetto) which can produce 12-ps pulses at 50 kHz and an average power of up to 10 W. We split these pulses into two parts, and further amplify one part in a home-built amplifier [44], based on the Innoslab concept [41]. This amplification yields 15.2 W (304 μJ) of power immediately before the final OPA stage, denoted OPA3.

The OPCPA chain consists of three aperiodically poled (i.e. chirped) MgO:LiNbO$_3$ gratings (denoted APPLN), each having the same apodized and chirped grating design [8]; the gratings are 11-mm-long, 1-mm-thick, and 3-mm-wide, with a chirp rate of $\Delta k' = -2.5$ mm^{-2} in order to achieve a broad phase-matching bandwidth spanning the 3- to 4-μm spectral range. All stages are operated in a collinear beam geometry. The first two OPA stages (denoted OPA1 and OPA2) are pumped by the residual Duetto output of 5.7 W (the part not used to seed the Innoslab amplifier). The transmitted pump from OPA1 is used to pump OPA2, so as to maximize the peak power in both stages given the available power. OPA3 is pumped by the output of the Innoslab amplifier. The OPCPA chain is seeded by the signal wave at 1.56-μm, and the amplified signal is propagated through the system until the final OPA stage, after which we extract and compress the collinearly-generated 3.4-μm idler wave. The idler is compressed by low-loss bulk propagation through 50 mm of AR-coated sapphire. These design choices are explained in sections 3-7, and the various constraints are summarized in subsection 8.1. A more detailed account of the experimental setup and results is given in [1].

The compressed idler pulses have a duration of 41.6 fs and an energy of 12 μJ, at a repetition rate of 50 kHz. We currently use uncoated APPLN samples; accounting for these and other linear losses, we estimate an energy of 19 μJ inside OPA3, which represents a reasonable quantum conversion efficiency of 24.5% in the final stage. The study we perform in the following sections explains our improved system layout and design, the limiting factors in terms of OPCPA physics, and points the way towards further improvements in pulse duration and energy.

3. OPCPA in chirped QPM gratings

In this section, we introduce the fundamental properties of chirped QPM gratings for OPCPA. In subsection 3.1, we introduce general coupled-wave equations which will be used later as the starting point to establish several system design constraints. In subsection 3.2 we recapitulate the interaction between plane- and continuous-wave (cw) pump, signal, and idler fields in the

chirped QPM OPA regime. In subsection 3.3, we discuss pump depletion (saturation) in this regime, and corresponding implications for OPCPA system layout. The paper involves various definitions and symbols: for convenience, these are summarized in appendix B.

3.1. Coupled-envelope equations

OPCPA ideally involves the interaction between individual signal and idler frequency components, and a corresponding region of the pump pulse in the time domain. However, other mixing processes are possible and can perturb the desired interaction. In recent years, general single-envelope descriptions of $\chi^{(2)}$ mixing processes have emerged that account for all of the interactions between co-propagating waves [45–47]. In Ref. [46], interactions in QPM waveguides were considered, accounting for both $\chi^{(2)}$ and $\chi^{(3)}$ processes in a general frequency-domain approach for the first time; all orders of QPM, multiple waveguide modes (with a single envelope used to describe the spectrum of each mode), and a re-calibration of the $\chi^{(3)}$ coefficients (both instantaneous and Raman nonlinearities) were included. We found that this level of generality was needed to accurately model previous supercontinuum generation results [46, 48].

In the case of OPCPA, the chirped structure of the pulses involved means that even for very broad bandwidths, the electric field can be split up naturally into multiple envelopes. Here, we present a multiple-envelope model allowing for any number of additional envelopes corresponding to various sum and difference frequency mixing between the signal, idler and pump envelopes. By accounting for all the possible mixing processes between these envelopes, the resulting dynamics can be captured with generality comparable to single-envelope techniques, but with the advantage of clearly modelling and isolating the important processes involved, and without the need to resolve the optical carrier frequency.

Building on the frequency-domain approach of Ref. [46] and the general formalism which has been shown for unidirectional wave propagation problems as an important extension of conventional slowly-varying envelope approximations [49], we arrive at a set of coupled-envelope equations describing the extraordinary-wave (e-wave) polarization components of the electric field in the nonlinear crystal, assuming paraxial and collinear beams and a uniaxial crystal:

$$\frac{\partial \tilde{A}_j(\omega - \omega_j)}{\partial z} + \hat{L}_j(\omega)\tilde{A}_j(\omega - \omega_j) = -i\frac{\omega^2 u(\omega)}{k_e(\omega)c^2\varepsilon_0}\mathscr{F}\left[P_{NL,j}\right](\omega - \omega_j). \tag{1}$$

In this equation, coordinate z represents the propagation direction and x is along the c-axis of the crystal. k_o and k_e denote the frequency-dependent propagation constants for the o- and e-wave polarizations. The field envelope for wave j is denoted A_j, and tilde's denoting frequency domain envelope quantities [46]. ω_j is the carrier frequency of wave j, and ω (lower-case) represents absolute optical frequencies. $P_{NL,j}$ is the nonlinear polarization driving wave j. $\mathscr{F}$ is the Fourier transform, defined as $\tilde{g}(\Omega) = \mathscr{F}[g(t)](\Omega) = \int_{-\infty}^{\infty} g(t)\exp(-i\Omega t)dt$. $\hat{L}_j$ denotes the (frequency-dependent) diffraction and dispersion operator for wave j, and is given by

$$\hat{L}_j(\omega) = \frac{i}{2}\left(\frac{k_e(\omega)}{k_o(\omega)^2}\frac{\partial^2}{\partial x^2} + \frac{1}{k_e(\omega)}\frac{\partial^2}{\partial y^2}\right) + i\left[k_e(\omega) - k_e(\omega_j) - \frac{\omega - \omega_j}{v_{ref}}\right]. \tag{2}$$

We use a moving coordinate system based on a reference group velocity v_{ref}, which is typically chosen to be a weighted average of the pump, signal, and idler group velocities. The total, real-valued electric field $E(x, y, z, t)$ can be expressed in terms of the envelopes A_j in the frequency domain according to

$$\tilde{E}(\omega)u(\omega) = \frac{1}{2}\sum_j \tilde{A}_j(\omega - \omega_j)e^{-ik_e(\omega_j)z}, \tag{3}$$

where $u(\omega)$ appearing in Eqs. (1) and (3) is the Heaviside step function; the form of these equations arises because we assume A_j are (shifted) analytic signals (i.e. spectral components equal to zero for *absolute* optical frequencies $\omega < 0$).

The nonlinear polarization for each wave is given by

$$\frac{P_{NL,j}(t)}{\varepsilon_0} = \frac{d_{33}}{2} \sum_{k,l} \sum_m \bar{d}_m \left[\left(X_{j,kl} e^{+i(\Delta k_{j,kl}z - m\phi_G(z))} \right) A_k(t) A_l(t) \right.$$
$$\left. + \left(2X_{k,jl} e^{-i(\Delta k_{j,kl}z - m\phi_G(z))} \right) A_k(t) A_l(t)^* \right], \tag{4}$$

where this form accounts for all possible $\chi^{(2)}$ mixing processes between the envelopes included in the model, implicitly assuming an all-e-wave interaction for simplicity, that all other envelopes (corresponding to different sums and differences of the included carrier frequencies) are negligible, and that $\chi^{(2)}$ is non-dispersive. Note that dependencies of both the nonlinear polarization and the fields on spatial coordinates have been suppressed for compactness. The coefficients $X_{j,kl}$ specify which waves are coupled to each other according to energy conservation, and hence satisfy

$$X_{j,kl} = \begin{cases} 0, & \omega_j \neq \omega_k + \omega_l \\ 1, & \omega_j = \omega_k + \omega_l \end{cases}. \tag{5}$$

For numerical calculations, of course, terms with $X_{j,kl} = 0$ can be ignored, and duplicated terms can be calculated once and multiplied by two. The phase mismatches Δk appearing in Eq. (4) are given by

$$\Delta k_{j,kl} = k_e(\omega_j) - k_e(\omega_k) - k_e(\omega_l). \tag{6}$$

For a QPM interaction, we can express the spatially-varying nonlinear coefficient in terms of its Fourier orders, even for cases with an aperiodic grating. Following [50], $d(z)$ is given by

$$\frac{d(z)}{d_{33}} = \text{sgn}\left[\cos(\phi_G(z)) - \cos(\pi D(z))\right]$$
$$\equiv \bar{d}_0(z) + \sum_{\substack{m=-\infty \\ m \neq 0}}^{\infty} \bar{d}_m(z) \exp\left(im\phi_G(z)\right) \tag{7}$$

where m denotes the Fourier orders of the grating, the grating phase is $\phi_G(z) = \int_0^z K_g(z')dz'$ for local grating k-vector $K_g(z)$, d_{33} is the relevant nonlinear coefficient of the material for an all-e-wave interaction, and $D(z)$ is local grating duty cycle. The Fourier coefficients are given by $\bar{d}_0 = (2D(z) - 1)$ and $\bar{d}_m = 2\sin(\pi m D(z))/(\pi m)$ for $m \neq 0$. Note that the signs of the $\pm[\Delta k_{j,kl}z - m\phi_G(z)]$ phases in Eq. (4) are needed in order to satisfy energy conservation for each of the individual interactions involved (i.e. a particular set of envelopes $\{j, k, l\}$ and a particular QPM order m). The coefficients $X_{j,kl}$ and the form of Eqs. (1) and (4) mean that all interactions involving only the envelopes included in the model are accounted for, and that the full system of equations conserves energy.

3.2. Quasi-cw mixing in the undepleted-pump regime

While Eq. (1) is very general, simplified sets of equations are also useful in order to gain insight into the processes involved. In this subsection, we model plane-wave and quasi-cw interactions between the three nominal envelopes (pump, signal, and idler), including only the first QPM

order. Under these approximations, Eq. (1) can be reduced to the following, more familiar set of coupled-wave equations [8]:

$$\frac{dA_{i,s}}{dz} = -i\frac{\omega_{i,s}\left(d_{33}\bar{d}_1\right)}{n_{i,s}c}A_p A_{s,i}^* \exp\left[-i\int_0^z \Delta\beta(z')dz'\right] \tag{8a}$$

$$\frac{dA_p}{dz} = -i\frac{\omega_p\left(d_{33}\bar{d}_1\right)}{n_p c}A_i A_s \exp\left[+i\int_0^z \Delta\beta(z')dz'\right], \tag{8b}$$

where $\Delta\beta = k_e(\omega_p) - k_e(\omega_s) - k_e(\omega_i) - K_g(z)$, and n_j denotes the refractive index of wave j. The effective first-order-QPM nonlinear coefficient is $d_{\text{eff}} = d_{33}\bar{d}_1$, where $\bar{d}_1 = 2/\pi$ for a 50-% duty cycle grating.

Following [8], based on the coefficients in these equations, we can define coupling rates satisfying $\gamma_p^2 = (\omega_i\omega_s d_{33}^2\bar{d}_1^2)/(n_i n_s c^2)|A_p(z=0)|^2$ and $\gamma_s^2 = (\omega_i\omega_p d_{33}^2\bar{d}_1^2)/(n_i n_p c^2)|A_s(z=0)|^2$. From [2], the OPA power gain for the input signal wave in a long, linearly chirped grating assuming a strong and undepleted pump and zero input idler is given by

$$G_s = \exp\left(2\pi\frac{\gamma_p^2}{|\Delta k'|}\right) \tag{9}$$

where $\Delta k' = -dK_g/dz$ is the QPM chirp rate (the rate of change of the phase mismatch with respect to z).

For OPCPA, we must account for the time-dependent pump intensity and the temporal localization of signal and idler spectral components. In the limit of highly chirped pulses, there is a mapping between signal and idler frequencies and time, and hence pump intensity, resulting in gain narrowing effects. In this chirped-pulse limit, a frequency-dependent coupling rate between signal and idler fields can be defined to account for such effects. We explained this procedure in the context of chirped QPM OPCPA in [12], arriving at the following general expression for the frequency-dependent gain:

$$G_s(\Omega) \approx \exp\left[2\int_{z_{tp,1}(\Omega)}^{z_{tp,2}(\Omega)}\sqrt{\gamma_p(\Omega)^2 - \left(\frac{\Delta k_0(\Omega) - K_g(z)}{2}\right)^2}\,dz\right], \tag{10}$$

the form of which is reminiscent of the OPA gain rate in unchirped structures [51]. The frequency-dependent signal-idler coupling coefficient is given by

$$\gamma_p(\Omega)^2 = \frac{(\omega_i - \Omega)(\omega_s + \Omega)(\bar{d}_1 d_{33})^2}{n_e(\omega_i - \Omega)n_e(\omega_s + \Omega)c^2}\frac{2}{n_e(\omega_p)\varepsilon_0 c}I_p(\tau_s(\omega_s + \Omega)), \tag{11}$$

$I_p(t)$ is the pump intensity, the single-frequency-argument material phase mismatch is given by

$$\Delta k_0(\Omega) = k_e(\omega_p) - k_e(\omega_s + \Omega) - k_e(\omega_i - \Omega), \tag{12}$$

$\tau_s(\omega_s + \Omega)$ denotes the delay at which signal frequency $\omega_s + \Omega$ is localized, and $z_{tp,j}(\Omega)$ denote the 'turning points' in Eq. (10), i.e. the points at which the integrand is zero. Since this integrand is the gain coefficient in an unchirped OPA device, these turning points represent the points where the local phase-mismatch is large enough that the OPA gain coefficient vanishes. Another important variable is $z_{pm}(\Omega)$, defined as frequency-dependent phase-matching point satisfying

$$\Delta k_0(\Omega) - K_g(z_{pm}(\Omega)) = 0. \tag{13}$$

Further insight into these quantities is given in Fig. 2, where we show an overview of chirped-QPM OPA interactions.

The form for the gain in Eq. (10) can be used to find globally optimal chirp profiles to obtain custom gain (and phase) spectra, as shown via a convex optimization framework in [12]. Here, we use simplified design criteria for this aspect of the problem, but the general procedures of [12] can be applied provided that the additional constraints we will discuss in this paper are addressed. An important property of Eq. (10), described in more detail in Ref. [2], is that gain takes place between the 'turning points' $z_{tp,1}(\Omega)$ and $z_{tp,2}(\Omega)$. For a linear chirp rate $\Delta k' = -dK_g/dz = $ constant, there is a dephasing length, which is the distance required to go from perfect phase-matching ($\Delta k_0 - K_g = 0$) to zero amplification rate ($|\Delta k_0 - K_g| = 2\gamma_p$). This dephasing length is given by

$$L_{\mathrm{deph}} = \frac{2\gamma_p}{|\Delta k'|}. \tag{14}$$

We can define an OPA bandwidth as the range of frequencies which experience complete amplification according to Eq. (10). Assuming for simplicity a linear, unapodized chirp profile and approximating $\gamma_p(\Omega) \approx \gamma_{p0}$ for peak coupling coefficient γ_{p0}, we find the following for the range of material phase mismatches that are fully amplified:

$$\Delta k_{\mathrm{OPA}} \approx |\Delta k'|L - 4\gamma_{p0}$$
$$\equiv \Delta k_{BW} - 4\gamma_{p0}. \tag{15}$$

In turn, the material dispersion determines the spread of the phase mismatch for a given pump wavelength and signal/idler spectral region of interest. Given a desired gain and bandwidth, Eqs. (9) and (15) can be used to determine the grating length L and chirp rate $\Delta k'$ required as a function of the coupling coefficient γ_{p0}. For any given nominal grating design, it is essential to also append apodization regions in order to obtain a useful gain spectrum, as discussed in [8].

The value of γ_{p0} is related to the peak intensity of the pump; a useful relation for the signal gain coefficient in terms of the pump peak power P_{pk}, confocal parameter ξ_p, and phase-matching bandwidth is

$$\Lambda_{R,p} \equiv \frac{\gamma_{p0}^2}{|\Delta k'|} = \frac{4\omega_i\omega_s\omega_p(\bar{d}_1 d_{33})^2}{\pi\varepsilon_0 c^4 n_i n_s} \frac{\xi_p P_{pk}}{|\Delta k'|L}. \tag{16}$$

where $\xi_p = L/(k_p w_p^2)$, $\Lambda_{R,p}$ is the peak gain factor, and Eq. (16) implicitly assumes a pump with $M^2 = 1$ and $1/e^2$ beam radius w_p. Equation (16) can provide intuition for some of the required experimental conditions for a given peak small-signal gain $G_s = \exp(2\pi\Lambda_{R,p})$, especially in cases where $\Delta k_{\mathrm{OPA}} \approx |\Delta k'|L$ (although this latter approximation is not always accurate).

3.3. Quasi-cw mixing with saturation effects

Another important aspect of the problem is the effects of saturation. A key feature of chirped QPM devices is adiabatic frequency conversion (AFC) [6, 7], which in the context of OPA enables a conversion efficiency of the pump to the sum of the signal and idler which asymptotes to 100% with respect to both the pump and signal input intensities, provided that the chirp rate is sufficiently slow with respect to the coupling between the waves, and that the range of grating k-vectors is sufficiently large. AFC was recently studied in detail theoretically for the general nonlinear three-wave mixing cases [8, 9]. The essentially arbitrary conversion efficiencies predicted by simplified three-wave models is made challenging by several practical constraints such as limits on how strong the coupling between the fields can be made, as well as the onset of additional, unwanted processes. We discuss such processes in subsequent sections.
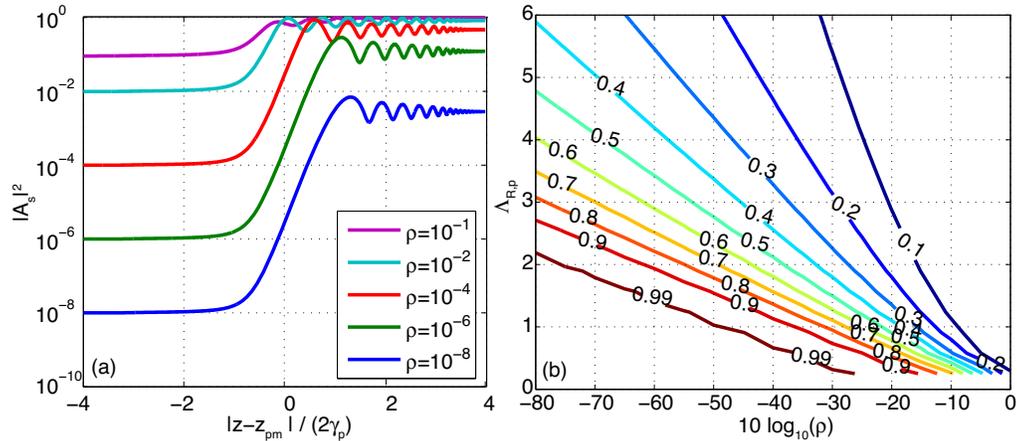
Fig. 2. (a) Example evolution of the three waves in a cw OPA interaction. For small ρ, the amplification corresponds closely to Eqs. (9) and (10). For larger ρ, the interaction approaches the adiabatic frequency conversion case [8, 9], and for $\rho \gg 1$ (corresponding to DFG or SFG rather than OPA), correspond to the case considered in [7]. The predicted conversion efficiency increases with both $\Lambda_{R,p}$ and ρ, as can be seen from (b). The turning points $z_{tp,j}$ appearing in Eq. (10) are the two points where the normalized position coordinate $(z - z_{pm})/(2\gamma_p) = \pm 1$: the $\rho = 10^{-8}$ curve in the figure clearly shows that the exponential gain takes place between these two points. Note also that z_{pm} is frequency dependent due to the dispersion of the material, so different wavelengths are amplified around different longitudinal positions. (b) Simulated pump depletion $\eta_p = |A_p(L)/A_p(0)|^2$ as a function of $\Lambda_{R,p}$ (which determines the small-signal OPA gain) and ρ (which denotes the ratio of input signal and pump photon fluxes, and hence how much gain is required in order to saturate the pump). Contours are labelled with values of η_p. The grating length is chosen such that $L \gg 2L_{\mathrm{deph}}$ in each case [L_{deph} defined in Eq. (14)], and hence has L negligible impact on the pump depletion .

Important characteristic quantities of the three-wave mixing interaction [see Eqs. (8)] are $\Lambda_{R,p} = \gamma_p^2/|\Delta k'|$ and $\Lambda_{R,s} = \gamma_s^2/|\Delta k'|$, and $\rho = N_s(0)/N_p(0)$, where $N_j(z)$ denote the photon fluxes of wave j. It can be shown that $\Lambda_{R,s} = \rho\Lambda_{R,p}$. In the case of a strong signal and weak pump (i.e. $\Lambda_{R,s} > 1$ and $\rho \gg 1$), the pump depletion, defined as $\eta_p = |A_p(L)/A_p(0)|^2$, can be approximated as $\eta_p = \exp(-2\pi\Lambda_{R,s})$ [7].

For OPA, we will generally have $\Lambda_{R,p}$ of order unity. Therefore we show in Fig. 2(b) the predicted pump depletion η_p in terms of $\Lambda_{R,p}$ and ρ, for a suitably apodized nominally linearly chirped QPM grating, modelling a spectral component phase-matched in the middle of the grating. Example curves showing propagation of the seeded signal wave versus position in the grating are also shown in Fig. 2(a) for several values of ρ at constant $\Lambda_{R,p} = 2$ to illustrate the process being modelled.

Figure 2 can provide guidelines for the values of ρ required in a final power amplifier stage in order to effectively saturate the pump. For example, obtaining a peak conversion efficiency of 80% at a reasonable small-signal gain parameter of $\Lambda_{R,p} \approx 2$ [corresponding to $G_s = \exp(2\pi\Lambda_{R,p}) \approx 2.9 \times 10^5$] requires a corresponding value of $\rho = 10^{-2}$, which then places constraints on pre-amplifier stages to achieve such an input photon flux. If the input photon flux is limited to $\rho = 10^{-3}$ by the pre-amplifier properties, 80% peak conversion efficiency requires $\Lambda_{R,p} = 3$, which may be challenging in practice (for example due to the effects discussed in section 5), and will also lead to additional noise amplification. Achieving such a high peak

conversion efficiency (i.e. corresponding to the peak of the pump intensity profile in space and time) is important, since the total efficiency will be lower (unless using shaped, e.g. flat-top beam and pulse profiles). Based on these considerations, combined with estimations of overall system performance via simulations based on Eq. (1), as well as the effects considered in later sections of this paper, we split our OPCPA system into three OPA stages, as depicted in Fig. 1. The stages have low pump depletion in OPA1, moderate depletion in OPA2, and substantial depletion in OPA3. We summarize the various system design considerations in subsection 8.1.

Concerning the applicability of Fig. 2, the use of chirped pulses helps to support the assumption of a series of continuous wave interactions [see Eq. (10) for example; we revisit this point in more detail in section 7]. With the use of sufficiently wide beams (while maintaining the required intensities), diffraction can be neglected [see also section 4]. However, even under these conditions, the interaction is still complicated by the temporally and transverse-spatially varying intensities of the pump and signal beams. To obtain quantitative predictions of total system conversion efficiency, numerical simulations [see Eq. (1)] are required. Our focus in this paper is on establishing the relevant physics and constraints, which can then guide more detailed numerical simulations or adjustments of experimental conditions, with which performance can be optimized around a nominal system layout.

4. Transverse beam effects: suppression of gain guided modes

The plane-wave physics discussed in section 3 can break down due to non-collinear gain-guiding effects. Gain guiding is a general feature of OPA, but has unique properties for the case of chirped QPM gratings, due to the combination of transverse spatial walk-off of the signal and idler waves and dephasing due to the QPM chirp [3]. Under certain conditions [3,52], non-collinear gain-guided modes can exist where the signal and idler fields adapt during amplification to the QPM grating chirp, enabling amplification over long distances. As a result, the overall gain of such modes can greatly exceed that of the desired collinear OPA interaction. If the modes are seeded by quantum noise, this process results in a large increase in the optical parametric generation (OPG) background of the system. If the modes are seeded by the desired signal or idler wave, the result can be a reduction in beam quality. While the noise content at the output of the device can be partly reduced by spatial filtering, eventually the noise can be amplified to the point where it saturates the pump. It is thus critical in designing an OPCPA system to ensure that these gain-guided modes are suppressed. The essential physics of these gain-guided modes was considered in [3,52], and can be modelled using Eq. (1) assuming idler, signal and pump waves, and neglecting dispersion. Here, we consider the case of broadband OPCPA: we show that with proper system design, gain guided modes can be fully suppressed, enabling high-noise-contrast amplification [1].

4.1. Non-collinear phase-matching conditions

We first introduce non-collinear phase-matching in the context of QPM devices. We assume a plane-wave interaction with k-vectors $\mathbf{k}_j$ for $j \in \{i, s, p\}$ and a grating k-vector $\mathbf{K}_g$. Each $\mathbf{k}_j$ satisfies $|\mathbf{k}_j| = k(\omega_j)$, where $k(\omega_j)$ is one of the propagation constants associated with the direction of $\mathbf{k}_j$. The vector phase mismatch is given by

$$\Delta \mathbf{k} = \mathbf{k}_p - \mathbf{k}_s - \mathbf{k}_i - \mathbf{K}_g \qquad (17)$$

This equation can support phase-matching ($\Delta \mathbf{k} = \mathbf{0}$) for both collinear and non-collinear signal and idler waves. We assume $\mathbf{k}_p = k_p \hat{\mathbf{z}}$ and $\mathbf{K}_g = K_g \hat{\mathbf{z}}$ for scalars $k_p = k_e(\omega_p)$ and K_g. Phase-matching along the transverse coordinates x and y implies that the transverse components of $\mathbf{k}_i$ and $\mathbf{k}_s$ are equal and opposite. The z-component of the resulting phase mismatch can be written as a function of the transverse spatial frequency components of the signal. As before,

we assume a uniaxial crystal, extraordinary-polarized waves, and small propagation angles with respect to the c-axis, resulting in

$$\frac{\mathbf{k}_j \cdot \hat{\mathbf{z}}}{k_e} \approx 1 - \frac{1}{2}\left[\left(\frac{\mathbf{k}_j \cdot \hat{\mathbf{x}}}{k_o}\right)^2 + \left(\frac{\mathbf{k}_j \cdot \hat{\mathbf{y}}}{k_e}\right)^2\right]. \tag{18}$$

Since the magnitudes of the transverse spatial frequencies for the signal and idler are equal, it is useful to define $k_x = \mathbf{k}_s \cdot \hat{\mathbf{x}}$ and $k_y = \mathbf{k}_s \cdot \hat{\mathbf{y}}$. By applying these definitions and substituting Eq. (17), the z component of the phase mismatch can be written as

$$\Delta\mathbf{k} \cdot \hat{\mathbf{z}} \approx \Delta\beta + \sum_{j=i,s}\left[\frac{k_e(\omega_j)}{2k_o(\omega_j)^2}k_x^2 + \frac{1}{2k_e(\omega_j)}k_y^2\right] \tag{19}$$

where $\Delta\beta = k_e(\omega_p) - k_e(\omega_s) - k_e(\omega_i) - K_g$ is the collinear phase mismatch introduced in Eqs. (8a) and (8b). With some additional assumptions, Eq. (19) can be simplified significantly. If we neglect the anisotropy of the material (via the substitution $k_o \to k_e$), define the resulting magnitude of the transverse components of the k-vectors as $k_\perp = (k_x^2 + k_y^2)^{1/2}$, simplify the resulting coefficients of $k_\perp$ with the approximation $k_i + k_s \approx k_p$, and define a geometric mean angle according to

$$\theta_{is} = \pm\frac{|k_\perp|}{\sqrt{k_e(\omega_i)k_e(\omega_s)}}, \tag{20}$$

then Eq. (19) can be simplified as

$$\Delta\mathbf{k} \cdot \hat{\mathbf{z}} \approx \Delta\beta + \frac{k_e(\omega_p)}{2}\theta_{is}^2. \tag{21}$$

From Eqs. (19) and (21), $\Delta\mathbf{k} \cdot \hat{\mathbf{z}} > \Delta\beta$. Hence, non-collinear phase-matching can be obtained whenever $\Delta\beta < 0$ (within the limits of the small-angle approximation). Note that the phase-matching angle $\theta_{is}(z,\Omega)$ is frequency-dependent, mainly due to the frequency dependence of $\Delta\beta(z,\Omega)$. Frequency dependencies have been suppressed in the above equations for compactness. Note also that in a chirped QPM grating, $\Delta\beta(z,\Omega)$, and hence the phase-matching angle $\theta_{is}(z,\Omega)$, changes with position, and hence the required mean angle of the signal and idler fields must be able to evolve with position as well for amplification to continue; it turns out that this evolution is connected with the size of the pump beam.

4.2. Non-collinear gain-guiding cut-offs

The gain-guided modes supported in chirped QPM devices were considered experimentally and theoretically in [3], and then in additional theoretical detail in [52]. The main processes which determine the gain rate are: the rate of spatial walk-off, determined by the size of the pump beam and by the phase-matched signal and idler angles; the rate of dephasing, determined by the QPM chirp rate; and the coupling rate between the signal and idler fields, given by γ_p. We can thus define a gain distance $L_g = \gamma_p^{-1}$, a walk-off distance $L_{wo} = w_p/\theta_{is}$, and a dephasing distance $L_{\text{deph}} = 2\gamma_p/|\Delta k'|$ [see also Eq. (14)]. This dephasing distance can be understood in the context of Eq. (10): it is the distance required for the integrand to go from its peak, with $(\Delta k_0 - K_g) = 0$, to zero, with $(\Delta k_0 - K_g) = 2\gamma_p$ (for a plane-wave interaction).

The exponential gain rate Γ of the gain-guided modes can be normalized to the maximum possible gain rate γ_p associated with collinear, plane-wave propagation. Figure 3(a), adapted from [3], shows this normalized gain rate (for the electric field) as a function of $L_g/L_{wo} = \theta_{is}/(\gamma_p w_p)$ for several values of $L_{\text{deph}}/L_g = 2\gamma_p^2/|\Delta k'| = 2\Lambda_{R,p}$. The quantity L_g/L_{wo} can be
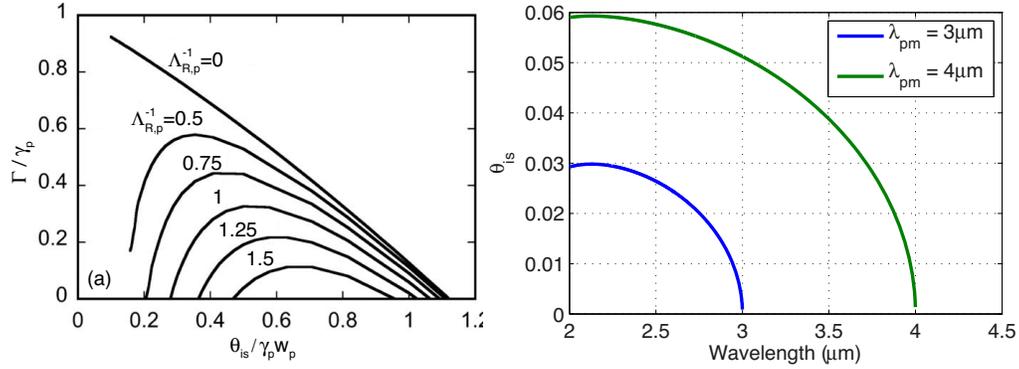
Fig. 3. (a) Simulated normalized gain rate Γ/γ_{p0} of non-collinear gain guided modes, for different normalized angles and values of $\Lambda_{R,p}$. The $\Lambda_{R,p}^{-1} = 0$ case corresponds to an unchirped grating. This figure is adapted from Fig. 2 of [3] and Fig. 12 of [52], with minor modifications to notation. (b) Geometric mean angle θ_{is} versus idler wavelength, for two particular grating k-vectors (chosen to satisfy collinear phase-matching for 3 or 4 μm). The maximum angle occurs at degeneracy.

viewed as a normalized angle, $\bar{\theta} = \theta_{is}/(w_p\gamma_p)$, while $\Lambda_{R,p}$ determines the overall small-signal plane-wave gain, as discussed in section 3.

For sufficiently large phase-matching angles, gain guiding is suppressed because the signal and idler beams walk off the pump faster than they are amplified; for sufficiently small angles, gain guiding is suppressed in the case of chirped QPM gratings because the beams are dephased faster than they walk off the pump [3]. It is this latter property that allows the modes to be suppressed in practice. From Fig. 3, an approximate condition for the gain to be cut-off is

$$\frac{\theta_{is}}{\gamma_p w_p} \lesssim \frac{1}{\pi \Lambda_{R,p}}. \tag{22}$$

This condition can be expressed as $L_{\text{deph}}/L_{wo} < (2/\pi)$, i.e. that the waves dephase before they walk off the pump.

Fig. 3(a) and Eq. (22) show that sufficiently small normalized phase-matching angles are required in order to suppress gain guided modes. Therefore, to see how to obtain this condition in practice, we next determine the range of phase-matching angles supported by the crystal, for a given QPM grating profile. The range of $K_g(z)$ associated with the nominal part of the grating (i.e. excluding apodization regions) is determined primarily by the required spectral bandwidth, although it depends on γ_p as well [see Eq. (15)]. For a given material and pump wavelength, there is a range of the material phase mismatch $\Delta k_0(\Omega)$ [see Eq. (12)]. For each frequency shift Ω, the largest phase-matching angle is the one corresponding to the most-negative value of $\Delta\beta(z,\Omega)$, and hence to the largest grating k-vector contained in the nominal grating profile, which we denote $K_{g,\text{max}}$; if for a particular frequency $\Delta\beta(z,\Omega) > 0$, then no gain-guided modes are supported for that frequency. We therefore arrive at the largest phase-matching angle associated with each frequency shift Ω from some chosen carrier frequency:

$$\theta_{is,\text{max}}(\Omega) \approx \text{Re} \sqrt{\frac{2(K_{g,\text{max}} - \Delta k_0(\Omega))}{k_p}}, \tag{23}$$

Fig. 3(b) shows the geometric mean angle θ_{is} as a function of idler wavelength, assuming a 1064-nm pump and an MgO:LiNbO$_3$ QPM grating, for two grating k-vectors, chosen to

satisfy collinear phase-matching of 3 or 4 μm [53]. In a grating supporting amplification across this spectral range, the curve corresponding to 4 μm would closely represent $\theta_{is,\max}$, up to a correction to the range of grating k-vectors needed based on Δk_{OPA} given in Eq. (15). It is useful to note that for the chosen configuration, $\theta_{is,\max}$ corresponds to degeneracy ($\lambda_i = \lambda_s = 2\lambda_p$).

Quantum noise seeds the amplifier at all temporal and spatial frequencies, and we thus require that Eq. (22) be satisfied for *all* frequencies Ω, not just those we are trying to amplify, in order to fully suppress gain-guided modes. For a collinear interaction, a given material, and a given pump wavelength, $\theta_{is,\max}(\Omega)$ is essentially fixed by the required gain bandwidth (since this determines the range of grating k-vectors required). For the purposes of OPCPA system design, the remaining degree of freedom to satisfy Eq. (22) is the factor $\gamma_p w_p$, which must be sufficiently large. Since γ_p^2 is proportional to pump intensity, $(\gamma_p w_p)^2$ is proportional to the peak power of the pump, independent of its beam size. Thus, suppression of gain guided modes requires using a pump of sufficient peak power. To quantify this constraint, we substitute Eq. (23) into Eq. (22) and express $\gamma_p w_p$ in terms of the pump peak power, which yields

$$P_{pk} > \frac{\pi^3 \varepsilon_0 n_i n_s n_p c^3}{4 \omega_i \omega_s d_{33}^2 \overline{d}_1^2} \left(\Lambda_{R,p} \theta_{is,\max} \right)^2, \tag{24}$$

where the signal and idler quantities in this equation should be evaluated at the frequencies corresponding to $\theta_{is,\max}$. We have written Eq. (24) in terms of $\Lambda_{R,p}$ since this gain factor is fixed by the desired OPCPA gain.

4.3. Implications for OPCPA

Consider an example with a 1.064-μm pump pulse and a 50%-duty-cycle QPM grating in an MgO:LiNbO$_3$ crystal. The relevant nonlinear coefficient for OPA is $d_{33} \approx 19.5$ pm/V [54]. For a range of K_g satisfying phase-matching between 3- and 4-μm, $\max(K_g) \approx 2.198 \times 10^5$ m^{-1}, which results in a maximum angle $\theta_{is,\max} \approx 0.06$. This angle occurs at pump degeneracy, so the corresponding signal and idler frequencies are $\omega_i = \omega_s = \omega_p/2$. For these parameters, Eq. (24) can be expressed as

$$P_{pk} > (0.56\,\mathrm{MW}) \times \Lambda_{R,p}^2. \tag{25}$$

For peak powers below this level, there will exist a finite range of signal frequencies which can excite gain-guided modes, and thereby experience excessive gain through non-collinear phase-matching. Note that Eq. (25) should be satisfied both for pre-amplifier as well as power-amplifier stage(s).

For Gaussian pump pulses with 12-ps FWHM duration and an energy of 400 μJ, the peak power is 31.3 MW. If 10% of the pulse is used for a pre-amplifier stage, Eq. (25) can be satisfied, within a good margin, while still obtaining high gain (e.g. $\Lambda_{R,p} > 2$). In contrast, with a 100-μJ pump such as the one used in our earlier OPCPA experiments [4] (prior to the implementation of an additional amplifier [44]), satisfying Eq. (25) in a high-gain pre-amplifier stage is quite challenging. In our current OPCPA system shown in Fig. 1, the average powers reaching OPA1, OPA2, and OPA3 are 5.7 W, 3.8 W, and 15.2 W, respectively. The peak power inside the (uncoated) crystals is relevant for considering gain-guided mode properties; these internal peak powers are approximately 7.7 MW, 5.1 MW, and 20.6 MW, respectively. Operation at 50 kHz and re-using the transmitted pump from OPA1 to pump OPA2 ensured that we are able to satisfy Eq. (25) in each OPA stage, even for relatively large values of $\Lambda_{R,p} \sim 3$. Experimentally, we observe no evidence of gain-guided mode related effects, and demonstrate good OPG properties of the overall system (as discussed in more detail in [1]), indicating that we have indeed suppressed these modes.

5. Role of QPM duty cycle errors

In the previous section, we considered an unwanted effect which can arise due to the use of finite-sized beams. In the following sections, we consider plane-wave interactions, but go beyond the three-wave mixing processes modelled by Eqs. (8a) and (8b). We first consider the effects on OPCPA of random duty cycle (RDC) errors in the QPM grating. We recently studied such effects in detail for several device configurations [50], including parasitic pump SHG in the context of OPCPA. Here, we review the relevant results of [50], and then expand on the analysis for the specific case of OPCPA. Note that while our focus in this paper is on the case of chirped QPM gratings, RDC errors are relevant for OPCPA employing both chirped and unchirped gratings, and explain the intense green light typically generated in 1-μm-pumped QPM-based OPCPA systems; our results in this section are applicable to both chirped and unchirped gratings.

5.1. Essential features of QPM gratings with RDC errors

A schematic of RDC errors is depicted in Fig. 4(a). For these types of errors, the statistics of the QPM domain boundaries (from sample to sample) are assumed to be independent, identical, normal distributions. The mean boundary positions (corresponding to the nominal grating design) are denoted $\mathbf{z}_0[n]$ for boundary n (element n of vector $\mathbf{z}_0$), and their standard deviations are σ_z. As an example of this notation, for a periodic 50-% duty cycle grating with period $2l_D$ and domain length l_D, $\mathbf{z}_0[n] = nl_D$. RDC errors lead to a pedestal in the spatial frequency spectrum of the grating which is approximately flat after performing an ensemble-average over many gratings with different random errors.

To quantify the pedestal, we state the ensemble average of the spatial frequency spectrum of the QPM grating, denoted $\left\langle |\tilde{g}_{\mathbf{z}}(k)|^2 \right\rangle$ for longitudinal spatial frequency k. From Eq. (9) of [50], this averaged spectrum is given by

$$\left\langle |\tilde{g}_{\mathbf{z}}(k)|^2 \right\rangle = e^{-k^2\sigma_z^2} |\tilde{g}_{\mathbf{z}_0}(k)|^2 + N\left(\frac{\pi}{kL}\right)^2 \left(1 - e^{-k^2\sigma_z^2}\right), \tag{26}$$

where $\mathbf{z}_0$ is the vector of ideal (designed) grating domain boundary positions, $\mathbf{z}$ is a vector of actual boundary positions (including RDC errors), and N is the number of domains in the grating. For a given grating, $|\tilde{g}_{\mathbf{z}}(\Delta k)|^2$ is proportional to the cw conversion efficiency for spectral components having material phase mismatch Δk. For a periodic grating of period $2l_D$, $|\tilde{g}_{\mathbf{z}_0}(\Delta k)|^2$ is thus approximately a sinc^2 function in the vicinity of first-order QPM ($\Delta k \approx \pi/l_D$), and is normalized to have peak equal to 1; see Eq. (10) of [50]. The second term in Eq. (26) is a noise pedestal that originates from the RDC errors; it applies for gratings with at least several domains ($N \gg 1$). It leads to an enhancement of the conversion efficiency for nominally phase-mismatched processes.

Fourier spectra of an example apodized chirped MgO:LiNbO$_3$ grating, designed for mid-IR OPCPA, are illustrated in Fig. 4(b). We assume RDC errors with $\sigma_z = 0.5\ \mu$m. The figure shows ideal, actual, and ensemble-averaged spectra. For the ensemble average, averaging is performed over 250 gratings with different errors. The regions corresponding to some additional processes are also shown by vertical dashed lines (idler-pump SFG; signal-pump SFG; and pump SHG). In particular, pump SHG is relatively close to 5$^{\text{th}}$-order QPM. The efficiency of these nominally phase mismatched processes are enhanced by RDC errors, and also, potentially, by the apodization profile employed (since it broadens the wings of the phase-matching regions).

RDC errors can also influence the desired process directly. This is illustrated by Fig. 4(c), which shows the same curves as Fig. 4(b) but plotted on a linear scale in the vicinity of first-order QPM. There is a residual fluctuation in the ideal (blue) curve due to imperfect apodization. The averaged (black) curve closely corresponds to the ideal grating, apart from a $\exp(-k^2\sigma_z^2)$
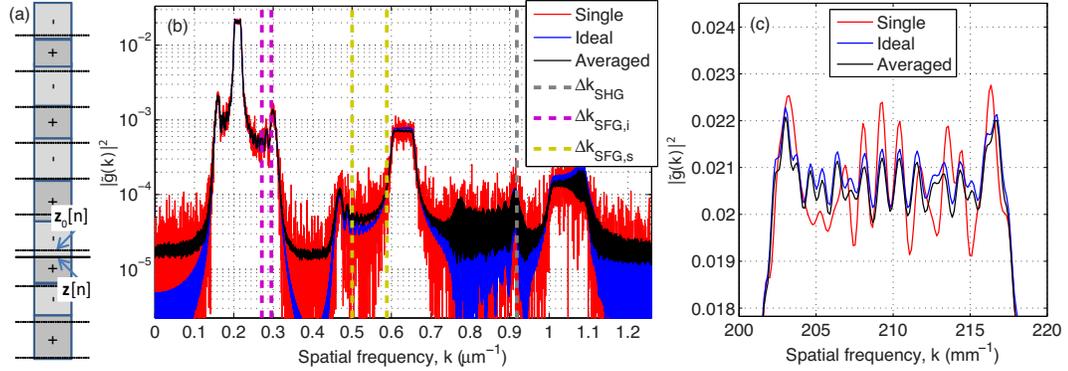
Fig. 4. (a) Schematic of a QPM grating with random duty cycle (RDC) errors. Horizontal dashed lines indicate the ideal, equally-spaced domain boundary positions. Elements of the domain boundary vectors $\mathbf{z}$ (with RDC errors) and $\mathbf{z}_0$ (ideal) are indicated. (b) Fourier spectra $|\tilde{g}(k)|^2$ with parameters $\sigma_z = 0.5$ μm and a 10-mm crystal, and approximately a 30 μm average period. For the averaged case (black curve), averaging is performed over 250 gratings. The vertical dashed lines show the spatial frequencies corresponding to phase-matching for some additional processes (signal-pump SFG; idler-pump SFG; and pump SHG). (c) The same curves as (b), but shown on a linear scale in the vicinity of first-order QPM. This plot reveals the influence of RDC errors on the nominal 'tuning curve' of the device.

scale factor which originates from the first term in Eq. (26). The single (red) curve shows an individual grating with RDC errors, and clearly exhibits additional fluctuations compared to the other curves. This effect will apply to all chirped QPM devices (not just OPCPA devices), causing distortions to their "tuning curves", and should therefore not be ignored; it emphasizes the importance of minimizing RDC errors through fabrication improvements in the future.

5.2. Implications for QPM-based OPCPA

The RDC-enhanced efficiency of processes such as pump SHG can be calculated via $\tilde{g}(k)$. When using narrow-band pulses, this efficiency can fluctuate versus crystal temperature (as in any phase-matching process) and due to lateral translation of the nonlinear crystal (if the RDC errors vary along this coordinate). When using ultrashort pulses, however, the efficiency can correspond closely to the ensemble average in Eq. (26), if the bandwidth of the pulses exceeds the "natural linewidth" of the QPM peak (that is, the bandwidth for an ideal periodic grating). Following the approach of Eq. (19) of [50], the pump SHG conversion efficiency can be estimated. It is convenient to express the result in terms of the characteristic quantities associated with the OPA process. Assuming Gaussian beam profiles and a sech² pump temporal profile, we find

$$\frac{\langle U_{SH} \rangle}{U_p} \approx \frac{1}{3} \left(\frac{1 - e^{-\Delta k_{SHG}^2 \sigma_z^2}}{\Delta k_{SHG}^2 \sigma_z^2} \right) \left(\frac{\pi \sigma_z}{l_D} \right)^2 \left(\frac{n_i n_s}{n_{SH} n_p} \frac{\omega_p^2}{\omega_i \omega_s} \frac{d_{SHG}^2}{d_{OPA}^2} \right) \left(\gamma_p^2 L l_D \right). \quad (27)$$

Note that for a Gaussian temporal profile, the $1/3$ factor becomes $1/(2\sqrt{2})$. In Eq. (27), the first quantity in parenthesis approaches 1 for small RDC errors, and the third quantity in parentheses corresponds to the different strengths of the SHG and OPA interactions. In terms of chirped QPM OPA quantities, $\gamma_p^2 L = \Lambda_{R,p} \Delta k_{BW}$, and hence this product is determined mainly by the required gain and spectral bandwidth. As such, assuming the RDC-related contributions to SHG

dominate, the ensemble-averaged SHG efficiency is a function only of the OPA requirements and the RDC errors. For unchirped devices, $\gamma_p^2 L$ is also proportional to the product of the k-space gain bandwidth of the device times the logarithmic gain [2], which are also constrained quantities.

In our OPCPA system [1], we observe the pump SHG to vary ($\sim$factor-of-2 changes) due to lateral translation of the crystal even in OPA1 and OPA2, in which the grating is 3-mm-wide and the beams are only a few hundred μm wide, suggesting some inhomogeneity in the QPM duty cycle errors along the grating width. We also observe the pump SHG to fluctuate with temperature, exhibiting a dependence consistent with RDC errors (again, $\sim$factor-of-2 changes over a range of ≈ 100 °C), given the acceptance bandwidth of the device with respect to pump- and second-harmonic frequencies. Experimentally, in OPA1 and OPA2 we translate the QPM gratings laterally and optimize their temperature to minimize pump SHG. In OPA3, the beam width is comparable to the grating width, so we only optimize with respect to temperature.

As discussed in [50], at the corresponding intensities of green light, two-photon absorption (TPA) can become significant, which may lead to photorefractive effects or an excessive thermal load on the crystal; it is also worth noting that such TPA-induced photorefraction may differ phenomonologically from normal one-photon photorefraction. After an analysis similar to that detailed in [50], the TPA can be estimated as

$$\frac{\langle U_{TPA}\rangle}{U_p} \approx \frac{24}{35}\left(\frac{\langle U_{SH}\rangle}{U_p}\right)^2 \left(\beta_{TPA} I_{p,pk} L\right) \tag{28}$$

where β_{TPA} is the two-photon absorption coefficient for the SH. Note that the 24/35 factor becomes 2/3 for a Gaussian pulse. The TPA is clearly related to the SHG efficiency given by Eq. (27), but also includes the final factor in parenthesis, which is the TPA factor for a SH pulse having intensity equal to the peak of the pump, neglecting TPA-induced changes to that intensity; this factor can be quite large. Note also that we have assumed small losses, which is a reasonable constraint to apply to a practical system.

To quantify the powers expected for SHG and TPA, we next apply Eqs. (27) and (28) to our OPCPA system, assuming $\sigma_z = 0.5$ μm, a nonlinear coefficient of 19.5 pm/V for the OPA process and 25.2 pm/V for the pump-SHG process. Based on our measured powers and beam sizes, we estimate peak pump intensities inside the OPA1, OPA2, and OPA3 stages of 4.9, 6.8, and 4.4 GW/cm^2, respectively. For these values, we predict generated SHG powers (directly after the uncoated crystals) of 188, 171, and 446 mW; note that with a slightly different $\sigma_z = 0.4$ μm, the latter value would be 296 mW. These predictions are in good agreement with the $\approx$ 300 mW green power we observe after OPA3 at full power. Using the same parameters and the TPA coefficient of LiNbO$_3$ [55], Eq. (28) predicts two-photon-absorbed powers of 13.6, 23.1, and 25.6 mW, respectively.

At intensities somewhat above those reported in [1], we begin to observe slight time-dependent fluctuations in the generated green light, and also fanning of the transmitted pump beam along the crystal c-axis. These observations appear consistent with photorefractive effects arising from the non-negligible TPA predicted by Eq. (28). Several photorefractive effects relevant to our operating regime have been studied, for example, in Refs. [56–58]. While the photorefractive effects we observe seem to be completely reversible, they place a limit on the signal-idler coupling rate γ_p which we can employ, and hence on the single-pass small-signal gain, and other properties of the amplifiers. A more detailed theoretical and experimental study of such photorefractive effects in the high-power, high-intensity, QPM, TPA-dominated absorption regime may be warranted, to elucidate the most important material properties, beyond the RDC characteristics, for maximizing the signal-idler coupling rate in the context of OPCPA.

6. Spectral effects: coincidentally phase-matched processes

Even in an ideal structure without any RDC errors, a number of factors can cause the minimal plane-coupled-wave model considered in subsections 3.2 and 3.3 to break down. For example, many components of the nonlinear polarization are neglected by the three-wave mixing equations (8). In deriving these equations, the only components of the nonlinear polarization that were retained were those with carrier frequency equal to that of the idler, signal, or pump. In this section, we consider several additional processes, explaining their influence on QPM OPCPA, in particular when using chirped gratings. Our main focus will be on $\chi^{(2)}$ sum and difference frequency mixing processes. We justify this focus in appendix A, where we estimate the severity of several $\chi^{(3)}$ and $\chi^{(3)}$-like processes.

6.1. Phase-matching of additional $\chi^{(2)}$ mixing processes

We can gain information about the significance of the neglected $\chi^{(2)}$ terms for a chirped-QPM OPCPA device by performing a series of phase-matching calculations, assuming a pump with a single-frequency component ω_p. For each signal frequency ω_s, all sum and difference frequencies involving ω_s, ω_p, and $\omega_i = \omega_p - \omega_s$ are generated (and in turn, all processes involving sums and differences of the resulting set also occur, and so on). As an example, the most relevant DFG-like process (excluding the OPA process itself) is the generation of frequency $\omega_{DF} = |\omega_s - \omega_i|$; the corresponding phase mismatch for this process is

$$\Delta k_{si}^{(DFG)} = k_e(\omega_s) - k_e(\omega_s - \omega_i) - k_e(\omega_i), \qquad (29)$$

where this equation assumes $\omega_s > \omega_i$. Many SFG processes also occur, generating frequencies $\omega_{pq}^{(SFG)} = \omega_p + \omega_q$ for indices p and $q \in \{i, s, p\}$. The corresponding phase mismatches are given by Eq. (6).

The phase mismatches can be compared to the range of grating k-vectors required to quasi-phase-match the desired OPA process (which would be $\Delta k_{is}^{(SFG)}$ in the above notation) by plotting each $\Delta k_{pq}(\omega_s)$ over the frequency range of interest. In Fig. 5, we plot the phase-matching period Λ for several processes, assuming a pump wavelength of 1.064-μm and all-e-wave polarized interactions in a MgO:LiNbO$_3$ crystal operated at 150°C. For the purposes of the figure we assume $\omega_s > \omega_i$ (that is, signal refers to the short-wavelength wave).

To interpret Fig. 5, consider an example case where OPA phase-matching must be satisfied for idler wavelengths between 3-4 μm: the corresponding range of grating periods is approximately 28.6-30.9 μm (solid blue curve). Consider the 3.8-μm idler component. If the grating is positively chirped ($\Delta k' > 0$; short QPM periods near the input end of the crystal) then this component is first amplified where the local period is ≈ 29.1 μm. Near the end of the grating, where the period is ≈ 30.5 μm, SHG of this component is satisfied. If the amplified idler is sufficiently intense, this process can be efficient, leading to distortions of the pulse and a reduction in efficiency. If an even wider range of periods is present, for example 28-32 μm, then the idler is first amplified where the period $\Lambda \approx 29.1$ μm, up-converted to its SH around $\Lambda \approx 30.5$ μm, and this SH is itself amplified (by the pump of frequency ω_p) around $\Lambda \approx 31.7$ μm (dashed curve). If the SHG process is reasonably efficient, then the idler SHG can effectively experience OPA twice, and hence have very high gain. Similar arguments can be made for the other spectral components and processes illustrated. When the QPM periods for different processes are quite close, the k-space extent of these processes is important (for example, OPA occurs over the region for which $|\Delta k| < 2\gamma_p$).

In apodizing the grating, a highly nonlinear chirp profile is imposed at the beginning and end of the device to achieve a weak interaction at the input and output regions [8]. Such a profile entails a wide range of QPM periods, and hence the period is swept through the various processes
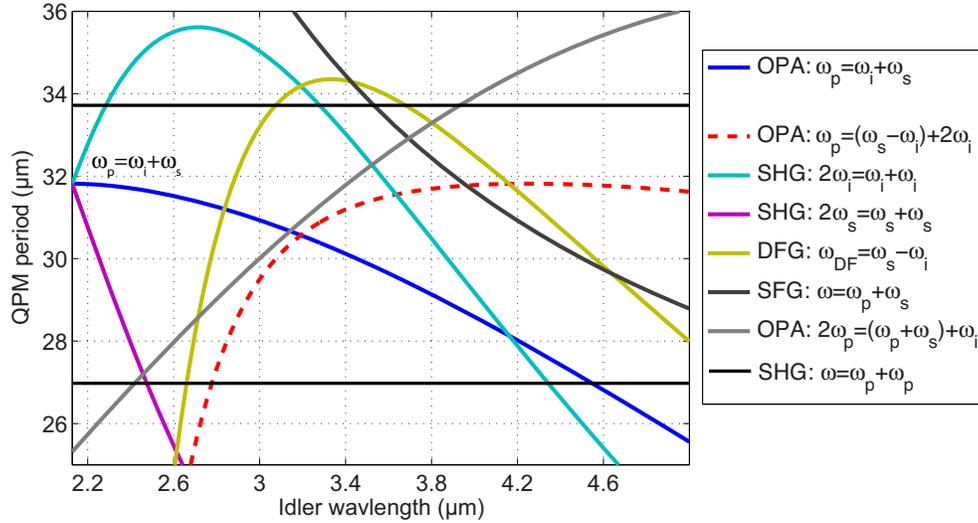
Fig. 5. Coincidentally phase-matched processes, assuming a pump wavelength of 1.064 μm, as a function of the long-wave idler wavelength. The legend indicates the type of interaction (SHG, OPA, or SFG) and the frequencies involved. The desired OPA interaction is $\omega_p = \omega_i + \omega_s$; the corresponding curve is indicated. For each process, we consider phase-matching for the nearest-odd-order of QPM (except for pump SHG process, for which we show 4th- and 5th-order QPM).

illustrated in 5. For example, the period may be swept through pump SHG phase-matching. Even though the chirp rate is rapid, the pump may be intense enough for the SHG process to have non-negligible efficiency. Since pump SHG occurs at 4th- and 5th-order QPM, it is possible in principle to suppress this process by an appropriate choice of QPM duty cycle in the regions where SHG phase-matching is satisfied (50% for 4th-order, and 40% or 60% for 5th). This level of control of the duty cycle can be challenging in practice. Therefore, it is important to maximize the chirp rate in the apodization regions (while still keeping the apodization itself effective) so as to minimize the efficiency of such processes; we discussed such optimal procedures for apodization in [8].

Based on Fig. 5, in order to avoid efficient long-wave SHG ($2\omega_i = \omega_i + \omega_i$) in a collinear amplifier designed for wavelengths between 3 and 4 μm, the chirp rate should be negative ($\Delta k' < 0$), since with this choice SHG of the long-wave idler is phase-matched before that idler has been amplified via the OPA process, and so the parasitic SHG process has low efficiency. It is for this reason that we use a negative chirp rate in all of our OPCPA stages.

6.2. Numerical Example

When the phase-matching regions for the different processes are sufficiently separated, simple expressions for their efficiency can be obtained. This is not always the case, however, so it is useful to simulate all of the processes which are close to or pass through phase-matching using the generalized coupled-envelope model in Eq. (1).

In the examples shown in Fig. 6(a) and 6(b), we consider quasi-cw interactions involving several different spectral components. The set of frequencies included in these simulations is as follows: ω_i, ω_s, ω_p, $2\omega_i$, $2\omega_s$, $2\omega_p$, $(\omega_i + \omega_p)$, $(\omega_s + \omega_p)$, and $(\omega_s - \omega_i)$. The assumed parameters are $\Lambda_{R,p} = 2$ and $\rho = 10^{-6}$. The chirp rate $|\Delta k'| = 3$ mm^{-2}, and grating length $L = 10$ mm.
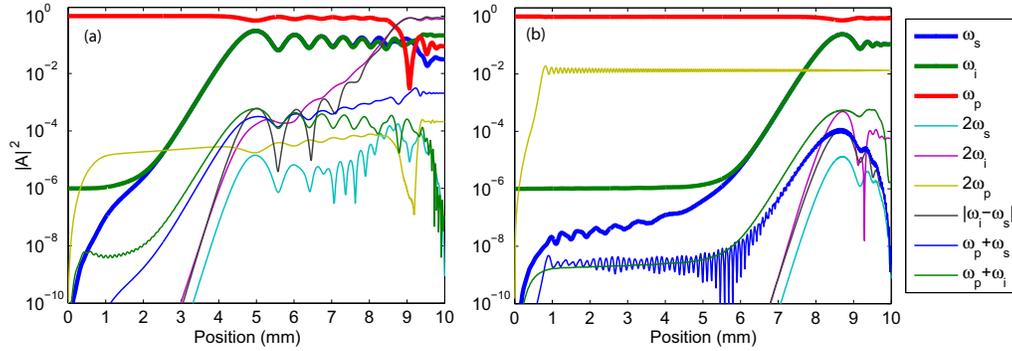
Fig. 6. Numerical example including several carrier waves. The pump and seeded idler wavelengths are 1.064-μm and 3.8-μm, respectively. The legend shows the frequency of each wave included in the model. The sign of the chirp rate ($\mathrm{sgn}(\Delta k')$) is (a) positive (showing significant coupling to unwanted field envelopes and hence distortion of the desired OPA process), and (b) negative (showing negligible distortions). The parameters are given in the text

Several features are apparent from these figures. In Fig. 6(a), where the chirp rate is positive, the signal and idler are fully amplified around 5 mm from the input. Shortly after this point, the idler SHG process is phase-matched, and then the idler-SH OPA process is phase-matched. This latter process leads to exponential growth of the ($\omega_s - \omega_i$) and ($2\omega_i$) spectral components. Near the end of the grating, these components actually become stronger than the idler and signal themselves, and can even deplete the pump. This operating regime is poorly suited to OPCPA. The other curves in Fig. 6(a) exhibit no prominent features, except an overall growth for up-converted components, since these are driven by waves which are amplified.

The behavior of Fig. 6(b), where the chirp rate is negative, is much more favorable. The only non-negligible waves at the output are the desired signal and idler, the pump, and a significant but still comparatively small pump second harmonic (which may actually be further enhanced in reality due to the RDC errors in the grating, as discussed in section 5). Since idler SHG and idler-SH-OPA occur earlier in the grating than idler OPA, these former two processes are inefficient and do not play a significant role. Therefore, the undesired coincidentally-phase-matched processes which occur in 6(a) have been avoided by using a negative chirp rate.

7. Temporal dynamics: saturation and group velocity mismatch

The quasi-cw chirped-pulse limit we have assumed so far breaks down when the relative group delay between the idler, signal and pump accumulated during propagation through the QPM grating is too large with respect to their (stretched) durations. While the fact that such breakdown occurs is obvious, the point at which it does, and the implications of the breakdown mechanism(s) for system design, are not always obvious.

In this section, we show how this breakdown can in some situations lead to pronounced ripples in the output signal spectrum, even in apodized QPM gratings. We explain the physics of these ripples, and how they can be suppressed by appropriate combinations of pulse and grating chirp rates (i.e. by overall design of the OPCPA system), while still satisfying other constraints of the system and QPM devices (such as the requirement of $\Delta k' < 0$ imposed by the coincidental phase-matching issues discussed in section 6).

7.1. Effects of group velocity mismatch (GVM)

To explain the important effects involved in saturated chirped QPM OPA devices in combination with non-zero temporal walk-off between the interacting signal, idler, and pump waves, we first consider the much simpler case of unsaturated amplification of an unchirped signal input (seed) pulse. Given imperfect apodization, two idler pulse components are generated at the input to the device.

The temporal structure of the pulses in chirped QPM OPA with an unsaturated, continuous-wave pump was discussed in [59]. The evolution of the waves in the saturated-pump regime, and the influence of QPM apodization, was discussed in detail in [8]. More specifically, the existence of two idler pulse components is evident from several other sources. For example, in Eq. (E5) of [2], which represents the signal and idler in the frequency domain for an undepleted-pump chirped-QPM OPA device, multiple idler pulse components are implied by setting $A_{s0} = 0$ and then interchanging the i and s subscripts. That equation is still quite accurate near the *input* of saturated OPA devices, provided the signal and idler are much weaker than the pump. The two pulse components can also be understood in the context of cascaded $\chi^{(2)}$ interactions, the physics of which are relevant to chirped QPM devices in spatial regions where the phase-mismatch is high for all of the spectral components involved. As an example, see the two second-harmonic pulse components illustrated in Fig. 5(b) of Ref. [60] for a phase-mismatched SHG interaction.

Of the two idler pulse components, the first, main component travels with the signal in time until its constituent spectral components (frequency Ω) are amplified at the corresponding phase-matched points $z_{pm}(\Omega)$ (i.e. the points where $\Delta\beta(z,\Omega) = 0$). The second component travels at the idler group velocity, and hence walks off of the signal pulse, and then experiences an essentially separate OPA interaction, based on the same set of phase-matched points $z_{pm}(\Omega)$.

The resulting amplified output of both waves involves multiple pulse components: the main part, associated with the first pulse component described above, and pre- or post pulses, which originate from the secondary idler pulse component. The corresponding spectrum has ripples, associated with these multiple, delayed components [2]. Apodization serves to suppress the secondary pulse component, by optimally matching the input eigenmodes of the device to the input conditions (finite seeded wave, zero unseeded wave) [8]. However, in practice, apodization is never perfect in a device with $d(z)/d_{33} = \pm 1$, and so there is always at least a small secondary pulse component generated at the device input.

In the absence of pump saturation, the gain for each pulse component is essentially the same (except for slight changes due to the time-dependent intensity of the pump). However, with saturation, the weaker, unwanted pulse component can experience higher gain, since it saturates its temporal region of the pump less than the main pulse. The resulting pulse components cause an increased and unwanted spectral ripple. The use of a chirped seed pulse can either exacerbate or, when properly arranged, completely resolve this problem. We discuss the chirped-pulse case in the following subsection.

7.2. Influence of saturation and input pulse chirp

To understand the combined effects of GVM, saturation, and pulse chirp, it is useful to first consider the characteristic velocities involved in the chirped-pulse interaction.

There are the temporal walk-off rates associated with the carrier frequencies of the three waves, determined by their group velocities. There is in addition an "amplification wave-front" which corresponds to the delay of the seed spectral component $\Omega_{pm}(z)$ being amplified at position z (subscript pm indicates "phase-matched"). We denote this delay as $\tau_{sw}(z, \Omega_{pm}(z))$, where $\tau_{sw}(z, \Omega)$ is the group delay of frequency Ω and "sw" denotes seeded wave. Note that this delay is related to the instantaneous frequency $\Omega_{inst}(z,t)$ by $\Omega_{inst}(z, \tau_{sw}(z, \Omega)) = \Omega$. Note also that in

this section we will use Ω and Ω_{pm} to refer to frequency shifts of the *seeded* wave with respect to its carrier frequency ω_{sw}, which is equal either to ω_i or ω_s. The unseeded wave has carrier frequency $\omega_{uw} = \omega_p - \omega_{sw}$.

As well as an amplification wave-front, there is also a "secondary wave-front" related to the accumulated delays of the spectral components of the secondary (unwanted) pulse component which is generated in the envelope of the unseeded wave at the input to the grating, as described above in subsection 7.1.

In order for the secondary pulse to not saturate the pump before the main components are able to, it is necessary that these components travel at an opposite group velocity, relative to the pump, compared to the amplification wave-front. In the following, we quantify this constraint. In Fig. 7 and corresponding movies (Media 1 and Media 2), we illustrate the dynamics involved for an example signal-seeded configuration involving positive or negative chirp on the signal pulse. In the following paragraphs, we quantify the relevant processes and arrive at constraints for system design.

Each spectral component of the secondary pulse propagates at the corresponding group velocity of the material, given by $v_{uw}(-\Omega)^{-1} = (\partial k_e / \partial \omega)|_{\omega = \omega_{uw} - \Omega}$. The total group delay of these spectral components is determined by this group velocity and also by their initial group delays at the input to the grating, which are in turn determined by the chirp of the input (i.e. seeded) pulse. The secondary wave-front can therefore be expressed as:

$$\tau_{uw,\text{eff}}(z) = \tau_{uw}(0, -\Omega_{pm}(z)) + v_{uw}(-\Omega_{pm}(z))^{-1}z, \tag{30}$$

where the initial group delay spectrum of the secondary pulse satisfies $\tau_{uw}(0, -\Omega) = \tau_{sw}(0, \Omega)$, where $\tau_{sw}(0, \Omega)$ is the group delay spectrum of the seeded pulse, determined by its chirp. We can now introduce an effective group velocity of the secondary wave-front given by

$$
\begin{aligned}
v_{uw,\text{eff}}(z)^{-1} &= \frac{d\tau_{uw,\text{eff}}}{dz} \\
&= \frac{1}{v_{uw}(-\Omega_{pm}(z))} + \left(\frac{d\tau_{sw}(0,\Omega)}{d\Omega} \bigg|_{\Omega=\Omega_{pm}} - \beta_{uw,GVD}(-\Omega_{pm}(z))z \right) \frac{d\Omega_{pm}}{dz}. \quad (31)
\end{aligned}
$$

where we use $\beta_{j,GVD} = d(1/v_j)/d\Omega$ to denote the GDD coefficient of wave j (related to group velocity dispersion, GVD), and $\beta_{j,GDD} = d\tau_j/d\Omega$ to denote the GDD itself. Next, we consider the amplification wave-front group velocity, $v_{amp}(\Omega)$. The QPM chirp and material dispersion determine the rate at which the phase-matched frequency of the seeded wave changes with position, according to the implicit relation $\Delta k_0(\Omega_{pm}(z)) - K_g(z) = 0$. Hence, Ω_{pm} satisfies

$$
\begin{aligned}
\frac{d\Omega_{pm}}{dz} &= \frac{dK_g}{dz} \frac{d\Delta k_0}{d\Omega} \bigg|_{\Omega=\Omega_{pm}}^{-1} \\
&= -\Delta k'(z) \delta v_{uw,sw}(\Omega_{pm})^{-1} \quad (32)
\end{aligned}
$$

where $\Delta k' \equiv \partial \Delta \beta / \partial z = -dK_g/dz$, and $\delta v_{uw,sw}(\Omega) \equiv d\Delta k_0/d\Omega = (v_{uw}(-\Omega)^{-1} - v_{sw}(\Omega)^{-1})$. From the change in phase-matched frequency versus position and the (position-dependent) pulse chirp of the seeded wave, we can calculate the group velocity of the amplification wave-front. We thereby arrive at

$$
\begin{aligned}
v_{amp}(z)^{-1} &= \frac{d}{dz} \left(\tau_{sw}(z, \Omega_{pm}(z)) \right) \\
&= \frac{1}{v_{sw}(\Omega_{pm}(z))} - \left(\frac{\partial \tau_{sw}}{\partial \Omega} \bigg|_{\Omega=\Omega_{pm}(z)} + \beta_{sw,GVD}(\Omega_{pm}(z))z \right) \frac{\Delta k'(z)}{\delta v_{uw,sw}(\Omega_{pm}(z))}. \quad (33)
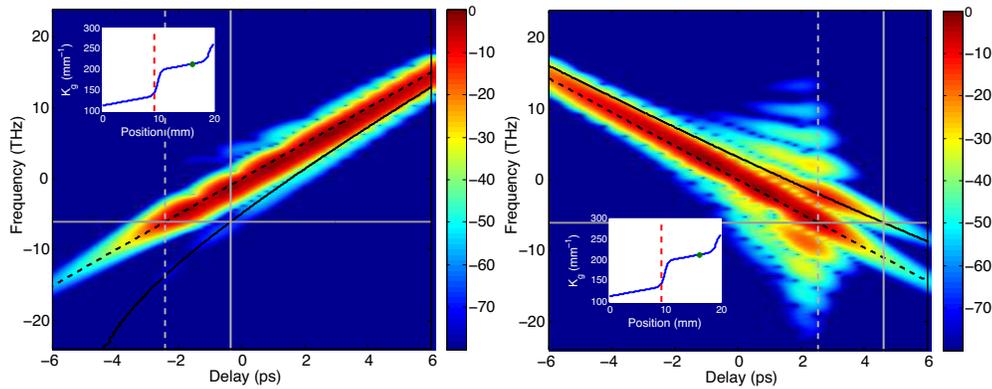\end{aligned}
$$

Fig. 7. Illustration of group velocity walk-off effects in saturated-pump OPCPA. (a) Negative signal GDD (Media 1), (b) Positive signal GDD (Media 2). The figures and movies show the evolution of cross- frequency resolved optical gating (FROG) spectrograms (dB scale; 400 fs gate pulse) of the unseeded wave (in this case, the long-wavelength idler) as it propagates through the QPM grating. The pump pulse is 12 ps long and the 1.55-μm signal input is stretched from 30 fs to 6 ps with pure second-order phase. The z-dependence of K_g is shown in the inset. The first ~10 mm of the grating is a highly phase mismatched region, added to illustrate the relevant dynamics: this region allows the secondary pulse to propagate away from the main pulse, making it easier to distinguish; in a practical device, this region would not be included. The current position in the grating is marked for each frame.

Several curves are included in the main plot to highlight important features. The dashed black line shows the group delays of the main pulse, determined by the input chirp and propagation of the seeded pulse. The solid black line shows the group delays of the secondary pulse. The horizontal grey line shows the local phase-matched frequency. The dashed vertical line shows the amplification wave-front, corresponding to velocity $v_{amp}(z)$ [see Eq. (33)]. The solid vertical line shows the secondary wave-front, travelling at velocity $v_{uw,\text{eff}}(z)$ [see Eq. (31)]. The intersection of the horizontal and vertical lines indicate the points of the pulse components which are currently phase-matched.

Distortions occur when the amplification wave-front passes through temporal regions of the pump which have already been depleted by the secondary pulse. This case is seen in (b) for positive signal GDD. Due to the highly amplified secondary pulse, there are two spectral regions of the signal and idler overlapped with each temporal region of the pump; cross-talk between these multiple pulse components lead to generation of additional spectral components, as seen in the image displayed for (b). In (a), the secondary wave-front 'lags behind' the amplification wave-front, so the secondary pulses are amplified less, and the output spectrogram quality is much higher.

The terms in Eqs. (31) and (33) dependent on $\tau_{sw}(0,\Omega)$ can be simplified by noting that $d\tau_{sw}(0,\Omega)/d\Omega = \beta_{sw,GDD}(\Omega)$, which is the frequency-dependent group delay dispersion of the seeded wave.

Given $v_{uw,\text{eff}}(z)$ and $v_{amp}(z)$, the criteria introduced above for the secondary pulse components to not interact with temporal regions of the pump before the main pulse can be quantified:

$$\left(v_{uw,\text{eff}}(z)^{-1} - v_{amp}(z)^{-1}\right)\left(v_{amp}(z)^{-1} - v_p^{-1}\right) < 0. \tag{34}$$

To interpret this equation: if $\left(v_{amp}^{-1} - v_p^{-1}\right) > 0$, the amplification wave-front moves from the leading edge of the pump to the trailing edge. We then want the secondary wave-front to be

closer in time to the leading edge of the pump than the amplification wave-front, so that it is temporally overlapped with pump components which have already been partially depleted. Thus, we need $v_{uw,\text{eff}}^{-1} < v_{amp}^{-1}$, so that the secondary wave-front accumulates less delay with position. An analogous argument applies if both signs are reversed.

A convenient form for Eq. (34) results if we suppress dependencies of the various quantities on position z and frequency $\Omega_{pm}(z)$, and neglect group delay dispersion accumulated by both envelopes *within* the crystal, i.e. neglecting $\beta_{j,GVD}$. Equation (34) can then be re-written as

$$\beta_{sw,GDD}\Delta k' > \left(v_{uw}^{-1} - v_{sw}^{-1}\right)\left(v_{sw}^{-1} - v_p^{-1}\right). \tag{35}$$

Even further simplification of this inequality is possible in the case of a large enough GDD that the magnitude of the left hand exceeds that of the right hand side. In this case, we simply require that $\beta_{sw,GDD}\Delta k' > 0$. Since we found in section 6 that for the mid-IR OPCPA case under consideration, $\Delta k' < 0$ is required, Eq. (35) reduces, for strongly chirped pulses and gratings, to $\beta_{sw,GDD} < 0$, i.e. the seeded wave (whether the signal or idler) should have negative GDD.

In our OPCPA system [Fig. 1], the final idler output is compressed with bulk sapphire, which has a negative GDD coefficient in the 3- to 4-μm range. Prior to compression, the idler therefore has positive GDD. In the OPCPA stages, the even-orders of dispersion of the generated wave acquire a sign flip with respect to those of the seeded wave (note that the odd orders do not acquire such a sign flip). The seeded signal wave prior to OPA3 must therefore have negative GDD, in accordance with Eq. (35). We designed the silicon prism pair and 4-f pulse shaper seed-stretching system depicted in Fig. 1 so as to obtain such a negative signal GDD while also being able to compensate for higher order dispersion terms of the generated idler wave.

In addition to the somewhat subtle points discussed so far in this section, there is also a more obvious constraint based purely on temporal overlap of the pulses. To remain overlapped with the pump throughout the grating, using Eq. (15) to find the grating length L as a function of γ_{p0} and $\Lambda_{R,p}$, the pump duration should satisfy

$$\tau_p \gg \left(\frac{\Delta k_{\text{OPA}}}{\gamma_{p0}^2 c} + \frac{4}{\gamma_{p0} c}\right)\delta n_g \Lambda_{R,p}, \tag{36}$$

where δn_g is a characteristic group index difference, corresponding to the largest group index minus the smallest group index involved in the three-wave interaction. With this inequality, the required pump duration can be estimated given the required gain and bandwidth. The minimum required pump pulse duration is obtained when the pump intensity equals the damage threshold, although this damage threshold is also a function of the pump duration.

To emphasize the results of this section: while the dynamics we have considered in Fig. 7 are quite complicated, the constraint imposed on OPCPA system design is very simple, requiring only that in any OPA stage with significant depletion of part of the pump temporal profile, the seed should have the appropriate sign of GDD (negative in the case of our system, since we also require $\Delta k' < 0$). The pulse stretching / compression can then be arranged with this constraint in mind, in addition to standard linear-optical considerations.

8. Summary and conclusions

8.1. *Summary of OPCPA design constraints*

In this subsection, we summarize the design constraints developed throughout this paper. One aspect of these constraints is that they apply to both the OPCPA system as well as the individual QPM devices, so it is important to design both at the same time.

To obtain sufficient gain, the factor $\Lambda_{R,p} = \gamma_p^2/|\Delta k'|$ must be large enough; the corresponding gain is given by Eq. (9). The actual gain and saturation in individual stages when using

Gaussian beams and non-flat-top pulses must be calculated numerically using e.g. Eq. (1). The amplification bandwidth is given by Eq. (15) or more generally by Eq. (10). For a given bandwidth and gain, there are two equations for the three quantities γ_p, L, and $\Delta k'$. Avoiding $\chi^{(3)}$ and $\chi^{(3)}$-like processes, which typically scale with the intensity-length product (but also depend in some cases on the temporal structure of the waves) is also important. We considered such processes in appendix A.

The peak signal-idler coupling rate γ_p [Eq. (11)] is in addition constrained by the damage threshold, which is a function of duration (for peak-intensity related damage), and also by the thermal load on the crystal (for average power- and intensity- related damage). The grating length L is also constrained by fabrication, but lengths of ~ 50 mm are available, so this constraint can usually be ignored for OPCPA. The QPM crystal aperture along the c-axis can be quite narrow (e.g. ~ 3 mm available commercially with good domain quality). Nonetheless, samples of up to 10 mm aperture have been demonstrated [61], as well as rotated-cut wafer poling supporting wafer-sized beams [62], so QPM devices can be scaled to high powers and energies. Wider gratings and elliptical beams may be necessary sometimes for power scaling. In our case we used 1x3 mm gratings, but 2x2 mm gratings would be a natural alternative.

Achieving high conversion efficiency in a single high-gain OPA stage is difficult and requires the parametric interaction to be driven very strongly, as indicated by Fig. 2. Use of a pump which is too strong will result in excess noise amplification and other, unwanted effects such as those discussed in sections 4, 5 and 6 and appendix A. Keeping a moderate pump intensity, corresponding for example to a peak $\Lambda_{R,p}$ of $1.5 < \Lambda_{R,p} < 3$ means that multiple OPA stages must be used in order to achieve good conversion efficiency in the final stage. Based on these considerations and the properties of our pump source, we split our OPCPA system up into two pre-amplifier stages followed by the power amplifier. Previously [4, 5], only a single strongly-driven pre-amplifier was used.

Splitting the power amplifier into two parts and re-using the same pump, as we did for the pre-amplifier stages, would be a promising approach, since in this way the first power amplifier stage has (approximately) the same pump energy as the final stage, so a large ρ can be obtained in the final stage without very high saturation in the penultimate stage. To be able to re-use the pump in this way, its spatial and temporal properties must not be too heavily distorted in the penultimate stage; these properties are related to saturation effects and the QPM grating quality.

Imperfections in the QPM grating, in particular RDC errors, lead to parasitic SHG and TPA, and it is likely that these place limitations on the largest γ_p which we can use in practice before the onset of beam fanning due to photorefractive effects. Minimizing these RDC errors will be an important step for using larger γ_p without beam distortions and with less risk of crystal fracture. We estimate $\sigma_z \sim 0.4$ μm for our present devices based on the generated green light. Evaluation of the RDC errors and minimizing them (to the extent possible given available fabrication technology) is likely to be important in optimizing system performance, particularly when using the same part of the pump for multiple stages.

Keeping a small-to-moderate level of group velocity mismatch between the waves relative to their durations imposes a further constraint, given by Eq. (36). Minimizing GVM will generally favor operation at the maximum intensity for a given pump duration and repetition rate (this maximum may correspond to a reversible onset of beam distortions or to irreversible damage of the crystal). Minimizing GVM is not necessarily a very strong constraint, however. With $\gamma_p = \gamma_{max}$, the other nominal design quantities $\Delta k'$ and L of each stage can be determined. The use of a linear chirp is not required: shaping of the gain spectrum is possible, as described in Ref. [12] for OPCPA as well as other parametric mixing configurations. Once a nominal grating profile is chosen, suitable apodization profiles must be appended in order to achieve as clean a gain spectrum as possible. This aspect of the design, as well as a detailed discussion of the

underlying three-wave mixing process, was given in [8].

In terms of system constraints, the most important is likely the pump peak power constraint given in Eq. (24) (in the context of gain-guided non-collinear mode suppression), since this indicates the appropriate pump sources. For example, consider a system with a single pump beam which is then split into multiple parts to pump the different stages. With $P_{pk}/\Lambda_{R,p}^2 > 0.5$ MW [comparable to Eq. (25)], using $\Lambda_{R,p} = 2.5$, and using 10% of the total pump to drive one or more pre-amplification stages, one arrives at $P_{pk} > 30$ MW. To satisfy the constraint by a factor of $\sim$2 safety margin, one would need $P_{pk} > 60$ MW. Fortunately, such peak powers are now readily achievable in a variety of laser systems, but this constraint is still important in scaling to high repetition rates. In our system, we re-used the OPA1 pump for OPA2, and operated at 50 kHz in order to achieve a sufficient safety margin in the pre-amplifiers given the peak power available from our pump source.

Given operation at the damage threshold, characterized by $\gamma_{\max}(\tau_p, f_{rep})$ (i.e. assuming a damage threshold, and corresponding maximum signal-idler coupling rate, which is a function of both the pump duration and its repetition rate), the GVM constraint Eq. (36) can turn the above peak power requirement into a pulse energy requirement.

To avoid unwanted coincidentally phase-matched processes in the OPA stages, it is important to inspect the relevant phase-matching maps, taking into account the range of QPM periods required for the desired interaction. For the mid-IR OPCPA case we focused on in this paper, this consideration imposed the constraint $\Delta k' < 0$. Note that with our definitions, $\Delta k' = \partial \Delta k/dz = -dK_g/dz$, so $\Delta k' < 0$ implies an increasing $K_g(z)$ and hence a decreasing QPM period versus position in the grating. Note also that if $\Delta k_0(\Omega)$ was negative for some mixing configuration, then the residual QPM phase-mismatch would be $(\Delta k_0 + K_g)$ rather than $(\Delta k_0 - K_g)$; one would then have $\Delta k' = +dK_g/dz$w.

The presence of GVM between the waves and the use of chirped pulses and gratings can lead to unwanted temporal effects, as discussed in section 7. These effects can be avoided by satisfying Eq. (34), which will often reduce to Eq. (35) in practice. For our case, this constraint together with the above $\Delta k'$ constraint meant a negative chirp on the signal was needed. This chirp resulted in a positive idler chirp, requiring a negative-GVD material (such as sapphire) for bulk compression of the generated idler. As such, the pulse stretching/compression should be arranged with OPCPA constraints in mind. We use general ray-tracing procedures for evaluating and optimizing linear-optical pulse chirping and compression strategies [63], incorporating both the constraints discussed here and the spectral phase imposed onto the generated wave in the chirped QPM structure [64]. We note, also, that the pulse-distortion effects discussed in section 7 may become negligible for very long ($\gg 10$ ps) pump pulses.

The above constraints, in addition to more "standard" OPCPA considerations, have proven sufficient for development of our OPCPA system. In some cases, they represent subtle issues not previously discussed or quantified in the context of chirped-QPM OPCPA design. Deciding on specific beam sizes, distribution of gains between stages, arrangement of pulse chirping and compression stages, and other experimental aspects, can be facilitated by (1) the comprehensive analytical design equations and constraints we developed here, (2) more detailed numerical calculations based on a generalized coupled-envelope model [Eqs. (1) and (4)], accounting for all propagation effects including diffraction, dispersion, nonlinearities, presence of multiple OPCPA stages, and so on (which is beyond the scope of this paper), and (3) optimization of performance experimentally, guided by (1) and (2).

More generally, it is important to decide on appropriate pump sources (based on criteria such as cost/complexity, wavelength, pulse energy, duration, and repetition rate) and seed sources (based on criteria such as wavelength, bandwidth, energy, stability, and spectral quality, as well as cost/complexity). These considerations will continue to evolve as the relevant laser

technologies improve and become more available, and so we have not focused on them here.

8.2. Conclusions

The design and operation of chirped QPM devices can be subtle and complex. Initially unexpected effects can arise and amplify noise, distort beam and/or pulse profiles, or even damage the nonlinear crystals. In this paper, we have presented a systematic analysis of the design of OPCPA systems based on these devices, identifying several important constraints beyond those usually present for OPCPA. While the underlying spatio-temporal dynamics can be complex, the resulting design constraints, summarized above in subsection 8.1, are often comparatively simple. For example, imposing particular signs on the grating and pulse chirps, necessitating a pump with sufficient peak power, placing limits on the local disorder of the QPM grating domains, and indicating the number of OPA stages required in the system.

As a result, our analysis provides a roadmap for development of chirped QPM OPCPA systems in the lab while avoiding the subtle unwanted effects which the combination of pulse and grating chirp can introduce. So far, this enabled us to obtain almost a factor-of-2 improvement in pulse duration, resulting in our latest 41.6-fs mid-IR OPCPA result [1]. The constraints we have developed here reveal several important steps in further advancing QPM OPCPA towards fewer-cycle pulses, higher energies, and new wavelength regions, while pumping with power-scalable 1-μm laser sources and maintaining simple and compact experimental setups.

There is no relevant limit to the achievable bandwidth with respect to phase-matching, except for the crystal transparency window. Therefore, understanding the physics of the nonlinear processes involved (including the role of multiple, potentially competing nonlinearities), and evaluating that physics in the context of system design, is the key to making use of the broadband phase-matching which QPM technology supports. The general frequency-domain multiple-envelope model we introduced will be useful in modelling a wide variety of parametric interactions, especially when augmented by $\chi^{(3)}$ effects. Our results will also make it possible to evaluate the feasibility of exploiting engineered QPM in emerging far-IR materials, for example to achieve OPA and OPCPA in orientation-patterned GaAs [65, 66].

Beyond OPCPA, our results apply to chirped QPM devices in general. In particular, for DFG and SFG interactions, especially when both of the input waves are intense, most of the constraints we have developed will also apply directly or with minor modifications. Furthermore, the spatial, spectral, and temporal effects discussed in sections 4, 6, and 7, respectively, will apply to media with spatially inhomogeneous phase-matching conditions, not just chirped QPM media, and thus our results have broad applicability to designing and understanding strongly-driven parametric systems in general.

A. Justification of a model based on $\chi^{(2)}$ effects

There are a number of $\chi^{(3)}$ and $\chi^{(3)}$-like processes which can also influence the desired OPCPA interaction, beyond the $\chi^{(2)}$ dynamics predicted by the nonlinear polarization in Eq. (4). In this appendix, we consider the significance of some of these neglected $\chi^{(3)}$ effects in order to help justify the use of the simplified $\chi^{(2)}$-based model in Eqs. (1) and (4).

Relevant processes include the (near-)instantaneous electronic susceptibility $\chi_E^{(3)}$ and stimulated Raman scattering (SRS), which we denote by a frequency dependent susceptibility $\chi_R^{(3)}(\Omega)$. Furthermore, optical rectification (OR)-related processes can also occur: specifically, the optical field can generate quasi-phase-matched counter-propagating THz waves, which in turn can couple different spectral regions of the optical field together [67, 68]. These latter effects have been quantified in the context of singly resonant OPO operation [69, 70].

Absolutely calibrating the third-order susceptibilities in LiNbO$_3$ is challenging, owing for example to contributions from cascaded $\chi^{(2)}$ (even in bulk and with no QPM grating), as well

as non-instantaneous nonlinearities such as SRS. In [46], we attempted to calibrate these effects in the context of supercontinuum generation based on the measurements performed in [55], and arrived at an electronic susceptibility of $\chi_E^{(3)} = 5480$ pm^2/V^2 and a peak SRS susceptibility of $\chi_{R,pk}^{(3)} = 5230$ pm^2/V^2, together with a corresponding complex SRS response function. Here we use these values, but note that further, direct measurements of these quantities would be useful.

The corresponding pump SPM via $\chi_E^{(3)}$ is 0.75 rad for an intensity of 5 GW/cm^2 and a grating length of 11 mm. There is also a near-instantaneous SPM-like response from cascaded quadratic nonlinearities, originating from all Fourier orders far from phase-matching. Such contributions influence both the pump SPM, the calibration of $\chi_E^{(3)}$, and also the different nonlinear phase shifts incurred by the signal and idler waves. Furthermore, there is significant uncertainty in the above phase from $\chi_E^{(3)}$. If one just uses the n_2 reported in [55] to determine $\chi_E^{(3)}$ (without accounting for other nonlinear processes), the SPM predicted is ≈ 3.4 times smaller.

The maximum SRS gain supported is comparable to the B-integral from $\chi_E^{(3)}$ owing to their comparable susceptibilities, but its influence on the pulse spectrum can be expected to be minor, since the strongest Raman peak is at ≈ 19 THz, which is well outside the range of spectral components supported by the *intensity* of a few-ps pulse. Nonetheless, SRS effects may not be vanishingly small in OPA3, in which the signal and idler intensities grow enough to substantially saturate the pump, because our pulses exhibit significant spectral structure. Such structure maps to temporal structure for a chirped pulse and will thus broaden the Fourier spectrum of the chirped pulses' intensity, thereby sampling a broader range of the Raman spectrum (which also has peaks at lower frequencies such as 7.6 THz).

The OR-related sources of pulse distortion lead to SRS-like effects, but they depend on the QPM grating structure. Specifically, phase-matching for counter-propagating THz waves is governed, approximately, by $\Delta k_T(z, \Omega) = (n_T + n_g)\Omega/c - K_g(z) = 0$, where n_T is the THz refractive index (~ 5.2 for LiNbO$_3$ [71]), and n_g is the optical group index (≈ 2.2 at 1 μm). This relation yields a phase-matched THz frequency Ω_{pm} satisfying $\Omega_{pm} = K_g(z)c/(n_T + n_g)$. For 1-$\mu$m-pumped mid-IR OPCPA in MgO:LiNbO$_3$, the QPM periods are around 30 μm, which yields a frequency of 1.35 THz, respectively.

The bandwidth of the generated THz waves depends on the driving field, but in the limit of a short intensity profile of the pulse, the THz field scales according to $\tilde{A}_T(\Omega) \propto \Omega/[\alpha_T(\Omega)/2 + i(n_T + n_g)(\Omega - \Omega_{pm})/c]$, where α_T is the frequency-dependent THz absorption coefficient. This Lorentzian-like response has a relatively narrow bandwidth, determined by the absorption and index mismatch parameters according to $\Omega_{BW} = \alpha_T(\Omega_{pm})c/[2(n_T + n_g)]$. For the counter-propagating 1.35 THz case considered above, $\Omega_{BW} = 2\pi \times 0.014$ THz. The effective susceptibility seen by the optical field is given by

$$\chi_T^{(3)}(\Omega) = \frac{16d_T^2}{3n_T c} \frac{\Omega}{\alpha_T + i(n_T + n_g)(\Omega - \Omega_{pm})}. \tag{37}$$

In the context of narrow-band OPOs, this susceptibility can also be viewed as a THz OPA process [69]. Assuming $d_T = 2/\pi \times 152.4$ pm^2/V^2 [71], Eq. (37) yields a peak of 125.6×10^3 pm^2/V^2, i.e. much greater than the $\chi_E^{(3)}$ and $\chi_R^{(3)}$ responses discussed above. This large effective susceptibility helps explain the susceptibility of cw-pumped OPOs to this nonlinearity. In the context of OPCPA, the distortion of the pulse is weak for pulses with narrow-band intensity Fourier spectra; if the pulses are short enough (or have a sufficiently modulated structure) to have intensity spectra approaching Ω_{BW}, the significance of the resulting pulse distortion can be (over-)estimated in the same manner as a calculation for the small-signal SRS gain (based on the pump intensity and the effective third-order susceptibility), but multiplying by $\Omega_{BW}/\Omega_{pm} \approx 0.01$. This calculation yields an an "effective coupling" due to OR of ~ 0.36.

While this coupling is not vanishingly small, the use of a chirped QPM grating strongly smears out the THz response, since $K_g(z)$, and hence $\Omega_{pm}(z)$, varies with position in the grating. Furthermore, the actual coupling obtained in practice will be much weaker than the above estimation, because the signal and idler have lower intensity than the pump, and the pump can be very narrow-band compared to Ω_{pm} (if its pulse duration is long enough). If in addition the signal and idler spectra are slowly-varying and the pulses are chirped to comparable duration to the pump, there will be very little coupling to the THz wave. It should also be noted, however, that the above treatment of coupling to THz waves is by no means comprehensive: for example, we have not considered any effects involving phonon-polariton dynamics or the possible influence of periodic poling in the ferroelectric crystal on such processes [72].

Based on the above discussion, we expect that $\chi^{(3)}$ effects are minor, but not completely negligible in all cases. Such effects should thus be kept in mind when designing and characterizing OPCPA systems, including SRS-like processes in addition to B-integral considerations. A greater knowledge of the relevant third-order nonlinear coefficients for $LiNbO_3$ will also be useful in order to more reliably quantify these issues.

B. Definitions and important quantities

This paper involves many definitions and symbols, and draws on various results. For ease of reference, the tables 1-4 summarize the important quantities defined in the main text.

Table 1. Summary of basic quantities defined in the paper

Symbol	Description	Defined
$\hat{L}_j$	Diffraction and dispersion operators	Eq. (2)
A_j	Electric field envelopes	Eq. (3)
$P_{NL,j}$	Nonlinear polarizations	Eq. (4)
$X_{k,jl}$	Interaction coefficients ($= 0$ or $= 1$)	Eq. (5)
$\Delta k_{j,kl}$	Phase-mismatches for various carrier frequencies	Eq. (6)
$\Delta\beta(z)$	Carrier-frequency quasi-phase-mismatch for OPA	Eq. (8)
$\Delta k'$	QPM chirp rate, $\Delta k' = \partial\Delta\beta/\partial z = -dK_g/dz$	After Eq. (9)
$\Delta k_0(\Omega)$	Frequency-dependent phase-mismatch (OPA)	Eq. (12)
$\mathbf{\Delta k}$	Vector phase mismatch	Eq. (17)
$\phi_G(z)$	Accumulated QPM grating phase, $\int_0^z K_g(z')dz'$	Eq. (7)
$K_g(z)$	Local QPM grating k-vector	Eq. (7)
$D(z)$	Local QPM grating duty cycle	Eq. (7)
$d(z), \bar{d}_m$	Absolute & normalized nonlinear coefficients	Eq. (7)
d_{eff}	Effective nonlinear coefficient, $d_{\text{eff}} = d_{33}\bar{d}_1$	Eq. (8)
γ_p	Signal-idler coupling rate (OPA); $\propto |A_p|$	Preceding Eq. (9)
γ_{p0}	Peak of γ_p (when γ_p varies vs. space or time)	See Eq. (15)
γ_s	Idler-pump coupling rate (SFG/DFG); $\propto |A_s|$	Preceding Eq. (9)
γ_{max}	Max. γ_p possible (at damage threshold)	

Table 2. Summary of basic chirped QPM OPCPA related quantities

Symbol	Description	Defined
G_s	$\sim \exp(2\pi\Lambda_{R,p})$; Signal gain (no pump depletion)	Eqs. (9) and (10)
z_{pm}	Frequency-dependent phase-matching point	Eq. (13)
L_{deph}	$2\gamma_p/|\Delta k'|$; half the distance over which gain occurs	Eq. (14)
Δk_{OPA}	$|\Delta k'|L - 4\gamma_{p0}$; OPA gain bandwidth (k-space)	Eq. (15)
Δk_{BW}	$|\Delta k'|L$; bandwidth of QPM grating (k-space)	Eq. (15)
$\Lambda_{R,p}$	$\gamma_p^2/|\Delta k'|$; Gain factor (determines small-signal gain)	Eq. (16)
$\Lambda_{R,s}$	$\gamma_s^2/|\Delta k'|$; Pump depletion factor for SFG/DFG	Subsection 3.3
ρ	Ratio of input signal and pump photon fluxes	Subsection 3.3
η	Pump depletion (output / input pump intensity)	Subsection 3.3
L	QPM grating length	

Table 3. Summary of definitions used primarily in sections 4, 5, and 6.

Symbol	Description	Defined
ξ_p	Pump confocal parameter	See Eq. (16)
L_g	Gain length	$L_g = \gamma_{p0}^{-1}$
L_{wo}	w_p/θ_{is}; Spatial walk-off length ($1/e^2$ radius w_p)	Subsection 4.2
θ_{is}	Geometric mean phase-matching angle	Eq. (20)
$\theta_{is,\max}$	Maximum of θ_{is} (vs. wavelength)	Eq. (23)
Γ	Gain-guided mode gain rate ($\Gamma \leq \gamma_{p0}$)	Fig. 3(a)
$\tilde{g}_{\mathbf{z}}(k)$	Spatial Fourier transform of QPM grating	Eq. (26)
σ_z	Standard deviation of QPM RDC errors	See Eq. (26)
N	Number of domains in the QPM grating	Eq. (26)
l_D	Half the QPM period	Subsection 5.1
U_{SH}	Generated pump SHG (RDC errors)	Eq. (27)
U_{TPA}	Two-photon-absorbed pump SHG (RDC errors)	Eq. (28)
β_{TPA}	Two-photon absorption coefficient	Eq. (28)
d_{OPA}	Nonlinear coefficient for OPA	Eq. (27)
d_{SHG}	Nonlinear coefficient for pump-SHG	Eq. (27)
$\Delta k_{si}^{(DFG)}$	Phase-mismatch for signal-idler DFG	Eq. (29)

Table 4. Summary of definitions used primarily in section 7.

Symbol	Description
$v_{sw}(\Omega)$	Group velocity of the seeded wave
$v_{uw}(\Omega)$	Group velocity of the unseeded wave
$v_{amp}(z)$	Effective velocity of the amplification wavefront
$\tau_{sw}(z,\Omega)$	Group delay spectrum of the seeded wave
$\tau_{uw}(z,\Omega)$	Group delay spectrum of the unseeded wave
$\tau_{uw,\text{eff}}(z)$	Effective delay of the secondary wavefront
$v_{uw,\text{eff}}(z)$	Effective velocity of the secondary wavefront
$\beta_{j,GVD}(\Omega)$	GDD coefficient of wave j ($j = sw$ or $j = uw$)
$\beta_{j,GDD}(z,\Omega)$	GDD of wave j ($j = sw$ or $j = uw$)
$\Omega_{pm}(z)$	Phase-matched seeded-wave frequency at position z
$\Omega_{\text{inst}}(z,t)$	Instantaneous seeded-wave frequency
$\delta v_{uw,sw}(\Omega)$	GVM coefficient between the seeded and unseeded waves

Acknowledgments

m) T. Guerreiro, E. Pomarico, B. Sanguinetti, N. Sangouard, J.S. Pelc, C. Langrock, M.M. Fejer, H. Zbinden, R.T. Thew, N. Gisin, "Nonlinear interaction of independent single photons based on integrated nonlinear optics," *Nature Communications* **4**, art. 2324 (August 2014).

Interaction of independent single photons based on integrated nonlinear optics

T. Guerreiro[1], E. Pomarico[1,†], B. Sanguinetti[1], N. Sangouard[1], J.S. Pelc[2], C. Langrock[2], M.M. Fejer[2], H. Zbinden[1], R.T. Thew[1] & N. Gisin[1]

The parametric interaction of light beams in nonlinear materials is usually thought to be too weak to be observed when the fields involved are at the single-photon level. However, such single-photon level nonlinearity is not only fundamentally fascinating but holds great potential for emerging technologies and applications involving heralding entanglement at a distance. Here we use a high-efficiency waveguide to demonstrate the sum-frequency generation between a single photon and a single-photon level coherent state. The use of an integrated, solid state, room temperature device and telecom wavelengths makes this type of system directly applicable to future quantum communication technologies such as device-independent quantum key distribution.

[1] Group of Applied Physics, University of Geneva, Geneva 1211, Switzerland. [2] E.L. Ginzton Laboratory, Stanford University, 348 Via Pueblo Mall, Stanford, California 94305, USA. † Present address: Laboratory of Ultrafast Spectroscopy, EPFL, Lausanne 1015, Switzerland. Correspondence and requests for materials should be addressed to T.G. (email: thiago.barbosa@unige.ch).

1

Photons are ideal carriers of quantum information, as they can be easily created and can travel long distances without being affected by decoherence. For this reason, they are well suited for quantum communication[1]. However, the interaction between single photons is negligible under most circumstances. Realizing such an interaction is not only fundamentally fascinating but holds great potential for emerging technologies. It has recently been shown that even weak optical nonlinearities between single photons can be used to perform important quantum communication tasks more efficiently than methods based on linear optics[2], which have fundamental limitations[3]. Nonlinear optical effects at single-photon levels in atomic media have been studied[4,5] and demonstrated[6–9], but these are neither flexible nor compatible with quantum communication, as they impose restrictions on photons' wavelengths and bandwidths. Here we use a high-efficiency nonlinear waveguide (WG)[10,11] to observe the sum-frequency generation (SFG) between a single photon and a single-photon level coherent state from two independent sources.

The potential of parametric interactions used for quantum information processing has been demonstrated in a variety of interesting experiments[12–14]. Although these interactions have been shown to preserve coherence[15–17], they are generally performed using strong fields[18–20]. It is only recently that parametric effects such as cross-phase modulation[21,22] and spontaneous downconversion[23,24] have been observed with a single-photon level pump. We take the next step and realize a photon–photon interaction, which can enable some fascinating experiments. For example, Fig. 1 shows how the SFG of two photons γ_2 and γ_3 from independent spontaneous parametric down conversion (SPDC) sources can herald the presence of two distant photons γ_1 and γ_4, as proposed in ref. 2. If the photon pairs are initially entangled using time-bin encoding, the detection of the photon γ_5 on a basis that erases the 'which path' information about its creation time projects the pair $\gamma_1\gamma_4$ in an entangled state. If we compare this approach for the heralded creation of entangled pairs with the linear optics scheme presented in ref. 25 (which is shown to be optimal with respect to the number of photon pairs needed), to obtain a generated state with fidelity $F \geq 0.9$, and assuming an overall detection and coupling efficiency of $\eta = 0.6$, our nonlinear optical proposal represents a competitive alternative as soon as the efficiency[2] of the SFG is 10^{-8}. Such efficiencies of 10^{-8} are, however, extremely challenging to achieve in common nonlinear crystals.

In our experiment, we increase the interaction cross-section by strongly confining the photons, both spatially and temporally, over a long interaction length. The spatial confinement is achieved with a state-of-the-art nonlinear WG[10,11], whereas the temporal confinement is obtained by using pulsed sources[26]. The efficiency of the process is proportional to the square of the WG length L^2 and inversely proportional to the duration of the input photons. L is limited by the group velocity dispersion between the input photons and the unconverted photon[2]. We maximize the SFG efficiency by matching the spectrotemporal characteristics of the single photons with the phase-matching constraints of the WG. A 4-cm WG and 10-ps photon satisfy these conditions. The use of an integrated, room temperature device and telecom wavelengths makes this approach to photon–photon interaction
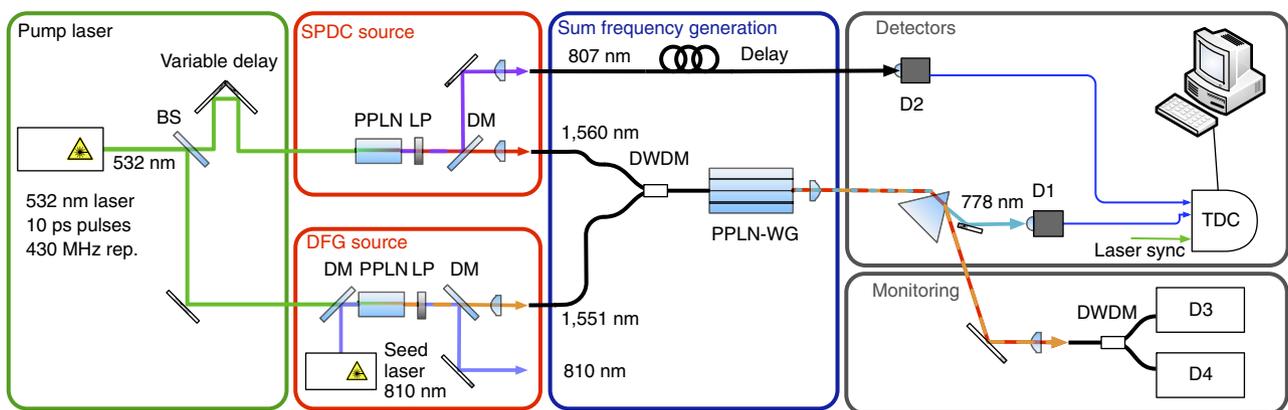

Figure 1 | Concept. The SFG of photons from separate sources. A photon from each of two pair sources S_1 and S_2 is sent over a distance to a nonlinear WG. This WG performs the sum-frequency generation (SFG) of photons γ_2 and γ_3 and outputs a photon γ_5. Detecting this photon heralds the distant presence of photons γ_1 and γ_2. Critically, the SFG process will work only for γ_2 and γ_3 and not for two photons coming from the same source. This feature would allow for faithful entanglement swapping, which is otherwise impossible to perform with two probabilistic pair sources and linear optics.

Figure 2 | Experimental set-up. A mode-locked laser that generates 10 ps pulses at 532 nm with a repetition rate of 430 MHz is used to pump the two sources. The SPDC source consists of a periodically poled lithium niobate (PPLN) crystal set to produce pairs of photons at 807 and 1,560 nm. These are deterministically separated by a dichroic mirror (DM) and collected into optical fibres. The remaining pump light is removed with a long pass filter (LP). The DFG source consists of a similar PPLN crystal seeded by a continuous wave laser at 810 nm producing coherent state pulses at 1,551 nm by DFG. These pulses are combined into the same fibre via a 200-GHz three-port dense wavelength divsion multiplexer (DWDM; ACPhotonics) and directed to the PPLN waveguide (WG). The PPLN-WG is 4.5 cm long and has a SHG efficiency of 41% W^{-1}cm^{-2} at 1,556 nm. The upconverted light is separated from the remaining telecom light via a prism, and sent to D1, a free space Si detector. The remaining unconverted telecom light is demultiplexed by another DWDM and sent to detectors D3 and D4, two free running InGaAs detectors. D3 and D4 are used for monitoring the coupling stability during the experiment and for optimizing the transmission of the input fields through the WG by optimising their polarization. We record threefold coincidences between detectors D1, D2 and the laser clock signal using a time-to-digital converter (QuTools).

well adapted to long-distance quantum communication, moving quantum nonlinear optics one step further towards complex quantum networks and future applications such as device-independent quantum key distribution.

Results

Sources. A schematic of the experimental set-up is shown in Fig. 2. A 532-nm mode-locked laser produces pulses that pump two distinct sources. The first source produces pairs of photons by spontaneous parametric downconversion at 807 and 1,560 nm (SPDC source). Further details can be found in ref. 26. The second source produces weak coherent state pulses at 1,551 nm by difference frequency generation (DFG) source. The process is stimulated by a 810-nm continuous wave seed laser. The average number of photons in the coherent state pulse can be adjusted by changing the seed and pump powers. All photons are coupled into single-mode fibres.

The telecom photons generated by the SPDC source are combined with the coherent state pulses from the DFG source using a dense wavelength division multiplexer (DWDM). We verified the single-photon nature of the SPDC source by measuring the conditional second-order correlation function of the telecom photon after the DWDM to be $g^{(2)}(0) = 0.03$.

SFG device. The photons are then sent to a fibre pigtailed reverse proton exchange type 0 periodically poled lithium niobate WG, 4.5 cm long[10]. This WG produces SFG of the input fields according to the phase-matching conditions shown in Fig. 3.

The overall system efficiency for second harmonic generation (SHG) is measured to be 41% $W^{-1} cm^{-2}$ at 1,556 nm, and is used to estimate the SFG efficiency as described in the Methods. In addition to high efficiency, the WG exhibits almost ideal phase matching, as can be seen from Fig. 3b, as well as a high coupling of the fibre to the WG of 70%.

Measurement results. To verify the signature of our photon–photon interaction, we record threefold coincidences between detectors D1 and D2 (both Si detectors) and the laser clock signal. When an upconverted photon is detected at D1 (3.5 Hz dark counts, 62% detection efficiency at 780 nm), an electric signal is sent to D2 (probability of dark count per gate 10^{-3}, detection efficiency 40% at 810 nm)[27] opening a 10-ns-detection window. Conditioning the upconversion events on the laser clock signal helps to reduce the noise. We ensure that the photons arrive at the same time inside the WG by moving a motorized delay. Figure 4a shows the upconverted signal as a function of the delay between the photons. When performing this temporal alignment, the mean number of photons in the coherent state was increased

to 25 per pulse. Each point of Fig. 4a corresponds to the number of threefold coincidences between D1, D2 and the laser clock that occur over 10 min. The full width at half maximum (FWHM) of the graph seen in Fig. 4 is 14.8 ps, which corresponds to the convolution of two 10 ps pulses from the pump laser. From the spectra of the photons that are 1.2 nm for the SPDC and 0.8 nm for the DFG, we can deduce their coherence times, respectively, 6.76 and 10.03 ps. This is a good indication that our photons are close to being pure.

Once the SPDC and DFG sources have been characterized, we set the temporal delay to zero and measure the performance of the nonlinear interaction. For this measurement, the coherent
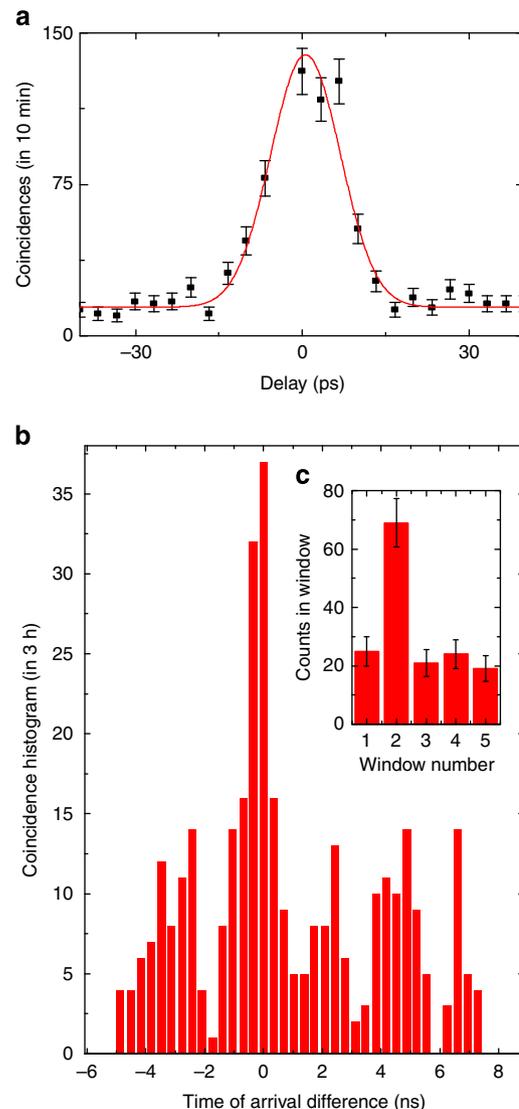
Figure 4 | Temporal delay and coincidence measurement. (**a**) Temporal overlap of input signals at the WG measured by introducing a delay between the photons' arrival times. The Gaussian fit (solid line) gives a FWHM 14.8 ps, which corresponds to a convolution of two pulses of 10 ps from our laser. The spectra of the SPDC and of the DFG are, respectively, 1.2 nm and 0.8 nm, corresponding to 6.76 ps and 10.03 ps, respectively. This indicates that to within the resolution of our measurement, our photons are close to being single mode. (**b**) Coincidence histogram between D1 and D2 showing strict time correlation between the heralding upconverted photon and the 807 nm photon. The spread of the coincidence peak is mainly dominated by detector jitter. Side peaks are due to the periodicity of the laser. (**c**) Bar chart histogram is obtained by integrating the two central bins of each peak. Error bars, 1 s.d.
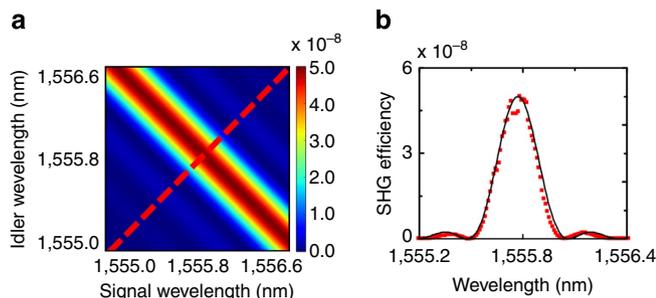
Figure 3 | WG efficiency. (**a**) Calculation of the WG efficiency taking into account the quasi-phase-matching conditions. The red-dashed line represents points corresponding to SHG. (**b**) Measured values for the efficiency of SHG (red points) compared with the theoretical prediction (solid line), showing an almost ideal phase-matching of the PPLN-WG.

state had a mean number of 1.7 photons per pulse inside the WG. A histogram of arrival time differences is shown in Fig. 4b (each bin corresponds to 0.32 ns). The main peak is the signature of photon–photon conversion. It is also possible to see side peaks, which correspond to a dark count at D1 owing to intrinsic noise of the detector followed by a detection of a photon at D2 (see Methods). The periodicity of these side peaks corresponds to the period of the pump laser.

To more clearly see the signal-to-noise characteristics of the experiment, we integrate over the events in the two central bins for each peak. This is shown in Fig. 4c, where a peak with a signal-to-noise of 2 can be seen.

The coincidence rate between D1 and D2 was 25 ± 5 counts per hour. To determine the efficiency of the SFG, we can use this rate along with other independently measured parameters from our set-up. We estimate the overall efficiency of the process at the single-photon level to be $\eta_{SFG} = (1.5 \pm 0.3) \times 10^{-8}$. Alternatively, using the measurement of SHG efficiency, the calculation of the SFG efficiency shown in Fig. 3 and accounting for the bandwidth of the interacting beams, we estimated the efficiency to be 1.56×10^{-8}, which agrees well with the value estimated from the measured data. We highlight that this is the overall conversion efficiency, which includes the effects of coupling into the WG, internal losses and losses through the set-up up to D1. Correcting for all of these losses, we obtain the intrinsic device efficiency of $(2.6 \pm 0.5) \times 10^{-8}$.

Discussion

We have demonstrated the nonlinear interaction between a single photon and a single-photon level coherent state. Such single-photon level parametric interactions open new perspectives for emerging quantum technologies. At the level of efficiency (1.5×10^{-8}) demonstrated here, the technique is already competitive with linear optics protocols[25,28,29], and offers new possibilities such as heralding entanglement at a distance[2]. This approach also opens the way towards device-independent quantum key distribution[30]. Unlike previously proposed linear optics schemes, there is significant scope for improvements as higher nonlinearities are realised. Work in this field is advancing rapidly, using materials with higher nonlinear coefficients[31] as well as methods for tighter field confinement[32]. The use of an integrated, solid state, room temperature device and a flexible choice of wavelengths will further aid the applicability of this type of system in future quantum communication technologies and beyond.

Methods

Evaluation of the number of photons in the coherent state. To evaluate the number of photons per pulse in the coherent state, we measure the average power P_α at the output of the DWDM. The average number of photons per pulse at this point is

$$\bar{n} = \frac{\lambda P_\alpha}{hc} \times \frac{1}{f} \qquad (1)$$

where f is the laser repetition rate of 430 MHz. To have the number of photons inside the WG, we multiply $\bar{n}$ by the overall transmission of the set-up from the DWDM to the interior of the WG, including the coupling of the pigtail inside the WG of 70%. The overall transmission is 64%.

Noise characterization. Understanding the origin of the side peaks present in the graph of Fig. 5 is crucial. To do this, we blocked the telecom photon coming from the SPDC source but not the coherent state from the DFG source, and recorded threefold coincidences between D1, D2 and the laser clock. The scaling of such noise in detector D2 as a function of the average power in the coherent state can be seen in Fig. 5. Each point in the graph corresponds to a coincidence histogram integrated over 20 min. The quadratic behaviour of this noise suggests a possible contribution of SHG from 1,551-nm pulses to these side peaks.

To evaluate this, we estimate the effective SHG efficiency from the second harmonic spectrum seen in Fig. 4b. The peak value of such spectrum corresponds to a measured efficiency of 41% $W^{-1} cm^{-2}$. From a fit of such a spectrum, we conclude that the effective SHG efficiency for 1,551 nm is $\eta_{SHG}(1,551) = 2.35 \times 10^{-4} \times 41\%$ $W^{-1} cm^{-2}$.

Taking into account this effective efficiency, we can estimate the expected rates at detector D1 due to SHG of the coherent state pulses. These rates are simply

$$R_{SHG}(P_\alpha) = (P_\alpha \times \mu)^2 \times \eta_{SHG}(1,551) \times L^2 \times \frac{\lambda}{hc} \qquad (2)$$

where μ is the coupling efficiency of the coherent state into the optical fibre, which was measured to be 76% and L is the length of the WG. The result of this estimation compared with the actual measured values can be seen in Table 1.

From such an analysis, we can conclude that the SHG contribution to the noise at the single-photon level can be neglected. The side peaks are then dominated by coincidence between a dark count at D1 and a detection at D2. This confirms that a detection of an upconverted photon does not come from conversion of two photons from the same DFG pulse.

SFG efficiency measurement. Using the data shown in Fig. 5, we can extract the rate of coincidences between D1 and D2, R_{SFG}. By combining these with other numbers from the set-up, independently characterised, we can then extract the overall SFG efficiency from a single-photon measurement. The numbers used to obtain this efficiency can be seen in Table 2.

The SFG efficiency is then given by

$$\hat{\eta}_{SFG} = \frac{R_{SFG}}{\beta} \qquad (3)$$

where β is the product of all the quantities in Table 2 times the laser repetition rate of 430 MHz. From the experimental data, we obtained $R_{SFG} = 25 \pm 5$ counts per hour, yielding an overall efficiency of $\eta_{SFG} = (1.5 \pm 0.3) \times 10^{-8}$.

SFG efficiency estimation. It is natural to ask whether the value found for the SFG efficiency agrees with the value for the efficiency of the SHG, measured classically, shown in Fig. 3. To do that, we modelled the phase-matching conditions of the WG using the appropriate Sellmeier equations[33].

The peak value of the SHG efficiency, corresponding to a wavelength of 1,556 nm, is 41% $W^{-1} cm^{-2}$. Given an efficiency measured at the classical level η,
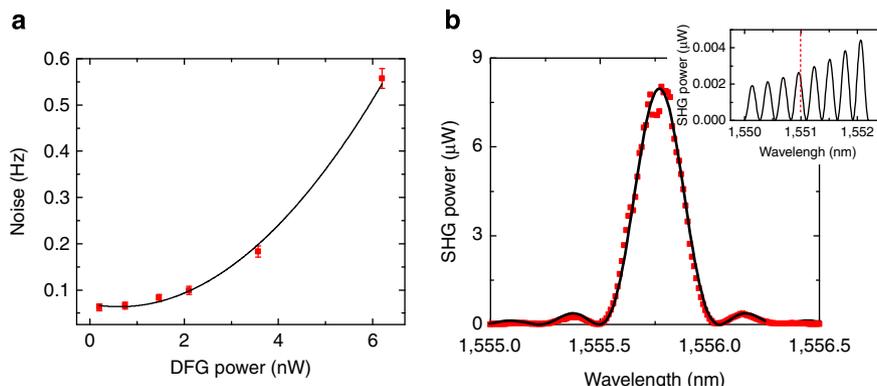

Figure 5 | Noise in D2 and SHG. (**a**) Quadratic behaviour of noise in detector D2 as a function of DFG source power. (**b**) The SHG spectrum. Solid line indicates fit of the data with a sinc^2 function. (Inset: zoom of fit) Dashed red line shows the predicted intensity of SHG at 1,551 nm. Error bars, 1 s.d.

Table 1 | Noise in D1 as a function of the coherent state size.

P_α (nW)	Measured (Hz)	Calculated (Hz)
6.20	15.30	18.60
3.54	5.70	6.60
2.10	3.80	2.30
1.47	4.00	1.10
0.75	3.20	0.30
0.00	3.50	0.00

Measured and calculated counts at D1 as a function of the power of the coherent state. As the power is reduced, the SHG contribution to clicks at D1 falls below the detector noise level. During the experiment, we operate in this regime.

Table 2 | Key parameters of the set-up.

SPDC source	
p_{SPDC}	0.03 ph per mode
t_{807}	0.4
$t_{grating}$	0.7
η_{807}	0.4
t_{DWDM}^{SPDC}	0.86
$t_{bandwidth}$	0.4
DFG source	
p_{DFG}	1.7 ph per mode
t_{DWDM}^{DFG}	0.96
η_{780}	0.6

DFG, difference frequency generation; DWDM, dense wavelength division multiplexer; p, number of photons per mode; t, transmission.
These parameters were independently characterized. Each particular index refers to a different optical element.

we can obtain the corresponding value at the single-photon level $\hat{\eta}$ using the equation[2]

$$\hat{\eta}(\lambda) = \frac{\eta(\lambda)}{2} \times \frac{hc}{\lambda} \times \frac{\Delta\hat{v}L}{tbp} \qquad (4)$$

where for our system, $L = 4.5$ cm, $\Delta\hat{v} \geq 296$ GHz cm and tbp $= 0.66$. To give an example, the peak level for the SHG efficiency then reads $\hat{\eta}(1,556) = 5 \times 10^{-8}$, which is of the same order of magnitude of the SFG efficiency obtained experimentally. This estimation, however, did not take into account the bandwidth of the interacting fields.

To take this into consideration, we use the matrix shown in Fig. 3 to obtain $\hat{\eta}(\lambda_s, \lambda_i)$, the efficiency as a function of the new wavelengths of the input fields. We then integrate over the spectra of the interacting beams, normalized by the area, denoted by $p_s(\lambda_s)$ and $p_i(\lambda_i)$. The total effective efficiency reads

$$\hat{\eta}_{SFG}^{eff} = \iint p_s(\lambda_s)p_i(\lambda_i)\hat{\eta}(\lambda_s, \lambda_i)d\lambda_s d\lambda_i = 1.56 \times 10^{-8} \qquad (5)$$

which is in agreement with the value found from the measured data.

References

1. Gisin, N. & Thew, R. Quantum communication. *Nat. Photonics* **1**, 165–171 (2007).
2. Sangouard, N. *et al.* Faithful entanglement swapping based on sum-frequency generation. *Phys. Rev. Lett.* **106**, 120403 (2011).
3. Kok, P. & Braunstein, S. L. Limitations on the creation of maximal entanglement. *Phys. Rev. A* **62**, 064301 (2000).
4. Schmidt, H. & Imamoglu, A. Giant kerr nonlinearities obtained by electromagnetically induced transparency. *Opt. Lett.* **21**, 1936–1938 (1996).
5. Chuang, I. L. & Yamamoto, Y. Simple quantum computer. *Phys. Rev. A* **52**, 3489–3496 (1995).
6. Turchette, Q. A., Hood, C. J., Lange, W., Mabuchi, H. & Kimble, H. J. Measurement of conditional phase-shifts for quantum logic. *Phys. Rev. Lett.* **75**, 4710–4713 (1995).
7. Birnbaum, K. M. *et al.* Photon blockade in an optical cavity with one trapped atom. *Nature* **436**, 87–90 (2005).
8. Pritchard, J. D. *et al.* Cooperative atom-light interaction in a blockaded rydberg ensemble. *Phys. Rev. Lett.* **105**, 193603 (2010).
9. Peyronel, T. *et al.* Quantum nonlinear optics with single photons enabled by strongly interacting atoms. *Nature* **488**, 57–60 (2012).
10. Parameswaran, K. R. *et al.* Highly efficient second-harmonic generation in buried waveguides formed by annealed and reverse proton exchange in periodically poled lithium niobate. *Opt. Lett.* **27**, 179–181 (2002).
11. Tanzilli, S. *et al.* On the genesis and evolution of integrated quantum optics. *Laser Photonics Rev.* **6**, 115–143 (2012).
12. Kim, Y. H., Kulik, S. P. & Shih, Y. Quantum teleportation of a polarization state with a complete bell state measurement. *Phys. Rev. Lett.* **86**, 1370–1373 (2001).
13. Dayan, B., Pe'er, A., Friesem, A. A. & Silberberg, Y. Nonlinear interactions with an ultrahigh flux of broadband entangled photons. *Phys. Rev. Lett.* **94**, 043602 (2005).
14. Langford, N. K. *et al.* Efficient quantum computing using coherent photon conversion. *Nature* **478**, 360–363 (2011).
15. Giorgi, G., Mataloni, P. & De Martini, F. Frequency hopping in quantum interferometry: efficient up-down conversion for qubits and ebits. *Phys. Rev. Lett.* **90**, 027902 (2003).
16. Tanzilli, S. *et al.* A photonic quantum information interface. *Nature* **437**, 116–120 (2005).
17. Curtz, N., Thew, R., Simon, C., Gisin, N. & Zbinden, H. Coherent frequency-down-conversion interface for quantum repeaters. *Opt. Express.* **18**, 22099–22104 (2010).
18. Roussev, R. V., Langrock, C., Kurz, J. R. & Fejer, M. M. Periodically poled lithium niobate waveguide sum-frequency generator for efficient single-photon detection at communication wavelengths. *Opt. Lett.* **29**, 1518–1520 (2004).
19. Vandevender, A. P. & Kwiat, P. G. High efficiency single photon detection via frequency up-conversion. *J. Mod. Optic* **51**, 1433–1445 (2004).
20. Thew, R. T., Zbinden, H. & Gisin, N. Tunable upconversion photon detector. *Appl. Phys. Lett.* **93**, 071104 (2008).
21. Matsuda, N., Shimizu, R., Mitsumori, Y., Kosaka, H. & Edamatsu, K. Observation of optical-fibre kerr nonlinearity at the single-photon level. *Nat. Photonics* **3**, 95–98 (2009).
22. Lo, H. Y., Su, P. C. & Chen, Y. F. Low-light-level cross-phase modulation by quantum interference. *Phys. Rev. A* **81**, 053829 (2010).
23. Hubel, H. *et al.* Direct generation of photon triplets using cascaded photon-pair sources. *Nature* **466**, 601–603 (2010).
24. Shalm, L. K. *et al.* Three-photon energy-time entanglement. *Nat. Phys.* **9**, 19–22 (2013).
25. Sliwa, C. & Banaszek, K. Conditional preparation of maximal polarization entanglement. *Phys. Rev. A* **67**, 030101 (2003).
26. Pomarico, E., Sanguinetti, B., Guerreiro, T., Thew, R. & Zbinden, H. Mhz rate and efficient synchronous heralding of single photons at telecom wavelengths. *Opt. Express.* **20**, 23846–23855 (2012).
27. Lunghi, T. *et al.* Advantages of gated silicon single-photon detectors. *Appl. Optics* **51**, 8455–8459 (2012).
28. Barz, S., Cronenberg, G., Zeilinger, A. & Walther, P. Heralded generation of entangled photon pairs. *Nat. Photonics* **4**, 553–556 (2010).
29. Wagenknecht, C. *et al.* Experimental demonstration of a heralded entanglement source. *Nat. Photonics* **4**, 549–552 (2010).
30. Gisin, N., Pironio, S. & Sangouard, N. Proposal for implementing device-independent quantum key distribution based on a heralded qubit amplifier. *Phys. Rev. Lett.* **105**, 070501 (2010).
31. Kemlin, V. *et al.* Phase-matching properties and refined sellmeier equations of the new nonlinear infrared crystal cdsip2. *Opt. Lett.* **36**, 1800–1802 (2011).
32. Kurimura, S., Kato, Y., Maruyama, M., Usui, Y. & Nakajima, H. Quasi-phase-matched adhered ridge waveguide in linbo3. *Appl. Phys. Lett.* **89**, 191123 (2006).
33. Jundt, D. H. Temperature-dependent sellmeier equation for the index of refraction, n(e), in congruent lithium niobate. *Opt. Lett.* **22**, 1553–1555 (1997).

Author contributions

T.G., E.P. and B.S. carried out the experiment; J.S.P., C.L. and M.M.F. fabricated and tested the PPLN Waveguide; B.S., N.S., R.T.T., H.Z. and N.G. conceived and supervised the project. All authors participated in writing the manuscript.

Additional information

Accession codes: The complete consensus mt genome sequences have been deposited to NCBI GenBank under Accession numbers KC553980–KC554018.

Competing financial interests: The authors declare no competing financial interests.

Reprints and permission information is available online at http://npg.nature.com/reprintsandpermissions/

How to cite this article: Guerreiro, T. *et al.* Interaction of independent single photons based on integrated nonlinear optics. *Nat. Commun.* 4:2324 doi: 10.1038/ncomms3324 (2013).

n) D. Chang, C. Langrock, Y.W. Lin, C.R. Phillips, C.V. Bennett, M.M. Fejer, "Complex-transfer-function analysis of optical-frequency converters," *Opt. Lett.* **39**, pp. 5106-09 (September 2014)

Complex-transfer-function analysis of optical-frequency converters

Derek Chang,[1,2,*] Carsten Langrock,[1] Yu-Wei Lin,[1] C. R. Phillips,[1,3] C. V. Bennett,[2] and M. M. Fejer[1]

[1]E. L. Ginzton Laboratory, Stanford University, Stanford, California 94305, USA

[2]Lawrence Livermore National Laboratory, Livermore, California 94551, USA

[3]Department of Physics, Institute of Quantum Electronics, ETH Zurich, Zurich 8093, Switzerland

*Corresponding author: djychang@stanford.edu

The measurement of the magnitude and phase of the complex transfer function (CTF) of aperiodically poled lithium niobate waveguide devices using frequency resolved optical gating (FROG) is demonstrated. We investigate the sources of CTF distortions which are related to variations in the spatial distribution of the nonlinear coefficient and phase-mismatch profile and present a method to infer fabrication errors from the CTF discussed.　© 2014 Optical Society of America

OCIS codes:　(190.4360) Nonlinear optics, devices; (190.7110) Ultrafast nonlinear optics.
http://dx.doi.org/10.1364/OL.39.005106

Quasi-phase-matching (QPM) gratings can be used to tailor the frequency response of wavelength converters, a degree of freedom particularly useful for optical signal processing devices. In Ref. [1], the phase response was engineered to compensate for group-velocity mismatch and a transfer function formalism for second harmonic generation (SHG) was derived. The transfer function here represents the magnitude and phase of the output spectrum of a nonlinear mixing process compared to the inputs. This transfer function is independent of the input waves and only depends on intrinsic material properties and QPM design. This concept is useful for designing devices as well as analyzing the performance of QPM-based optical-frequency converters (OFC).

Transfer functions may exhibit distortions because of material defects or fabrication errors. In waveguide-based OFCs, longitudinally varying phase velocity inhomogeneities can arise from longitudinal variations in the waveguide lithography or processing conditions. In devices with a uniform, periodic grating, such inhomogeneities reduce the peak conversion efficiency and distort the ideal sinc^2 transfer function [2,3]. In chirped (aperiodic) gratings, each frequency component of the input converts at distinct positions along the propagation direction, and perturbations create uneven conversion efficiencies and therefore distort the passband of the transfer function. In practical devices, the QPM waveguide parameters are often designed to minimize the sensitivity of the phase-matching to fabrication errors; if the first-order dependence of the phase-mismatch with respect to a particular fabrication parameter, e.g., waveguide width, vanishes, the design is said to be noncritical [4], in relation to noncritical phase-matching in bulk frequency converters. However, large fabrication errors, or deviations of the design from the noncritical condition, may still introduce unwanted distortions to the transfer function, degrading device performance beyond acceptable limits.

While the transfer function can be measured by tuning a CW input laser across the bandwidth of the device and monitoring the amplitude and phase of the generated output [5], measuring the phase response by this approach is experimentally difficult. In this Letter, we introduce and experimentally demonstrate a method for measuring the CTF by characterizing the complex input and output spectra of ultrafast pulses, as well as the extraction of the spatial dependence of the effective nonlinear coefficient $d(z)$ and the phase mismatch $\Delta\beta(z)$. These functions, in turn, are useful for diagnosing fabrication defects, as well as for predicting the performance of the device in various phase-sensitive applications. We focus here on the SHG process, though the concepts can be extended straightforwardly to other mixing processes [6].

The CTF, $\hat{D}(\Omega) \equiv \hat{A}_2(\Omega)/\hat{A}_1^2(\Omega)$, for SHG, in the low conversion regime, is the ratio of the spectrum of output second harmonic (SH), $\hat{A}_2(\Omega)$, to the spectrum of the square of the input fundamental harmonic (FH) $\hat{A}_1^2(\Omega)$ here $\Omega = \omega - \omega_2$ is the frequency detuning from the SH carrier ω_2 and the hat notation denotes a Fourier transform such that $\hat{f}(\Omega)$ is the Fourier transform of $f(t)$. Assuming an undepleted pump and negligible group velocity dispersion (GVD) over the bandwidth of the pulse, the CTF is related to the nonlinear coefficient $d(z)$ by the following integral [7]:

$$\hat{D}(\Omega) = \int_{-\infty}^{\infty} d(z)\exp\left[-\frac{1}{2}(2\alpha_1 - \alpha_2)z\right]\exp[i\Delta\phi(\Omega,z)]dz, \quad (1)$$

where $\Delta\phi(\Omega, z) = \int_{-\infty}^{z} \Delta\beta(\Omega, z')dz'$ is the phase mismatch, $\Delta\beta$ is the wave-vector mismatch, and $d(z)$ is the nonlinear coefficient. We assume $\hat{A}_2(\Omega, z = 0) = 0$ and that $d(z) = 0$ outside of the range $[0, L]$, where L is the length of the QPM grating. This form expands on that of Ref. [7] by including propagation power loss α_1 at the FH and α_2 at the SH. In the general case, we consider an apodized [8], nonuniform QPM grating whose apodization profile and variations in the local grating period and duty cycle are slow compared with the grating period itself, such that $d(z)$ can be accurately represented as a sum of distinct Fourier components $d_m(z)$, with a z-dependent amplitude and k-vector. We also assume that the mth component of the grating is phase-matched and dominates all other orders of the grating. In this case, the general form of $d(z)$ becomes

$$d(z) = d_m(z) = |d_m(z)| \exp[iK_{0m}z + i\Phi_m(z)], \qquad (2)$$

where $|d_m(z)|$ is the amplitude of the mth Fourier component of the grating and $\Phi_m(z)$ represents the phase of the grating beyond the $K_{0m}z$ carrier phase.

Material and waveguide dispersion are represented by $\Delta\beta(\Omega, z)$. To introduce the functional dependence of $\Delta\beta$ on the spatial coordinate z, we introduce a parametric representation $\xi(z)$ such that $\Delta\beta(\Omega, z) = \Delta\beta(\Omega, \xi(z))$. If we assume the typical variation $\delta\xi$ in the parameter, e.g., the waveguide width, is small compared to the nominal parameter value ξ, we can perform a Taylor series expansion resulting in

$$\Delta\beta(\Omega, \xi(z)) = \Delta\beta_0 + \frac{\partial\Delta\beta}{\partial\Omega}\Omega + \frac{\partial\Delta\beta}{\partial\xi}\delta\xi + \frac{1}{2}\frac{\partial^2\Delta\beta}{\partial\Omega^2}\Omega^2$$
$$+ \frac{1}{2}\frac{\partial^2\Delta\beta}{\partial\xi^2}\delta\xi^2 + \frac{\partial^2\Delta\beta}{\partial\Omega\partial\xi}\Omega\delta\xi$$
$$+ \frac{1}{2}\frac{\partial^3\Delta\beta}{\partial\Omega\partial\xi^2}\Omega\delta\xi^2 + \cdots, \qquad (3)$$

where $\Delta\beta_0 = \Delta\beta(0,0)$ and all derivatives are evaluated at $\Omega = 0, \xi = 0$. We consider situations where only terms up to second order are significant. For the reverse proton-exchange waveguides considered here, the following inequality holds:

$$\frac{\partial\Delta\beta}{\partial\xi}\delta\xi + \frac{\partial^2\Delta\beta}{\partial\xi^2}\delta\xi^2 \gg \frac{\partial}{\partial\Omega}\left(\frac{\partial\Delta\beta}{\partial\xi}\delta\xi + \frac{\partial^2\Delta\beta}{\partial\xi^2}\delta\xi^2\right)\Omega_b. \quad (4)$$

This inequality shows that the first and second-order variations of $\Delta\beta$ with respect to the parameter ξ have negligible dependence on frequency over the bandwidth of the SH, Ω_b. As a result, $\Delta\beta$ is additively separable up to second-order and hence can be written as

$$\Delta\beta(\Omega, \xi(z)) = \Delta\beta_0 + \Delta\beta_\Omega(\Omega) + \Delta\beta_\xi(\xi(z)), \qquad (5)$$

where

$$\Delta\beta_\Omega(\Omega) = \frac{\partial\Delta\beta}{\partial\Omega}\Omega + \frac{1}{2}\frac{\partial^2\Delta\beta}{\partial\Omega^2}\Omega^2$$
$$\Delta\beta_\xi(\xi) = \frac{\partial\Delta\beta}{\partial\xi}\delta\xi + \frac{1}{2}\frac{\partial^2\Delta\beta}{\partial\xi^2}\delta\xi^2. \qquad (6)$$

If the device is designed to be noncritical for the parameter ξ, then phase-matching does not have a first-order dependence in ξ [3], i.e., $(\partial\Delta\beta/\partial\xi)\delta\xi = 0$.

Here, we introduce the notation $\hat{D}(\Omega) \equiv \hat{d}(\Delta k(\Omega))$ and the transfer function can be written as

$$\hat{d}(\Delta k_m) = \int_{-\infty}^{\infty} |d_m(z)| \exp\left[-\frac{1}{2}(2\alpha_1 - \alpha_2)z\right]$$
$$\times \exp[i\phi_m(z)] \exp[i\Delta k_m z] \mathrm{d}z, \qquad (7)$$

where

$$\Delta k_m(\Omega) = \Delta\beta_0 - K_{0m} + \Delta\beta_\Omega(\Omega), \qquad (8)$$

$$\phi_m(z) = \Phi_m(z) + \int_0^z \Delta\beta_\xi(\xi(z')) \mathrm{d}z'. \qquad (9)$$

The transfer function has a Fourier transform relationship with the product of the nonlinear coefficient and propagation loss factor. It follows that $|d_m(z)|$ and $\Delta\beta(\xi(z))$ can be derived directly from the transfer function:

$$|d_m(z)| = \exp\left[\frac{1}{2}(2\alpha_1 - \alpha_2)z\right] \cdot |\mathcal{F}^{-1}[\hat{d}(\Delta k_m)]|, \qquad (10)$$

$$\Delta\beta_\xi(\xi(z)) = \frac{d}{dz}(\mathrm{Arg}\{\mathcal{F}^{-1}[\hat{d}(\Delta k_m)]\} - \Phi_m(z)), \qquad (11)$$

where $\mathcal{F}^{-1}$ denotes the inverse Fourier transform. Deriving $|d_m(z)|$; and $\Delta\beta_\xi(\xi(z))$ from the transfer function $\hat{D}(\Omega)$ gives useful information about deviations of the device from its design values, because of issues such as fabrication errors and photorefractive effects. Deviations of $|d_m(z)|$; from ideal could result from duty cycle variations or QPM domain dropouts. Variations in $\Delta\beta_\xi(\xi(z))$ result from variations in waveguide dispersion which distort phase-matching.

The devices under test are aperiodically poled lithium niobate (A-PPLN) waveguides. The linearly chirped QPM gratings are 43 mm long and phasematch a bandwidth of 22 nm with a center wavelength of 1560 nm. Waveguides are formed by proton exchange (PE) in benzoic acid through a lithographically defined mask. The exchange depth is determined by the exchange time and temperature [9]. This step is followed by annealing and reverse-proton-exchange (RPE) steps which decrease propagation loss while increasing the modal overlap between interacting fields [10–12].

In our experimental setup, a Ti:sapphire-pumped optical parametric oscillator that outputs 150 fs duration transform-limited pulses at 80 MHz with an average power of 200 mW is used as the pump source (Opal, Spectra-Physics). The magnitude and phase of the pump are characterized by SHG Frequency Resolved Optical Gating (FROG) [13]. This FH pump has a full width half-maximum bandwidth exceeding the bandwidth of the QPM grating to ensure that the entire transfer function is sufficiently sampled. The SH pulse out of the PPLN waveguide device is characterized by a sum-frequency generation cross-FROG (SFG XFROG), where a fraction of the pump pulse is mixed with the SH pulse via noncollinear, type-I phase-matching in a 250 μm thick BBO crystal cut at an angle of 22.4°. The spectrum of the generated output of the BBO crystal is measured by a spectrometer (HR4000, Ocean Optics) centered at 520 nm. FROG software (FROG Scan 8, Mesaphotonics) was used to automate the measurement and retrieve the FROG trace.

We obtain low SHG (64 × 64 grid) and SFG (256 × 256 grid) FROG errors, 0.002 and 0.006, respectively. The spectra of the retrieved FH and SH are compared with independent measurements using an optical spectrum analyzer (Yokogawa AQ6370C), confirming measurement accuracy.

Once the input FH and output SH are measured, the CTF is calculated by dividing the spectrum of the SH by the spectrum of the square of the FH. Figure 1 shows the magnitude and phase of the measured CTF. Theoretically, the curvature of the phase is proportional to the chirp rate of the QPM grating, $D_g = \delta k/(2L)$, the ratio
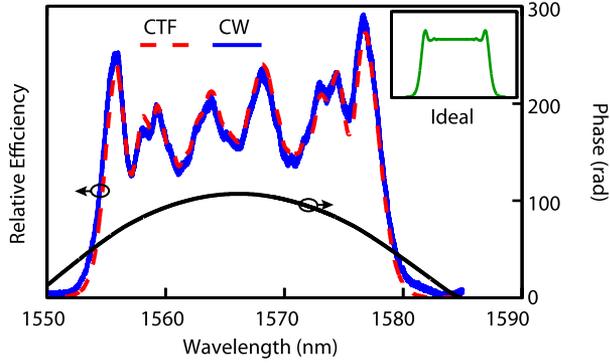
Fig. 1. Complex transfer magnitude (dashed, red) compared with CW magnitude (thick, blue) and ideal magnitude (inset). The phase (gray) curvature matches the theory to within 1%.

of the k-vector bandwidth δk of the linearly chirped QPM grating to the length of the QPM grating L [7]; the experimentally observed curvature agrees to within 1% with the predicted phase curvature based on the grating design. The magnitude of the transfer function was also measured with a tunable, continuous-wave (CW) laser at the FH wavelength. The ratio of the FH and SH power,

$\sqrt{P_{\mathrm{SH}}/P_{\mathrm{FH}}^2}$, represents the magnitude of the transfer function. As can be seen from Fig. 1, the two independent measurements show good agreement. Slight discrepancies come from small errors in the FROG measurement, which can be further minimized by incorporating frequency marginals [14]; our FROG software did not have this capability. For comparison, the inset represents the designed magnitude transfer function. The sample shown here exhibits significant deviations from the ideal transfer function; the best devices we have fabricated show ~5% deviation from a flat passband.

Insight into the cause for these distortions is found by extracting $|d_m(z)|$; and $\Delta\beta(z)$ using Eqs. 10 and 11. The loss coefficients α_1 and α_2 were previously measured and correspond to 0.2 dB/cm at the FH and 0.1 dB/cm at the SH. Errors in the loss measurement will add an artificial slope to $|d_m(z)|$;. The grating phase is $\Phi(z) = D_g z^2$.

The measured nonlinear coefficient profile, $|d_m(z)|$;, shown in Fig. 2, is plotted together with the as-designed profile. It is nearly constant for the majority of the device and apodized near the edges at $z = 0$ and $z = L$ to
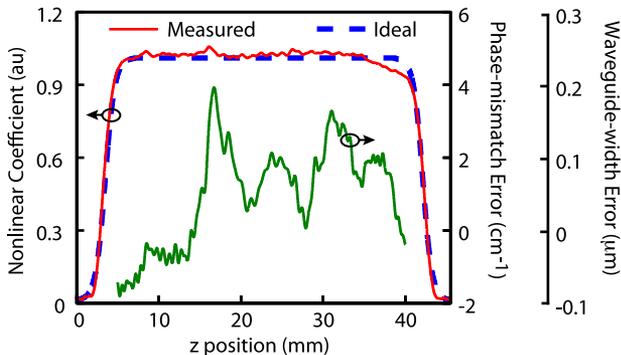
prevent high-frequency ripples in the transfer function [8]. The measured apodization profile and length closely follows the design. The measured phase-mismatch error, $\Delta\beta_\xi(\xi(z))$, ideally zero for all z, clearly exhibits distortions. It can vary by as much as 500 m^{-1} over a length of about 10 mm. These ripples in $\Delta\beta_\xi(\xi(z))$ are the dominant cause of transfer function distortions.

The phase-mismatch errors can be attributed to four possible causes in our fabrication process: variations in the lithographically defined waveguide width, longitudinal variations in PE temperature, anneal furnace temperature, or RPE temperature. The effect of these variations is estimated by using a 2D diffusion model to map variations in these parameters to changes in the guided-mode effective indices, and hence to phase-mismatch errors. The variations in observed phase-mismatch errors correspond to either a 0.2 μm variation in the wet-etched SiO$_2$ mask, a 0.3°C variation in the PE bath temperature, a 2°C variation in the anneal furnace temperature, a 0.2°C variation in the RPE bath temperature, or a combination thereof. The corresponding waveguide-mask width error is illustrated in Fig. 2. To test the uniformity of the waveguide width, we measured the mask openings of two waveguides on a chip fabricated under identical conditions to the chip mentioned above. Using an atomic force microscope (AFM), the chip is sampled 32 times every 2 mm in the longitudinal direction. The standard deviation of widths of each waveguide over the 32 scans has an average value of 0.04 μm with a median value that varies about 0.2 μm over the length of the device, which is consistent with the CTF calculation. This waveguide width error appears to be the dominant effect and explains the majority of the $\Delta\beta$ error. If these errors can be reduced significantly, investigation of and possible improvements to the temperature uniformity of the exchange processes should be performed.

The CTF of 12 waveguides, spaced 400 μm apart, are measured and the resulting $\Delta\beta_\xi(\xi(z))$ profiles are shown in Fig. 3. There are bright bands at $z = 17$ mm and $z = 31$ mm signifying a strong correlation across the entire device, which strongly suggests that the phase-matching error of each waveguide is caused by global fabrication problems.

There are a few things to note about this technique. The calculated $|d_m(z)|$; is not in absolute units. A

Fig. 2. Nonlinear coefficient $|d_m(z)|$; measured (solid) and as-designed (dash). Phase-mismatch error $\Delta\beta_\xi(\xi(z))$ and corresponding waveguide-mask width error.
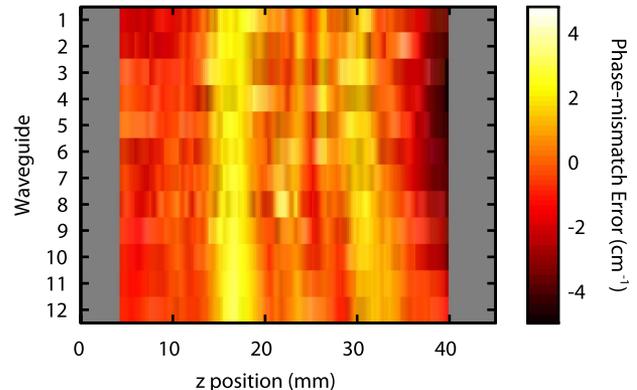

Fig. 3. Phase-mismatch error of 12 equidistantly spaced waveguides with a total separation of 4.4 mm.

separate measurement is needed for absolute scaling. The phase-mismatch, however, is in absolute units. Additionally, we neglect GVD and higher order dispersion at the FH. In our case, the effect of GVD is small as it contributes 0.1 rad of spectral phase over the bandwidth and length of the device. Neglecting GVD leads to a convenient one-to-one mapping between optical frequency of the generated wave and spatial frequencies of the QPM grating structure; this property is used to construct the CTF. In cases where the FH accumulates non-negligible group delay dispersion (GDD) over the length of the device, there is a finite spread of QPM grating spatial frequencies that can generate a particular SH optical frequency. To account for FH-GDD, a more general analysis discussed in [15] can be performed. In this analysis, the transfer function used here is replaced with a transfer matrix that describes the general mapping between grating spatial frequency and generated optical frequency including all orders of dispersion at both waves. Finally, the spatial resolution δz is limited by the resolvable frequency content of the CTF. If the CTF passband is resolved, then the bandwidth δk determines δz. For a chirped grating, δk is determined by the length L and chirp rate D_g of the QPM grating. Assuming the CTF to be a perfect top hat, the point spread function would have a sinc profile and the resolvable distance is $\delta z = 2\pi/\delta k = \pi/D_g L$. The device used in this study has a chirp rate of $D_g = 0.14$ mm^{-2} and a grating length of $L = 43$ mm, resulting in $\delta z = 0.5$ mm. However, in our measurement, we are able to resolve a spectral range of twice the CTF bandwidth, giving us a resolution of $\delta z = 0.25$ mm.

In conclusion, we have described and implemented a method for measuring the CTFs of QPM nonlinear devices and relating these CTFs to spatial variations in fabrication parameters. Further discussion of these errors and their implications for the performance of time lensing systems will be given in a subsequent paper.

References

1. M. A. Arbore, O. Marco, and M. M. Fejer, Opt. Lett. **22**, 865 (1997).
2. S. Helmfrid, G. Arvidsson, and J. Webjorn, J. Opt. Soc. Am. B **10**, 222 (1993).
3. M. L. Bortz, S. J. Field, M. M. Fejer, D. W. Nam, R. G. Waarts, and D. F. Welch, IEEE J. Quantum Electron. **30**, 2953 (1994).
4. E. J. Lim, S. Matsumoto, and M. M. Fejer, Appl. Phys. Lett. **57**, 2294 (1990).
5. R. Schiek, Y. Baek, and G. I. Stegeman, J. Opt. Soc. Am. B **15**, 2255 (1998).
6. G. Imeshev, M. M. Fejer, A. Galvanauskas, and D. Harter, J. Opt. Soc. Am. B **18**, 534 (2001).
7. G. Imeshev, M. A. Arbore, and M. M. Fejer, J. Opt. Soc. Am. B **17**, 304 (2000).
8. J. Huang, X. P. Xie, C. Langrock, R. V. Roussev, D. S. Hum, and M. M. Fejer, Opt. Lett. **31**, 604 (2006).
9. R. W. Boyd, *Nonlinear Optics* (Academic, 2008).
10. Y. N. Korkishko, V. A. Fedorov, T. M. Morozova, F. Caccavale, F. Gonella, and F. Segato, J. Opt. Soc. Am. A **15**, 1838 (1998).
11. J. Olivares and J. M. Cabrera, Appl. Phys. Lett. **62**, 2468 (1993).
12. R. Roussev, A. Sridharan, K. Urbanek, R. Byer, and M. M. Fejer, in *IEEE LEOS Annual Meeting Conference* (IEEE, 2003), pp. 334–335.
13. R. Trebino, K. W. Delong, D. N. Fittinghoff, J. N. Sweetser, B. A. Richman, M. A. Krumbu, and D. J. Kane, Rev. Sci. Instrum. **68**, 3277 (1997).
14. K. W. DeLong, D. N. Fittinghoff, and R. Trebino, IEEE J. Quantum Electron. **32**, 1253 (1996).
15. C. R. Phillips, L. Gallmann, and M. M. Fejer, Opt. Lett. **21**, 843 (2013).

o) T. Guerreiro, A. Martin, B. Sanguinetti, J.S. Pelc, C. Langrock, M.M. Fejer, N. Gisin, H. Zbinden, N. Sangouard, R.T. Thew, "Nonlinear Interaction between Single Photons," *Phys. Rev. Lett.* **113**, art. no. 173601 (Oct. 2014).

Nonlinear Interaction between Single Photons

T. Guerreiro,[1] A. Martin,[1] B. Sanguinetti,[1] J. S. Pelc,[2] C. Langrock,[2] M. M. Fejer,[2] N. Gisin,[1] H. Zbinden,[1]
N. Sangouard,[1,†] and R. T. Thew[1,*]

[1]*Group of Applied Physics, University of Geneva, 1211 Geneva 4, Switzerland*
[2]*E.L. Ginzton Laboratory, Stanford University, 348 Via Pueblo Mall, Stanford, California 94305, USA*
(Received 27 May 2014; published 22 October 2014)

Harnessing nonlinearities strong enough to allow single photons to interact with one another is not only a fascinating challenge but also central to numerous advanced applications in quantum information science. Here we report the nonlinear interaction between two single photons. Each photon is generated in independent parametric down-conversion sources. They are subsequently combined in a nonlinear waveguide where they are converted into a single photon of higher energy by the process of sum-frequency generation. Our approach results in the direct generation of photon triplets. More generally, it highlights the potential for quantum nonlinear optics with integrated devices and, as the photons are at telecom wavelengths, it opens the way towards novel applications in quantum communication such as device-independent quantum key distribution.

Observing nonlinear processes down to the quantum regime is a long sought after goal for quantum information science [1] as well as a fascinating concept in terms of fundamental physics, first being raised in the seminal work of Heisenberg and Euler [2]. It is only in recent years that materials and technologies have advanced to the point where one can probe this quantum nonlinear domain, and a few implementations have led to experimental realizations with attenuated classical laser light. This has included cross-phase modulation with weak classical light in atomic ensembles [3,4] and optical fibers [5], converting incident laser light into a nonclassical stream of photons [6,7] or Rydberg blockades [8] as well as all-optical switches with attenuated classical light in various atomic systems [9–15]. These atomic systems naturally operate with very narrow bandwidths and at specific wavelengths, typically in the visible regime. A grand challenge is to realize photon-photon interactions in materials that are less restrictive in terms of bandwidths and wavelengths. Of particular interest are photons at telecommunication wavelengths, as these provide the wiring, the flying qubits, for myriad applications in quantum communication [16,17]. A further challenge is to realize photon-photon interactions in a material that is not only less restrictive in terms of bandwidth, but also operating at room temperature.

Here we take an approach that exploits a parametric process, sum-frequency generation (SFG), in a nonlinear crystal [18–23]. The efficiency of nonlinear optical materials is constantly increasing and, by taking advantage of their inherently large bandwidth, one can work with pulsed systems and at higher repetition rates than with atomic systems. Important experimental results have been obtained in the context of quantum nonlinear optics with parametric processes [24–27], including the sum-frequency generation

from two weak coherent states and between a coherent state and a true single photon. Here we take the next step and report, for the first time, a nonlinear interaction between two true independent single photons (Fock states), at telecom wavelengths, via SFG. Note that this experiment cannot be seen simply as the time reversal process of the nonlinear interaction presented in Refs. [24,25], nor analogue to that of Ref. [20], as spontaneous parametric down-conversion (SPDC) typically generates photon pairs correlated in spectra, while our photons were generated in independent sources and therefore have uncorrelated spectra. Our approach opens up perspectives unreachable with classical light. As an example, it allows one to generate photon triplets directly, as depicted in Fig. 1. One photon from each of two independent photon pair sources—based
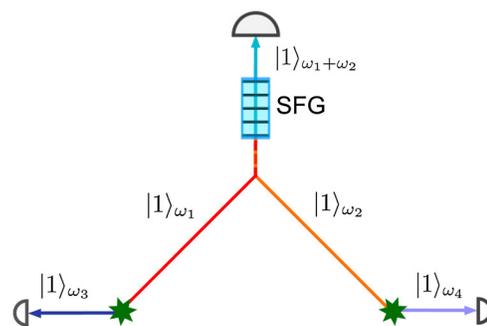

FIG. 1 (color online). Concept: Two single photons from independent photon pair sources are sent to a medium with $\chi^{(2)}$ nonlinearity and interact, generating a third photon carrying the sum of the energies and momenta of the input fields via SFG. As the photons sent to the SFG converter are at telecom wavelengths, the resulting photon triplet state allows, for example, the converted photon to herald the entanglement of the remaining two photon state at a distance.

on SPDC—is sent to a nonlinear crystal where the two photons undergo SFG to generate a third photon. As the SFG requires one photon from each pair, the original pairwise correlation for each SPDC source is now mapped to the remaining three photon state—the SFG converted photon can herald the presence of the remaining two photons at distributed locations. This approach offers unique opportunities, for example, to herald entangled photon pairs—even remotely—and to perform quantum key distribution where the security is independent of the internal workings of the devices used to generate the secret key [28].

The experiment has three distinct parts: the generation of entangled photon pairs from independent SPDC sources [we can also interpret this as generating two independent single photons by two heralded single photon sources (HSPS)]; the parametric interaction of two single photons in a nonlinear waveguide; and, finally, the detection of the resulting single photon of higher energy in coincidence with the two remaining photons—the photon triplet. A schematic of the setup is shown in Fig. 2.

The single photons are generated via SPDC in two independent sources. HSPS1 and HSPS2 generate pairs at 807–1560 nm and 810–1551 nm, respectively. By ensuring that the probability of creating a single pair in each source is much smaller than one, the detection of the visible (807, 810 nm) photons heralds the creation of two independent single telecom wavelength (1560, 1551 nm) photons. All of the photons are coupled into single-mode fibers with efficiencies ∼50%. In principle this could be increased close to unity but is limited here by available pump power, which enforces a compromise in coupling geometry [30]. Importantly, the heralding photons are filtered such that the bandwidth of telecom photons is matched to the acceptance bandwidth of the SFG process; cf. below. To verify the single photon nature of these sources, we measured the conditional second-order autocorrelation functions $g_1^{(2)}(0) = 0.0300 \pm 0.0005$ and $g_2^{(2)}(0) = 0.0360 \pm 0.0004$, for HSPS1 and HSPS2, respectively. In this configuration, errors due to multipair emission are negligible [31].

The two fiber coupled telecom photons are then directed to a 4.5 cm fiber-pigtailed periodically poled lithium niobate (PPLN) waveguide that is quasi–phase matched to perform the SFG process $1560\,\text{nm} + 1551\,\text{nm} \rightarrow 778\,\text{nm}$. Figure 3 shows the results of a classical measurement of the phase matching conditions of the waveguide. The diagonal ridge corresponds to the SFG process, while the horizontal and vertical ridges result from the second harmonic generation (SHG) of each independent field. Following [27] and taking into account the acceptance bandwidth of the waveguide and the bandwidth of the interacting photons, which are measured to be 0.27 nm, we determine a system conversion efficiency of 1.56×10^{-8}. This is close to the independently measured value, found to be $(1.5 \pm 0.3) \times 10^{-8}$.
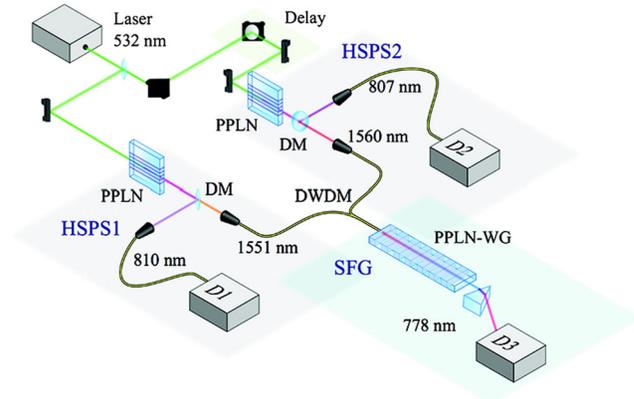

FIG. 2 (color online).   Experimental setup. A mode-locked laser (Time-Bandwidth) generates 10 ps pulses at 532 nm with a repetition rate of 430 MHz and is used to pump the two heralded single photon sources (HSPS1 and HSPS2) based on PPLN nonlinear crystals. Each source receives an average pump power of 50 mW. The generated photons are deterministically separated by dichroic mirrors (DM), collimated, and then collected into single-mode optical fibers. The pump light is extinguished by using high-pass filters with an extinction greater than 70 dB (Semrock), as well as a prism (not shown) before coupling into the optical fibers. Diffraction gratings (not shown) are employed to filter the heralding photons (810, 807 nm) down to ∼0.3 nm. In this configuration the telecom photons are projected onto a spectral mode that is matched to the acceptance bandwidth of the SFG process, which was measured to be 0.27 nm. The two fiber coupled telecom photons are combined via a dense wavelength division multiplexer (DWDM) and directed to a 4.5 cm-long fiber-pigtailed type-0 PPLN waveguide [29]. Propagation loss in the waveguide is as small as 0.1 dB/cm. The unconverted photons are deterministically separated from the SFG photons by a prism (not shown) and the upconverted light is sent to a single photon detector $D3$. The final photon triplet state is then detected by coincidence measurements between detectors $D1$, $D2$, and $D3$. The overall SFG conversion efficiency is 1.56×10^{-8}, including the coupling of the fiber pigtail, which is 70%.

Finally, the detection scheme consists of three single photon detectors—$D1$, $D2$, and $D3$—based on Si avalanche photodiodes. Detector $D3$ (PicoQuant: τ-SPAD-20) operates in free-running mode with an efficiency of 60% at 778 nm and a dark-count rate of 3.5 s^{-1}. Detectors $D1$ and $D2$ (Excelitas diodes with custom electronics) are gated (18 ns) devices with an efficiency of 60% and a dark-count probability of 10^{-6}/ns [32]. All of the detection events from $D1$, $D2$, and $D3$ are recorded by a time-to-digital converter.

Before running the nonlinear interaction measurement, it is necessary to make sure the interacting photons arrive at the same time into the nonlinear waveguide. To guarantee this, we seed HSPS2 with a continuous wave laser at 810 nm, producing a pulsed coherent state at 1551 nm by difference frequency generation [33] to improve the signal to noise level. We record twofold coincidences between $D3$ and $D2$ as we scan the delay line placed before HSPS2.
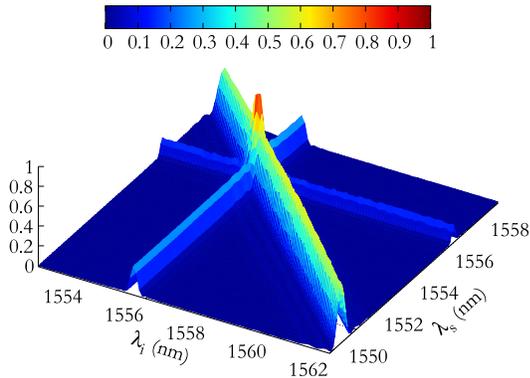
FIG. 3 (color online). Intensity plot of the classical SFG efficiency as a function of the wavelength of two input fields. The diagonal trace represents SFG between the input fields, while the horizontal and vertical traces signal the contributions from SHG of each independent input field. Note that the difference in height between the SFG and SHG signals is of about a factor of 4, as expected. It is also possible to see the oscillations from the sinc^2 structure of the phase matching on the leading edge.

This allows for the temporal alignment of the interacting photons with picosecond resolution and also allows us to determine the exact position of the threefold coincidence peak in Fig. 4(a).

Once the two photons are temporally aligned, we can remove the seed laser and use the two sources in the heralded single photon configuration. We then proceed to record threefold coincidences between $D1$, $D2$, and $D3$, where the appearance of a peak in the threefold detection time histogram signals the correlated generation of triplets of photons and hence that the interaction between the two

independent telecom photons has taken place. We denote the delay between $D1$ and $D3$ as τ_{31}, and the delay between $D2$ and $D3$ as τ_{32}.

The threefold coincidences between $D1$, $D2$, and $D3$ are shown in the time-of-arrival histogram in Fig. 4(a). Each bin of this histogram corresponds to an acquisition window of 2.3 ns for each detector matching the repetition rate of the pump laser. We integrate for 260 hours and observe a well-defined coincidence peak exactly where it is expected. Moreover, Fig. 4(b) shows the histogram of threefold coincidence counts. One sees a Poissonian distribution for the background noise with a mean value of 35, calculated by averaging overall counts in the 100 bins of Fig. 4(a). The background noise is dominated by the detection of photons at $D1$ and $D2$ in coincidence with dark counts ($3.5 \ \mathrm{s}^{-1}$) from detector $D3$ [27]. The three photon signature is the single bin containing 80 counts, which has a statistical significance of over 7 standard deviations with respect to the background. Furthermore, given the Poisson distribution with a mean value of 35, the probability of having a pixel with 80 accidental counts is of the order of 10^{-11}.

Our theoretical model of the system takes into account the source emission probability, the losses of the setup, the SFG conversion probability, and the detector efficiency and noise levels. We estimated a rate of 0.40 threefold coincidences versus a rate of 0.20 threefold noise events, per hour, while the observed values are 0.31 and 0.13 coincidences, respectively. The measured values are both slightly reduced due to source alignment drifting over the long integration time. Nonetheless, the signal to noise ratio is in good agreement with our predictions.
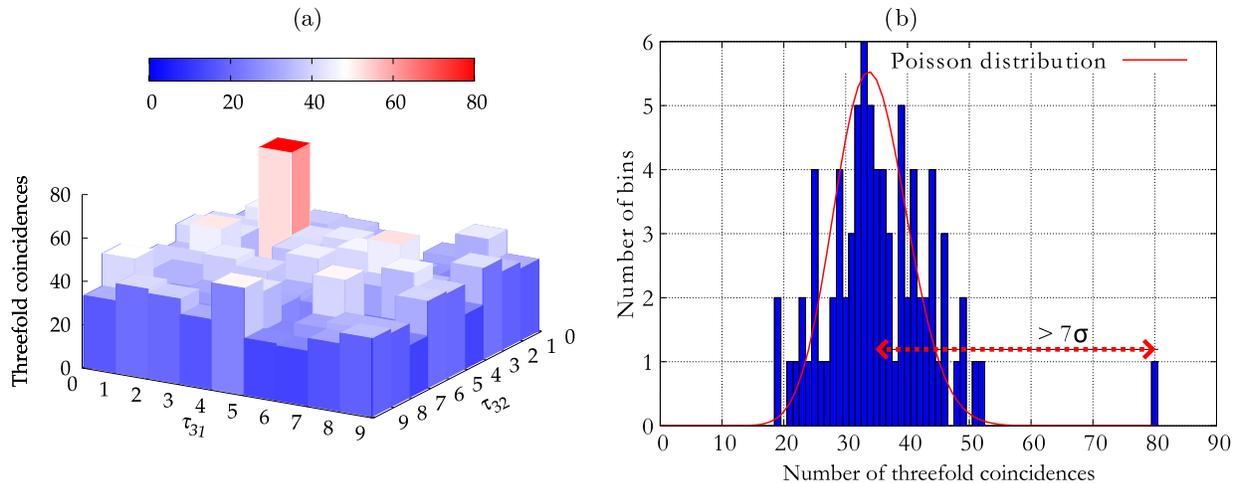

FIG. 4 (color online).   (a) The central peak (red) emerging from the background noise in the time-of-arrival threefold coincidence histogram is a clear signature of the photon-photon interaction and the nonclassical correlations for the photon triplet state. The axis labeled τ_{31} shows the delay between detectors $D1$ and $D3$, while τ_{32} shows the delay between $D2$ and $D3$. Each pixel is composed of 2.3 ns bins, defined by the laser repetition rate. (b) The histogram of threefold coincidence counts shows a Poissonian distribution for the noise with a mean value of 35. The single peak at 80 corresponds to the true threefold coincidences and exceeds the mean value by over 7 standard deviations (7σ).

Despite the challenging nature of the current experiment, higher nonlinear conversion efficiencies allowed us to go from interactions between two coherent states [28] to interacting a single photon and a weak coherent state [27]. Further improvements for the photon pair sources [30] and detectors [32] have now made it possible to demonstrate the first nonlinear interaction between two independent quantum systems. The nonlinearity reported here already offers promising perspectives—for example, the implementation of quantum key distribution—where the secrecy is independent of the internal workings of the devices that are used to create the key (device-independent quantum key distribution). An important aspect of this framework is that the combination of entangled photon pairs at telecom wavelengths and the SFG process allows for maximally entangled photon pairs to be created at a distance while being heralded through the detection of converted photons [28]. The presented demonstration of photon triplets by photon-photon interaction is also promising from a fundamental perspective: for instance, unambiguously excluding local hidden variable models of entanglement in a loophole-free Bell-type experiment [34,35], opening the way for investigating novel quantum correlations [36], and providing a platform for studying exotic states of light and quantum optical solitons [37].

Looking further ahead, higher efficiency nonlinear interactions could be obtained by using tight spatial confinement of the optical modes [38], from the use of highly nonlinear organic materials [39], or by exploiting weak measurements based on pre- and postselected states, as pointed out in Ref. [40]. In addition to these exciting perspectives, we believe that our demonstration of an interaction between two independent single photons will strongly stimulate research in nonlinear optics in the quantum regime.

---

*robert.thew@unige.ch; http://www.unige.ch/gap/optics

,†Present address: Department of Physics, University of Basel CH-4056, Basel, Switzerland.

[1] M. A. Nielsen and L. I. Chuang, *Quantum Computation and Quantum Information*, Cambridge Series on Information and the Natural Sciences (Cambridge University Press, Cambridge, England, 2000).

[2] W. Heisenberg and H. Euler, Z. Phys. **98**, 714 (1936).

[3] H. Kang and Y. Zhu, Phys. Rev. Lett. **91**, 093601 (2003).

[4] Y. F. Chen, C. Y. Wang, S. H. Wang, and I. A. Yu, Phys. Rev. Lett. **96**, 043603 (2006).

[5] N. Matsuda, R. Shimizu, Y. Mitsumori, H. Kosaka, and K. Edamatsu, Nat. Photonics **3**, 95 (2009).

[6] K. M. Birnbaum, A. Boca, R. Miller, A. D. Boozer, T. E. Northup, and H. J. Kimble, Nature (London) **436**, 87 (2005).

[7] A. Kubanek, A. Ourjoumtsev, I. Schuster, M. Koch, P. Pinkse, K. Murr, and G. Rempe., Phys. Rev. Lett. **101**, 203602 (2008).

[8] T. Peyronel, O. Firstenberg, Q.-Y. Liang, S. Hofferberth, A. V. Gorshkov, T. Pohl, M. D. Lukin, and V. Vuletić, Nature (London) **488**, 57 (2012).

[9] R. J. Thompson, G. Rempe, and H. J. Kimble, Phys. Rev. Lett. **68**, 1132 (1992).

[10] M. Brune, F. Schmidt-Kaler, A. Maali, J. Dreyer, E. Hagley, J. Raimond, and S. Haroche, Phys. Rev. Lett. **76**, 1800 (1996).

[11] A. M. C. Dawes, L. Illing, S. M. Clark, and D. J. Gauthier, Science **308**, 672 (2005).

[12] J. Hwang, M. Pototschnig, R. Lettow, G. Zumofen, A. Renn, S. Götzinger, and V. Sandoghdar., Nature (London) **460**, 76 (2009).

[13] D. Englund, A. Majumdar, M. Bajcsy, A. Faraon, P. Petroff, and J. Vučković, Phys. Rev. Lett. **108**, 093604 (2012).

[14] T. Volz, M. Pototschnig, R. Lettow, G. Zumofen, A. Renn, S. Götzinger, and V. Sandoghdar, Nature (London) **460**, 76 (2009).

[15] W. Chen, K. M. Beck, R. Bucker, M. Gullans, M. D. Lukin, H. Tanji-Suzuki, and V. Vuletic, Science **341**, 768 (2013).

[16] N. Gisin and R. T. Thew, Nat. Photonics **1**, 165 (2007).

[17] N. Sangouard and H. Zbinden, J. Mod. Opt. **59**, 1458 (2012).

[18] S. Tanzilli *et al.*, Laser Photonics Rev. **6**, 115 (2012).

[19] Y. H. Kim, S. P. Kulik, and Y. Shih, Phys. Rev. Lett. **86**, 1370 (2001).

[20] B. Dayan, A. Peer, A. A. Friesem, and Y. Silberberg, Phys. Rev. Lett. **94**, 043602 (2005).

[21] G. Giorgi, P. Mataloni, and F. De Martini, Phys. Rev. Lett. **90**, 027902 (2003).

[22] A. P. Vandevender and P. G. Kwiat, J. Mod. Opt. **51**, 1433 (2004).

[23] R. T. Thew, H. Zbinden, and N. Gisin, Appl. Phys. Lett. **93**, 071104 (2008).

[24] H. Hübel, D. R. Hamel, A. Fedrizzi, S. Ramelow, K. J. Resch, and T. Jennewein, Nature (London) **466**, 601 (2010).

[25] L. K. Shalm, D. R. Hamel, Z. Yan, C. Simon, K. J. Resch, and T. Jennewein, Nat. Phys. **9**, 19 (2013).

[26] N. K. Langford, S. Ramelow, R. Prevedel, W. J. Munro, G. J. Milburn, and A. Zeilinger., Nature (London) **478**, 360 (2011).

[27] T. Guerreiro, E. Pomarico, B. Sanguinetti, N. Sangouard, J. S. Pelc, C. Langrock, M. M. Fejer, H. Zbinden, R. T. Thew, and N. Gisin, Nat. Commun. **4**, 2324 (2013).

[28] N. Sangouard, B. Sanguinetti, N. Curtz, N. Gisin, R. Thew, and H. Zbinden., Phys. Rev. Lett. **106**, 120403 (2011).

[29] K. R. Parameswaran, R. K. Route, J. R. Kurz, R. V. Roussev, M. M. Fejer, and M. Fujimura, Opt. Lett. **27**, 179 (2002).

[30] T. Guerreiro, A. Martin, B. Sanguinetti, N. Bruno, H. Zbinden, and R. T. Thew, Opt. Express **21**, 27641 (2013).

[31] P. Sekatski, N. Sangouard, F. Bussières, C. Clausen, N. Gisin, and H. Zbinden, J. Phys. B **45**, 124016 (2012).

[32] T. Lunghi, E. Pomarico, C. Barreiro, D. Stucki, B. Sanguinetti, and H. Zbinden, Appl. Opt. **51**, 8455 (2012).

[33] N. Bruno, A. Martin, and R. T. Thew, Opt. Commun. **327**, 17 (2014).

[34] A. Cabello and F. Sciarrino, Phys. Rev. X **2**, 021010 (2012).

[35] V. Caprara Vivoli *et al.*., arXiv:1405.1939.

[36] K. Banaszek and P. L. Knight, Phys. Rev. A **55**, 2368 (1997).

[37] K. V. Kheruntsyan and P. D. Drummond, Phys. Rev. A **58**, 2488 (1998).

[38] S. Kurimura, Y. Kato, M. Maruyama, Y. Usui, and H. Nakajima, Appl. Phys. Lett. **89**, 191123 (2006).

[39] M. Jazbinsek, L. Mutter, and P. Gunter, IEEE J. Sel. Top. Quantum Electron. **14**, 1298 (2008).

[40] A. Feizpour, X. Xing, and A. M. Steinberg, Phys. Rev. Lett. **107**, 133603 (2011).

[41] See Supplemental Material at http://link.aps.org/supplemental/10.1103/PhysRevLett.113.173601 for details about the calculation of the expected rates.

p) Derek Chang, Yu-Wei Lin, C. Langrock, C.R. Phillips, C.V. Bennett, M.M. Fejer, "Phase-mismatched localized fields in A-PPLN waveguide devices," *Opt. Lett.* **41**, pp 400-3 (January 2016).

Optics Letters

Phase-mismatched localized fields in A-PPLN waveguide devices

Derek Chang,[1,2,*] Yu-Wei Lin,[1] Carsten Langrock,[1] C. R. Phillips,[1,3] C. V. Bennett,[2] and M. M. Fejer[1]

[1]E. L. Ginzton Laboratory, Stanford University, Stanford, California 94305, USA
[2]Lawrence Livermore National Laboratory, Livermore, California 94551, USA
[3]Department of Physics, Institute of Quantum Electronics, ETH Zurich, Zurich 8093, Switzerland
*Corresponding author: djychang@stanford.edu

Highly phase-mismatched nonlinear interactions can generate spatially localized optical fields that can affect the performance of nonlinear optical devices. We present a theoretical description of the generation of such spatially localized optical fields by ultrafast pulses. The effects of temporal walk-off and pump depletion are discussed, along with methods for suppression of the localized field while maintaining the performance of the nonlinear device. The model is validated by the measurement of the spatial profile of the localized field in a quasi-phase-matched (QPM) aperiodically poled lithium niobate (A-PPLN) waveguide. Finally, we fabricate and characterize A-PPLN devices with a 33% duty cycle to reduce the locally generated field by 90%. © 2016 Optical Society of America

Lithium niobate (LiNbO$_3$) is widely used for nonlinear optical frequency conversion [1], and the advent of quasi-phase matching [2,3] has led to a wide range of practical applications [4]. Unfortunately, congruent LiNbO$_3$ (CLN) suffers from optically induced changes in the refractive index, which causes beam distortion and alters phase matching of nonlinear optical interactions [5]. Photo-refractive damage (PRD) can be reduced by using magnesium-doped LiNbO$_3$ [6] or by modifying the QPM structure [7]. However, CLN is still advantageous in applications where PRD does not limit the performance [4] due to its more advanced waveguide technologies.

In many applications, both the spectral amplitude and phase imposed by the mixing process, as quantified in the ratio of output field to the appropriate product of input fields, are relevant performance parameters. Distortions in this complex transfer function (CTF) [8] can be caused by PRD-induced changes in the local phase matching, hence compromising device functionality. If the effects of PRD are small and uni-form along the length of the device, then the phase-matching error is uniform, and the CTF simply shifts in spectrum, leaving the overall profile unchanged. However, if the effects of PRD are not uniform, then phase-matching errors vary spatially and the CTF will exhibit distortions. Such spatially nonuniform changes in phase matching can be generated by spatially localized fields resulting from phase-mismatched interactions in a nonuniform QPM grating.

We begin with a discussion of the generation of localized fields in pulsed interactions, including effects of temporal walk-off and pump depletion. Next, we present measurements of the spatial profile of the local field for various wavelengths and powers in a typical linearly chirped PPLN second-harmonic generation (SHG) device pumped with femtosecond pulses. Finally, we demonstrate how this field can be suppressed via QPM grating design. We focus on the generation and effects of the local fields, rather than the complex topic of PRD [9,10].

The localized field is illustrated by analyzing SHG in a linearly chirped QPM A-PPLN waveguide device. The QPM grating profile is chosen to phase match SHG of the first-harmonic pulse $\mathcal{A}_1$. However, with enough power, $\mathcal{A}_1$ and its second-harmonic, $\mathcal{A}_2$, can generate noticeable amounts of third-harmonic $\mathcal{A}_3$, despite this process being far from phase matched, i.e., $\Delta k \approx 10^3$ cm^{-1}; here, $\Delta k = k_3 - k_2 - k_1$ is the wave vector mismatch. $\mathcal{A}_3$ is the localized field that can deleteriously affect device performance. The propagation equation for $\mathcal{A}_3$ is

$$\frac{\partial}{\partial z}\mathcal{A}_3 = -i\kappa_3 \bar{d}\mathcal{A}_1\mathcal{A}_2 \exp(i\Delta kz), \tag{1}$$

where $\bar{d}(z)$ is the z-dependence of the nonlinear coefficient. The envelope $\mathcal{A}_j$ is related to the electric field E_j by $E_j(x, y, z) = \sqrt{2/n_j\varepsilon_0 c}\mathcal{A}_j(z)\mathcal{E}_j(x, y) \exp(-ik_jz)$ for $j \in \{1, 2, 3\}$, where $\mathcal{E}_j$ is the normalized transverse field amplitude. These functions are normalized such that $\iint |\mathcal{E}_j|^2 \mathrm{d}x\mathrm{d}y = 1$ and $|\mathcal{A}_j|^2$ is equal to the optical power of field j. The coupling coefficient κ_j is defined as $\kappa_j \equiv \theta(8\pi^2 d_0^2/n_1 n_2 n_3 c\varepsilon_0 \lambda_j^2)^{\frac{1}{2}}$, where c is the speed of light, λ_j is the center wavelength of field $\mathcal{A}_j$, n_j is the index of refraction for the jth wave, $d_0 = \chi^{(2)}/2$ is the amplitude of the pertinent component of the nonlinear susceptibility

tensor, and $\theta = \iint \tilde{d}\mathcal{E}_1\mathcal{E}_2\mathcal{E}_3 dx dy$ is the spatial overlap of the interacting modes, where $\tilde{d}(x, y)$ is the transverse spatial distribution of the nonlinear coefficient, but assumed constant in later analysis. We restrict our analysis to the fundamental spatial modes in $\mathcal{A}_1$ and $\mathcal{A}_2$; our devices were designed to use input/output waveguide tapers to ensure single-mode operation. From simulations of proton diffusion in lithium niobate [11], we computed spatial mode indices and concluded that higher-order spatial modes in $\mathcal{A}_3$ are negligible as they contribute less than 2% to the total local field.

We consider a nonuniform QPM grating where variations in the local grating period and duty cycle are slow, compared with the grating period itself, such that $\tilde{d}$ can be accurately represented by a sum of distinct Fourier components G_m, with a z-dependent k-vector. The general form of $\tilde{d}(z)$ is

$$\tilde{d}(z) = \sum_m G_m \exp[iK_m z + i\Phi_m(z)], \quad (2)$$

where $G_m = 1/(m\pi)\sin(m\pi\mathcal{D})$ is the amplitude of the mth Fourier component of the grating, and $\mathcal{D}$ is the grating duty cycle. A linear component $K_m = 2\pi m/\Lambda$ is explicitly separated out of the total grating phase, where Λ is the period of the grating, and $\Phi_m(z)$ represents the phase of the grating beyond the K_m component. The average coherence length for generating $\mathcal{A}_3$ is $\pi/\Delta k_m$, where $\Delta k_m = k_3 - k_2 - k_1 - K_m$. Since the grating is designed to phase match SHG, the corresponding coherence length for generating $\mathcal{A}_3$ is very short, compared with the length of the device and the distances over which $\mathcal{A}_1$ and $\mathcal{A}_2$ amplitudes change significantly, suggesting the use of multiple scales analysis [12] to understand the generation of $\mathcal{A}_3$. This analysis leads to

$$\mathcal{A}_3 = \kappa_3 \sum_m \frac{G_m}{\Delta k_m} \mathcal{A}_1 \mathcal{A}_2 \exp(i\varphi_m), \quad (3)$$

where $\varphi_m = \Delta k_m z + \Phi_m$ is the total phase mismatch. Cross-terms from combinations of different grating Fourier components are of the order $\mathcal{O}(1/\Delta k_m^2)$ and are considered to be insignificant. As a result, $\mathcal{A}_3$ is generated from the sum of contributions from distinct Fourier components of the grating and is proportional to the spatial and temporal overlap of $\mathcal{A}_1$ and $\mathcal{A}_2$.

The time-domain picture of generating $\mathcal{A}_3$ from SFG in a linearly chirped QPM grating is illustrated in Fig. 1. Pulse $\mathcal{A}_1$ with bandwidth Ω_0 propagates through the grating with group velocity u_1. Frequencies in A_1 phase match to generate second-harmonic frequencies in $\mathcal{A}_2$ over a phase-match length $L_p = \delta\nu\Omega_0/4D_g$, where D_g is the chirp rate of the grating and $\delta\nu = 1/u_2 - 1/u_1$ is the group velocity mismatch parameter. $\mathcal{A}_2$ then travels freely with group velocity $u_2 \neq u_1$. While $\mathcal{A}_1$ and $\mathcal{A}_2$ overlap in space and time, $\mathcal{A}_3$ is generated, but once SHG for $\mathcal{A}_1$ is no longer phase matched, $\mathcal{A}_2$ is no longer generated, and the overlap between $\mathcal{A}_1$ and $\mathcal{A}_2$ decreases as the
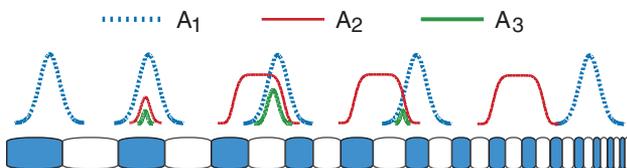
fields walk off each other over a length $L_w = 1/\delta\nu\Omega_0$. $\mathcal{A}_3$ vanishes once $\mathcal{A}_1$ and $\mathcal{A}_2$ no longer overlap and, as a result, it can only exist locally in a finite spatial region of the grating, which we define as w.

If this local field A_3 causes PRD, then its spatial extent determines the portion of the transfer function that is distorted, and its maximum pulse energy affects the magnitude of the distortion. These factors depend on parameters such as pulse bandwidth Ω_0, pulse chirp C, and grating chirp D_g.

To understand the relationship between these factors and parameters, we must evaluate Eq. (3). It will be convenient to work in the frequency domain so we define a frequency domain envelope $\hat{A}_j(z, \Omega_j) = \hat{\mathcal{A}}_j(z, \Omega_j)\exp\{i[k(\omega_j + \Omega_j) - k(\omega_j)]z\}$, where $\hat{\mathcal{A}}_j(z, \Omega_j)$ is the Fourier transform of $\mathcal{A}_j(z, t)$ and $\Omega_j = \omega - \omega_j$ is the angular frequency detuning from carrier frequency ω_j. For simplicity, we assume $\hat{A}_1$ is undepleted and that there is negligible GVD so that $\hat{A}_1(z, \Omega_1) = \hat{A}_1(0, \Omega_1)$ and, thus, write $\hat{A}_2$ in terms of the fundamental $\hat{A}_1$ via the transfer function $\hat{D}(z, \Omega_2)$ [13], according to $\hat{A}_2(z, \Omega_2) = \hat{D}(z, \Omega_2)\widehat{A_1^2}(\Omega_2)$, where $\widehat{A_1^2}(\Omega_2)$ is the convolution $\hat{A}_1(\Omega_1) \otimes \hat{A}_1(\Omega_1)$. With these representations for the fields, Eq. (3) becomes

$$\hat{A}_3^{(m)}(z, \Omega_3) = \kappa_3 \frac{G_m}{\Delta k_m}\{\hat{D}(z, \Omega_2)[\hat{A}_1(\Omega_1) \otimes \hat{A}_1(\Omega_1)]\}$$
$$\otimes \hat{A}_1(\Omega_1)\exp[i\varphi_m(z)]. \quad (4)$$

To compute $\hat{A}_3$ and illustrate the basic properties of local fields, we consider a linearly chirped pulse $\hat{A}_1$ with chirp rate $C = C_1\Omega_0^2$ and bandwidth Ω_0 propagating through a linearly chirped grating with chirp rate D_g as defined in [13]. To simplify the analysis, we only consider the first Fourier component, $m = 1$, and assume an infinitely long grating in which $\tilde{d}(x, y)$ is constant. By computing $\hat{A}_3$, we can calculate the spatial extent w and maximum pulse energy U of the localized field.

In Fig. 2, we explore how the normalized length $\bar{w} = w/L\sqrt{D_g L/(1/L)}$ varies with normalized bandwidth $\bar{\Omega}_0 = \delta\nu\Omega_0/\sqrt{4D_g} = \sqrt{L_p/L_w}$ for different chirp C. The length $\bar{w}$ represents the fraction of the grating, of length L, where $\hat{A}_3$
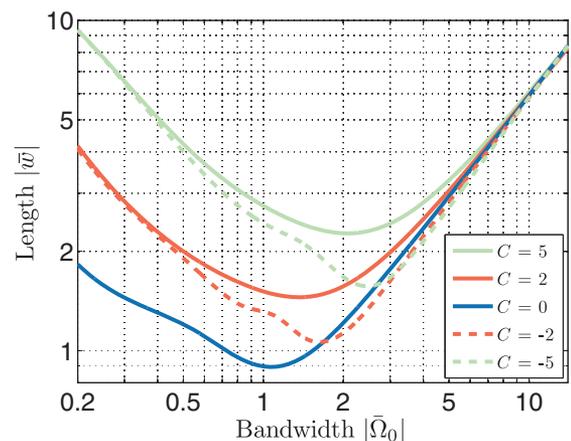
Fig. 2. Length $\bar{w}$ of locally generated field $\hat{A}_3$ varies with pulse bandwidth $\bar{\Omega}_0$ for different chirp C, where $D_g > 0$ is assumed.

Fig. 1. Time-domain illustration of local field A_3 generation due to SFG in a chirped QPM grating.

exists, scaled by the square root of the ratio of the chirped grating bandwidth, D_gL, to the uniform grating bandwidth $1/L$. $\bar{w}$ grows with increased phase-match length L_p or walk-off length L_w. First, consider $\hat{A}_1$ to be a transform-limited pulse ($C = 0$). For small bandwidths ($L_w \gg L_p$), $\hat{A}_1$ is broad in time which increases the walk-off length and results in increased $\bar{w}$. For large bandwidths ($L_p \gg L_w$), $\hat{A}_1$ phase matches over a longer length which also increases $\bar{w}$. However, for bandwidths near unity ($L_p \approx L_w$), neither effect dominates, and $\bar{w}$ is at its minimum.

Now consider a chirped pulse ($C \neq 0$). For larger chirp rates $|C|$, $\hat{A}_1$ is broader in time which increases the walk-off length and results in increased $\bar{w}$. The curves shift toward larger lengths, and the minimum shifts toward larger bandwidths. Pulses with chirp C, such that $C/D_g < 0$, have a chirp that partially cancels out the grating chirp and temporally compresses $\hat{A}_2$. This decreases the walk-off length L_w and, therefore, $\bar{w}$ is smaller compared with those generated by pulses with $C/D_g > 0$.

In Fig. 3, we explore how the normalized pulse energy $\bar{U} = U/[\kappa_2^2 \kappa_3^2 G_m^2 U_0^3/(2D_g \Delta k_1^2)]$ of $\hat{A}_3$ depends on $\bar{\Omega}_0$. The normalization factor represents the energy in the third-harmonic generated by a CW first-harmonic with power equal to that of a flat-top pulse of energy U_0 and duration $1/\Omega_0$, where U_0 is the pulse energy of $\hat{A}_1$. For small bandwidths ($L_w \gg L_p$), $\hat{A}_1$ is broad in time and, therefore, the peak power is less, which means $\hat{A}_3$ will have lower power $\bar{U}$. For large bandwidths ($L_p \gg L_w$), $\hat{A}_1$ is compressed, and its peak power increases, resulting in higher $\bar{U}$. For larger chirp rates $|C|$, $\hat{A}_1$ is broader and $\bar{U}$ decreases. Pulses with chirp C, such that $C/D_g < 0$, generate a temporally compressed $\hat{A}_2$ and, therefore, increase $\bar{U}$.

To the extent that a localized field is causing PRD, it is important to choose parameters so that $\bar{w} > \sqrt{D_gL/(1/L)}$; as a result, $w > L$ and, therefore, the CTF only shifts in spectrum. Additionally, it is advantageous to choose a smaller bandwidth $\bar{\Omega}_0$ so that the pulse energy is minimized.

The position of the local field within the grating can change due to changes in the center wavelength or depletion level of $\hat{A}_1$. This effect is potentially important as it can alter the spatial
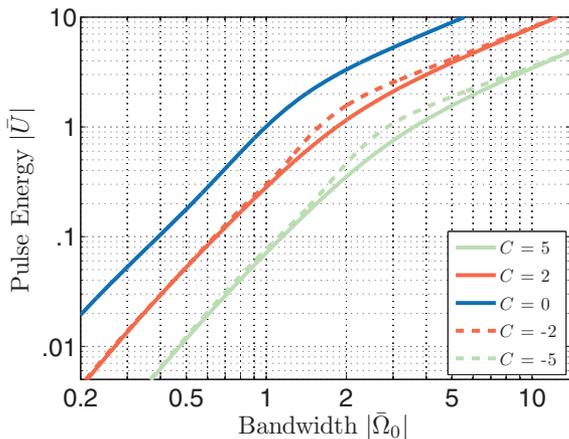
profile of the localized field. We explore these effects experimentally in an A-PPLN waveguide device by measuring the spatial profile of the locally generated field, $\hat{A}_3$, by collecting light scattered out of the waveguide at the chip surface along the length of the waveguide. A 400 μm core fiber, oriented at 45° with respect to surface normal, is scanned along the waveguide, and the collected light is detected with a silicon avalanche photodiode; a bandpass filter ensures that only $\hat{A}_3$ is detected. We assume the scattered light measured at any given position is proportional to $|\hat{A}_3|^2$.

Our A-PPLN device has a QPM grating length of 43 mm and a bandwidth of 22 nm, centered at 1560 nm with a grating chirp rate of $D_g = 0.07$ mm^{-2}. The sign of the chirp is such that shorter wavelengths phase match later in the grating. Our transform-limited input $\hat{A}_1$ has a bandwidth of 16 nm, which is equivalent to $\bar{\Omega}_0 = 7.4$; we therefore expect $\bar{w} = 4.7$, i.e., $w = 18$ mm based on Fig. 2. We launch 2.5 mW of $\hat{A}_1$ into the waveguide and measure the local field profile for $\lambda_1 = 1550$ nm, 1560 nm, and 1570 nm, shown as the blue lines in Figs. 4(a)–4(c). Theoretical plots, obtained via numerical simulations of Eq. (1) and the corresponding equations for the evolution of $\mathcal{A}_1$ and $\mathcal{A}_2$ to enable inclusion of pump-depletion effects, are shown as the red lines. The peak position shifts toward the end of the grating as λ_1 becomes shorter, and the length matches the expected value of 20 mm, as shown in Fig. 4(b). In Figs. 4(d)–4(f), we fix the center wavelength at 1550 nm and change the input power of $\hat{A}_1$ for each scan (2.5 mW, 10 mW, and 20 mW). As the power is increased, $\hat{A}_1$ depletes as a larger fraction is converted to $\hat{A}_2$. As a result, the product $\hat{A}_1\hat{A}_2$ decays along the waveguide, and the peak position shifts closer to the beginning of the grating.

Distortions in the CTF due to local-field-induced PRD can be minimized by reducing the local field intensity through lowering the input power of $\hat{A}_1$ at the expense of reduced efficiency of the main interaction. Another way is to increase the operating temperature of the device such that the space charge field can be screened more effectively by increased electron mobility [14]; however, excessive temperatures can change waveguide
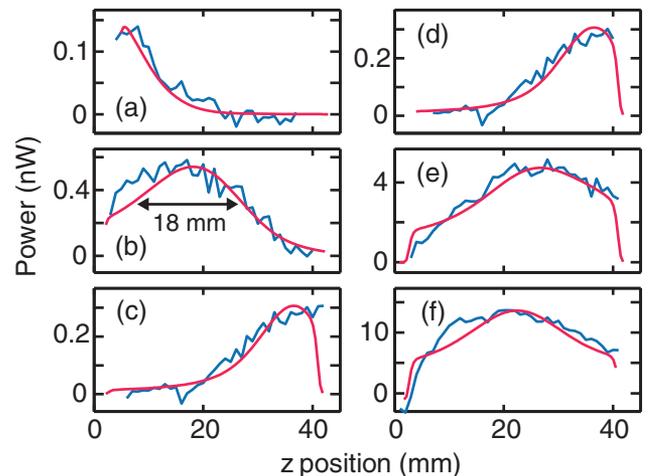

Fig. 3. Maximum pulse energy $\bar{U}$ of locally generated field $\hat{A}_3$ varies with pulse bandwidth $\bar{\Omega}_0$ for different chirp C, where $D_g > 0$ is assumed.

Fig. 4. Measurement (blue) and simulation (red) of local field spatial profile using input power of 2.5 mW with center wavelengths at (a) 1570 nm, (b) 1560 nm, and (c) 1550 nm, and using center wavelength at 1550 nm with input powers of (d) 2.5 mW, (e) 10 mW, and (f) 20 mW.
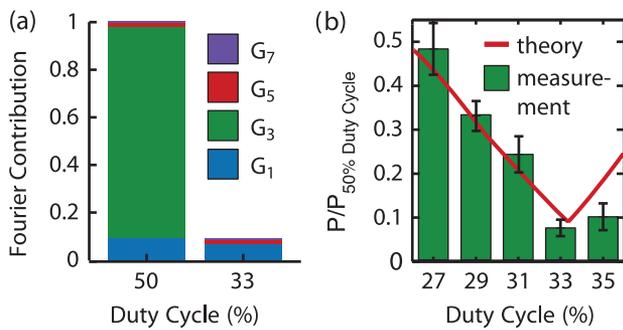
Fig. 5. (a) QPM Fourier component contribution to local field power for 50% and 33% duty cycles. (b) Fabricated 33% duty cycle gratings suppress the local field power by an average of 90%, compared with standard 50% duty cycle grating.

properties. It is also possible to consult Fig. 2 and design the length of the local field to span the entire length of the grating such that transfer function distortion is uniform, and the overall effect is a constant frequency shift, though these designs may not be consistent with the requirements for a given application. Therefore, it is often advantageous to design the QPM grating to minimize local field generation. This can be achieved by adjusting the grating duty cycle $\mathcal{D}$. The locally generated field, $\hat{A}_3$, is composed of contributions from different orders of the QPM grating as seen in Eq. (3). Each contribution is weighted by the factor $G_m / \Delta k_m$. In Fig. 5(a), we illustrate the contribution of each grating order to the total local field for a grating with 50% duty cycle. The third-order Fourier component G_3 provides the largest contribution, but can be eliminated by setting $\mathcal{D} = 33\%$. The ratio of $|\hat{A}_3|^2$ for 33% to 50% duty cycles is about 13%; by setting $\mathcal{D} = 33\%$, $|\hat{A}_3|^2$ can be reduced by almost 90%. The trade-off is a 14% reduction in SHG efficiency due to the reduction of the first-order Fourier component G_1.

To demonstrate this effect, we test devices with 33% duty cycle QPM gratings. We measured the amount of $\hat{A}_3$ generated by scanning a tunable, CW laser at 1550 nm across the bandwidth of our devices and measured $|\hat{A}_3|^2$ with a lock-in detection scheme. Figure 5(b) illustrates the amount of $\hat{A}_3$ generated for different gratings with duty cycles bracketed around 33% as a percentage of the amount of $\hat{A}_3$ generated for a 50% duty cycle grating. The values are averages over different gratings of identical design. The minimum amount of $\hat{A}_3$ generated is

about 8%, and the measured results follow the theoretical trend. The slight discrepancy at larger duty cycles can be attributed to measurement inaccuracy as the amount of $\hat{A}_3$ is quite small. With this design, the local field power is suppressed by almost 10 dB, and one can expect much improved device performance.

In summary, we have provided a model for understanding a general class of parasitic effects called localized fields in A-PPLN waveguide devices. This theory is supported by strong agreement between simulation and measurement results. To improve device performance, we have demonstrated that the average power of localized fields can be suppressed by 10 dB by using a 33% duty cycle grating. The analysis and design presented offers guidance for designing optical frequency converters that avoid the effects of localized fields.

REFERENCES

1. R. S. Weis and T. K. Gaylord, Appl. Phys. A **37**, 191 (1985).
2. M. M. Fejer, G. A. Magel, D. H. Jundt, and R. L. Byer, IEEE J. Quantum Electron. **28**, 2631 (1992).
3. J. A. Armstrong, N. Bloembergen, J. Ducuing, and P. S. Pershan, Phys. Rev. **127**, 1918 (1962).
4. C. Langrock, S. Kumar, J. E. McGeehan, A. E. Willner, and M. M. Fejer, J. Lightwave Technol. **24**, 2579 (2006).
5. A. M. Glass, Opt. Eng. **17**, 175470 (1978).
6. D. A. Bryan, R. Gerson, and H. E. Tomaschke, Appl. Phys. Lett. **44**, 847 (1984).
7. H. H. Lim, S. Kurimura, and N. E. Yu, Opt. Express **22**, 5209 (2014).
8. D. Chang, C. Langrock, Y.-W. Lin, C. R. Phillips, C. V. Bennett, and M. M. Fejer, Opt. Lett. **39**, 5106 (2014).
9. M. Carrascosa, J. Villarroel, J. Carnicero, and J. M. Cabrera, Opt. Express **16**, 115 (2008).
10. J. Villarroel, J. Carnicero, F. Luedtke, M. Carrascosa, A. García-Cabañes, J. M. Cabrera, A. Alcazar, and B. Ramiro, Opt. Express **18**, 20852 (2010).
11. R. V. Roussev, C. Langrock, J. R. Kurz, and M. M. Fejer, Opt. Lett. **29**, 1518 (2004).
12. C. Conti, S. Trillo, P. Di Trapani, J. Kilius, A. Bramati, S. Minardi, W. Chinaglia, and G. Valiulis, J. Opt. Soc. Am. B **19**, 852 (2002).
13. G. Imeshev, M. A. Arbore, and M. M. Fejer, J. Opt. Soc. Am. B **17**, 304 (2000).
14. G. D. Miller, R. G. Batchko, W. M. Tulloch, D. R. Weise, M. M. Fejer, and R. L. Byer, Opt. Lett. **22**, 1834 (1997).

q) A.S. Mayer, C.R. Phillips, C. Langrock, A. Klenner, A.R. Johnson, K. Luke, Y. Okawachi, M. Lipson, A.L. Gaeta, M.M. Fejer, U. Keller, "Offset-Free Gigahertz Mid-infrared Frequency Comb Based on Optical Parametric Amplification in a Periodically Poled Lithium Niobate Waveguide," *Phys. Rev. Applied* **6**, art. no. 054009 (November 2016).

Offset-Free Gigahertz Midinfrared Frequency Comb Based on Optical Parametric Amplification in a Periodically Poled Lithium Niobate Waveguide

A. S. Mayer,[1] C. R. Phillips,[1] C. Langrock,[2] A. Klenner,[3,1] A. R. Johnson,[3,4] K. Luke,[5] Y. Okawachi,[3] M. Lipson,[6] A. L. Gaeta,[3] M. M. Fejer,[2] and U. Keller[1]

[1]*Department of Physics, Institute for Quantum Electronics, ETH Zurich, CH-8093 Zurich, Switzerland*
[2]*Edward L. Ginzton Laboratory, Stanford University, Stanford, California 94305, USA*
[3]*Applied Physics and Applied Mathematics, Columbia University, New York, New York 10027, USA*
[4]*School of Applied and Engineering Physics, Cornell University, Ithaca, New York 14853, USA*
[5]*School of Electrical and Computer Engineering, Cornell University, Ithaca, New York 14853, USA*
[6]*Department of Electrical Engineering, Columbia University, New York, New York 10027, USA*

We report the generation of an optical-frequency comb in the midinfrared region with 1-GHz comb-line spacing and no offset with respect to absolute-zero frequency. This comb is tunable from 2.5 to 4.2 μm and covers a critical spectral region for important environmental and industrial applications, such as molecular spectroscopy of trace gases. We obtain such a comb using a highly efficient frequency conversion of a near-infrared frequency comb. The latter is based on a compact diode-pumped semiconductor saturable absorber mirror–mode-locked ytterbium-doped calcium-aluminum gadolynate (Yb:CALGO) laser operating at 1 μm. The frequency-conversion process is based on optical parametric amplification (OPA) in a periodically poled lithium niobate (PPLN) chip containing buried waveguides fabricated by reverse proton exchange. The laser with a repetition rate of 1 GHz is the only active element of the system. It provides the pump pulses for the OPA process as well as seed photons in the range of 1.4–1.8 μm via supercontinuum generation in a silicon-nitride (Si_3N_4) waveguide. Both the PPLN and Si_3N_4 waveguides represent particularly suitable platforms for low-energy nonlinear interactions; they allow for mid-IR comb powers per comb line at the microwatt level and signal amplification levels up to 35 dB, with 2 orders of magnitude less pulse energy than reported in OPA systems using bulk devices. Based on numerical simulations, we explain how high amplification can be achieved at low energy using the interplay between mode confinement and a favorable group-velocity mismatch configuration where the mid-IR pulse moves at the same velocity as the pump.

I. INTRODUCTION

The midinfrared spectral region between 2 and 20 μm covers the strong vibrational transitions of a variety of molecules that play an important role in environmental, medical, and industrial diagnostics. The ability to detect and quantify the presence of such molecules or to investigate their properties on a more fundamental level is thus directly linked to the availability of a light source capable of probing these transitions. Laser-frequency combs—i.e., lasers whose spectra consist of a series of equally spaced discrete optical lines—combine three essential assets: the high brightness of the light leads to a high detection sensitivity, the narrow linewidth of the individual comb lines allows for high-resolution measurements, while the large spectral bandwidth enables fast simultaneous detection of multiple species.

The success of optical-frequency combs in the near-infrared region has been strongly tied to the advancement of mode-locked lasers in that wavelength range [1–5]. Well-established gain media include Ti:sapphire [6] emitting around 800 nm, and various host crystals doped with

ytterbium (Yb) or erbium (Er) emitting in the 1- and 1.5-μm regions, respectively [7–9]. Various approaches have recently been pursued to extend the spectral coverage of frequency combs into the midinfrared region [10]. Direct approaches include alternative laser gain materials for mode-locked solid-state and fiber lasers [11–13] or semiconductor devices such as quantum-cascade lasers [14,15]. Another approach relies on exploiting different aspects of nonlinear optics, such as supercontinuum generation (SCG) in fibers [16–18] and waveguides [19–21], or Kerr-comb generation in microresonators [22,23].

The challenge these approaches have in common is the difficulty to detect and control the comb offset frequency [24–26], i.e., the parameter that defines the exact position of the evenly spaced frequency-comb lines on the absolute-frequency axis. This problem can be circumvented by difference-frequency generation (DFG): in this nonlinear process, the low-frequency part of a comb (termed the "signal") is mixed with the high-frequency components (the "pump") of the same comb in a medium exhibiting a second-order ($\chi^{(2)}$) nonlinearity, resulting in

a difference-frequency comb (the "idler") which will be offset-free [27].

A configuration where the signal gets significantly amplified during this mixing process is known as an optical parametric amplifier (OPA). DFG- and OPA-based mid-IR frequency combs have already been demonstrated using bulk devices of various materials, such as periodically poled lithium niobate (PPLN) [28–32], GaSe [33], AgGaSe$_2$ [34], CdSiP$_2$ [35], and orientation-patterned GaAs [36]. Because of the limited interaction length caused by diffraction and material dispersion, single-pass bulk OPAs typically require watt-level pump beams and several hundreds of milliwatts of initial signal power to achieve powers per comb line >1 μW in the mid-IR region. Schemes based on high-power oscillators [37], laser preamplification of a pump and/or signal beam [38], or an intracavity OPA [39] have been demonstrated. Higher efficiencies in converting a near-IR frequency comb to the mid-IR region can be obtained in a resonant cavity, i.e., by turning the OPA into an optical parametric oscillator [40–45]. However, the passive comb-offset stability will be lost and the implementation of an active stabilization [46] is instead required to eliminate the offset. The development of stabilized mid-IR frequency combs therefore benefits from a robust and compact configuration that allows for efficient frequency conversion at low energies with passive comb-offset stabilization, using a single mode-locked laser oscillator as the only active medium.

Here, we demonstrate chip-scale waveguide technology as a compact low-energy platform for generating widely tunable, offset-free mid-IR frequency combs. A diode-pumped solid-state laser operating at 1 μm with a repetition rate of 1 GHz serves as a single active source with two output beams. While one beam is directly used to pump an OPA process in a PPLN waveguide, the other is spectrally broadened in a silicon-nitride (Si$_3$N$_4$) waveguide to generate signal photons in the wavelength range of 1.4–1.8 μm. The idler can be tuned from 2.5 to 4.2 μm by laterally translating the PPLN chip across waveguides with varying quasi-phase-matching (QPM) periods [47]. With just 300 pJ of pump-pulse energy and initial seed powers of <20 nW per comb line, we achieve microwatt-level comb-line powers in the mid-IR region. Compared to systems based on nonlinear fibers for SCG and bulk PPLN for the OPA process [38], the required pulse energy for obtaining the same power per comb line is lowered by nearly 2 orders of magnitude.

In the following, we provide the details of the experimental setup, present the mid-IR comb results, and explain via numerical simulations how the approach leverages favorable aspects of the waveguide dispersion in order to maximize the achievable OPA gain. Moreover, our simulations, which are in excellent agreement with our experimental results, show that waveguides offer the possibility to enter high-gain OPA regimes that are inaccessible to bulk devices at low energies. The ability to perform efficient

supercontinuum-seeded frequency conversion at low pulse energies, as demonstrated and explained here, could enable multigigahertz comb-resolved sources based on chip-scale nonlinear-optical devices, directly driven by highly compact laser oscillators, thereby removing the need for laser amplifiers and bulk frequency converters in such systems.

II. EXPERIMENTAL SETUP

The passively mode-locked laser oscillator shown in Fig. 1(a) consists of a 2-mm-long ytterbium-doped calcium-aluminum gadolynate (Yb:CALGO) [48] emitting at 1053 nm and pumped at 980 nm using a spatially multimode pump diode. The laser is mode locked with a semiconductor saturable absorber mirror (SESAM) [49] and can produce pulses as short as 63 fs at a repetition rate of 1.025 GHz, with an output power of up to 1.7 W (when both output beams are combined) [50]. One of the output beams is coupled to a 7.5-mm-long Si$_3$N$_4$ waveguide (spiraled onto a square of 1×1 mm) with a cross section of 690×900 nm [Fig. 1(b)] [51–53]. A coupled pulse
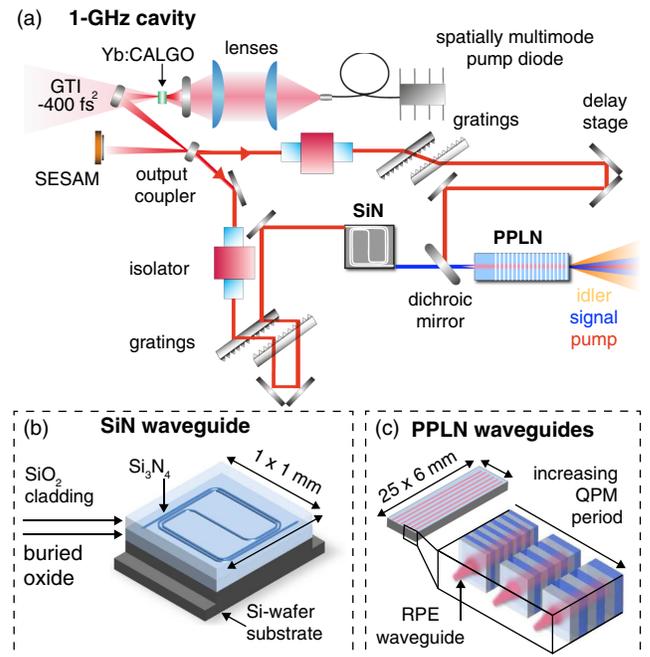

FIG. 1. (a) Experimental setup showing the two output beams of the 1-GHz laser cavity. The negative second-order intracavity dispersion necessary to achieve soliton mode locking is provided by a Gires-Tournois-interferometer- (GTI-)type mirror. Isolators prevent potential back reflections from the waveguide facets into the laser. Grating pairs are used to compensate for the isolator dispersion and additionally stretch the pulse in the OPA pump arm. (b) Sketch of the (1×1)-mm chip with the 7.5-mm-long Si$_3$N$_4$ waveguide embedded in silicon dioxide (SiO$_2$). (c) Excerpt of the PPLN chip containing buried RPE waveguides in regions with different poling periods. The first 6.5 mm of the 2.5-cm-long chip are unpoled, and the waveguides are tapered to facilitate single-mode coupling.
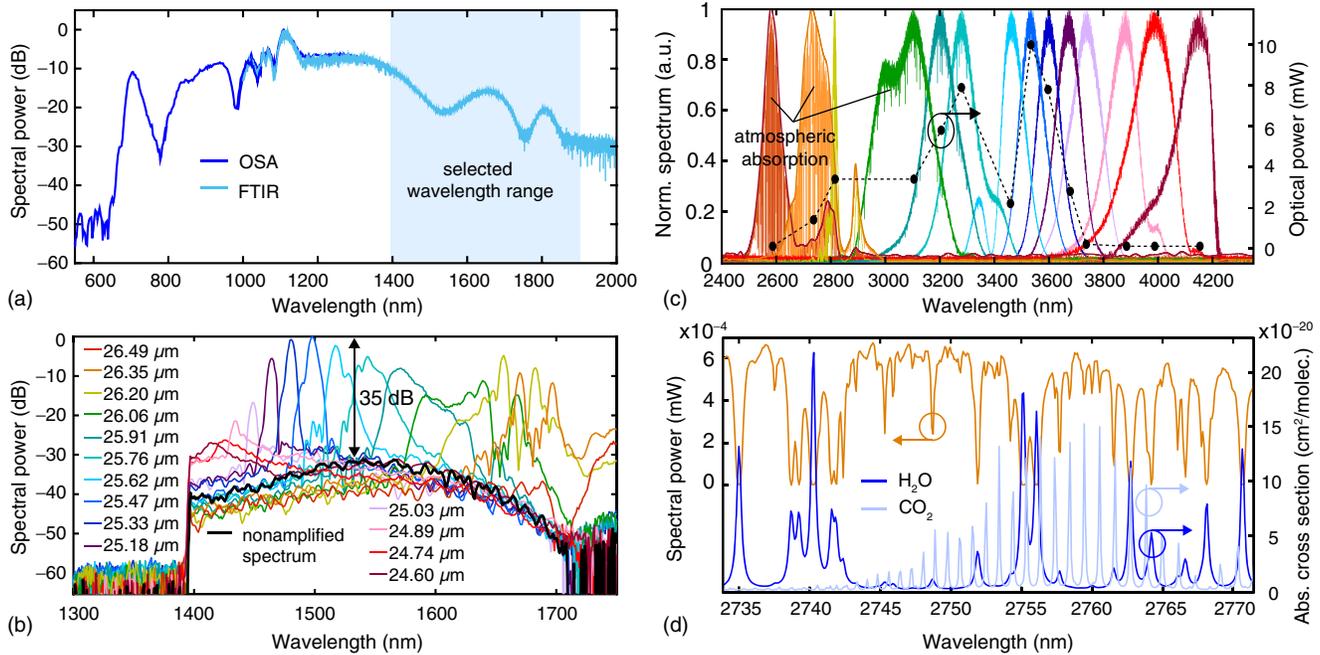
FIG. 2. (a) Supercontinuum obtained with 40 pJ of coupled pulse energy in the Si_3N_4 waveguide. The shaded part is used as a signal input for the OPA. (b) Scan of the amplified signal spectra obtained by laterally scanning the chip across the different QPM periods, recorded with a grating-based optical spectrum analyzer (OSA). (c) Normalized mid-IR spectra recorded with a Fourier-transform infrared spectrometer (FTIR) ranging from 2.5 to 4.2 μm and corresponding to the amplified signal spectra shown in (b). The right axis displays the absolute power levels, with a maximum of 10 mW at 3.55 μm. The power drop near 3.45 μm is due to a slight defect in this particular waveguide, resulting in less overall transmitted power. (d) Enlargement of an FTIR trace recorded with instrument-limited resolution of 3.6 GHz using the free-space port after approximately 1 m of propagation in air (orange) and absorption cross sections of water (dark blue) and carbon dioxide (light blue) taken from the HITRAN database.

energy of 40 pJ (coupling efficiency 15%) is sufficient to obtain a supercontinuum spanning from 650 to 1800 nm, as shown in Fig. 2(a). Using a long-pass filter, the spectrum is cut at 1400 nm and sent into the PPLN waveguide as a seed for the OPA process.

The PPLN-waveguide chip with a dimension of 25 × 6 × 0.5 mm contains 90 waveguides fabricated by reverse proton exchange (RPE). The RPE method exhibits a first step of exchanging lithium ions with protons, using a diffusion process to create a region with a higher refractive index capable of guiding light. In order to obtain buried waveguides that support Gaussian modes and efficient nonlinear mixing, the protons near the surface are subsequently removed in a reverse-proton-exchange step. The RPE waveguides used here are fabricated with a 12 μm width and an exchange depth of 2.3 μm. This depth, which is larger than in typical PPLN waveguides designed for telecom applications [54], is chosen in order to guide the mid-IR wavelengths. At the input side of the waveguide, the width of the lithography-mask pattern is adiabatically tapered to 2 μm to allow for efficient and single-mode coupling of the input near-IR beams. The different waveguides are periodically poled, with poling periods ranging from 17 to 30 μm to achieve QPM. Coupling into both waveguides as well as beam collimation at the output is performed in free space using antireflection-coated lenses.

A Faraday isolator protects the laser cavity from potential back reflections from the waveguide facets. Grating pairs are used to compensate for the dispersion introduced by the isolators. Angled waveguide facets could be used in the future to eliminate the isolators. While the pulse at the input of the Si_3N_4 waveguide is recompressed to a nearly-transform-limited 85 fs, the pulses in the pump arm are purposely stretched to nearly 800 fs to maximize the pump-signal interaction in the PPLN waveguide. The general advantage of pump-pulse stretching in a waveguide configuration is discussed in Sec. IV.

III. RESULTS

A. Amplification and mid-IR spectra

Amplified spectra, obtained by scanning through the waveguides with QPM periods from 24.60 to 26.49 μm, are shown in Fig. 2(b). With a maximum pump-average power of 310 mW coupled into the PPLN waveguides, we are able to amplify the spectral region from 1.4 to 1.8 μm obtained by SCG in the Si_3N_4 waveguide by up to 35 dB. The corresponding mid-IR idler spectra range from 2.5 to 4.2 μm, with an average power reaching 10 mW at 3.5 μm [Fig. 2(c)]. Given the comb-line spacing of 1.025 GHz set by the laser, this value corresponds to an average power per comb line of 4 μW. The DFG process

leads to passive cancellation of the laser-comb offset; therefore, the stability of the mid-IR comb lines depends only on the stability of the laser repetition rate—and thus the laser-cavity length. Here, sufficient stability is achieved with low-drift mirror mounts and by boxing the setup. By mounting the SESAM on a piezoelectric actuator as described in Ref. [55], such ultrafast laser combs can be fully stabilized with a long-term stabilization loop, and the comb lines can also be shifted by a desired amount.

The amplified signal spectra are recorded with a grating-based optical spectrum analyzer [(OSA), Ando AQ-6315A]. A Fourier-transform infrared spectrometer [(FTIR), Thorlabs OSA2015] is used for the idler spectra. The path length of approximately 1 m between the output of the PPLN waveguide and the free-space input of the FTIR analyzer is sufficient to observe distinctive absorption features in the ambient air. By magnifying the mid-IR comb generated in the waveguide with the QPM period of 26.35 μm [Fig. 2(d)], we can clearly identify the presence of water (H_2O) and carbon-dioxide (CO_2) absorption lines by comparing the spectrum recorded by the FTIR with the corresponding absorption cross sections provided by the high-resolution transmission molecular absorption (HITRAN) database.

B. Noise analysis

The relative intensity noise (RIN) of a frequency comb is an important parameter, as it can limit the achievable signal-to-noise ratio in spectroscopic applications such as dual-comb spectroscopy [56]. In an OPA-based system, the RIN can increase during preamplification of the pump and/or signal, nonlinear broadening steps, and the OPA process itself. RIN characterization at each stage of the setup thus helps us to identify the bottlenecks and, ultimately, to design low-noise systems. Figure 3 shows the RIN in our setup measured at base band using appropriate photodiodes (Silicon Thorlabs PDA100-EC for 980 nm, InGaAs Thorlabs PDA10CS-EC for 1–1.8 μm, HgCdTe VIGO PVI-4TE-6 + MIPDC-5 for 3.5 μm) and a signal-source analyzer (Agilent E5052B). The noise performance of the gigahertz-laser oscillator is set by its multimode pump diode. Since no preamplifier is used, this noise level also corresponds to the RIN of the OPA pump.

To investigate the impact of the OPA process itself, noise measurements are recorded using the waveguide that provides the highest gain and absolute idler power (QPM period 25.47 μm, signal wavelength 1.50 μm). The RIN of the idler is, as expected, very similar to the RIN of the amplified signal. We observed, however, a noise increase of approximately 30 dB with respect to the pump noise level (Fig. 3).

In order to determine the origin of this noise increase, further measurements are performed. We verify that the shot-noise levels, which depend on the wavelength and the optical power of the photodiode, are well below each of the respective RIN measurement results. The measured RIN of the supercontinuum over the full wavelength range
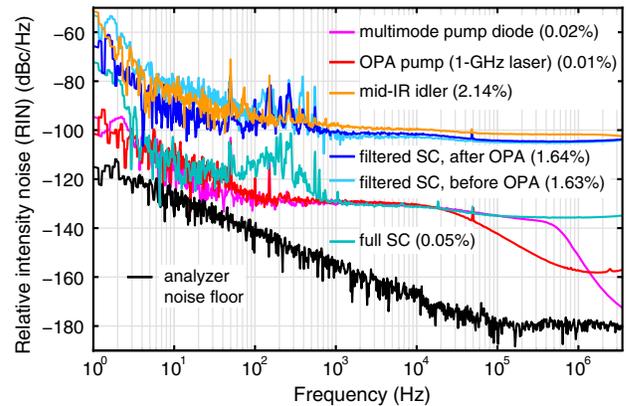

FIG. 3. Relative-intensity-noise (RIN) measurements showing the influence of supercontinuum (SC) generation, supercontinuum filtering, and optical parametric amplification for the waveguide where highest amplification is achieved. The root-mean-square (rms) RIN noise integrated over the interval (1 Hz, 3.5 MHz) is indicated in parentheses for each measurement. The overall noise limit is set by the pump diode of the 1-GHz laser.

accessible by the InGaAs photodiode (1–1.8 μm) is comparable to the gigahertz-laser output, with the exception of white-noise contributions above 100 kHz and technical noise around 100 Hz [Fig. 3, full supercontinuum (SC)]. However, the RIN of the supercontinuum after a 15-nm bandpass filter centered at 1.5 μm is similar to the OPA output (Fig. 3, filtered SC, before OPA). This filter bandwidth is chosen to correspond to the bandwidth of the amplified signal. It is well known that the interplay of the various mechanisms responsible for spectral broadening during the SCG process can lead to strongly-wavelength-dependent RIN [57], which becomes apparent when using narrow-band filters.

We can thus conclude from these observations that, despite the high gain, the OPA process itself is not adding a significant amount of noise, but that the noise increase stems rather from the SCG process in the Si_3N_4 waveguide. In the experiment presented here, the supercontinuum is optimized, above all, for broad bandwidth and spectral coherence [52], but the RIN may be minimized further by numerically analyzing the wavelength dependence of various noise types [58] and adapting the waveguide design accordingly.

IV. DISCUSSION

The experimental OPA results presented above exploit several advantageous properties that waveguides offer in comparison to bulk devices. Simulations in agreement with our experiments will be shown in this section, along with a general discussion on how to take advantage of those waveguide properties to achieve high gain—and thus high conversion efficiency—of a near-IR into a mid-IR comb.

A. Energy-dependent gain

For a phase-matched interaction assuming an undepleted, plane-wave pump field E_p and no initial idler field $[E_i(0) = 0]$, the signal field at the output of an OPA device with length L can be written as [59]

$$E_s(L) = E_s(0)\cosh(\Gamma L), \qquad (1)$$

where Γ is the gain parameter defined as

$$\Gamma = \sqrt{\kappa_i \kappa_s}|E_p|, \qquad (2)$$

with $\kappa_j = 2\pi d_{\text{eff}}/(n_j \lambda_j)$, $j = i$, s (idler and signal) and where d_{eff} denotes the material-dependent effective nonlinear coefficient.

Assuming sufficiently long pump pulses to provide constant pump intensity for the signal pulse during their interaction, we can approximate the magnitude of the pump field E_p as a function of the peak power $P_{\text{pk}} \sim U_p/\tau_p$:

$$|E_p| \sim \sqrt{\frac{2}{n_p \epsilon_0 c}}\sqrt{\frac{2U_p}{\pi w_0^2 \tau_p}}, \qquad (3)$$

where U_p is the pulse energy, τ_p the pulse duration, n_p the refractive index, and w_0 the beam waist. To maximize the interaction in a bulk device, the diffraction length of the beam (and thus the beam radius) is often set to match the distance L_{GVM} over which the pump and signal pulses walk off each other due to group-velocity mismatch (GVM),

$$w_0^2 k_p \approx L_{\text{GVM}} = \tau_p \left(\frac{1}{v_p} - \frac{1}{v_s}\right)^{-1}, \qquad (4)$$

where $k_p = n_p 2\pi/\lambda_p$ denotes the pump wave number.

For a given set of phase-matched pump-signal-idler frequencies, the achievable gain will be independent of the pump-pulse duration and can only be scaled via the pulse energy,

$$\Gamma L_{\text{GVM}} \sim C_{p,s,i}\sqrt{U_p} \quad \text{(bulk)}, \qquad (5)$$

with a proportionality factor $C_{p,s,i}$ containing the wavelength-dependent material properties. If the pump pulse is too short, then confocal focusing, according to Eq. (4), may yield an intensity above the material damage threshold. In this case, the pump pulse can be stretched to avoid damage. However, the diffraction still limits the achievable gain, according to Eq. (5).

In a waveguide device, however, the interaction is not limited by diffraction anymore, thus eliminating the relation imposed in Eq. (4) for the mode size as a function of GVM. The gain can now additionally be scaled via the pump-pulse duration and the effective mode area A_{eff}, which takes into account the modal overlap inside the waveguide,

$$\Gamma L_{\text{GVM}} \sim C'_{p,s,i}\sqrt{U_p}\sqrt{\frac{\tau_p}{A_{\text{eff}}}} \quad \text{(waveguide)}, \qquad (6)$$

where $C'_{p,s,i} = C_{p,s,i}\sqrt{\pi/(2k_p(v_p^{-1} - v_s^{-1}))}$. Thus, high gain can be maintained by stretching the pump-pulse duration despite lowering the pulse energy.

The waveguide cross section is then chosen such as to optimize the overlap of the guided pump, signal, and idler modes (see Sec. III B). Stretching our pump pulses to approximately 800 fs, as described in the experimental section, and taking advantage of the tight mode confinement provided by the PPLN waveguide thus allow us to achieve high gain with nearly one order of magnitude less pulse energy than a best-case estimate of a bulk interaction.

B. Pump versus idler group-velocity mismatch

In the presence of not only GVM between pump and signal but also idler walk-off and group-velocity dispersion of all of the waves, a more-general description of the OPA process is required [60]. In order to explain the gain variations observed experimentally across the broad signal spectral range, we perform numerical simulations based on a general model of the dynamics inside the PPLN waveguides. The model describes the propagation of the pump, signal, and idler pulses through the waveguide, accounting for the wavelength-dependent effective index and modal-overlap coefficients in the waveguide, and it includes both second- and third-order nonlinear properties of the PPLN waveguides [61,62].

In order to determine the dispersion profile of the waveguides, we proceed as follows. First, we simulate the proton diffusion inside the waveguide during the waveguide fabrication process, to obtain a proton concentration profile over the cross section of the waveguide [63]. Following Ref. [63], we obtain the change in refractive index as a function of the wavelength and the transverse position, then calculate the corresponding properties of the fundamental waveguide mode versus the wavelength. These properties are reasonably accurate for IR wavelengths, but less is known about the mid-IR properties. To account for this uncertainty, we apply an additional fixed offset to the effective index for the mid-IR part of the spectrum (wavelengths $> 2~\mu$m). This offset is chosen such that the numerically predicted set of the phase-matched signal wavelength versus the QPM period is in good agreement with the experimentally measured dependence.

As can be seen in Fig. 4(a), we also include the change in refractive index induced by OH absorption in the material around 2.85 μm [61]. Having calculated the spatial profile of the fundamental mode, an effective area for the OPA process can be defined,

$$A_{\text{eff}}(\omega_p, \omega_s) = \left\{\int_{-\infty}^{0}\int_{-\infty}^{\infty} \bar{d}(x, y)B(x, y, \omega_p)B(x, y, \omega_s)\right.$$
$$\left. \times B(x, y, \omega_p - w_s)dxdy\right\}^{-2}, \qquad (7)$$
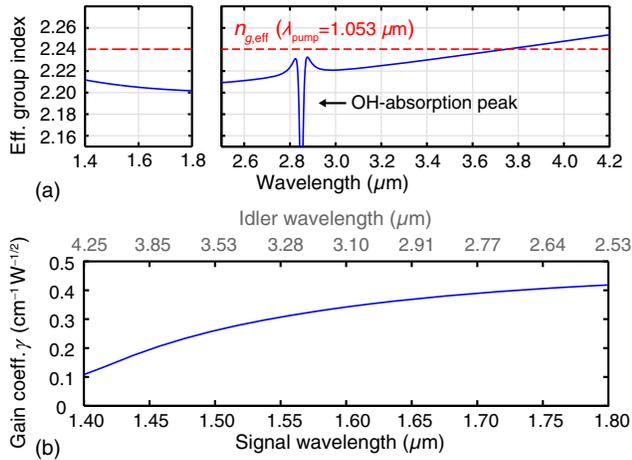
(a)

(b)

FIG. 4.   (a) Effective group index as a function of wavelength over the range used in the experiment. (b) Gain coefficient normalized with respect to power and propagation length. The gain decreases for shorter signal wavelengths as the mode size of the corresponding idler (the gray wavelength scale on top) increases, reducing the modal overlap.

FIG. 5.   Simulated amplification of a flat-top signal spectrum (the black line) when scanning through the experimentally used QPM periods.

where $\bar{d}$ is a normalized nonlinear coefficient accounting for the so-called dead layer (the layer at the top of the waveguide, where the second-order susceptibility is erased during fabrication) [54], and $B(x, y, \omega)$ is the spatial profile of the fundamental waveguide mode with frequency ω, normalized according to $\int_{-\infty}^{0} \int_{-\infty}^{\infty} |B(x, y, \omega)|^2 dx dy = 1$.

An effective pump intensity, P_{pk}/A_{eff}, can be introduced, which leads to a normalized OPA gain rate $\gamma = \Gamma/(\sqrt{\text{pump power}})$. Figure 4(b) shows how the modal-overlap integral in Eq. (7) affects the normalized-gain coefficient γ over the range of signal wavelengths used in this experiment.

In order to directly visualize the spectrally dependent effect of modal overlap and GVM on the achievable gain, the pulse-propagation simulations assume a flat-top initial signal spectrum with a flat spectral phase. The following input parameters corresponding to the experimental values are used: 280-mW pump power, 1-mW signal power over the whole flat-top spectrum (1300–1850 nm) and 70-fs pump pulses with a negative chirp of $-25, 000$ fs^2. A general propagation loss of 0.1 dB/cm is included. We assume a nonlinear coefficient of $d_{33} = 19.5$ pm/V [64] and, to obtain improved agreement with the experimentally measured gain, A_{eff} is scaled by a small factor of 1.17 compared to the directly calculated value from Eq. (7). Without any further adjustments, the simulations (Fig. 5) are able to reproduce remarkably well the features observed in the experiment [Fig. 2(b)].

Looking at the gain curve displayed in Fig. 4(b), one may expect the amplification to monotonically increase with increasing signal wavelength. However, the simulated spectra shown in Fig. 5 are in good agreement with the experimental data presented above: instead of a monotonic
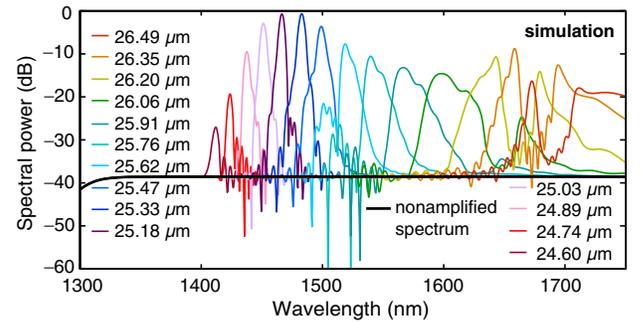
increase, a maximal amplification of 35–40 dB is reached in the range of 1450–1500 nm and then a decrease can be observed until the effect of the OH absorption becomes visible for signal wavelengths of around 1650–1700 nm. This trend can be explained as follows: while the gain coefficient γ contains information about the spatial overlap of the idler with the pump and the signal mode inside the waveguide, it does not take into account the temporal behavior of the idler pulses. As can be inferred from Fig. 4(a), the effective group velocity of the idler, $v_{g,eff}(\lambda_i) = c/n_{group,eff}(\lambda_i)$, crosses the velocity of the pump (intersection with the red dashed line) when scanning the QPM periods. It is for the signal wavelengths corresponding to this intersection—i.e., where the idler moves at nearly the same velocity as the pump—that we observe maximum signal amplification. Figure 6 illustrates and describes the three regimes that we encounter in the scan:

(1) At a signal wavelength of between 1500 and 1650 nm, both the signal and the idler propagate with a higher velocity than the pump. Although a high spatial overlap is given, the short temporal overlap inhibits further amplification [Fig. 6(a)].

(2) For wavelengths of around 1450–1500 nm, the corresponding idler temporally stays with the pump, leading to the buildup of a strong idler pulse and maximal signal amplification [Fig. 6(b)].

(3) In the third regime ($<$1450 nm), the signal and the idler have opposite group velocities with respect to the pump [Fig. 6(c)]. This configuration acts as a "trap" for the signal and idler pulses, as they are pulled towards each other, therefore ensuring a long interaction length and, potentially, high amplification. However, the amplification becomes highly suppressed in this wavelength range due to the increasing mode size of the idler and the resulting poor spatial overlap.

From these experimental and numerical observations, we conclude that the highest gain—and thus the most efficient mid-IR idler generation—is achieved by designing a waveguide where the idler group velocity is as close as possible to that of the pump while maintaining a high spatial overlap.
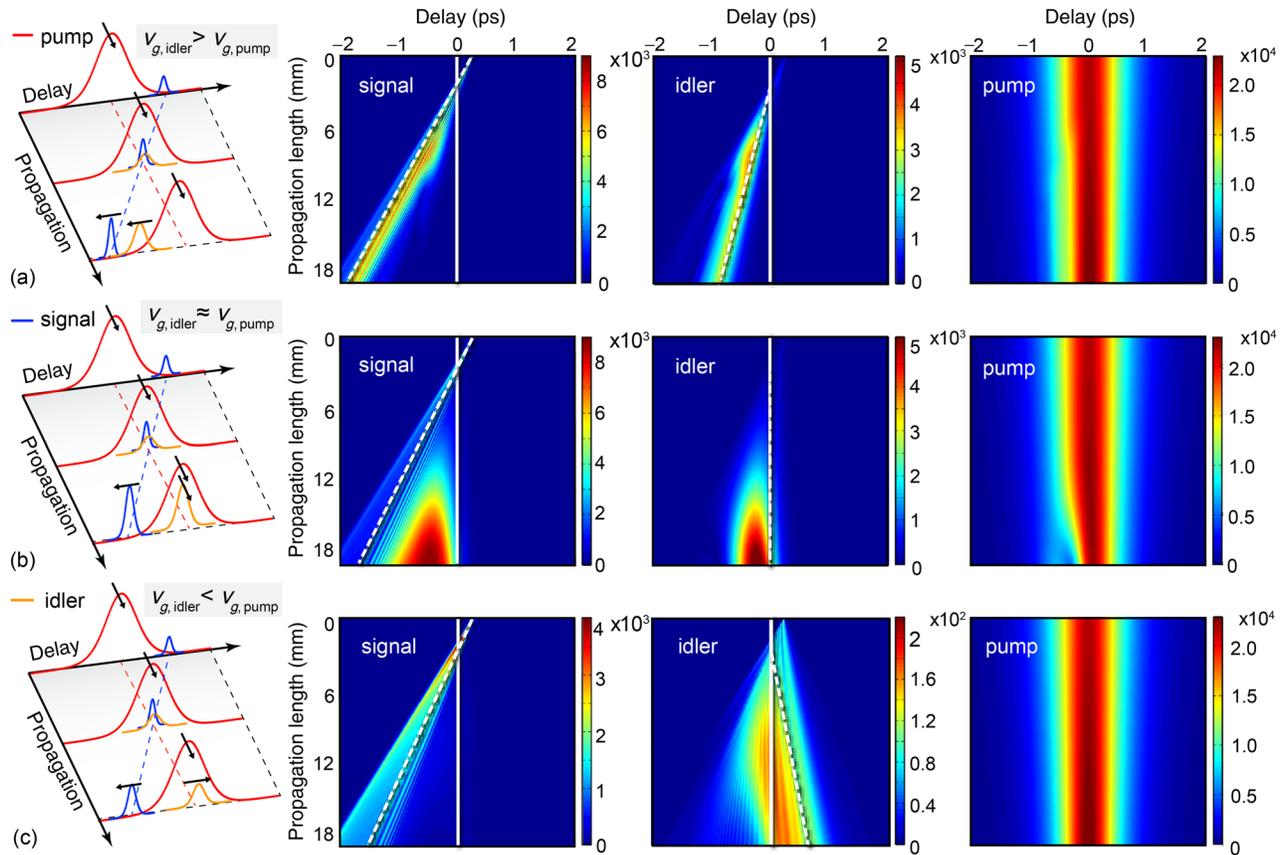
FIG. 6.   Illustrative sketch and magnitude of the interacting fields with the center of the pump pulse setting the reference frame for all figures. The dashed white lines indicate the expected temporal lead or lag of signal and idler pulses with respect to the pump due to group-velocity mismatch (GVM). (a) Idler faster than pump. The three pulses overlap over only a short distance: the energy transfer from pump to signal and idler is limited. (b) Idler follows pump. As the signal is passing through the pump pulse, the generated idler photons stay overlapped with the pump and coherently add up to form a strong pulse. (c) Idler slower than pump, i.e., opposite signs for signal and idler. Signal and idler "drag" each other along, leading to a longer interaction with the pump (the "trapped" state). Note the change in magnitude of the electric field (the color bar) compared to (a) and (b). The lower field magnitudes are a consequence of the reduced spatial-mode overlap, which considerably lowers the gain [as shown in Fig. 4(b)].

V. CONCLUSION

In this paper, we address the challenge of nonlinear-optical frequency conversion at low pulse energies with the aim of transferring a 1-GHz frequency comb at 1 μm into the application-relevant mid-IR spectral region. Using a SESAM-mode-locked laser at 1 μm, we have achieved tunable offset-free combs from 2.5 to 4.2 μm with up to 4 μW of power per comb line around 3.5 μm. The comb spectra are generated in a PPLN RPE waveguide by optical parametric amplification. The signal photons for the OPA process are obtained by supercontinuum generation in a silicon-nitride waveguide with only 40 pJ of coupled pulse energy. During the OPA stage, this signal beam is amplified by up to 35 dB using 300 pJ of pump energy. We show that, in contrast to bulk devices, signal amplification in a waveguide OPA can be increased by stretching the pump pulse and exploiting the waveguide dispersion to obtain a similar effective group velocity for pump and idler pulses. Those degrees of freedom provide interesting design opportunities for low-energy frequency conversion of a variety of compact laser sources, including semiconductor lasers [65], without the need for additional laser power amplifiers.

[1] U. Keller, Recent developments in compact ultrafast lasers, Nature (London) **424**, 831 (2003).

[2] W. Sibbett, A. A. Lagatsky, and C. T. A. Brown, The development and application of femtosecond laser systems, Opt. Express **20**, 6989 (2012).

[3] Martin E. Fermann and Ingmar Hartl, Ultrafast fibre lasers, Nat. Photonics **7**, 868 (2013).

[4] Jungwon Kim and Youjian Song, Ultralow-noise mode-locked fiber lasers and frequency combs: Principles, status, and applications, Adv. Opt. Photonics **8**, 465 (2016).

[5] U. Keller, Ultrafast solid-state laser oscillators: A success story for the last 20 years with no end in sight, Appl. Phys. B **100**, 15 (2010).

[6] P. F. Moulton, Spectroscopic and laser characteristics of $Ti:Al_2O_3$, J. Opt. Soc. Am. B **3**, 125 (1986).

[7] C. Hönninger, R. Paschotta, M. Graf, F. Morier-Genoud, G. Zhang, M. Moser, S. Biswal, J. Nees, A. Braun, G. A. Mourou, I. Johannsen, A. Giesen, W. Seeber, and U. Keller, Ultrafast ytterbium-doped bulk lasers and laser amplifiers, Appl. Phys. B **69**, 3 (1999).

[8] V. P. Gapontsev, S. M. Matitsin, A. A. Isineev, and V. B. Kravchenko, Erbium glass lasers and their applications, Opt. Laser Technol. **14**, 189 (1982).

[9] Federico Pirzio, Matthias Kemnitzer, Annalisa Guandalini, Florian Kienle, Stefano Veronesi, Mauro Tonelli, Juerg Aus der Au, and Antonio Agnesi, Ultrafast, solid-state oscillators based on broadband, multisite Yb-doped crystals, Opt. Express **24**, 11782 (2016).

[10] Albert Schliesser, Nathalie Picque, and Theodor W. Hänsch, Mid-infrared frequency combs, Nat. Photonics **6**, 440 (2012).

[11] E. Sorokin, I. T. Sorokina, J. Mandon, G. Guelachvili, and N. Picqué, Sensitive multiplex spectroscopy in the molecular fingerprint 2.4 μm region with a $Cr^{2+}:ZnSe$ femtosecond laser, Opt. Express **15**, 16540 (2007).

[12] A. A. Lagatsky, P. Koopmann, P. Fuhrberg, G. Huber, C. T. A. Brown, and W. Sibbett, Passively mode locked femtosecond $Tm:Sc_2O_3$ laser at 2.1 μm, Opt. Lett. **37**, 437 (2012).

[13] Simon Duval, Martin Bernier, Vincent Fortin, Jérôme Genest, Michel Piché, and Réal Vallée, Femtosecond fiber lasers reach the mid-infrared, Optica **2**, 623 (2015).

[14] Andreas Hugi, Gustavo Villares, Stephane Blaser, H. C. Liu, and Jerome Faist, Mid-infrared frequency comb based on a quantum cascade laser, Nature (London) **492**, 229 (2012).

[15] Q. Y. Lu, M. Razeghi, S. Slivken, N. Bandyopadhyay, Y. Bai, W. J. Zhou, M. Chen, D. Heydari, A. Haddadi, R. McClintock, M. Amanti, and C. Sirtori, High power frequency comb based on mid-infrared quantum cascade laser at $\lambda \sim 9$ μm, Appl. Phys. Lett. **106**, 051105 (2015).

[16] Alireza Marandi, Charles W. Rudy, Victor G. Plotnichenko, Evgeny M. Dianov, Konstantin L. Vodopyanov, and Robert L. Byer, Mid-infrared supercontinuum generation in tapered chalcogenide fiber for producing octave-spanning frequency comb around 3 μm, Opt. Express **20**, 24218 (2012).

[17] Christian Rosenberg Petersen, Uffe Møller, Irnis Kubat, Binbin Zhou, Sune Dupont, Jacob Ramsay, Trevor Benson, Slawomir Sujecki, Nabil Abdel-Moneim, Zhuoqi Tang, David Furniss, Angela Seddon, and Ole Bang, Mid-infrared supercontinuum covering the 1.4–13.3 μm molecular

fingerprint region using ultra-high NA chalcogenide step-index fibre, Nat. Photonics **8**, 830 (2014).

[18] Yi Yu, Xin Gai, Ting Wang, Pan Ma, Rongping Wang, Zhiyong Yang, Duk-Yong Choi, Steve Madden, and Barry Luther-Davies, Mid-infrared supercontinuum generation in chalcogenides, Opt. Mater. Express **3**, 1075 (2013).

[19] Ryan K. W. Lau, Michael R. E. Lamont, Austin G. Griffith, Yoshitomo Okawachi, Michal Lipson, and Alexander L. Gaeta, Octave-spanning mid-infrared supercontinuum generation in silicon nanowaveguides, Opt. Lett. **39**, 4518 (2014).

[20] Neetesh Singh, Darren D. Hudson, Yi Yu, Christian Grillet, Stuart D. Jackson, Alvaro Casas-Bedoya, Andrew Read, Petar Atanackovic, Steven G. Duvall, Stefano Palomba, Barry Luther-Davies, Stephen Madden, David J. Moss, and Benjamin J. Eggleton, Midinfrared supercontinuum generation from 2 to 6 μm in a silicon nanowire, Optica **2**, 797 (2015).

[21] Bart Kuyken, Takuro Ideguchi, Simon Holzner, Ming Yan, Theodor W. Hänsch, Joris Van Campenhout, Peter Verheyen, Stéphane Coen, Francois Leo, Roel Baets, Gunther Roelkens, and Nathalie Picqué, An octave-spanning mid-infrared frequency comb generated in a silicon nanophotonic wire waveguide, Nat. Commun. **6**, 6310 (2015).

[22] C. Y. Wang, T. Herr, P. Del'Haye, A. Schliesser, J. Hofer, R. Holzwarth, T. W. Hänsch, N. Picqué, and T. J. Kippenberg, Mid-infrared optical frequency combs at 2.5 μm based on crystalline microresonators, Nat. Commun. **4**, 1345 (2013).

[23] Austin G. Griffith, Ryan K. W. Lau, Jaime Cardenas, Yoshitomo Okawachi, Aseema Mohanty, Romy Fain, Yoon Ho Daniel Lee, Mengjie Yu, Christopher T. Phare, Carl B. Poitras, Alexander L. Gaeta, and Michal Lipson, Silicon-chip mid-infrared frequency comb generation, Nat. Commun. **6**, 6299 (2015).

[24] H. R. Telle, G. Steinmeyer, A. E. Dunlop, J. Stenger, D. H. Sutter, and U. Keller, Carrier-envelope offset phase control: A novel concept for absolute optical frequency measurement and ultrashort pulse generation, Appl. Phys. B **69**, 327 (1999).

[25] S. A. Diddams, D. J. Jones, J. Ye, S. T. Cundiff, J. L. Hall, J. K. Ranka, R. S. Windeler, R. Holzwarth, T. Udem, and T. W. Hänsch, Direct Link between Microwave and Optical Frequencies with a 300 THz Femtosecond Laser Comb, Phys. Rev. Lett. **84**, 5102 (2000).

[26] D. J. Jones, S. A. Diddams, J. K. Ranka, A. Stentz, R. S. Windeler, J. L. Hall, and S. T. Cundiff, Carrier-envelope phase control of femtosecond mode-locked lasers and direct optical frequency synthesis, Science **288**, 635 (2000).

[27] V. Petrov, F. Rotermund, and F. Noak, Generation of high-power femtosecond light pulses at 1 kHz in the mid-infrared spetral range between 3 and 12 μm by second-order nonlinear processes in optical crystals, J. Opt. A **3**, R1 (2001).

[28] C. Erny, K. Moutzouris, J. Biegert, D. Kühlke, F. Adler, A. Leitenstorfer, and U. Keller, Mid-infrared difference-frequency generation of ultrashort pulses tunable between 3.2 and 4.8 μm from a compact fiber source, Opt. Lett. **32**, 1138 (2007).

[29] Samuel A. Meek, Antonin Poisson, Guy Guelachvili, Theodor W. Hänsch, and Nathalie Picqué, Fourier transform

spectroscopy around 3 μm with a broad difference frequency comb, Appl. Phys. B **114**, 573 (2014).

[30] Feng Zhu, Holger Hundertmark, Alexandre A. Kolomenskii, James Strohaber, Ronald Holzwarth, and Hans A. Schuessler, High-power mid-infrared frequency comb source based on a femtosecond Er:fiber oscillator, Opt. Lett. **38**, 2360 (2013).

[31] Tyler W. Neely, Todd A. Johnson, and Scott A. Diddams, High-power broadband laser source tunable from 3.0 μm to 4.4 μm based on a femtosecond Yb:fiber oscillator, Opt. Lett. **36**, 4020 (2011).

[32] Joachim Krauth, Andy Steinmann, Robin Hegenbarth, Matteo Conforti, and Harald Giessen, Broadly tunable femtosecond near- and mid-IR source by direct pumping of an OPA with a 41.7 MHz Yb:KGW oscillator, Opt. Express **21**, 11516 (2013).

[33] Axel Ruehl, Alessio Gambetta, Ingmar Hartl, Martin E. Fermann, Kjeld S. E. Eikema, and Marco Marangoni, Widely-tunable mid-infrared frequency comb source based on difference frequency generation, Opt. Lett. **37**, 2232 (2012).

[34] David G. Winters, Philip Schlup, and Randy A. Bartels, Subpicosecond fiber-based soliton-tuned mid-infrared source in the 9.7–14.9 μm wavelength region, Opt. Lett. **35**, 2179 (2010).

[35] D. Sánchez, M. Hemmer, M. Baudisch, K. Zawilski, P. Schunemann, H. Hoogland, R. Holzwarth, and J. Biegert, Broadband mid-IR frequency comb with $CdSiP_2$ and $AgGaS_2$ from an Er,Tm:Ho fiber laser, Opt. Lett. **39**, 6883 (2014).

[36] C. R. Phillips, J. Jiang, C. Mohr, A. C. Lin, C. Langrock, M. Snure, D. Bliss, M. Zhu, I. Hartl, J. S. Harris, M. E. Fermann, and M. M. Fejer, Widely tunable midinfrared difference frequency generation in orientation-patterned GaAs pumped with a femtosecond Tm-fiber system, Opt. Lett. **37**, 2928 (2012).

[37] Tobias Steinle, Andy Steinmann, Robin Hegenbarth, and Harald Giessen, Watt-level optical parametric amplifier at 42 MHz tunable from 1.35 to 4.5 μm coherently seeded with solitons, Opt. Express **22**, 9567 (2014).

[38] Flavio C. Cruz, Daniel L. Maser, Todd Johnson, Gabriel Ycas, Andrew Klose, Fabrizio R. Giorgetta, Ian Coddington, and Scott A. Diddams, Mid-infrared optical frequency combs based on difference frequency generation for molecular spectroscopy, Opt. Express **23**, 26814 (2015).

[39] I. Galli, F. Cappelli, P. Cancio, G. Giusfredi, D. Mazzotti, S. Bartalini, and P. De Natale, High-coherence mid-infrared frequency comb, Opt. Express **21**, 28877 (2013).

[40] Florian Adler, Kevin C. Cossel, Michael J. Thorpe, Ingmar Hartl, Martin E. Fermann, and Jun Ye, Phase-stabilized, 1.5 W frequency comb at 2.8–4.8 μm, Opt. Lett. **34**, 1330 (2009).

[41] Zhaowei Zhang, Tom Gardiner, and Derryck T. Reid, Mid-infrared dual-comb spectroscopy with an optical parametric oscillator, Opt. Lett. **38**, 3148 (2013).

[42] Ville Ulvila, C. R. Phillips, Lauri Halonen, and Markku Vainio, High-power mid-infrared frequency comb from a continuous-wave-pumped bulk optical parametric oscillator, Opt. Express **22**, 10535 (2014).

[43] Alireza Marandi, Kirk A. Ingold, Marc Jankowski, and Robert L. Byer, Cascaded half-harmonic generation of femtosecond frequency combs in the mid-infrared, Optica **3**, 324 (2016).

[44] M. Vainio and L. Halonen, Mid-infrared optical parametric oscillators and frequency combs for molecular spectroscopy, Phys. Chem. Chem. Phys. **18**, 4266 (2016).

[45] Delphine Descloux, Jean-Baptiste Dherbecourt, Jean-Michel Melkonian, Myriam Raybaut, Jui-Yu Lai, Cyril Drag, and Antoine Godard, Rapidly tunable optical parametric oscillator based on aperiodic quasi-phase matching, Opt. Express **24**, 11112 (2016).

[46] Richard A. McCracken, Jinghua Sun, Christopher G. Leburn, and Derryck T. Reid, Broadband phase coherence between an ultrafast laser and an OPO using lock-to-zero CEO stabilization, Opt. Express **20**, 16269 (2012).

[47] Valdas Pasiskevicius, Gustav Strömqvist, Fredrik Laurell, and Carlota Canalias, Quasi-phase matched nonlinear media: Progress towards nonlinear optical engineering, Opt. Mater. **34**, 513 (2012).

[48] Johan Petit, Philippe Goldner, and Bruno Viana, Laser emission with low quantum defect in $Yb:CaGdAlO_4$, Opt. Lett. **30**, 1345 (2005).

[49] U. Keller, K. J. Weingarten, F. X. Kärtner, D. Kopf, B. Braun, I. D. Jung, R. Fluck, C. Hönninger, N. Matuschek, and J. Aus der Au, Semiconductor saturable absorber mirrors (SESAMs) for femtosecond to nanosecond pulse generation in solid-state lasers, IEEE J. Sel. Top. Quantum Electron. **2**, 435 (1996).

[50] Alexander Klenner, Stéphane Schilt, Thomas Südmeyer, and Ursula Keller, Gigahertz frequency comb from a diode-pumped solid-state laser, Opt. Express **22**, 31008 (2014).

[51] A. S. Mayer, A. Klenner, A. R. Johnson, K. Luke, M. R. E. Lamont, Y. Okawachi, M. Lipson, A. L. Gaeta, and U. Keller, Frequency comb offset detection using supercontinuum generation in silicon nitride waveguides, Opt. Express **23**, 15440 (2015).

[52] Adrea R. Johnson, Aline S. Mayer, Alexander Klenner, Kevin Luke, Erin S. Lamb, Michael R. E. Lamont, Chaitanya Joshi, Yoshitomo Okawachi, Frank W. Wise, Michal Lipson, Ursula Keller, and Alexander L. Gaeta, Octave-spanning coherent supercontinuum generation in a silicon nitride waveguide, Opt. Lett. **40**, 5117 (2015).

[53] Alexander Klenner, Aline S. Mayer, Adrea R. Johnson, Kevin Luke, Michael R. E. Lamont, Yoshitomo Okawachi, Michal Lipson, Alexander L. Gaeta, and Ursula Keller, Gigahertz frequency comb offset stabilization based on supercontinuum generation in silicon nitride waveguides, Opt. Express **24**, 11043 (2016).

[54] A. Galvanauskas, K. K. Wong, K. El Hadi, M. Hofer, M. E. Fermann, D. Harter, M. H. Chou, and M. M. Fejer, Amplification in 1.2–1.7 μm communication window using OPA in PPLN waveguides, Electron. Lett. **35**, 731 (1999).

[55] S. Schilt, V. Dolgovskiy, N. Bucalovic, C. Schori, M. C. Stumpf, G. Di Domenico, S. Pekarek, A. E. H. Oehler, T. Südmeyer, U. Keller, and P. Thomann, Noise properties of an optical frequency comb from a SESAM-mode-locked 1.5-μm solid-state laser stabilized to the 10^{-13} level, Appl. Phys. B **109**, 391 (2012).

[56] Nathan R. Newbury, Ian Coddington, and William Swann, Sensitivity of coherent dual-comb spectroscopy, Opt. Express **18**, 7929 (2010).

[57] K. L. Corwin, N. R. Newbury, J. M. Dudley, S. Coen, S. A. Diddams, B. R. Washburn, K. Weber, and R. S. Windeler, Fundamental amplitude noise limitations to supercontinuum spectra generated in a microstructured fiber, Appl. Phys. B **77**, 269 (2003).

[58] T. Godin, B. Wetzel, T. Sylvestre, L. Larger, A. Kudlinski, A. Mussot, A. Ben Salem, M. Zghal, G. Genty, F. Dias, and J. M. Dudley, Real time noise and wavelength correlations in octave-spanning supercontinuum generation, Opt. Express **21**, 18452 (2013).

[59] R. Baumgartner and R. Byer, Optical parametric amplification, IEEE J. Quantum Electron. **15**, 432 (1979).

[60] A. V. Smith, D. J. Armstrong, and W. J. Alford, Increased acceptance bandwidths in optical frequency conversion by use of multiple walk-off-compensating nonlinear crystals, J. Opt. Soc. Am. B **15**, 122 (1998).

[61] C. R. Phillips, Carsten Langrock, J. S. Pelc, M. M. Fejer, I. Hartl, and Martin E. Fermann, Supercontinuum generation in quasi-phasematched waveguides, Opt. Express **19**, 18754 (2011).

[62] C. R. Phillips, Ph.D. thesis, Stanford University, 2012.

[63] R. V. Roussev, Ph.D. thesis, Stanford University, 2006.

[64] Ichiro Shoji, Takashi Kondo, Ayako Kitamoto, Masayuki Shirane, and Ryoichi Ito, Absolute scale of second-order nonlinear-optical coefficients, J. Opt. Soc. Am. B **14**, 2268 (1997).

[65] Bauke W. Tilma, Mario Mangold, Christian A. Zaugg, Sandro M. Link, Dominik Waldburger, Alexander Klenner, Aline S. Mayer, Emilio Gini, Matthias Golling, and Ursula Keller, Recent advances in ultrafast semiconductor disk lasers, Light Sci. Appl. **4**, e310 (2015).